ISBN 978-82-471-9063-0 (printed ver.)
ISBN 978-82-471-9077-7 (electronic ver.)
ISSN 1503-8181

Paul E. Thomassen

Theses at NTNU, 2008-149

NTNU

NTNU
Norwegian University of
Science and Technology
Thesis for the degree of
philosophiae doctor
Faculty of Engineering Science and Technology
Department of Marine Technology

Doctoral Theses at NTNU, 2008-149

Paul E. Thomassen

Methods for Dynamic Response Analysis and Fatigue Life Estimation of Floating Fish Cages

Paul E. Thomassen

Methods for Dynamic Response Analysis and Fatigue Life Estimation of Floating Fish Cages

Thesis for the degree of philosophiae doctor

Trondheim, May 2008

Norwegian University of
Science and Technology
Faculty of Engineering Science and Technology
Department of Marine Technology

NTNU
Norwegian University of
Science and Technology

NTNU
Norwegian University of Science and Technology

Thesis for the degree of philosophiae doctor

Faculty of Engineering Science and Technology
Department of Marine Technology

ISBN 978-82-471-9063-0 (printed ver.)
ISBN 978-82-471-9077-7 (electronic ver.)
ISSN 1503-8181

Theses at NTNU, 2008-149

Printed by Tapir Uttrykk

ABSTRACT

The present thesis is an effort to introduce state-of-the art methods for analysis of marine structures in relation to fatigue design of floating fish cages made of steel when they are exposed to wave loading.

Structural fatigue problems have been identified as a likely frequent cause for the collapse of floating fish farms made of steel by previous authors. The principal objective of this thesis is to improve the capabilities of fatigue analysis of floating fish farms exposed to waves through three steps:

- Development of a hydrodynamic and structural model appropriate for structural analysis within an engineering context.
- Development of a prototype software tool based on the Finite Element Method (FEM).
- To perform a parameter study employing the developed tool.

All the presented analysis results are related to a Base Case Structure (BCS). This is a simplified floating fish farm consisting of only one cage. The cage is $30\,m$ by $30\,m$ and is made of steel pipes with $1\,m$ diameter. Each corner has a horizontal, linear mooring in each perpendicular direction. The netpen is represented as linear damping — horizontally and vertically.

A set of four typical regular waves (TRW) have first been defined corresponding to the wave classes given in NS 9415. The wave height varies from $1\,m$ to $5.7\,m$ and the wave period from $2.5\,s$ to $6.7\,s$. The TRW are applied for representation of the wave climate based on regular waves. The hydrodynamic load model is a combination of linear potential theory and horizontal drag for the floater and horizontal and vertical drag damping for the netpen. It has been shown that the vertical wave force can be conservatively approximated as the product of water plane stiffness and wave surface elevation: $F_{vert} = k_w\zeta$. The potential damping is quite high, typically between 15 and 20%. The total damping level is up to 30% horizontally and 40% vertically. For the nonlinear analysis, the instantaneous water plane stiffness is taken into account.

The rigid body natural periods have values between $1.7\,s$ and $2.4\,s$. The highest flexural natural period is approximately $0.6\,s$.

The discretization of the structure is based on the FEM and the time integration is based on the Newmark-β method with $\beta = 0.25$ and $\gamma = 0.5$, i.e. constant average acceleration. This method is unconditionally stable for a linear system. Linear 3D beam

elements were used to model the floater and linear springs were used to model the mooring and the buoyancy. In the nonlinear analysis the buoyancy springs were nonlinear. The structural and added mass as well as the hydrodynamic damping were lumped. The structural damping was modeled using Rayleigh damping.

Comparison of linear and nonlinear analysis in regular waves shows that the nonlinear effects increase with wave height. Typically, when the cross section is fully submerged or dry in the nonlinear analysis the bending moments about the horizontal axis do not exceed certain limiting values.

The fatigue analysis for irregular waves were based on SN curves, the Miner-Palmgren rule, and rainflow counting. The software library WAFO was used. SN curves C2 and F were chosen to be used in the parameter study. Further, the parameter study was based on wave class C. The wave scatter diagram was generated from a Weibull distribution of the mean wind speed. A JONSWAP wave spectrum was used with a peakedness factor of 3.3. All waves are assumed to be long-crested and perpendicular to the BCS. The critical details are assumed to be located at the top of the mid-sections for both a perpendicular and a parallel cylinder, i.e. the bending moment about the horizontal axis is applied for computation of the stress range.

Fatigue analysis based on regular waves showed that the results are very sensitive to the wave period. Regular waves are therefore not recommended to be used for fatigue analysis. This recommendation also applies to the Ultimate Limit State.

For irregular waves, the nonlinear analysis gave approximately twice the fatigue life found from linear analysis. The difference between fatigue damage increases with significant wave height. This implies that the linear damage will be dominated by higher significant wave heights than for the nonlinear analysis.

The low level of the maximum stress range leads to the assumption that the fatigue limit state will be decisive for design. Additionally, the stress range interval dominating the fatigue damage will be in the domain governed by $m = 5$ (low stress range and high number of cycles) in the two-slope SN curves, i.e. the fatigue damage is very sensitive to the stress range.

Fitting a two parameter Weibull distribution to short-term and long-term stress ranges showed that a simplified method based on a long-term Weibull distribution can not be recommended.

Acknowledgment

The PhD-study resulting in this dissertation was supervised and inspired by Professor Bernt J. Leira, Department of Marine Technology, NTNU. I am grateful for his guidance, patience, and friendship through the ups and downs of this doctoral journey. I hope we can continue our cooperation in the future. My co-supervisor was Associate Professor Ludvig Karlsen, Department of Marine Technology. His practical knowledge and understanding of the Norwegian fish farming industry has been most valuable. Professor Odd M. Faltinsen and Professor Dag Myrhaug gave valuable suggestions regarding the hydrodynamic model and the wave model, respectively.

I want to thank the members of my committee Professor Gregory R. Miller (University of Washington), Dr. Daniel N. Karunakaran (Subsea 7), and Professor Bjørnar Pettersen (NTNU) for their participation and valuable comments.

The software developed as a part of this dissertation was based on the finite element framework developed by Dr. Jae Won Jang and Professor Gregory R. Miller, University of Washington. I want to express my sincere appreciation to them for sharing their work.

Many members of various branches of the fish farming industry have been forthcoming and helpful. In particular, I want to thank Ketil Roaldsnes (Noomas Sertifisering AS) and Alf E. Lønning (Bømlo Construction AS).

My many visits to the library for marine technology at Tyholt have always been a pleasant and uplifting experience due to the friendly and helpful staff. The staff has changed, but the friendliness has been consistent. I want to thank all the library staff members over the last five years for helping me out and putting me in a good mood.

My studies were funded by a scholarship from the strategic program Marine and Maritime Technology at NTNU. Additional funding were provided by the Department of Marine Technology. Finally, monetary (and moral) support were provided at a time when it was most needed by the *Eli og Jens Eggvins fond til fremme av norsk havforskning* at the Institute of Marine Research, Bergen.

The work with this dissertation has been a long journey for me and those closest to me. It has mostly been a pleasant one — at least looking back. My wife Elin has been my greatest fan and has made it all possible. She gave birth to Birk, Alvar, and Nora over the course of this work and they have all been a constant reminder that getting a PhD is not the only important thing in life... This dissertation is dedicated to Elin and our children.

Nomenclature

Latin symbols

Symbol	Description
A_{ii}	Added mass in direction i
$A_{w,buoy}$	Water plane area of mooring buoy used in BCS
A_{steel}	Steel area of cross section (pipe) used in BCS
A_{buoy}	Buoyancy area of cross section (pipe) used in BCS
A_{sub}	Submerged area of pipe
A_w	Water plane area
a_i	Undisturbed water particle acc. component at $z = 0$ in the dir. i
a_1	Undisturbed horizontal fluid particle acceleration
D	Outer diameter of the pipe used in the BCS
B_{distr}	Distributed buoyancy of the pipe used in the BCS
B_{buoy}	Buoyancy of mooring buoy used in the BCS
C_D	Drag coefficient of Morison's equation
$C_{D,y}$	Drag coefficient of yarn
C_M	Mass coefficients of Morison's equation
C_m	Diffraction part of C_M
$C_{m,eq,i}$	Equivalent added mass coefficient in direction i
D	Accumulated fatigue damage. Or outer diameter of pipe used in BCS (i.e. D_{pipe})
$D_{sc,1y}$	Fatigue damage for 1 year assuming only one wave height/wave period combination (for regular waves)
$D_{sc,t}$	Fatigue damage for a duration t assuming only one seastate
D_{L_0}	Fatigue damage corresponding to L_0
$D_{N=1}$	Fatigue damage for one stress cycle
D_{buoy}	Diameter of mooring buoy used in BCS
D_{pipe}	Outer diameter of pipe used in BCS
D_y	Diameter of yarn
DAF	Dynamic amplification factor

Continued on next page

Symbol	Description
DAF_m	Maximum dynamic amplification factor
d	Draft of the pipe used in the BCS
E	Modulus of elasticity for steel
F	Fetch
$F_{diff,i}$	Amplitude of diffraction force in direction i
$F_{drag,a}$	Amplitude of drag load
F_{el}	Elastic axial force capacity
F_{mass}	Mass force
$F_{mass,a}$	Amplitude of mass force
$F_{FK,x}$	Froude-Kriloff force in horizontal direction
$F_{FK,z}$	Froude-Kriloff force in vertical direction
F_{pre}	Pretensioning in mooring lines used in the BCS
f_y	Yield stress for steel
G	Shear modulus for steel
g	Acceleration of gravity
H	Wave height of regular wave
H_{max}	Maximum wave height of regular wave
H_s	Significant wave height
$H_{1/7}$	Wave height corresponding to maximum wave steepness
h	Shape parameter of a 2-parameter Weibull distribution
h_{buoy}	Height of mooring buoy used in BCS
I	2. moment of inertia
I_T	St. Venant's torsion constant
I_p	Polar moment of inertia
I_w	Warping constant
KC	Keulegan-Carpenter number
k_{moor}	Stiffness of mooring line used in BCS
k^*_{moor}	Stiffness of mooring line used in BCS at full submergence
k_w	Water plane stiffness
$k_{w,max}$	Maximum water plane stiffness
L	Fatigue life
L_0	Design fatigue life
L_{pipe}	Length of pipes used in BCS
L_{sc}	Fatigue life assuming only one seastate (irregular waves) or one wave height/wave period combination (regular waves)
l_w	Water plane length
M_a	Moment amplitude

Continued on next page

Symbol	Description
M_{el}	Elastic bending moment capacity
M_{pl}	Plastic bending moment capacity
M_T	Elastic torsional moment capacity
m	Negative inverse slope of SN curve
m_{cage}	Mass of BCS (four pipes)
m_{distr}	Distributed mass of pipe used in BCS
m_{pipe}	Mass of one pipe used in BCS
N	Predicted number of cycles for to failure for stress range $\Delta\sigma$
p_{sc}	Percentage of occurrence of the seastate sc
p_D	Dynamic pressure
q	Scale parameter of a 2-parameter Weibull dsistribution
r	Outer radius of the pipe used in the BCS
s_{buoy}	Relative submergence of mooring buoy used in BCS
S	Stress range ($= \Delta\sigma$) or wave elevation spectrum
T_1	Mean wave period of the wave spectrum
$T_{1/7}$	Wave period corresponding to maximum wave steepness
T_p	Peak period of the wave spectrum
t_{pipe}	Thickness of pipe used in BCS
U	Averaged 10 minutes mean wind
$\bar{U}_{10}$	10 minutes mean wind at $10m$ above the sea surface/ground
U_A	Adjusted wind speed
u	Undisturbed horizontal fluid particle velocity
W_{el}	Elastic section modulus
w_w	Water plane width
w_0	Initial vertical position of the center of the pipe used in the BCS
w	Instantaneous vertical response of the center of the pipe used in the BCS

Greek symbols

Symbol	Description
α	Scale parameter of the JONSWAP spectrum
α_0	Angle of mooring line
β	Frequency ratio
γ_m	Material coefficient for steel or peakedness parameter of s JONSWAP spectrum
$\Delta\alpha_{el}$	Additional rotation of mooring line at full submergence
Δ_{el}	Maximum elastic (mid-span) deformation
$\Delta_{h,el}$	Horizontal displacement of mooring buoy at full submergence

Continued on next page

Symbol	Description
Δ_r	Relative response amplitude
Δ_{stat}	Static response
$\Delta_{v,el}$	Vertical displacement of mooring buoy at full submergence
$\Delta\sigma_0$	Maximum stress range over the (fatigue) lifetime of the structure
$\Delta\sigma_{0,sc}$	Maximum stress range for a particular seastate in the case of irregular waves and for a particular wave height/wave period-combination in the case of regular waves
ζ_a	Amplitude of surface elevation
η	Usage factor or displacement
η_1	Horizontal response of cylinder
Φ	Phase angle
xi	Wave surface elevation
xi_a	Wave surface elevation amplitude
λ	Wave length
λ_{min}	Wave length for regular wave with maximum steepness
ν	Poisson's ratio for steel
ρ_{steel}	Density of steel
ρ_w	Density of sea water
σ_a	Shape parameter of the JONSWAP spectrum
σ_b	Shape parameter of the JONSWAP spectrum
ω	Circular wave frequency
ω^*	Nondimensional wave frequency
ω_p	Peak circular frequency of a wave spectrum

Abbreviations

	Description
BCS	Base Case Structure
COV	Coefficient of Variation
DAF	Dynamic Amplification Factor
DFF	Design Fatigue Factor
DOF	Degree of freedom
DSA	Deterministic Spectral Amplitude
FEM	Finite Element Method
FDA	Frequency Domain Analysis
FFT	Fast Fourier Transform
FK	Froude-Kriloff
GUI	Graphical User Interface
KC	Keulegan-Carpenter

Continued on next page

	Description
LD	Linearized Drag
LPT	Linear Potential Theory
JONSWAP	Joint North Sea Wave Project
NSA	Nondeterministic Spectral Amplitude
NTNU	Norwegian University of Science and Technology
OO	Object Oriented
PM	Pierson-Moskowitz
SCF	Stress Concentration Factor
SFA	SINTEF Fisheries and Aquaculture
TDA	Time Domain Analysis
TRW	Typical Regular Wave
WWF	World Wildlife Foundation

Contents

Abstract i

Acknowledgment iii

Nomenclature v

Contents xi

1 Introduction and Background 1
- 1.1 Vision . . . 1
- 1.2 Principal objectives . . . 1
- 1.3 Brief account of salmon escape . . . 2
- 1.4 From *trial-and-error* to *state-of-the-art*? . . . 3
- 1.5 Method of approach . . . 4
  - 1.5.1 Improvements along three axes . . . 5
  - 1.5.2 Structural simplicity . . . 5
  - 1.5.3 Waves vs. current . . . 5
  - 1.5.4 Leveraging the power of computer technology advances . . . 6
- 1.6 Previous work . . . 6
- 1.7 Outline of the thesis . . . 9

2 The Floating Fish Cage Structure 11
- 2.1 The floating fish cage concept . . . 11
  - 2.1.1 Floater . . . 11
  - 2.1.2 Mooring . . . 13
  - 2.1.3 Netpen . . . 13
- 2.2 The Base Case Structure . . . 14
  - 2.2.1 Rigid steel floater . . . 14
  - 2.2.2 Horizontal linear mooring . . . 19
  - 2.2.3 Netpen . . . 21

3 The Wave Loading Regime 23
- 3.1 Typical wave environment . . . 23
  - 3.1.1 Wave classes in NS 9415 . . . 23

3.1.2 Wave prediction for wind generated waves . . . 24
3.1.3 Typical Regular Waves (TRW) . . . 26
3.2 Wave loading for a floating, horizontal cylinder . . . 27
3.2.1 Water plane stiffness . . . 28
3.2.2 Buoyancy . . . 29
3.2.3 Hydrodynamic classification . . . 30
3.2.4 Submerged cylinder . . . 32
3.3 Linear analysis of the floater . . . 38
3.3.1 Motion of a floating rigid body . . . 38
3.3.2 Added mass and potential theory damping . . . 39
3.3.3 Excitation forces based on potential theory . . . 42
3.3.4 Linearized horizontal drag for the floater . . . 45
3.3.5 Linearized drag damping of the netpen . . . 47
3.3.6 Total damping in heave and sway . . . 49
3.3.7 Summary of the linear wave loading model . . . 51
3.4 Nonlinear analysis of the floater . . . 53
3.4.1 Nonlinear hydrodynamic effects . . . 53
3.4.2 Implementation of nonlinear buoyancy . . . 55

4 Static Analysis and Natural Periods 57
4.1 Static analysis . . . 57
4.2 Natural periods . . . 59
4.3 Vertical resonance . . . 61
4.3.1 Qualitative evaluation . . . 61
4.3.2 Linear heave . . . 62
4.3.3 Nonlinear heave . . . 63
4.4 Horizontal resonance . . . 65
4.4.1 Qualitative evaluation . . . 65
4.4.2 Linear sway . . . 65
4.5 Flexural natural periods . . . 67

5 Structural Dynamic Analysis 71
5.1 Nonlinear time domain analysis . . . 71
5.2 Linear dynamic analysis . . . 71
5.2.1 Stiffness . . . 71
5.2.2 Mass . . . 72
5.2.3 Damping . . . 72
5.2.4 Load modeling . . . 74
5.2.5 Time integration . . . 75
5.2.6 Choice of time step . . . 75
5.2.7 Disturbances from initial conditions . . . 75
5.3 Nonlinear dynamic analysis . . . 75
5.3.1 Nonconstant water plane stiffness . . . 76

5.3.2 Nonlinear load . . . 76
5.3.3 Modified Newton-Raphson iteration . . . 76
5.3.4 Convergence criteria . . . 77
5.3.5 Choice of time step . . . 77

6 Software Tools and Development 79
6.1 FEM software options . . . 79
6.2 The framework . . . 80
6.3 The prototype . . . 81
6.4 Use and extensions of the framework . . . 83
6.5 Additional software used . . . 84

7 Regular Wave Parameter Study 85
7.1 Analysis procedure . . . 85
7.1.1 Verification of steady state conditions . . . 86
7.2 Single cylinder . . . 87
7.2.1 Perpendicular cylinder . . . 87
7.2.2 Parallel cylinder . . . 92
7.3 Sensitivity to time step and element length . . . 95
7.4 Sensitivity to wave period in a linear analysis . . . 96
7.5 Sensitivity to damping . . . 97
7.6 Perpendicular wave direction . . . 99
7.7 Oblique wave direction . . . 103

8 Fatigue Analysis Procedure 107
8.1 Loading . . . 108
8.1.1 The stress range history . . . 108
8.1.2 Irregular waves . . . 109
8.1.3 The relevant stress component . . . 109
8.2 Resistance . . . 110
8.3 Design criteria . . . 111
8.3.1 Miner-Palmgren law . . . 111
8.3.2 Fatigue analysis using a scatter diagram . . . 111
8.3.3 Simplified fatigue analysis . . . 113
8.4 Fatigue design of the BCS . . . 114
8.4.1 Loading . . . 114
8.4.2 Resistance . . . 122
8.5 Summary: Suggested methodology . . . 127

9 Fatigue Analysis Parameter Study 129
9.1 Regular waves . . . 129
9.1.1 Sensitivity to wave period in a nonlinear analysis. . . . 130
9.1.2 Analysis based on scatter diagram . . . 132

9.1.3 Maximum stress range . . . 135
9.2 The irregular wave implementation . . . 135
9.3 Sensitivity to analysis duration . . . 137
9.4 Sensitivity to peak period . . . 140
9.5 Sensitivity to significant wave height . . . 143
9.6 Peak period vs. significant wave height sensitivity . . . 145
9.7 Analysis based on scatter diagram . . . 147
9.8 Statistical properties of stress range distributions . . . 148
9.8.1 Weibull probability paper . . . 150
9.8.2 Stress range histograms and damage plots . . . 153
9.8.3 Short-term distributions . . . 157
9.8.4 Long-term distribution . . . 162
9.8.5 Applicability of the simplified method . . . 167
9.9 Implications for the Ultimate Limit State . . . 170

10 Conclusions and Further Work **171**
10.1 Fatigue analysis and irregular waves . . . 171
10.2 Statistical distribution of stress range . . . 172
10.3 Recommendations for further work . . . 173

References **175**

A Natural modes **185**

B Screenshots from Dr.Frame3D **189**

C Quotes from relevant codes **193**
C.1 Parts of NS 9415 relevant for fatigue design . . . 193
C.1.1 Wind . . . 193
C.1.2 Peakedness factor . . . 193
C.1.3 Design working life . . . 194
C.1.4 Fatigue design . . . 194
C.2 Design working life in NS-EN 1990 . . . 195
C.3 DFF in DNV-OS-C101 Design of offshore steel structures . . . 196

D Scatter Diagram **199**

E The Beaufort Wind Scale **201**

F Linear system **203**

G Tables **205**

Chapter 1

INTRODUCTION AND BACKGROUND

1.1 Vision

The vision of this thesis is that improving the structural analysis of floating fish cages will reduce the occurrences of structural failure due to environmental loads and thereby reduce accompanying escape of fish causing environmental damage and economic loss.

1.2 Principal objectives

This thesis has three principal objectives:

1. Increase the hydrodynamic and structural understanding of a floating fish cage system

To develop and use methodologies as well as (software) tools effectively and correctly, a good understanding of the structural system is essential.

The structural system — exemplified by a base case structure (BCS) — is investigated from both a theoretical and numerical (i.e. parameter study) point of view. Of particular interest are:

- Dynamic characteristics, i.e. natural periods, structural and hydrodynamic damping, as well as added mass.
- The interaction between the loading and the structure.
- Linear vs. nonlinear analysis
- The relative importance of the different load components and load effects
- Short-term and long-term statistical distribution of stress ranges.

2. Propose and investigate a methodology for fatigue design suitable in an engineering context.

Several authors (e.g. (Ormberg, 1991) and (Lien et al., 2006)) have identified fatigue failure as an important limit state for steel floaters, and the lack of a verified methodology is one of the factors that renders a reliable analysis within an engineering context virtually impossible. A methodology is suggested largely building on *state-of-the-art* in related disciplines of fatigue design of steel structures. The basis is a dynamic, nonlinear finite element analysis in the time domain, including the use of wave spectrum and scatter diagram. However, opposed to what has typically been the case, it is a guiding assumption that it is realistic (even within an engineering context) to perform a time domain analysis based on the complete scatter diagram given the ever present improvements in computer technology. After suggesting and implementing a fatigue methodology, a parameter study has been performed to investigate important aspects of fatigue design of floating fish cages.

3. Develop a software tool that facilitates the previous two objectives.

Structural analysis and design of floating fish cage systems is highly complex and requires specialized software. Thus, the development of a software tool based on the finite element method was defined as a principal objective. The tool was given functionality to be used in an engineering design context as well as to investigate the methodology implemented in it.

1.3 Brief account of salmon escape

Fish farming in Norway has from its beginning in the 1970s grown to a multi billion euro industry of great importance and future potential for the nation. Despite this obvious success story, there are problems that must be tackled to assure sound future foundations for the industry. Among these problems are escape of domesticated fish. Escaped salmon is believed to be a serious threat to the wild Atlantic salmon in Norway, in particular through genetic pollution.

Over the last years the possible environmental problems connected to the escape of farmed salmon in the ocean has received more attention as the industry does not seem to have the situation under control. Each year, hundreds of thousands of bred salmon are reported to have escaped from floating fish cages (Fiskeridirektoratet, 2007). According to statistics from Fiskeridirektoratet (Directorate of Fisheries), the main cause for escape of salmonoid fish from 2001 to September 2006 was failure of equipment. This category represented 52% of the total number of escaped fish (Bellona, 2007) and includes structural failures in bad weather conditions. However, the proportion of the subcategory structural failures is not specified.

Two important trends of the industry have probably worsened problems with structural failures:

- More exposed locations are being used, thus leading to higher exposure to waves and current
- The size (circumference) of the floaters and netpens are increasing to enable a higher number of fish in each cage, thus increasing the consequences of a collapse, and at the same time introducing new and untested structures.

Environmental organizations and others have called for restrictions on the industry due to the problem of escape, see e.g. (WWF Norge, 2006). One response to salmon escape from the Norwegian government has been to close several fjords for further fish farming development, despite protests from the industry. The Government views escape as the most important environmental challenge facing the fish farming industry (Regjeringen, 2007), and in 2006 the Aquaculture Escape Commission (Rømmingskommisjonen for akvakultur, 2007) was established to investigate and learn from serious escape incidents.

The Institute of Marine Research says in their 2007 annual report of Norwegian aquaculture (Dahl, 2007) that the level of escape is far too high and states the following:

- The fish farming industry must take the problem of escape much more seriously
- Most reported escapes are due to equipment failure in bad weather
- Mapping the extent and cause of escape should be implemented immediately.

The Norwegian Research Council has presented the results of their aquaculture research program from 2000 to 2005 (Thomassen, 2006). One of the main goals of *Subprogram 7 Technology and equipment* was to produce knowledge with the potential to reduce escape by 50%. It is concluded that this goal has not been reached, due to lack of funding.

If the industry does not come to grips with escape of salmon, further economically damaging restrictions can be introduced to protect the wild Atlantic salmon. More importantly, the escape of salmon can seriously damage the public perception of the industry as a whole. Judging by the 2006 annual report of the worlds biggest fish farming corporation (Marine Harvest, 2006) it appears that the industry now *is* taking the problem seriously. The report has four references to escape, i.a. stating:

> (...) storms that result in damaged sea cages and escapes of fish (...) are environmental factors that can cause serious set-backs in production and economic loss. Although Marine Harvest has a zero tolerance for escapes, we have still not been able to prevent them entirely. This is not satisfactory, and we must continue to focus on this issue until our goal has been reached.

1.4 From *trial-and-error* to *state-of-the-art*?

Whereas advanced structural analysis are — and have been for decades — commonplace in related industries such as the offshore petroleum industry, structural analysis has been virtually absent in the design of floating fish cage systems to the benefit of *trial-and-error*

based design coupled with engineering judgment. Among the most important reasons for this are:

- Structural collapse has not led to the loss of human lives
- The economic losses have been limited for the industry as a whole
- The Government has not demanded structural analysis for fish cage structures (as opposed to e.g. offshore petroleum structures and onshore structures).
- The structural system is complicated, and neither an established analysis methodology nor necessary analysis tools readily available.
- Structural analysis services have been offered neither by academia nor commercially.
- Limited research interest and funding as well as engineering experience

To summarize: up until recently there has been neither the supply nor the demand for structural analysis of floating fish cages. However, the introduction of structural analysis *has* been on the agenda as a possible means to reduce escape of fish for more than a decade. The emphasis has been on structural analysis more in the form of a code check after the design has been done than as a tool in the design process. The rationale behind moving away from the trial-and-error regime to requiring structural analysis of floating fish farms is the assumption that it will provide safer structures and thereby reduce escape. It is assumed that a significant number of escapes today are caused by structural collapse due to environmental loads, see Section 1.3.

After years of to and fro, the code approach materialized in regulations for aquaculture systems accompanied by a Norwegian standard: *NS 9415 Marine Fish Farms. Requirements for Design, Dimensioning, Production, Installation and Operation* (Standard Norge, 2003). The code requires that the four common limit states are covered: ultimate, accidental, fatigue, and serviceability. However, as there are indeed no established methodology for analysis and design of floating fish cages, NS 9415 does not present any approach or methodology to an engineering level.

The code was published in August 2003 and the regulations went into effect January 1, 2006. Both a certification of every farm type as well as design check of plants on every location along the coast are required. Certifications and design checks are performed by companies accredited by Norsk Akkreditering (2007).

1.5 Method of approach

The work related to the present thesis has been shaped by some guiding principles briefly discussed below.

1.5.1 Improvements along three axes

There are several interrelated issues connected to structural analysis of floating fish cage systems. As opposed to focusing our research on one particular issue, we have made the choice to work with three topics, briefly discussed in the beginning of this chapter as the principal objectives and more thoroughly in the relevant chapters.

This choice was made because the usefulness of progress along a single axis is only realized by progress along the others, e.g. a seemingly excellent software tool is of limited use if we have no reason to trust the implemented load models and design methodologies. In other words: a chain is not stronger than its weakest link.

1.5.2 Structural simplicity

In structural analyses of floating fish cages previously published (e.g. (Ormberg, 1991), (Berstad et al., 2004)), the approach has been to analyze a complete floating fish farm, despite significant known uncertainties in loading models, structural models, and analysis and design methodology.

It is the view of the author that shortcomings in the state-of-the-art of floating fish cage structural engineering leads to a high level of uncertainty. Accordingly, instead of looking at a complete fish farm system, we start with a basic case and build our knowledge from there.

Although simplified, studying the base case structure (BCS) will give a better understanding of the structural behavior and characteristics of floating fish cages in general. Further, these are cases where analysis results should be accepted and verified before an analysis of a complete floating fish farm is the main focus. Thus, a complete facility with multiple cages hinged together is considered outside the scope of this work. In short, to uncover the structural response characteristics of a floating fish cage system, we must first understand the behavior of its basic components.

1.5.3 Waves vs. current

Both waves and current are of principal importance for a complete structural analysis of a floating fish cage system. In addition to structural integrity, waves and current are important for several operational aspects. In particular, current can severely deform (i.e. reduce the volume of) the netpen and thereby endanger the well-being of the fish. Waves can hamper operations by causing significant movement of the floater.

The relative importance of waves vs. current in a structural analysis depends on both the limit state and the structural component in question.

Although both kinds of loading should be assumed to act simultaneously, it can be a reasonable approach to first consider the main source to act alone for the sake of simplifying the problem to a manageable level.

As fatigue analysis of the floater is a main focus in the present thesis, the scope has been limited to only consider waves. Although, current will change the average (quasistatic)

loading of the floater, it is assumed the effect of waves on the dynamic stress fluctuations is not significant, i.e. current is not essential for the fatigue damage.

1.5.4 Leveraging the power of computer technology advances

The speed of advances in computer technology has in many ways become a cliché. Up until a few years ago, increasing the frequency (clock rate) of computer processors (CPUs) was the dominant force in computer performance increases, see e.g. (Wikipedia, 2008b). In the last few years the industry focus has shifted to multicore processors, see e.g. (Wikipedia, 2008c). Fatigue analysis based on multiple time domain analysis, which is the focus of the present work, lends itself very well to benefit from the new trend also as several simulations can be run independently.

Increased computer capabilities in general merit that we take a fresh look at approaches that earlier seemed impossible or unrealistic in practice. What was not deemed feasible then might be highly relevant today. Although speed of calculations is obviously important for structural engineering, advances within other arenas of computer science (such as graphics and GUI libraries) can also open up new, exciting, and foremost useful opportunities.

In this thesis we try to exploit the advances in computer science for marine structural analysis particularly by employing:

- Lengthy nonlinear time simulations
- Real-time analysis and visualization capabilities
- Integration of the analysis process within a convenient user interface

1.6 Previous work

Research efforts focusing particularly on environmental loading and structural design of (floating) fish farms appears to have been very limited prior to the end of the 1980's when it became apparent that escape of salmon could become a serious problem. Cairns and Linfoot (1990) wrote:

> There have been a significant number of incidents in Scottish waters where sea cage flotation collars have broken up, which demonstrates the need for improved design guidance on structural matters. A recent study of the research needs of the fish farming industry noted the lack of design guidance for ongrowing equipment.

DNV (1988) published tentative rules for certification of floating fish farms, but these rules were never adopted. At MARINTEK in Trondheim an early focus was on current forces on net structures, see (Aarsnes et al., 1990), (Løland, 1991). Also, Ormberg (1991) extended the existing FEM program RIFLEX (SINTEF, 1987) to perform dynamic, nonlinear analysis of floating fish farms in regular waves. The results were compared to model tests.

Recently, Bonnemaire and Jensen (2006) have reported good results using RIFLEX for structural analysis of a floating fish farm. Of particular interest for this work is the future work suggested by Ormberg (1991), i.e. that an irregular wave approach should be used for fatigue design, that the wave excitation load model should be improved, and that model tests with simple cross sections subjected to well defined waves should be performed.

Analysis of net structures have been and is still a focus area for researchers at MARINTEK's sister organization SINTEF Fisheries and Aquaculture (SFA). Both experimental and numerical results have been reported, see e.g. (Fredheim, 2005), (Lader and Fredheim, 2006), (Lader et al., 2007b), (Lader et al., 2007a), (Lader et al., 2008). Recent areas of research for SFA is the employment of tensegrity structures in floating fish farms (Wroldsen et al., 2006), (Jensen et al., 2007) and the material properties of the netpen (Moe et al., 2007).

In addition to the SINTEF/NTNU cluster in Trondheim, the most important location for research in hydrodynamics and structural engineering of fish farms has probably been the University of New Hampshire's Atlantic Marine Aquaculture Center (www.ooa.unh.edu), established in 1997 as the Open Ocean Aquaculture Project. They have been operating their own fish farm which has been used for full-scale measurements (in addition to fish farming). The measurements have been compared to numerical analysis, see (Fredriksson et al., 2004), (Fredriksson et al., 2005). Also, comparison with model tests have been reported, see e.g. (Fredriksson et al., 2003). The development of the FEM analysis software AquaFE (a.k.a. Ocean-FEA) was an early focus area, see (Gosz et al., 1996), (Swift et al., 1997), (Tsukrov et al., 2000). In his PhD thesis Fredriksson (2001) investigated dynamic behavior of both a submerged and floating, circular fish farm. Modeling and experimental verification of net panels have been addressed in (Tsukrov et al., 2003), (Swift et al., 2006). Recently, work related to the use of plastic floaters (see Section 2.1.1) in industry size fish farms have been published, see (Fredriksson et al., 2007a), (Fredriksson et al., 2007b).

Researchers at the certification company Aquastructrues (www.aquastructures.no) have published numerical results obtained from their own FEM software tool AquaSim and from model tests, see e.g. (Berstad et al., 2004), (Berstad et al., 2005), (Berstad and Tronstad, 2005). The latter article compares regular and irregular wave loading and concludes that "It is in general conservative to use a regular design wave approach based on wave height = 1.9 Hs."

At Pukyong National University, Korea, researchers have been working with numerical simulation and model tests applicable to fish farms and fishing gear, see e.g. (Lee et al., 2004), (Lee et al., 2005b), (Lee et al., 2005a). At the Bulgarian Ship Hydrodynamics Center model tests have been performed for a floater very similar to the floater used in the base case structure of the present thesis, see (Kishev et al., 2004), (Kishev et al., 2006). More recently, at Dalian University of Technology, China, and National Cheng Kung University, Taiwan, numerical end experimental investigations related to gravity cages (i.e. floating cages) and net structures have been performed, see e.g. (Gui et al., 2006), (Li et al., 2006), (Li et al., 2007), (Yang et al., 2007).

Intermediate results of the present PhD work have been published in (Thomassen and Leira, 2005) and (Thomassen and Leira, 2006).

Of particular interest and importance for the present work are the references above related to:

- Numerical analysis and experimental investigation of wave forces and damping models for a square floater and/or a straight pipe.

- Numerical analysis and experimental investigation of wave forces and damping models for the netpen.

- Numerical analysis of fatigue damage of floaters in steel.

Wave models for the floater can be grouped in two main categories, either they are focused on adapting Morison's equation (see (Morison et al., 1950)) for slender, floating objects, or (linear) potential theory is used as the starting point. E.g. the models applied by (Wroldsen et al., 2006), (Li et al., 2007), and (Fredriksson et al., 2007b) belong to the former group, whereas (Ormberg, 1991) is the only reference found with a discussion of a wave model based on potential theory. While current loading probably can be effectively modeled based on Morison's equation, it is the view of the author that potential theory is the better starting point for wave loading on a floater. A discussion of the applied wave model based on potential theory is included in the present work, see Section 3.3.

The most promising reference for comparison with the numerical results given in the present work are described in (Kishev et al., 2006). The results in (Li et al., 2007) for a floating cylinder in waves with a wave direction parallel with the cylinder axis also appear to be a candidate for comparison. The experiments reported in (Ormberg, 1991) for a steel floater seem less relevant because the model used is of a bigger cage system and it has a different cross section. Several experiment have been reported for circular cages. These results are also considered less relevant. The extent of the experiments reported in the literature merits a focus on generating further results. However, due to time constraints, no comparison of the numerical results with experimental results — neither old nor new — is included in the present work.

Whereas the early focus regarding netpen loading was on current loading rather than wave loading, a group of recent references from SFA have dealt with wave loading. (Lader and Fredheim, 2006) and (Lader et al., 2007a) are of particular relevance for the present work. However, there appears to be a need for further experiments related to wave loading on netpens, particularly in a system with a netpen connected to a floater moving in waves. The wave load effect on the netpen is discussed in Section 3.3.5.

(Ormberg, 1991) is the only reference found for fatigue analysis of a floating fish cage, and that analysis employs regular waves and the simplified method based on an assumed Weibull distribution (see Section 8.3.3). The results appear to be overly conservative. The fatigue analysis in the present work is based on irregular waves and rainflow counting, according to the recommendations for further work in (Ormberg, 1991).

1.7 Outline of the thesis

In Chapter 2, a general description of principal structural parts of a floating fish cage system is first given followed by a description of the base case structure (BCS). In Chapter 3, the wave loading regime is presented based on a theoretical approach. Particular emphasis is placed on the expected intervals of variation as well as the relative importance of the different wave load effects. The dynamic nonlinear structural analysis is discussed in Chapter 4. A static analysis and natural period analysis of the base case structure is presented in Chapter 5. In Chapter 6, the development of a software tool implementing the analysis procedure described in Chapter 3 and 4 is described. In Chapter 7, a preliminary verification of the software tool and investigation of sensitivity with regard to various parameters is presented. The methodology for fatigue design is presented in Chapter 8, and the fatigue parameter study in Chapter 9. Finally, in chapter 10, conclusions and recommendations for further work are presented.

Chapter 2

THE FLOATING FISH CAGE STRUCTURE

All numerical studies and results in this dissertation are based on a predefined base case structure (BCS), which is defined in this chapter. However, first we give a brief, general overview of a typical floating fish cage system from a structural point of view. Natural periods and damping characteristics are discussed in Chapter 4 as they need to be seen in connection with the added mass and hydrodynamic damping. Chapter 4 also includes a static analysis of the BCS.

2.1 The floating fish cage concept

A floating fish cage system typically used for salmon farming consists of three principal structural parts:

Floater Typically built in steel or plastic. In addition to providing structural integrity and keeping the netpens afloat (by providing buoyancy), the floater is also used as a work "platform". The typical dimensions used for floaters have increased considerably over the last years.

Netpen Made from plastic materials and attached to the floater. Normally weighed down to ensure limited deformations in current.

Mooring Attached to the floater. Consists of ropes, wires, and/or chains and is often held up by buoys to limit vertical loads on the floater.

Structural problems due to environmental loading are usually observed in connection with the floater or the mooring, whereas tearing of the netpen can occur during handling.

2.1.1 Floater

Presently, two competing materials share the market for floaters: steel and plastic.

Figure 2.1: Hinged steel cage. Lernes AS, Hemnfjorden, Sør-Trøndelag.

Steel floaters

Steel floaters have a rectangular foot print, built up from square cages. Typically, one or two cages are used in the short direction and six to ten in the long direction. The typical dimension of the side of a single (square) cage is between 20 and 35 m, making the typical length of a farm between 120 to 350 m and the width between 20 and 70 m.

There are two subgroups of steel floaters: rigid and hinged, referring to the way a single square cage is built. For hinged floaters, the elements (i.e. sides) are built up from open beams with a typical height of $20 - 40\,cm$. The elements are then hinged together to give a rectangular foot print with a square mesh. A rigid floater is typically built up from cylinders with a diameter around $1\,m$ which are welded together at the corners. The individual rigid squares are then hinged together to make the rectangular footprint (i.e. even rigid systems are not completely rigid).

Whereas all steel floaters take their structural strength from steel elements, sufficient buoyancy is achieved differently. For rigid floaters the closed cross section provide buoyancy whereas hinged floaters are supported by non-structural plastic buoys.

The main advantage with steel floaters as compared to plastic floaters is excellent work conditions, as sturdy and wide walkways are put on top. These can even carry machines such as fork lifts. On the negative side, steel floaters are more expensive and have turned out to be more prone to structural failure in rough waters than has been the case for plastic floaters. An example of a steel floater is shown in Figure 2.1.

Plastic floaters

Plastic floaters are built from flexible pipes with a diameter typically in the interval $25 - 40\,cm$. A pipe length is bent into a circular shape, i.e. a ring, typically with a circumference

Figure 2.2: Plastic floaters. Bjørøya Fiskeoppdrett, Flatanger kommune, Nord-Trøndelag

from $90 - 160\,m$ (diameter $30 - 50\,m$). $2 - 3$ adjacent rings hold one netpen and at the same time serve as a working/servicing platform. Rings are mounted together in systems of typically 4 to 8 netpens. The conventional wisdom of the industry holds that plastic rings are the best choice for harsh environmental conditions. Buoyancy is provided by the rings themselves. An example of a fish farm using plastic floaters is shown in Figure 2.2.

2.1.2 Mooring

Mooring is made using nylon ropes, wires and/or chains. The mooring configuration is dependent on the kind of floater used. For steel floaters the mooring lines are typically connected directly to the floater. For hinged steel floaters, the mooring is usually pretensioned using buoys so that the mooring force will act on the floater approximately horizontally. For rigid steel floaters, taut mooring is often used. Taut mooring is likely to yield smaller vertical movement than buoyed mooring. By increasing the pretensioning in taut mooring the floater behavior will change in the vertical direction from a flexible structure riding on the waves towards the characteristics of a fixed structure.

For plastic floaters a so-called system mooring is used, which sets up a submerged grid to which the individual rings can be attached. This mooring is also pretensioned by buoys.

2.1.3 Netpen

The netpens used in fish cages are made of netting similar to traditional nets used for trawl fisheries. They can be knotted or non-knotted, and squared or diamond shaped.

The twine diameter is typically around $2\,mm$ (thread 32 to 46, and the mesh size from $30\,mm$ to $50\,mm$). The preferred mesh size depends on the size of fish kept in the net, but also on the desire to keep wild fish out of the net.

The typical depth of the nets are today from 12 to $30\,m$. Thus, for typical wave lengths (e.g. $\lambda < 20\,m$, see Table 8.5) much of the net will be below the wave zone and therefore more affected by current than by waves.

The netpens are normally held down by weights to make sure that a satisfactory shape is maintained when exposed to high current. The way in which the weights are attached have changed over the years, mostly due to practical considerations. Today, it is common

to attach the weights directly to the floater (e.g. by means of rope of wire) and the netpen to the rope, instead of hanging the weights directly in the netpen. This way the netpen can move more independently from the weight ropes.

Although netpens can be damaged as a secondary effect after a structural collapse of the mooring or the floater, damage to the netpen due to environmental loading (i.e. waves and current) is unlikely. Structurally, it is thus reasonable to assume that the netpen will not be damaged by environmental loads. It is, however, likely to play a — possibly significant — role in the over all structural behavior of the system and should therefore be included in a structural analysis. Finally, although it is not a structural problem, it should be noted that high current velocities can severely deform a netpen and thereby worsen the biological conditions for the fish.

2.2 The Base Case Structure

The theoretical and numerical studies presented in this thesis are related to the base case structure (BCS) defined in this section. The three principal structural parts of a fish farm are included (be it in a simplified manner), but no attempt is made to model a realistic, complete fish farm. Instead, the BCS is chosen as simple as possible, yet capable of providing valuable structural understanding, also applicable to a complete fish farm system.

2.2.1 Rigid steel floater

As the BCS used in this dissertation, a rigid steel floater based on circular cylinders (pipes), is chosen. This kind of floater has been used for more than 10 years and has proven to be a common design choice — despite its high costs — mainly because it delivers an excellent work environment. The biggest producer of this kind of floater today is Bømlo Construction (www.bc.no). The diameter of steel pipes used typically varies between $800\,mm$ and $1500\,mm$. The maximum draft is typically between $500\,mm$ and $800\,mm$. Figure 2.3 and 2.4 show pictures of a floater from Bømlo Construction during fabrication and installation, respectively.

The complete BCS as well as its basic component in isolation are considere:

Pipe The pipe used for the sides of the quadratic BCS is a cylinder with diameter $D_{pipe} = 1\,m$, thickness $10\,mm$, and (midline) length $L_{pipe} = 30\,m$. A screenshot of the pipe from the software prototype is shown in Figure 2.5. The ocean surface, bottom, as well as the netpen are also included in the animation. The cross section of the pipe is shown on the right hand side of Figure 2.7.

BCS The pipe described above is used to build a square floater, $30\,m$ by $30\,m$. A screenshot of the BCS is shown in Figure 2.6. As for the pipe in Figure 2.5, the surface, bottom, and netpen are animated. Additionally, the mooring is animated. The plan of the BCS is shown on the left and side of Figure 2.7. Whereas the single floating

Figure 2.3: Fabrication of a steel floater (Photo: A. E. Lønning)

Figure 2.4: Installation of a steel floater (Photo: A. E. Lønning)

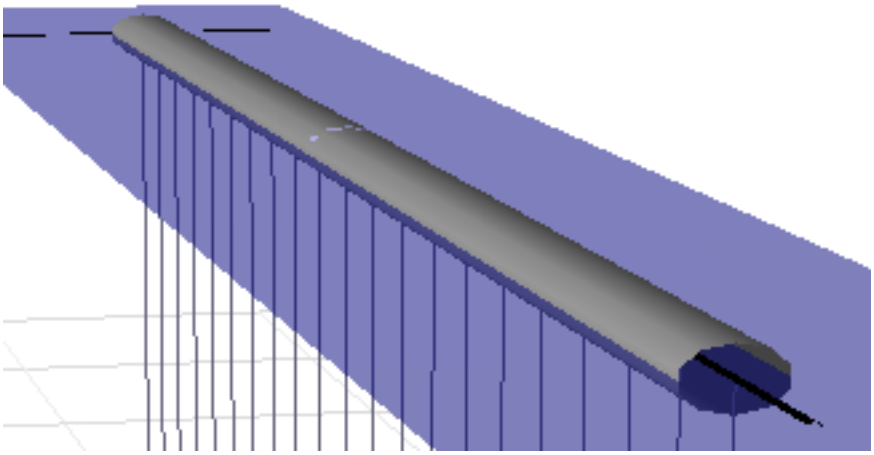

Figure 2.5: Screenshot of a single pipe used in the BCS including netpen.

L_{pipe} $[m]$	D_{pipe} $[mm]$	t_{pipe} $[mm]$	A_{steel} $[m^2]$	A_{buoy} $[m^2]$	m_{distr} $[kg/m]$	m_{pipe} $[t]$	m_{cage} $[t]$
30.0	1000	10	0.031	0.785	247	7.4	29.6

Table 2.1: Structural dimensions and properties of a (single) pipe used as sides for the BCS.

pipe is not a structure used in fish farming systems, the single square cage is used as a building block for a complete rectangular farm.

The structural dimensions, mass, and weight of the pipe and the BCS are shown in Table 2.1. The chosen dimensions are not related directly to a particular product, but reflect typical dimensions used by the industry. The assumed material parameters of steel and sea water are shown in Table 2.2. Structural parameters of the BCS cross section, based on Table 2.1 and 2.2, are shown in Table 2.3 and 2.4.

In addition to the pipe itself, a floater consists of railing, grating, equipment etc. giving an additional live load (i.e. mass). Thus, the static equilibrium submergence of the cage is increased. Further, the netpen is attached to the floater, but is typically neutrally buoyant. However, it is normally weighed down, see Section 2.1.3. The weights increase the live load

Sea Water	Steel					
$\rho_w(10°C)$ $[kg/m^3]$	ρ_{steel} $[kg/m^3]$	E $[MPa]$	G $[MPa]$	f_y $[MPa]$	γ_m $[-]$	ν $[-]$
1026.9	7850	$2.1 \cdot 10^5$	$0.8 \cdot 10^5$	360	1.0	0.3

Table 2.2: Material parameters for sea water and steel.

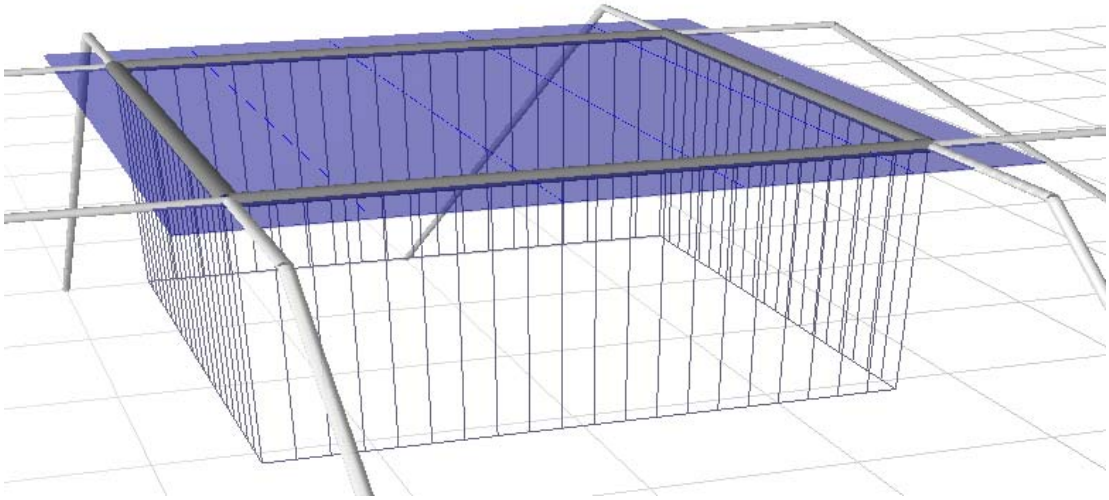

Figure 2.6: Screendump of the BCS including netpen and mooring.

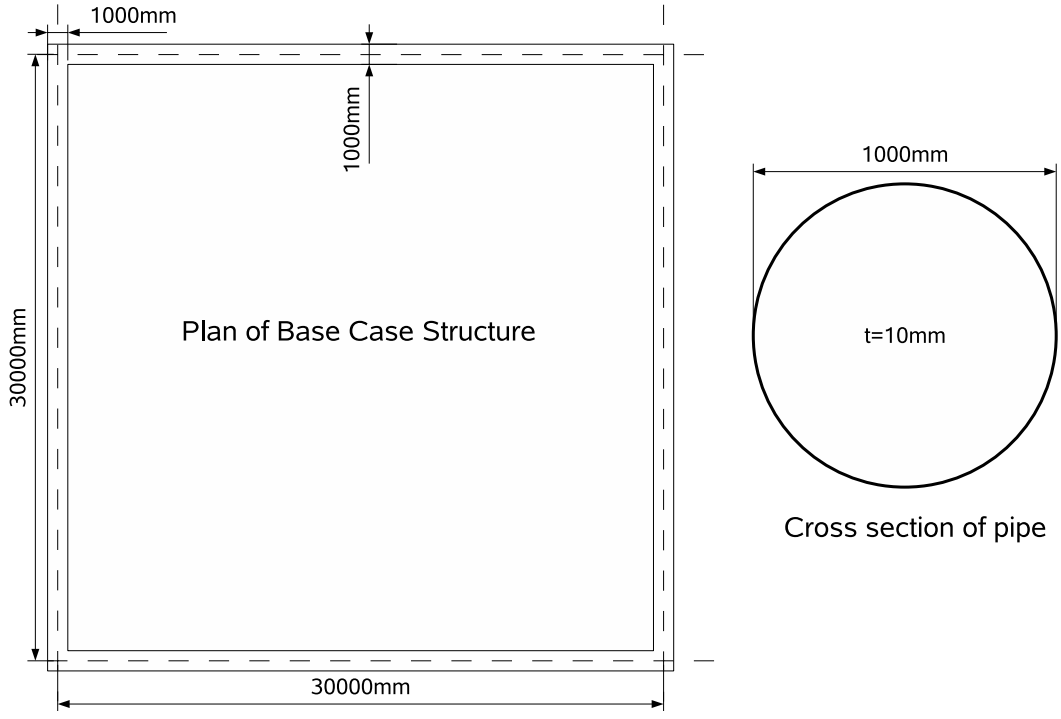

Figure 2.7: Plan of Base Case Structure and cross section of pipe.

I $[m^4]$	W_{el} $[m^3]$	$I_p(=I_T)$ $[m^4]$	EA_{steel} $[kN]$	EI $[kNm^2]$	GI_p $[kNm^2]$
$3.93 \cdot 10^{-3}$	$7.85 \cdot 10^{-3}$	$7.85 \cdot 10^{-3}$	$6.51 \cdot 10^{6}$	$8.25 \cdot 10^{5}$	$6.28 \cdot 10^{5}$

Table 2.3: Structural inertia and stiffness parameters of the pipe used as sides for the BCS.

F_{el} $[kN]$	M_{el} $[kNm]$	M_{pl} $[kNm]$	M_T $[kNm]$
11160	2827	3600	3265

Table 2.4: Cross section capacity of axial force, elastic bending moment, plastic bending moment, and torsional moment.

of the floater. For the BCS, we have assumed that the total (structural) mass of the cage causes a 50% submergence of the volume. Given this assumption, the live load can be found. In Table 2.5 the (equivalent) mass and weight (or force) of the pipe, live load, and buoyancy load are shown assuming that 50% of the volume is submerged and that the floater is horizontal (i.e. the live load corresponds to a constant distributed loading).

If we compare the dry mass of the pipe ($2.4\,kN/m$) with the maximum buoyancy load ($7.9\,kN/m$) we see that an unloaded pipe will have 30% of its volume ($0.24\,m^2$) submerged at static equlibrium, i.e. equivalent to a $0.34\,m$ draft (34% of its height).

To give a reference for the moment capacity of the pipe, the elastic loading capacity for two standard loading conditions for beams are shown in Table 2.6, assuming this beam (i.e. pipe) is pinned at both ends (of course, an actual fish cage will not be modeled as pinned). No load or material factors are applied. Comparing Table 2.6 with 2.5, we find that the dry weight of the pipe ($2.4\,kN/m$) is 10% of the elastic distributed loading capacity ($25.1\,kN/m$) whereas the dry weight and live load combined ($4.0\,kN/m$) are 16% of the capacity. The dry weight alone and the self and live weight combined will — for a pinned-pinned beam with a $30\,m$ span — give maximum moments of $270\,kNm$ and $450\,kNm$,

		Mass			Weight or Force		
		Distr $[kg/m]$	Pipe $[t]$	Cage $[t]$	Distr $[kN/m]$	Pipe $[kN]$	Cage $[kN]$
Mass	Steel	247	7.4	29.6	2.4	72	290
	Live	157	4.7	18.8	1.5	46	184
Buoyancy	Equil.	403	12.1	48.4	4.0	119	476
	Max.	807	24.2	96.8	7.9	237	948

Table 2.5: Mass and weight for steel and live load together with equivalent mass and force from maximum and (static) equilibrium buoyancy.

Load Case	Elastic Cap.	Plastic Cap.	Δ_{el}	Δ_{el}/L
Evenly Distributed	$25\,kN/m$	$32\,kN/m$	$321\,mm$	1.1%
Point Load, mid span	$376\,kN$	$480\,kN$	$257\,mm$	0.9%

Table 2.6: Elastic load capacity for the base case pipe assumed to be pinned at each end

respectively. Further, for both load cases, the maximum elastic (mid-span) deformation Δ_{el} is shown in millimeters and relative to the span of $L = 30\,m$. As the maximum elastic deformation is about 1%, the bending defomations are likely to be minor compared to the rigid body motions as long as the bending moments are below the elastic limit, which is assumed to be the case.

2.2.2 Horizontal linear mooring

All mooring lines are assumed to be horizontal, linear elastic, untensioned, and having equal stiffness.

For the BCS, each of the four corners is given two mooring lines, one in each direction of the two adjoining pipes, see Figure 2.6. Similarly, for a single pipe, each of the two ends is given two mooring lines, one in each direction, parallel and perpendicular to the pipe.

The horizontal direction of the mooring corresponds to buoyed (rather than taut) mooring. It is used in order to remove the effect of inclined mooring and thus making it possible to study the effects of the load components independent of vertical mooring loads.

Both taut and buoyed mooring are in practice pretensioned giving mainly tension (normal force) in the members, assuming the mooring is correctly adjusted. Pretensioning is initially assumed to have a minor effect on the structural design in general and fatigue damage in particular, as the pretensioning is static and assumed to be relatively small. Additionally, neglecting pretensioning is likely to be conservative as it will increase the geometric stiffness of the members. Thus, the pretensioning of the mooring is assumed to be zero in the present work: $F_{pre} = 0\,kN$.

Structural characteristics of a typical buoyed mooring line

To investigate reasonable assumptions and simplifications in the structural modeling of buoyed mooring, a basic model of a mooring line is examined, see Figure 2.8. The elasticity of the mooring lines depends on the material used. As a simplification, the mooring lines are assumed to be rigid and only the elasticity of the buoys is considered. Ignoring the elasticity of the mooring lines themselves, the linear mooring stiffness k_{moor} found can be considered as an upper limit. The system loses most of its stiffness when the buoy is fully submerged (or dry) and the system should be designed to avoid this situation, as it renders the system free to move until the mooring lines on the windward side are fully stretched. This is likely to be an unfavorable situation, and should probably be treated as a limit state in design.

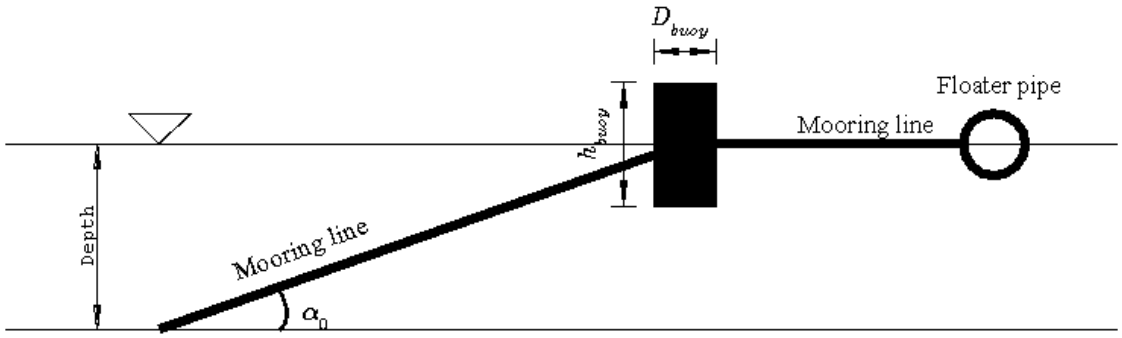

Figure 2.8: Model of mooring line with buoy

In practice, the height of mooring buoys varies from $1.0\,m$ to $2.0\,m$ whereas the diameter varies from $0.5\,m$ to $1.5\,m$. In this thesis we assume that large buoys are used, i.e. a circular cylinder with diameter $D_{buoy} = 1.5\,m$, height $h_{buoy} = 2.0\,m$, and submergence s_{buoy} as a fraction of the height. The instantaneous stiffness of the mooring line k_{moor} is horizontal and is a function of the water plane area of the buoy $A_{w,buoy}$ and the angle α_0, whereas the pretensioning F_{pre} is a function of buoyancy B_{buoy} and the angle α_0:

$$A_{w,buoy} = \frac{\pi D_{buoy}^2}{4} \tag{2.1}$$

$$k_{moor} = \frac{A_{w,buoy} \cdot \rho_w g}{\tan^2 \alpha_0} = \frac{\pi \rho_w g}{4} \cdot \frac{D_{buoy}^2}{\tan^2 \alpha_0} = 7.91 kN/m^3 \cdot \frac{D_{buoy}^2}{\tan^2 \alpha_0} \tag{2.2}$$

$$F_{pre} = \frac{B_{buoy}}{\tan \alpha_0} = \frac{\pi \rho_w g}{4} \cdot \frac{D_{buoy}^2 s_{buoy} h_{buoy}}{\tan \alpha_0} = 7.91 kN/m^3 \cdot \frac{D_{buoy}^2 s_{buoy} h_{buoy}}{\tan \alpha_0} \tag{2.3}$$

We see from the expressions that the smaller the angle α_0 the bigger are both stiffness and pretensioning for a given buoy. k_{moor} and F_{pre} for typical buoys and mooring angles are shown in Table 2.7. A rule of thumb used by the industry is to use a mooring line with a length from the buoy to the anchor three times the depth, i.e. $\alpha_0 = 19.5°$.

Interval of elastic response

When a mooring line is loaded the mooring buoy will rotate around the bottom mooring point, increasing the submergence until the whole buoy is submerged and the line loses (most of) its stiffness. Assuming the starting point is half submerged ($s_{buoy} = 50\%$), maximum additional submergence is half the height of the buoy $\Delta_{v,el} = h_{buoy}/2$. The corresponding horizontal displacement $\Delta_{h,el}$ can be found from trigonometric calculations. Also, it is of interest to find the corresponding stiffness $k_{moor,el}$, rotation $\Delta\alpha_{el}$, and maximum elastic force $F_{moor,el}$ of the mooring line to consider whether it is reasonable to assume a linear stiffness, and to determine the range of horizontal displacement for which the line

α_0 [°]	k_{moor} $[kN/m]$	F_{pre} $[kN]$	$\Delta\alpha_{el}$ [°]	$k_{moor,el}$ $[kN/m]$	$\Delta_{h,el}$ $[m]$	$F_{moor,el}$ $[kN]$
19.5	142.0	50.3	0.2	145.2	0.35	50.0
30	53.4	30.8	0.3	54.9	0.57	30.6
45	17.8	17.8	0.6	18.5	0.99	17.6

Table 2.7: Mooring line stiffness parameters.

Depth	Mesh	Diameter
$24\,m$	$45\,mm$	$3\,mm$

Table 2.8: Parameters of the netpen used for the BCS

has stiffness (i.e. the buoy is not fully submerged). This is done under the assumption of a large buoy. As opposed to k_{moor} and F_{pre}, these parameters depend on the water depth. $\Delta\alpha_{el}$, $k_{moor,el}$, $\Delta_{h,el}$, and $F_{moor,el}$ are included in Table 2.7. A water depth of $100\,m$ is assumed.

Discussion

From the above we conclude that assuming mooring lines are linear, untensioned and horizontal is a good approximation as long as the horizontal response is smaller than the elastic limit $\Delta_{h,el}$. Additionally, we note that the stiffness increases sharply with decreasing mooring line angle: the stiffness of a 19.5°-line is eight times the stiffness of a 45°-line. The maximum elastic force on the other hand only triples from 19.5° to 45°. Whereas a high maximum force is important to ensure sufficient capacity for the static force induced by the current, it is not important when only waves are considered.

In the subsequent chapters we assume that a large buoy and a 19.5°-line are used, i.e. a linear stiffness of $k_{moor} = 142.0\,kN/m$ and a maximum horizontal deflection of $\Delta_{h,el} = 0.35\,m$.

2.2.3 Netpen

The assumed parameters of the netpen are shown in Table 2.8 and are taken from the typical intervals for salmon farming today.

The weights typically used to keep the shape of the netpen in current are assumed to be included in the live load of the floater. There are several alternative methods and configurations for using weights, differing e.g. to what extent the weights actually make the netpen become taut. It is probably of major importance for the structural effect of the netpen to know the degree to which it remains stretched (over time), as a slack netpen exerts no or very limited loading on the floater.

It is assumed that the cases of no netpen on one hand, and a continuously (over time) stretched netpen on the other are reasonable extreme cases when considering the effect of a netpen.

The structural effect of the netpen is discussed in Section 3.3.5.

Chapter 3

THE WAVE LOADING REGIME

For a floating structure which is free to move, wave loading typically includes effects referred to as added mass, hydrodynamic damping, exciting forces, as well as restoring forces.

As there is no established and verified load model available to be used in an engineering structural analysis of a floating fish farm, the choice of load model and the reasoning behind it is discussed in this chapter. We start by discussing the typical wave climate for Norwegian salmon farming as defined by NS 9415 (Standard Norge, 2003). Next, hydrostatic wave loading for a floating cylinder and hydrodynamic wave loading for a submerged cylinder are discussed together with a hydrodynamic classification of the BCS. In Section 3.3 the wave load model used for linear analysis of the BCS is presented. In Section 3.4 the model used for nonlinear analysis of the BCS is presented, i.e. the modifications of the linear model.

3.1 Typical wave environment

3.1.1 Wave classes in NS 9415

NS 9415 specifies intervals of typical wave conditions called wave classes. A description of the wave classes is shown in Table 3.1[1]. The waves are wind-generated local waves, i.e. swell is neglected. The wave classes represent seastates with a 50-year return period. The wave class of a particular location shall be decided based on the local wave climate. It is then to be used for regular or irregular waves in a structural analysis.

An advantage of the NS 9415 wave classes is that they provide an overview of which wave climates that are to be expected for the 50-year storm of Norwegian fish farms. In this chapter they will be used for this purpose and to define a set of typical regular waves (TRW) assumed representative for Norwegian localities, see Section 3.1.3.

[1] A classification of current is presented in NS 9415, Section 5.11.1, Table 5.

Wave classes	H_s [m]	T_p [s]	H_{max} [m]	Designation
A	0.0 - 0.5	0.0 - 2.0	1.0	Light exposure
B	0.5 - 1.0	1.6 - 3.2	1.9	Moderate exposure
C	1.0 - 2.0	2.5 - 5.1	3.8	Heavy exposure
D	2.0 - 3.0	4.0 - 6.7	5.7	High exposure
E	> 3.0	5.3 - 18.0		Extreme exposure

Table 3.1: Wave classes at the locality defined in terms of significant wave height H_s and peak period T_p. NS 9415, Section 5.11.1, Table 4 (Standard Norge, 2003)

Wave classes of interest

The vast majority of Norwegian fish farms have non-extreme locations, i.e. a wave classification in class A to D. Waves at wave class A locations are not likely to cause structural damage. Thus, in this chapter wave class B, C , and D are considered. In Chapter 9 the focus is narrowed down to wave class C.

Maximum wave height

NS 9415, Section 5.11.3 specifies that the height H of regular waves (i.e. maximum wave height H_{max}) used in a structural analysis is:

$$H = H_{max} = 1.9 \cdot H_s \tag{3.1}$$

The corresponding wave period T shall be set equal to T_p. Using Equation 3.1, the H_{max} of each wave class interval is also shown in Table 3.1. The maximum wave height H_{max} for the wave classes considered (i.e. B — D) is $5.7\,m$.

Although it is not stated in NS 9415, it is assumed in the present work that this (maximum) wave height is only relevant for the ultimate limit state. The use of regular waves for the fatigue limit state is briefly discussed in Section 9.1.

3.1.2 Wave prediction for wind generated waves

NS 9415 presents formulas for calculation of H_s and T_p from wind speed U and fetch F. The formulas appear to be taken from the Shore Protection Manual from 1984 (US. Army Coastal Engineering Research, 1984), which are based on the JONSWAP (Hasselmann et al., 1973) relationships. The wind speed U is transformed to a so-called adjusted wind speed[2] U_A (units must be meter(m) and second(s)):

$$U_A = 0.71 \cdot U^{1.23} \tag{3.2}$$

[2]The use of adjusted wind speed has been questioned by Bishop et al. (1992). They conclude that the use of adjusted wind speed U_A over predicts both H_s and T_p as compared to using the unadjusted wind speed and recommends that it is not used in wave prediction.

$$H_s = c_1 \cdot U_A F^{1/2} \quad , \quad c_1 = 5.112 \cdot 10^{-4} \tag{3.3}$$

$$T_p = c_2 \cdot (U_A F)^{1/3} \quad , \quad c_2 = 6.238 \cdot 10^{-2} \tag{3.4}$$

A relationship between H_s, T_p and F (fetch) can be found independently of how the wind speed is calculated:

$$H_s = \frac{c_1}{{c_2}^3} \cdot \frac{{T_p}^3}{\sqrt{F}} \approx 2.106 \frac{{T_p}^3}{\sqrt{F}} \tag{3.5}$$

$$T_p = \frac{c_2}{{c_1}^{1/3}} F^{1/6} {H_s}^{1/3} \approx 0.7802 \cdot F^{1/6} {H_s}^{1/3} \tag{3.6}$$

These formulas assume that the waves are fetch limited, i.e. that the duration of the storm is not limiting the waves. The Shore Protection Manual (as opposed to NS 9415) also gives a formula for the required minimum duration t of a storm for the waves to be fetch limited (units are still meters and seconds):

$$t = 3.215 \cdot 10^1 \cdot \left[\frac{F^2}{U_A} \right]^{1/3} \tag{3.7}$$

Fetch and minimum duration intervals

According to NS 9415, the extreme wind speed (i.e. design wind speed) varies relatively little along the coast. If no empirical measurements have been made, the 50-year return period extreme wind speed shall be assumed to be $35\,m/s$ (see Appendix C.1.1 of the present thesis). To find extreme (i.e. design) H_s and T_p values for a given fish farm location, the extreme wind speed should be used. An interval for fetch can then be tied to each H_s and T_p interval in Table 3.1. This is shown in Table 3.2[3]. The intervals for minimum storm duration are also found (using Equation 3.7) and listed as a reference. The fetch varies from $0.3\,km$ to $22.0\,km$ and the minimum storm duration from $0.1\,h$ to $1.8\,h$ (i.e. from $6\,min$ to $1\,h\,48\,min$). The fetch interval seems appropriate to cover Norwegian fjords and the minimum storm durations seem so short that they will not limit the waves (as effectively assumed in NS 9415).

From Table 3.2 we see that fetch based on the minimum values of the H_s and T_p intervals correspond very well (i.e. $0.3\,km$ vs. $0.3\,km$, $1.2\,km$ vs. $1.1\,km$, and $4.8\,km$ vs. $4.7\,km$). However, for the maximum values the T_p-value gives a fetch that is roughly twice the fetch of the H_s-value (i.e $1.2\,km$ vs. $2.4\,km$, $4.8\,km$ vs. $9.7\,km$, and $10.9\,km$ vs $22.0\,km$). The reason for this apparent inconsistency in NS 9415 is not known. A possible explanation is to account for swell with longer periods.

[3]If the wind speed were not adjusted (U used instead of U_A), the fetch values would be smaller: approximately a third based on H_s, and two thirds based on T_p.

Wave classes	Fetch [km]		Minimum duration [h]	
	From H_s	From T_p	From H_s	From T_p
B	0.3-1.2	0.3-2.4	0.1-0.3	0.1-0.4
C	1.2-4.8	1.1-9.7	0.3-0.7	0.3-1.1
D	4.8-10.9	4.7-22.0	0.7-1.1	0.7-1.8

Table 3.2: Fetch F and minimum storm duration intervals for wave classes B-D assuming extreme wind speed of $35\,m/s$. Intervals are found based on both H_s and T_p intervals.

Deep water waves in $100\,m$ depth

To avoid local pollution and ensure sufficient oxygen supply Norwegian fish farms are today typically placed in deeper waters than $50\,m$. As shown in Table 3.3, it is reasonable to assume that the maximum wave length is about $70\,m$, i.e. deep water wave conditions for depths $> \lambda_{max}/2 = 35.0\,m$. Thus, it is reasonable to assume deep water conditions for fish farms in the wave regime considered.

A water depth of $100\,m$ is assumed for the case study.

3.1.3 Typical Regular Waves (TRW)

To investigate the characteristics of the 50-year storm wave environment for wave classes B, C, and D ($0.5\,m \leq H_s \leq 3.0\,m$ and $1.6\,s \leq T_p \leq 6.7\,s$) and the corresponding behavior of the BCS, we want to specify a typical 50-year storm regular wave for each class and for the maximum wave of class D. These four regular waves are subsequently referred to as B, C, D, and H_{max} and are collectively referred to as TRW. As a typical wave height H we choose the maximum significant wave height of each class. To establish corresponding T values, we use the wave prediction procedure of NS 9415, i.e. $T = T_p$. Using $H_s = H$, $U_A = 0.71 \cdot 35^{1.23}\,m/s = 56.3\,m/s$, and fetch F, the corresponding peak period T_p can be found using Equation 3.3 and Equation 3.4. The fetch value is set as the value corresponding to the maximum H_s in Table 3.2. For the H_{max}-wave, the maximum T_p value of class D is used with $H = 1.9 \cdot 3\,m = 5.7\,m$, cf. Equation 3.1. Regular wave parameters for each TRW are shown in Table 3.3.

In Table 3.3 the four sets of regular wave parameters are listed together with wave length λ. The wave length is calculated using the deep water wave relation: $\lambda = \frac{g \cdot T^2}{2 \cdot \pi} \approx 1.56\,m/s^2 \cdot T^2$. The minimum and maximum wave lengths of the TRW are thus $9.8\,m$ and $70.1\,m$. Finally, based on the maximum wave steepness $H/\lambda = 1/7 \approx 0.14$ (i.e. $H \approx 0.22\,m/s^2 \cdot T^2$) the corresponding minimum wave length λ_{min}, minimum wave period $T_{1/7}$, and maximum wave height $H_{1/7}$ are included in the table. The former two are found using the corresponding TRW wave height and the latter using the corresponding TRW wave period.

TRW	Fetch [km]	$H[m]$	$T[s]$	$\lambda[m]$	$H/\lambda = 1/7$		
					$\lambda_{min}[m]$	$T_{1/7}$ [s]	$H_{1/7}$ [m]
B	1.2	1	2.5	9.8	7.0	2.1	1.4
C	4.8	2	4.0	25.0	14.0	3.0	3.6
D	10.9	3	5.3	43.9	21.0	3.7	6.3
H_{max}	N/A	5.7	6.7	70.1	39.9	5.1	10.0
Avrg.	5.6	2.9	4.6	37.2	20.5	3.5	5.3

Table 3.3: Linear Wave Parameters for TRW B-D and H_{max}.

3.2 Wave loading for a floating, horizontal cylinder

The principal challenge in working with wave loading on fish cage floaters are two fold:

1. The fish farm transcends the traditional classification of hydrodynamic sub areas (as explained below), which are usually treated separately.

2. For higher waves nonlinearities are introduced

The floater of a sea cage can according to traditional procedures be hydrodynamically classified as a slender structure. It is also a moored, floating structure experiencing relatively large wave response. Parts of the floater may even be fully submerged or dry at times, i.e. it is similar to water entry/exit and impact problems. Using reformulated chapter titles of (Journée and Massie, 2001) and (Faltinsen, 1990), all of the following three areas of hydrodynamics seem relevant for a floater:

Wave loads and motions for floating structures. Normally based on linear potential theory. Typically stiff, massive structures, such as ships, modeled as a rigid body.

Wave loads on slender structures. Typically fully submerged structures such as pipelines and risers with loading represented by Morison's equation.

Water impact and entry. Typically high-speed problems e.g slamming and lifting operations.

The traditional approach of either area does not seem to cover the peculiarities of the floater. It is clearly a floating structure, but acceptable accuracy of linear potential theory assumes that both the wave height and the response are small compared to the cylinder diameter. This is typically not the case for the floater. Additionally, the floater is a slender, elastic structure, but not fully submerged. Finally, water entry and exit is likely to occur. However, traditionally the focus has been on high speed entry/exit and the initial, transient phase.

In this thesis, the initial load model will be based on the conventional approach for floating structures using linear potential theory. This is expected to give good results for

small waves. To account for the nonlinear effect of realistic wave heights, buoyancy is subsequently modeled nonlinearly. Linearized horizontal drag is included using the drag term of Morison's equation. Although it might be relevant, a water entry/exit approach will not be further discussed in this thesis.

In this section we start with discussing the traditional hydrostatic concepts of water plane stiffness and buoyancy, see Section 3.2.1. Then a traditional hydrodynamic classification of the BCS is performed, see Section 3.2.3. This classification is useful in an initial evaluation of hydrodynamic effects of importance for both submerged and floating cylinders. Finally, a discussion of a (fully) submerged cylinder based on Morison's equation is presented in Section 3.2.4.

The discussion of wave loading of the floater in the context of linear and nonlinear analysis (based on potential theory) is left to Section 3.3 and Section 3.4, respectively. The resonant behavior of the BCS in the vertical and horizontal direction is discussed in Section 4.3 and 4.4, respectively.

Is CFD a realistic alternative?

It is well known that the Navier-Stokes differential equations offer a theoretical description of various non-linear flow problems, including hydrodynamics. A variety of computer programs (both commercial and academic) have been developed to solve the Navier-Stokes equations using various numerical methods — collectively called Computational Fluid Dynamics or CFD. Unfortunately, the effective adoption of CFD has proven to be very complicated, and despite the extremely strong computer resources at disposal today, they have found limited use in engineering practice at present[4].

Due to the complexity and lacking maturity of CFD methods within an engineering context they were not investigated further in this thesis. The wave loading on floaters of floating fish farms is currently being investigated by Kristiansen (2008) using CFD methods.

3.2.1 Water plane stiffness

The water plane area A_w is the product of water plane length l_w and water plane width w_w: $A_w = l_w \cdot w_w$. Assuming that both the free surface and the cylinder are horizontal, the water plane stiffness k_w can, for a circular cross section with diameter D, be expressed as a function of the draft d (see Figure 3.1):

$$k_w = \rho_w \, g \, A_w = 10.1 kN/m^3 \cdot A_w = 20.1 kN/m^3 \cdot l_w \cdot \sqrt{dD - d^2} \, , \; 0 \leq d \leq D \qquad (3.8)$$

[4]Wikipedia (2007) states: "However, even with simplified equations and high speed supercomputers, only approximate solutions can be achieved in many cases. More accurate codes that can accurately and quickly simulate even complex scenarios such as supersonic or turbulent flows are an ongoing area of research."

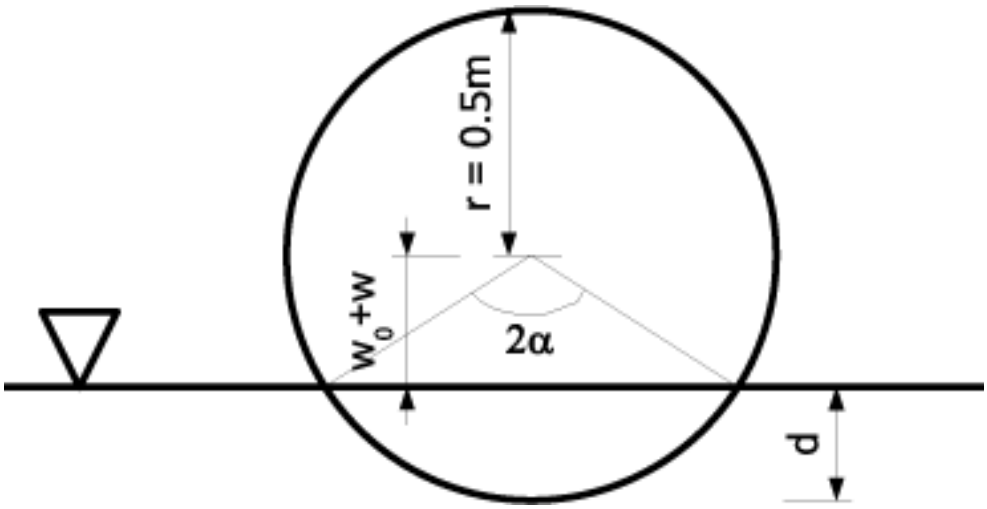

Figure 3.1: Cross section of submerged pipe

In the half submerged position ($d = D/2$) the BCS pipe has its maximum water plane stiffness $k_{w,max} = 1\,m \cdot \rho_w\, g\, l_w = 10.1\,kN/m^2 \cdot l_w$. The maximum water plane stiffnesses of a single $30\,m$ pipe and the BCS are thus, respectively: $10.1\,kN/m^2 \cdot 30\,m = 302\,kN/m$ and $10.1\,kN/m^2 \cdot 120\,m = 1209\,kN/m$.

In Table 3.4 the relative water plane stiffness is shown for varying draft d. Two points are particularly noteworthy. First, k_w is approximately constant for relative deflections less than $20\,cm$ ($70\,cm < d < 30\,cm$), and secondly, k_w is as high as 20% of the maximum value for a draft of only $1\,cm$.

3.2.2 Buoyancy

As for k_w, the submerged cross-section area A_{sub} and thus the distributed buoyancy B_{distr} can be expressed as a function of the draft d. The symbols used are illustrated in Figure 3.1.

$$B_{distr} = \rho_w\, g\, l_w\, A_{sub} \tag{3.9}$$

$$A_{sub} = \frac{2\alpha - \sin(2\alpha)}{2} \cdot r^2 = \left[\alpha - \frac{sin(2\alpha)}{2}\right] r^2\,,\ 0 \le \alpha \le \pi$$

$$\cos\alpha = \frac{r-d}{r} = 1 - \frac{d}{r} = 1 - \frac{2d}{D}$$

$$d = (w_0 + w) - \zeta - r = w - \zeta - 0.5\,m \tag{3.10}$$

w_0 is the initial vertical location of the pipe center and w is the instantaneous vertical deflection of the pipe center. ζ is the wave surface elevation. In Table 3.4 the relative submerged area is shown for varying draft.

Draft $[cm]$	50	40	30	25	20	10	1
$k_w/k_{w,max}[\%]$	100	98	92	87	80	60	20
$A_{sub}/A_{max}[\%]$	50	37.4	25.2	19.6	14.4	5.2	0.2

Table 3.4: Relative water plane stiffness as a function of draft.

3.2.3 Hydrodynamic classification

An initial hydrodynamic classification is traditionally based on the λ/D, H/D, and H/λ-relations. Since the maximum wave steepness is $H/\lambda = 1/7$ the relative wave steepness is calculated as $7 \cdot H/\lambda$. For (fully) submerged, slender cylinders (see Section 3.2.4) in particular — but also for floating cylinders — four additional non-dimensional numbers are also important:

- Keulegan-Carpenter number KC
- Reynolds number Rn
- Sarpkaya's β
- Roughness number

In Table 3.5, the definition of the numbers are given together with their value intervals for the BCS. In Table 3.6, the individual values for the TRW are listed. The numbers are referred to later when discussing the hydrodynamic loading. For KC and Rn the symbol U in Table 3.5 is the water particle velocity amplitude (at $z = 0\,m$). For an oscillating cylinder the velocity is often taken into account by using relative velocity. However, relative velocity is not considered when calculating KC and Rn in Table 3.5 and 3.6. The influence of cylinder oscillation is discussed in the next subsection.

Importance of wave diffraction effects

Wave diffraction effects are normally neglected for slender structures (see e.g. (Journée and Massie, 2001) and (Faltinsen, 1990)), i.e. where:

$$\lambda/D \geq 5 \tag{3.11}$$

For $D = 1\,m$ the limit case is $\lambda \geq 5\,m$, i.e. $T = \sqrt{\frac{2\,\pi\,\lambda}{g}} \geq 1.8\,s$. Thus, for waves with a period less than $1.8\,s$ wave diffraction effects should be considered.

The λ/D-ratios for the TRW are shown in Table 3.6, and we see that λ/D varies from 9.8 to 70.1. This ratio is (numerically) equal to the value of the wavelength for $D = 1\,m$. Using the above criteria, wave diffraction effects can be neglected for all the TRW. Additionally, for wave class C investigated in Chapter 8 and 9, the wave lengths for all seastates are greater than 5, see Table 8.5.

In this thesis we assume that wave diffraction effects can be neglected, i.e. that waves with $T < 1.8\,s$ will not cause significant structural damage.

Name	Symbol	Definition	Value range
Wavelength/Diameter		λ/D	$9.8 - 70.1$
Waveheight/Diameter		H/D	$1.0 - 5.7$
Waveheight/Wavelength		H/λ	$0.07 - 0.10$
Keulegan-Carpenter	KC	$\frac{U \cdot T}{D} = \pi \frac{H}{D}$	$3.1 - 17.9$
Reynolds	Rn	$\frac{UD}{\nu}$	$0.9 - 2.0$
Sarpkaya β	β	Rn/KC	$1.1 - 3.0$
Roughness number		k/D	0

Table 3.5: Nondimensional numbers for wave loading of (slender) cylinder. Range of values for base case structure are shown, assuming deep water and smooth surface. $\nu(10°C) = 1.35 \cdot 10^{-6}\, m^2/s$. Rn and β values must be multiplied by 10^6 and 10^5, respectively.

TRW	λ/D	H/D	H/λ	$7 \cdot H/\lambda$	KC	Rn	β
B	9.8	1.0	0.10	72%	3.1	0.9	3.0
C	25.0	2.0	0.08	56%	6.3	1.2	1.9
D	43.9	3.0	0.07	48%	9.4	1.3	1.4
H_{max}	70.1	5.7	0.08	57%	17.9	2.0	1.1
Avrg.	37.2	2.9	0.08	58%	9.2	1.3	1.8

Table 3.6: Nondimensional numbers for fixed (submerged) cylinder. Rn and β values must be multiplied with 10^6 and 10^5, respectively.

3.2.4 Submerged cylinder

Wave excitation of the BCS with a frequency close to the natural frequency in heave can cause full submergence for shorter intervals. The deeper a cylinder gets, the less influence the free surface will have. However, it is not likely that the floater reaches a depth where the free surface effects are not important.

Nevertheless, initially we choose to discuss hydrodynamic loading for a submerged, slender circular cylinder assuming no free surface effects. The reasons for discussing Morison's equation for submerged cylinders is that the drag part of Morison's equation subsequently is used both for horizontal drag on the floater (see Section 3.3.4) as well as drag on the net-pen (see Section 3.3.5). It does *not* mean that it is recommended to use Morison's equation directly as the load model for a floater. The numerical results from Morison's equation also serves as a reference for linear potential theory, see Section 3.3. Thus, the numerical results in this subsection are based on a cylinder with the dimensions of the cylinders used for the BCS. Finally, Morison's equation is relevant as it previously has been used in the context of floating fish farms, see e.g. (Ormberg, 1991), (Berstad et al., 2004), (Gosz et al., 1996), (Lekang, 2007), (Thomassen and Leira, 2005), (Thomassen and Leira, 2006) (the latter two by the present author as co-author).

Morison's equation (i.e separated flow)

The empirically based Morison's equation (Morison et al., 1950) is normally used for fully submerged cylinders (no free surface effects) when viscous effects are of importance. Morison's equation was originally developed in order to model loading on a fixed, surface piercing, circular, vertical, and rigid cylinder standing on the sea bed with viscous forces being important. It yields a force that is perpendicular to the cylinder axis. Flow components and any resulting forces parallel to the cylinder axis are neglected. Morison's equation tells us that the horizontal force dF per unit length on a vertical rigid cylinder can be written:

$$dF = \rho_w \frac{\pi D^2}{4} C_M a_1 + \frac{\rho_w}{2} C_D D \left|u\right| u \tag{3.12}$$

u and a_1 are the horizontal undisturbed fluid particle velocity and acceleration at the midpoint of the strip. The first and last terms of Morison's equation are called drag and mass[5] force, and the corresponding coefficients C_M and C_D are the mass and drag coefficients, respectively. C_M is often split into a diffraction part (i.e. C_m) and a Froude-Kriloff part (with coefficient equal to 1): $C_M = C_m + 1$.

Mass and drag coefficients

For a submerged cylinder potential theory is a good approximation as long as no separation occurs (as it is for a floating cylinder). According to potential theory $C_M = 2.0$.

[5]Journée and Massie (2001) use the term inertia instead of mass for the second term of Morison's equation. In the present thesis the term mass is chosen, i.e. in accordance with (Faltinsen, 1990).

TRW	B	C	D	H_{max}
$z_{KC=2}$ [m]	0.7	4.6	10.8	24.5

Table 3.7: Depth at which KC=2 for TRWs

Separation typically occurs for $KC > 2$, i.e. for all TRW ($KC \geq 3.1$). As the KC number is proportional to the velocity, it will also decrease exponentially with depth. The depth at which $KC = 2$ is shown in Table 3.7. From the table we see that KC will be greater than two for all expected depths, with a possible exception for TRW B.

For $KC > 2$, mass and drag coefficients C_M and C_D have to be empirically determined. Multiple researchers have indeed conducted laboratory tests to determine C_M and C_D, often for very specific situations (Journée and Massie, 2001).

The vast majority of experiments and recommendations quantifying numerical values for mass force and drag coefficients have been done for fully submerged cylinders with no influence from the free surface. However, even for this case, there is no consensus on which values are appropriate. In general, for the relevant KC and Rn intervals ($3 < KC < 20$ and $Rn \approx 10^6$) the flow is separated and turbulent. Most results and recommendations for a fixed, smooth cylinder fall in the intervals:

$$\begin{aligned} 1.6 &\leq C_M \leq 2.0 \\ 0.6 &\leq C_D \leq 1.0 \end{aligned} \tag{3.13}$$

For the numerical results of the floater presented later we have chosen to use the upper limits of Equation 3.13, yielding high values for the drag and mass force.

As briefly discussed later in this section, Morison's equation can be adapted to accommodate both an oscillating cylinder and any inclination of the cylinder axis. Both circumstances can affect the force coefficients, but this influence will not be considered further here.

Mass vs. viscous dominance

Mass force vs. drag force importance can be categorized based on a comparison of the respective terms in Morison's equation assuming fixed cylinder and maximum wave particle velocity and acceleration (i.e. zero depth)[6]. The ratio between the drag and mass force amplitudes for a regular wave with frequency ω is (Journée and Massie, 2001):

$$\frac{F_{drag,a}}{F_{mass,a}} = \frac{\frac{1}{2}\rho_w C_D D u_a |u_a|}{\frac{\pi}{4}\rho_w C_m D^2 \omega u_a} = \frac{2C_D|u_a|}{\pi C_m D \omega} = \frac{1}{\pi^2} \cdot \frac{C_D}{C_m} \cdot KC \tag{3.14}$$

Assuming the typical coefficient relation $C_M/C_D = 2$ (e.g. $C_M = 2.0$ and $C_D = 1.0$), we get equal amplitudes for $KC = 19.7$. Both the KC-number (i.e. $\pi \cdot H/D$)

[6]We ignore the apparent paradox that whereas using maximum amplitudes implicitly assume zero depth, Morison's equation is normally used under the assumption of no free-surface effects.

KC	H/D	Dominance
$KC < 3$	$H/D < 1.0$	Mass force is dominant. Drag force can be neglected.
$3 < KC < 15$	$1.0 < H/D < 4.8$	Drag force can be linearized.
$15 < KC < 45$	$4.8 < H/D < 14.3$	Full Morison equation.
$KC > 45$	$H/D > 14.3$	Drag force is dominant. Mass force can be neglected.

Table 3.8: Mass or drag force dominance as a function of KC-number (Journée and Massie, 2001)

(Journée and Massie, 2001) and H/D (Faltinsen, 1990) can be used to identify intervals of mass force vs. drag force dominance, see Table 3.8. For $KC < 3$, the drag force is less than 15% of the mass force and for $KC > 45$ mass force is less than 44% of drag force, cf. Table 3.8.

The H/D-relations for TRW are shown in Table 3.6 and vary from 1 to 5.7. According to Table 3.8, drag loads can be linearized for TRW B to D, whereas for the H_{max}-wave there is a transition into the domain of a full Morison equation, i.e. with a KC-number around 18.

Amplitude reduction with depth

As both the water particle velocity and acceleration decrease with depth as e^{kz}, the mass force and drag force (depth dependent) amplitudes decrease with depth as e^{kz} and e^{2kz}, respectively. Drag force shows a stronger reduction with depth than mass force. Thus, the mass force dominance established above will be further strengthened with depth. The respective decrease with depth is shown in Table 3.9 for the relevant depth interval: $z = -0.5\,m, -1.0\,m, -1.5\,m$. We see from the table that for TRW C, D, and H_{max} the reduction in mass force is less than 22% for depths less than $1\,m$. The corresponding number for drag is 40%. Thus, for these TRW the reduction in mass force is quite limited whereas the reduction in drag is more significant. For TRW B the reduction is considerable for both mass force and drag.

Later in this chapter horizontal mass force and drag force will be based on horizontal acceleration and velocity. For large submergence, the effect of amplitude reduction should be taken into account. However, assuming that the dominating level of submergence for the BCS is less than $1\,m$, we choose to ignore the amplitude reduction with depth and use the maximum amplitudes at the surface ($z = 0\,m$) — this is consistent with the long wave length approximation of Section 3.2.3. This is a conservative assumption as the maximum amplitudes are assumed. Finally, it is noted that the effect of amplitude reduction with submergence is probably less than other effects such as nonconstant added mass and hydrodynamic damping.

TRW	k	Mass			Drag		
	$[\frac{rad}{m}]$	-0.5m	-1.0m	-1.5m	-0.5m	-1.0m	-1.5m
B	0.64	72%	53%	38%	53%	28%	14%
C	0.25	88%	78%	69%	78%	60%	47%
D	0.14	93%	87%	81%	87%	75%	65%
H_{max}	0.09	96%	91%	87%	91%	84%	76%

Table 3.9: Reduced values of mass force and drag term of Morison's equation with depth.

Morison loading for a vertical cylinder in the free surface zone

Faltinsen (1990) notes that for a vertical cylinder, special care should be taken in the free-surface zone as a straightforward application of Morison's equation implies that the absolute value of force per unit length is largest at the free-surface, i.e. this clearly gives an unphysical result as the pressure is constant on the free surface and thus the force per unit length has to go to zero. Further, it is suggested that the maximum force occurs at a distance of 25% of the wave amplitude below the free-surface, i.e. from $0.13\,m$ to $0.71\,m$ depth for the TRW.

Morison loading for a horizontal cylinder in the free surface zone

The discussion of a vertical cylinder in the free surface zone above is not directly applicable to a floating horizontal cylinder, but it points to the fact that loading models in the free-surface zone should be applied with caution.

To account for the instantaneous wave surface elevation several modifications of the linear theory have been suggested. E.g. Ormberg (1991) used Wheeler stretching (Wheeler, 1970). In the present work no modification of the linear wave theory is introduced to find horizontal forces. The velocity used to calculate horizontal drag on the floater is found directly from linear wave theory and the mean position of the cylinder element in question — no account is taken of the instantaneous location of the floater, see Section 3.3.4. The reasons are twofold:

- For the fatigue parameter study (see Chapter 9), the focus is on load effects caused by vertical loading, i.e. vertical buoyancy is assumed to be the dominating (nonlinear) effect and is thus implemented and studied first.

- Finding drag effects of floating cylinders in waves has not been thoroughly investigated — e.g. in terms of coefficients — and an implementation based on Morrison's equation is associated with considerable uncertainty. Thus, a possible incremental improvement by considering only the instantaneous wave surface does not seem justified.

TRW	v_{max} $[m/s]$	a_{max} $[m/s^2]$	$F_{mass,a}$ $[kN/m]$	$F_{drag,a}$ $[kN/m]$	$\frac{F_{drag,a}}{F_{mass,a}}$	$\frac{2F_{mass,a}}{B_{max}}$	$\frac{2F_{drag,a}}{B_{max}}$
B	1.3	3.2	5.1	0.8	16%	129%	20%
C	1.6	2.5	4.0	1.3	32%	101%	32%
D	1.8	2.1	3.4	1.6	48%	86%	41%
H_{max}	2.7	2.5	4.0	3.7	91%	102%	93%
Avrg.	1.8	2.6	4.1	1.8	47%	104%	47%

Table 3.10: Velocity, acceleration and Morison forces for TRW. Assuming $C_D = 1$ and $C_M = 2$. Maximum buoyancy $B_{max} = 7.9\,kN/m$. Subscript a refers to amplitude.

Comparison of drag force, mass force, and buoyancy loads

Assuming linear wave theory and deep water waves, we can find numerical values for maximum water particle velocity and acceleration amplitudes (i.e. for $z = 0\,m$) and the corresponding mass force and drag force terms of Morison's equation as well as the mass force/drag force ratio, see Table 3.10.

A floater may oscillate between being fully submerged and dry, i.e. fluctuate between a buoyancy of $0\,kN/m$ and $7.9\,kN/m$ (see Table 2.5). The water particle velocity and acceleration required to produce a drag force or mass force of $7.9\,kN/m$ are $3.9\,m/s$ and $4.9\,m/s^2$, respectively (for $C_M = 2$ and $C_D = 1$). However, as mass forces and drag forces change sign (i.e. direction), it is more relevant to consider the values required to give half the maximum buoyancy, i.e. $2.8\,m/s$ and $2.5\,m/s^2$. In Table 3.10, the drag force and mass force terms are compared to half the maximum buoyancy for the TRW. We see that the (double) mass force is of the order of the (maximum) buoyancy. The ratio of the double mass force term to the (maximum) buoyancy is ($A = \frac{\pi D^2}{4}$):

$$\frac{2 \cdot F_{mass}}{B_{max}} = \frac{2\,\rho_w\,A\,C_M\,a_1}{\rho_w\,A\,g} = \frac{2\,C_M\,a_1}{g} = \frac{a_1}{2.5\,m/s^2} \tag{3.15}$$

Whereas the mass force term (and the wave particle acceleration) shows little change with wave height, the drag force term increases sharply with wave height. The mass force term dominates the drag term except for the H_{max}-wave. The domination will increase with depth, see Table 3.9. These results are in accordance with the KC-dependence of mass force vs. drag force dominance described in Table 3.8.

Influence of cylinder oscillation and orientation

The previous discussions and calculations were presented under the assumption that the cylinder is fixed and vertical. In practice neither of these is the case for a floater nor a netpen.

Morison's equation can be modified to accommodate oscillation of the cylinder as well as any orientation of the cylinder. An inclined orientation of the cylinder is taken into con-

sideration by using the velocity and acceleration components perpendicular to the cylinder axis. As an example of the effect of oscillation we look at a moving vertical circular cylinder and denote the horizontal rigid body motion of a strip of length dz by η_1. u and a_1 are the horizontal (i.e. x-component) water particle velocity and acceleration, respectively. The added mass coefficient is: $C_m = C_M - 1$. The horizontal hydrodynamic load dF is then (Faltinsen, 1990):

$$dF = \frac{1}{2}\rho_w C_D dz(u - \dot{\eta_1})|u - \dot{\eta_1}| + \rho_w C_M \frac{\pi D^2}{4} dz\, a_1 - \rho_w (C_M - 1)\frac{\pi D^2}{4} dz\, \ddot{\eta_1} \qquad (3.16)$$

The influence of cylinder oscillations (i.e. cylinder velocity and acceleration) on KC and Rn-values and subsequently C_D and C_M-values are typically expressed through the use of relative velocity u_R and acceleration a_R rather than water particle velocity v and acceleration a. Drag force is dependent on the relative velocity $u_R = u - \dot{\eta}$, whereas the mass force is divided in two parts dependent on water particle acceleration a_1 and cylinder acceleration $\ddot{\eta}_1$, respectively. The inherent decoupling of the acceleration terms makes the mass force easier to handle mathematically than is the case for drag. The $C_m\, \rho_w\, A\, \ddot{\eta}$-term can be moved to the "left hand side" in the equation of motion and added to the structural mass, leaving the water particle acceleration term ($C_M\, \rho_w\, A\, a$) as the mass force term on the "force side". It is mathematically convenient (and common practice) to assume that the added mass coefficient C_m is constant.

Due to the nonlinearity of the drag force term, linearization is a well-known technique to simplify the numerical analysis through decoupling of the velocity components, see e.g. (Leira, 1987) and (Krolikowski and Gay, 1980). Linearization typically introduces acceptable errors as long as the mass force is dominating over drag force (see Table 3.8). The linearized drag force can (as for mass force) be split into two terms. The term proportional to the response velocity perpendicular to the cylinder axis $\dot{\eta}_\perp$ is moved to the left hand side and added to the structural damping. The term proportional to the component of the water particle velocity perpendicular to the cylinder axis $u_\perp$ is left on the right hand side as a driving force. u_0 is the amplitude of the perpendicular component of water particle velocity, i.e. $u_\perp(t) = u_0 \cdot \sin(\omega \cdot t)$. We assume that the response velocity is much smaller than the water particle velocity, i.e. $\dot{\eta}_\perp << u_\perp$. Linearization in regular waves (harmonic loading) based on Fourier series then gives:

$$F_{drag} = \frac{1}{2}\rho_w C_D D \frac{8}{3\pi} u_0\, u_R = K_D \frac{8}{3\pi} u_0 u_R = B(u_\perp - \dot{\eta}_\perp) \qquad (3.17)$$

The damping coefficient is thus $B = K_D \frac{8}{3\pi} u_0$ and the exciting force is $F_{drag,lin} = K_D \frac{8}{3\pi} u_0 u_\perp$. Equation 3.17 is used to estimate the load effects of horizontal drag on the floater in Section 3.3.4 and vertical and horizontal drag effects on the netpen in Section 3.3.5.

3.3 Linear analysis of the floater

The loads acting on a floating cylinder in waves are typically found by applying potential flow theory, see e.g. (Newman, 1977), (Faltinsen, 1990). For simplicity and effectiveness, linear potential theory (first-order solution) is most often applied (e.g. enabling frequency domain response analysis). Linearization is normally valid if the wave amplitude is small relative to a characteristic wavelength and body dimension (Faltinsen, 1990).

Potential theory typically gives good results if viscous effects are of little importance. For a floating body viscous effects are usually only considered when the horizontal flow (current or waves) separates, thus giving a drag force which is important e.g. for damping of moored structures. A floater is typically moored and horizontal viscous effects are therefore taken into account as linearized drag, see Section 3.3.4. They can thus be included in a linear analysis. Likewise, movement of the netpen is assumed to have a viscous effect and is included as linearized drag damping.

This section describes the recommended wave load model for a linear structural analysis of the BCS, i.e. a combination of load effects according to:

- Linear potential theory (see Section 3.3.1 - 3.3.3)
- Linearized horizontal drag for the floater (see Section 3.3.4)
- Linearized drag damping of the netpen (see Section 3.3.5)

The results will be used in 1 DOF natural period analysis, see Section 4.3 and 4.4. As described in later chapters these results will also be used in linear time domain simulations (frequency domain analysis will not be performed). The linear analysis will be verified against hand calculations and serve as a reference for the nonlinear analysis. The recommended modifications for a nonlinear analysis are presented in Section 3.4.

3.3.1 Motion of a floating rigid body

According to linear theory the equations of motion for a floating rigid body are (Faltinsen, 1990):

$$\sum_{k=1}^{6}[(M_{jk} + A_{jk})\ddot{\eta}_k + B_{jk}\dot{\eta}_k + C_{jk}\eta_k] = F_j \exp(-i\omega_e t) \ , \ j = 1, ..., 6 \tag{3.18}$$

The hydrodynamic added mass A_{jk}, hydrodynamic damping B_{jk}, and the exciting wave force amplitudes F_j are found from linear potential theory. Generally, a numerical method is required for the calculations. Descriptions of the procedures and various methods can be found in e.g. (Faltinsen, 1990) and (Journée and Massie, 2001).

C_{jk} is the restoring force coefficient (i.e. water plane stiffness). For the BCS the (maximum) restoring coefficient in heave is (see Section 3.2.1): $C_{33} = k_w = A_w \rho_w g = 10.1 kN/m^3 \cdot l_w$. M_{jk} is the structural mass. In addition to the water plane stiffness, the mooring lines of the BCS act as restoring horizontal forces.

For added mass A_{jk}, damping B_{jk}, and exciting wave forces F_j only the heave (vertical) and the sway (perpendicular) translational DOFs are given a nonzero value. It is reasonable to assume that this is sufficiently accurate as the number of elements in the finite element discretization increases.

In structural dynamics the damping and stiffness is typically named C and K, respectively, as opposed to B and C in hydrodynamics, as described above. In the present thesis, (structural and hydrodynamic) damping will be denoted B and water plane stiffness k_w. C is used to designate force coefficients, as is typical for Morison's equation, see Section 3.2.4.

Strip theory

In strip theory, potential coefficients and exciting forces for three-dimensional bodies are based on two-dimensional potential theory, see e.g. (Faltinsen, 1990) and (Journée and Massie, 2001). This approach lends itself nicely to the BCS as it is built up from slender cylinders, and will therefore be used.

3.3.2 Added mass and potential theory damping

Bai and Yeung (1974) have investigated the added mass and hydrodynamic damping of a half submerged cylinder. The values are based on Frank's close fit method (Frank, 1967). Their results can be used to find the added mass A_{ii} and the hydrodynamic damping B_{ii} in heave and sway and are based on the nondimensional frequency ω^*, where R is the radius of the cylinder:

$$\omega^* = \frac{\omega^2 R}{g} \tag{3.19}$$

$$T = 2\pi\sqrt{\frac{R}{g\,\omega^*}} = \pi\sqrt{\frac{2\,D}{g\,\omega^*}} \tag{3.20}$$

Bai and Yeung (1974) cover the interval $\omega^* > 0.1$, i.e. $T < 4.5\,s$ for the BCS. We want to express the added mass in terms of a (nondimensional) equivalent added mass coefficient:

$$C_{m,eq,i} = \frac{A_{ii}}{\frac{\pi D^2}{4}\cdot\rho_w}\,,\ i = 2,3 \tag{3.21}$$

$C_{m,eq,i}$ is the ratio of added mass to the mass of the displaced water volume of the *whole* cylinder, i.e. it can be compared to the added mass coefficient used in Morison's equation — thus the name. In Table 3.11 and 3.12, added mass and damping in heave and sway, respectively, are listed for the TRW. The higher TRW have a period greater than $4.5\,s$, but values are found by extrapolation. $C_{m,eq,i}$-values are included in Table 3.11 and 3.12, as is the total mass of the BCS m_{tot}. Finally, the diffraction forces $F_{a,i}$ and $F_{u,i}$ are included, see Equation 3.22 and 3.23.

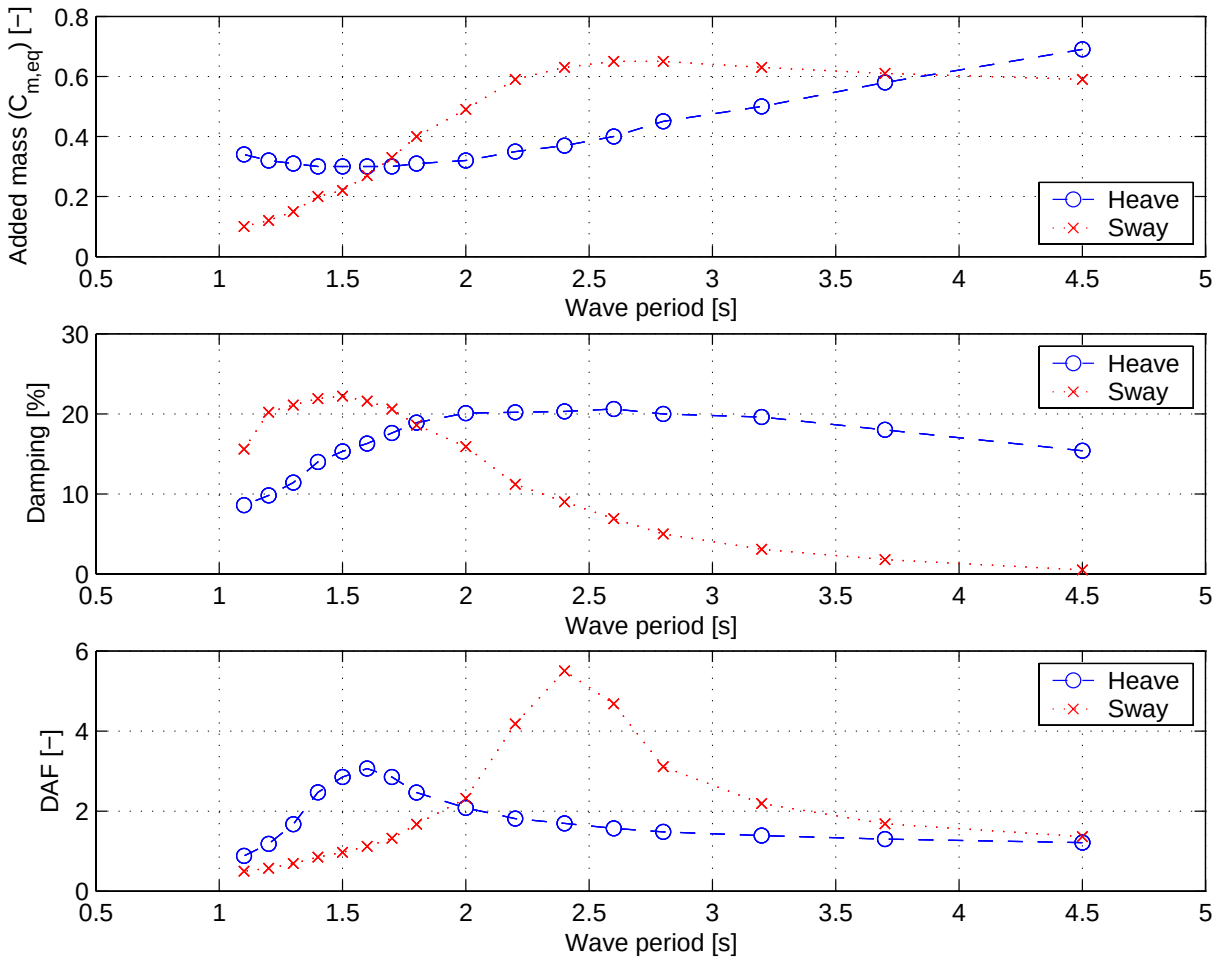

Figure 3.2: Equivalent added mass coefficient $C_{m,eq}$, damping coefficient ξ, and dynamic amplification factor DAF in heave and sway for the BCS.

Damping can be expressed in terms of the damping coefficient ξ, see Section 3.3.6. Based on added mass and relative damping, the dynamic amplification factor DAF can be calculated, see Appendix F. The added mass coefficients, the damping coefficients, and the dynamic amplification factors in heave and sway are plotted in Figure 3.2 as a function of wave period. The wave period interval is from $1\,s$ to $4.5\,s$.[7] A similar figure has been presented for a sphere in heave by Newman (1977). The added mass is considered when calculating the critical damping, see Section 3.3.6.

[7] As discussed in section 3.2.3, the relative importance of wave diffraction effects increases as the wave period decreases, and for $T < 1.8\,s$ wave diffraction effects should be considered according to the rule-of-thumb: $\lambda/D \geq 5$.

TRW	ω $[\frac{rad}{s}]$	$\frac{\omega^2 R}{g}$ $[-]$	A_{33} $[\frac{kg}{m}]$	$C_{m,eq}$ $[-]$	m_{tot} [t]	$F_{a,3}$ $[\frac{kN}{m}]$	B_{33} $[\frac{kNs}{m^2}]$	$F_{u,3}$ $[\frac{kN}{m}]$
B	2.5	0.32	323	0.40	87	1.0	1.1	1.5
C	1.6	0.13	508	0.63	109	1.3	1.0	1.6
D	1.2	0.07	605	0.75	121	1.3	0.9	1.5
H_{max}	0.9	0.04	689	0.85	131	1.7	0.7	2.0
Avrg.	1.6	0.14	530	0.66	112	1.3	0.9	1.6

Table 3.11: Linear hydrodynamic added mass and damping for a half submerged cylinder in heave.

TRW	ω $[\frac{rad}{s}]$	$\frac{\omega^2 R}{g}$ $[-]$	A_{22} $[\frac{kg}{m}]$	$C_{m,eq}$ $[-]$	m_{tot} $[t]$	$F_{a,2}$ $[\frac{kN}{m}]$	B_{22} $[\frac{kNs}{m^2}]$	$F_{u,2}$ $[\frac{kN}{m}]$
B	2.5	0.32	524	0.65	80	1.7	0.51	0.64
C	1.6	0.13	484	0.60	77	1.2	0.08	0.12
D	1.2	0.07	464	0.58	76	1.0	0.01	0.02
H_{max}	0.9	0.04	448	0.56	75	1.1	0.00	0.00
Avrg.	1.6	0.14	480	0.60	77	1.2	0.15	0.19

Table 3.12: Linear hydrodynamic added mass and damping for a half submerged cylinder in sway.

Discussion

For the equivalent added mass coefficients $C_{m,eq,i}$ the intervals of variation are from 0.3 to 0.7 in heave and 0.1 to 0.65 in sway. However, for the most important interval $T > 2\,s$, heave shows much more variation than sway: from 0.3 to 0.7 vs. from 0.5 to 0.65. Further, the added mass reaches a plateau level and decreases in sway whereas heave has a steady increase over this interval. Indeed, the added mass in heave approaches infinity as $\omega^* \to 0$ whereas added mass in sway reaches its maximum for $\omega^* \approx 0.5$.

The damping coefficient in heave is high over the whole interval. In sway, on the other hand, the damping coefficient decreases sharply from a very high level for short periods to almost zero for long periods. However, damping in both sway *and* heave approaches zero when $\omega^* \to 0$.

The DAF is quite small in heave due to the high damping levels. In sway, the maximum DAF is considerably higher and it occurs for a higher and more important wave period due to the strong decline in damping with increasing wave period.

3.3.3 Excitation forces based on potential theory

Excitation forces will be different for a cylinder perpendicular to the wave direction as compared to a cylinder parallel to the wave direction. For a parallel cylinder we will assume that the horizontal exciting forces can be neglected, whereas they will be considered for perpendicular waves. Below, the focus is on a cylinder perpendicular to the wave direction. The vertical load model will be adopted also for parallel cylinders on an element wise level, as the element length ($\approx 1.5\,m$) typically will be much shorter than the dominating wave lengths ($5 - 70\,m$).

Cylinder perpendicular to wave direction

Excitation forces are typically divided into Froude-Kriloff and diffraction effects. It can be shown that for long waves the exciting diffraction force can be found from the added-mass and damping coefficients, see e.g. (Faltinsen, 1990), (Newman, 1977). The mass diffraction force (i.e. proportional to the water particle acceleration) is:

$$F_{a,i} = A_{ii} \cdot a_i = C_{m,eq,i} \cdot \rho_w \frac{\pi D^2}{4} a_i \ , \ i = 2, 3 \tag{3.22}$$

a_i is the water particle acceleration component at $z = 0$ in the direction i. Likewise, the diffraction force proportional to the water particle velocity is:

$$F_{u,i} = B_{ii} \cdot u_i \ , \ i = 2, 3 \tag{3.23}$$

u_i is the water particle velocity component at $z = 0$ in the direction i. As $\omega \to 0$ the acceleration approaches zero faster than the added mass in heave approaches infinity, and thus the mass diffraction force approaches zero. Correspondingly, as $\omega \to 0$ the velocity approaches zero whereas the damping coefficient is finite, and thus $F_{u,i}$ approaches zero. $F_{u,i}$ is ninety degrees out of phase with $F_{a,i}$. The amplitudes of $F_{a,i}$ and $F_{u,i}$ are listed in Table 3.11 and 3.12.

The Froude-Kriloff (FK) force is the force due to the undisturbed (dynamic) pressure field and can be found by integrating the pressure over the wet contour. For a half submerged cylinder with wave direction perpendicular to its axis the expression for the linear, vertical FK-force is:

$$F_{FK,v} = \int_0^\pi p_D \, r \, \sin\alpha d\,\alpha = \rho_w \, g \, \zeta_a \int_0^\pi \exp(-kr \sin\alpha) \sin(\omega t + kr \cos\alpha) \sin\alpha \, d\alpha \tag{3.24}$$

ζ_a is the surface elevation amplitude. In the limit case of infinitely long waves — i.e. $kR \to 0$ — the expression is simplified:

$$\begin{aligned} \lim_{kr \to 0} F_{FK,v} = & \quad \rho_w g \zeta_a \textstyle\int_0^\pi (\sin(\omega t) + kr \cos(\omega t) \cos\alpha) \sin\alpha d\alpha \\ = & \quad \rho_w g \zeta_a D \sin(\omega t) = \rho_w g D \zeta(t) = C_{33}\, \zeta(t) = k_{w,max}\, \zeta(t) \end{aligned} \tag{3.25}$$

Thus, for very long waves, the Froude-Kriloff force (and the total force as $F_{a,3} \rightarrow 0$ and $F_{u,3} \rightarrow 0$) is proportional with the surface elevation $\zeta(t)$, i.e the Froud-Kriloff force for very long waves is equal to the buoyancy effect of the wave. This force is proportional to the wave elevation ζ rather than the water particle acceleration a_3. The corresponding vertical (quasi static) response amplitude of the cylinder is: $\Delta_v = \frac{F_{FK,v}}{k_{w,max}} = \zeta(t)$. As the amplitude is equal to the free surface elevation and the phase angle is zero (as $\omega \rightarrow 0$) the limit case illustrates that for very long waves a perpendicular cylinder will follow the wave elevation. The Froude-Kriloff force for long waves has the direction of the surface elevation, but opposite (180° out-of-phase) of the vertical acceleration a_3 and the vertical diffraction force $F_{a,3}$). The total vertical excitation force is thus:

$$F_{tot,3} = F_{FK,v} - F_{a,3} \tag{3.26}$$

The corresponding expressions for the horizontal force are:

$$F_{FK,h} = \int_0^{\pi} p_D r \cos\alpha d\alpha = \rho_w g \zeta_a \int_0^{\pi} \exp(-kr\sin\alpha)\sin(\omega t + kr\cos\alpha)\cos\alpha\, d\alpha \tag{3.27}$$

$$\begin{aligned} \lim_{kr\rightarrow 0} F_{FK,h} = & \quad \rho_w g \zeta_a \textstyle\int_0^{\pi} (\sin(\omega t) + kr\cos(\omega t)\cos\alpha)\cos\alpha d\alpha \\ = & \quad \tfrac{1}{2}\tfrac{\pi D^2}{4}\rho_w g k \zeta_a \cos(\omega t) = \tfrac{1}{2}\tfrac{\pi D^2}{4}\rho_w \omega^2 \zeta_a \cos(\omega t) = \tfrac{1}{2}\tfrac{\pi D^2}{4}\rho_w\, a_2(t) \end{aligned} \tag{3.28}$$

Thus, the horizontal Froude-Kriloff force is proportional to the perpendicular water particle acceleration at $z = 0$. It is interesting to note that while the vertical Froude-Kriloff force is independent of wave frequency, the horizontal component is proportional with ω^2. Thus, the horizontal FK-force approaches 0 for long waves.

$F_{FK,v}$ is found by numerical integration of Equation 3.24 and listed in Table 3.13. Further, the limit values for the FK-force $F_{FK,lim}$ is included — using Equation 3.25 — and this is compared to both the actual FK-force and the total force as $\frac{F_{FK,v}}{F_{FK,lim}}$ and $\frac{F_{tot}}{F_{FK,lim}}$.

In Table 3.14 the corresponding values are listed for sway based on Equation 3.27 and 3.28. An equivalent Froude-Kriloff parameter $C_{FK,eq}$ is also included in Table 3.14, cp. the $C_{m,eq}$ parameter of Table 3.11 and 3.12. This parameter is used to compare the calculated horizontal FK-forces with the Froude-Kriloff part of the mass force in Morison's equation: $F_{FK,Mor} = C_{FK} \cdot \frac{\pi D^2}{4}\rho_w a_i$. For a submerged cylinder with no free surface effects $C_{FK} = 1.0$. Thus, C_{FK} does not appear in Equation 3.16. We then get:

$$C_{FK,eq} = \frac{F_{FK,h}}{a_2 \frac{\pi D^2}{4}\rho_w} \tag{3.29}$$

$$F_{FK,h} = C_{FK,eq} \cdot a_2 \frac{\pi D^2}{4}\rho_w \tag{3.30}$$

Finally, based on the mass force in Morison's equation (i.e. $\rho_w C_M \frac{\pi D^2}{4} a_i$, cp. Equation 3.16) an equivalent total force coefficient $C_{M,eq}$ is found and included in Table 3.14:

$$C_{M,eq} = \frac{(F_{FK,h} + F_{a,2})}{a_2 \frac{\pi D^2}{4} \rho_w} \tag{3.31}$$

$$F_{mass,2} = F_{FK,h} + F_{a,2} = C_{M,eq} \cdot a_2 \frac{\pi D^2}{4} \rho_w \tag{3.32}$$

Discussion

Equation 3.25 and Equation 3.28 show that for long waves the F_{FK}-force is proportional to surface elevation and horizontal water particle acceleration, respectively. Comparing the numerical values with the limit case gives values in the range from $77-97\%$ (vertical) and $86-99\%$ (horizontal). This means even for the shortest waves the force is close to the value for infinitely long waves.

In heave (and as expected), the FK-force is dominating over the diffraction force, and the ratio of the total force to the long wave F_{FK}-force (i.e. $\frac{F_{tot}}{F_{FK,lim}}$) varies from 57% to 91%. Thus, using the limit value of the Froude-Kriloff force is a conservative approximation for the total vertical hydrodynamic force on a floating cylinder in perpendicular waves for all TRW:

$$F_{vert}(t) = k_w \, \zeta(t) \tag{3.33}$$

This implies that the sum of hydrostatic load (i.e. initial buoyancy) and hydrodynamic load can be approximated as the instantaneous total buoyancy.

The above result can also be supported through a different line of reasoning. For the free surface *above* $z = 0\,m$ the combined hydrostatic and hydrodynamic pressure are typically assumed to vary linearly (Faltinsen, 1990), and the total pressure has to be zero at the free surface. For small depths ($z > -1\,m$) in long waves, the exponential factor of the dynamic pressure amplitude ($p_{d,amp} = \rho_w \, g \, \zeta_a \, \exp(kz)$) will be approximately 1. Thus, for small depths and long waves the total pressure will be zero at the free surface and increase linearly with depth with the same slope as the static pressure increase, i.e. the combined hydrostatic and dynamic force results in a force equal to the instantaneous buoyancy.

The sum of the vertical force and the (linear) restoring force is: $F_{vert}(t) - k_{w,max} \, \eta(t) = k_{w,max}[\zeta(t) - \eta(t)]$, i.e. the instantaneous change in buoyancy. This result is not surprising as the long wave limit case is quasi static, i.e. for long waves the cylinder will follow the wave elevation and the sum will be (approximately) zero.

The velocity proportional diffraction components $F_{u,3}$ are slightly bigger than the acceleration proportional components $F_{a,3}$, see Equation 3.23, 3.22, and Table 3.11. Both components are ignored in the analyses as they are small compared to the FK-force, see above.

For sway, the coefficients show little variation and a $C_{M,eq}$-value of 1.1 is a good approximation for all TRW. This is approximately half of typical C_M-values for a fully submerged cylinder (i.e. $1.6 - 2.0$). The average value of $C_{m,eq}$ is 30% higher than $C_{FK,eq}$ (i.e. 0.60

TRW	$F_{FK,v}$ $[\frac{kN}{m}]$	$F_{FK,lim}$ $[\frac{kN}{m}]$	$\frac{F_{FK}}{F_{FK,lim}}$ $[-]$	F_{tot} $[\frac{kN}{m}]$	$\frac{F_{tot}}{F_{FK,lim}}$ $[-]$
B	3.9	5.0	77%	2.9	57%
C	9.1	10.1	90%	7.8	78%
D	14.3	15.1	95%	13.0	86%
H_{max}	27.8	28.7	97%	26.1	91%
Avrg.	13.8	14.7	90%	12.5	78%

Table 3.13: Linear Froude-Kriloff forces for a half submerged cylinder in heave.

TRW	$C_{FK,eq}$ $[-]$	$C_{M,eq}$ $[-]$	$F_{FK,h}$ $[\frac{kN}{m}]$	$F_{FK,lim}$ $[\frac{kN}{m}]$	$\frac{F_{FK}}{F_{FK,lim}}$ $[-]$	F_{mass} $[\frac{kN}{m}]$	$\frac{F_{mass}}{F_{FK,lim}}$ $[-]$
B	0.43	1.1	1.1	1.3	86%	2.8	216%
C	0.45	1.1	0.9	1.0	90%	2.1	210%
D	0.47	1.0	0.9	0.9	94%	1.8	209%
H_{max}	0.49	1.0	1.0	1.0	99%	2.1	210%
Avrg.	0.46	1.1	1.0	1.0	92%	2.2	211%

Table 3.14: Linear diffraction and Froude-Kriloff coefficients and forces for a half submerged cylinder in sway.

vs. 0.46). The velocity proportional diffraction components $F_{u,2}$ are much smaller than the acceleration proportional components $F_{a,2}$, see Table 3.12, and will be ignored in the analyses.

3.3.4 Linearized horizontal drag for the floater

Separation around a floating cylinder in waves will be different in the horizontal and vertical directions. Viscous effects are likely to be of minor importance in the vertical direction (heave and pitch/roll) as separation has limited time and distance to develop. This is particularly the case for a structure without sharp corners. Separation will be additionally suppressed for a flexible structure which tends to move with the waves as is the case for a floater in long waves.

In the horizontal direction separation has ("half-infinite") distance to develop. Thus, drag damping is typically of importance for motion of a moored, floating structure. The drag can be expressed as the drag part of Morison's equation, and by linearization split into a damping and an exciting force term, see Section 3.2.4. According to Faltinsen (1990), the free-surface acts similar to an infinitely long splitter plate. This means that one can apply drag coefficients for the double body with splitter plates. The splitter plate effect causes a significant reduction of the drag coefficient for high KC-numbers. When the KC-number is low the eddies will stay symmetric for the double body without a splitter plate

TRW	B $[kNs/m^2]$	$F_{drag,lin}$ $[kN/m]$	F_{mass} $[kN/m]$	$\frac{F_{drag,lin}}{F_{mass}}$ $[-]$	$F_{u,tot}$ $[kN/m]$	$\frac{F_{u,tot}}{F_{mass}}$ $[-]$
B	0.27	0.34	2.8	11%	1.3	46%
C	0.34	0.54	2.1	24%	0.66	31%
D	0.39	0.69	1.8	39%	0.71	39%
H_{max}	0.58	1.6	2.1	76%	1.6	76%
Avrg.	0.40	0.78	2.2	38%	1.1	48%

Table 3.15: Horizontal linearized drag damping B, horizontal linearized drag force $F_{drag,lin}$, horizontal mass forces F_{mass}, and total horizontal exciting force in-phase with the horizontal water particle velocity $F_{u,tot}$ for half submerged cylinder.

which means the free surface has little effect for low KC-numbers. Thus, for the TRW — with (fixed cylinder) KC-numbers varying from 3.1 to 17.9 — only the higher wave heights can be expected to have lowered C_D-values (compared to "no surface effect cylinders"). Based on the above and the uncertainty of coefficient values mentioned in Section 3.2.4, we choose to assume the same value for the drag coefficient as for a fully submerged cylinder with no free surface effects, i.e. $C_D = 1$. The values of the drag force and linearized damping coefficient are half of the submerged cylinder case, see Equation 3.17, keeping the assumption that the response velocity is much smaller than the water particle velocity. The linearized drag force is then:

$$F_{drag} = \frac{1}{2} K_D \frac{8}{3\pi} u_0 u_R = 218 kg/m^2 \cdot u_0 (v_\perp - \dot{\eta}_\perp) \tag{3.34}$$

The damping coefficients ($B = 218 kg/m^2 \cdot u_0$) and the excitation drag force amplitudes (i.e. $F_{drag,lin} = 218 kg/m^2 \cdot u_0^2$) of the TRW are shown in Table 3.15 assuming that the wave direction is perpendicular to the cylinder axis.

The assumption of small horizontal oscillations (see above and Section 4.4) leads to excitation drag force amplitudes that are $\frac{8}{3\pi}$ -times (i.e. 85%, cp. Equation 3.12 and 3.17) of the corresponding drag force amplitudes found in Table 3.10. The drag force is half the linearized value for a fixed, submerged cylinder and thus $50\% \cdot \frac{8}{3\pi} = 42\%$ of the the maximum drag value, see Table 3.10).

In Table 3.15 linear potential force (mass force) F_{mass}, and the drag/mass force-ratio $\frac{F_{drag,lin}}{F_{mass}}$ are also included. The total force is found from linear potential theory, see Table 3.14. Finally, the amplitude of the total, horizontal force proportional to the water particle velocity (i.e. $F_{u,tot} = F_{u,2} + F_{drag,lin}$, $F_{u,2}$ from Table 3.12) and the ratio of this force to F_{mass} are given in the table. This table is thus also a summary of the horizontal excitation forces. The two force components — proportional to water particle acceleration and velocity, respectively — are 90° out-of-phase. The phase is $\sin(\omega t)$ and $\cos(\omega t)$ for velocity and acceleration, respectively. The mass force is the dominating force, as was the case for Table 3.10.

If analyses indicate that the horizontal structural velocity is small compared to the horizontal water particle velocity — even for low levels of damping — the assumption of small response is justified and (drag) damping is of little importance. If on the other hand analyses show that the horizontal structural velocity is significant this assumption can be either conservative or non-conservative (i.e. under- or overestimate damping) and further investigations should be made. Additionally, if the importance of drag increases, the linearization itself may be a poor approximation and should be reevaluated. The response velocity is evaluated in Section 4.4.

3.3.5 Linearized drag damping of the netpen

The netpen is an important part of the structural system, in particular with respect to damping. Whereas current typically affects the whole netpen (i.e. the whole water column), waves will only affect the upper parts of the netpen directly because a large part of the netpen will typically be below the wave zone altogether (or in an area of very low water particle velocity due to waves). This is because of the exponential decay of the velocity. The ratio of the drag amplitude at depths $z < 0\,m$ to the maximum drag amplitude (i.e. at $z = 0\,m$) for the TRW are $(0\%, 8\%, 24\%, 41\%)$ for $z = -5\,m$ and $(0\%, 1\%, 6\%, 17\%)$ for $z = -10\,m$.

As an initial approximation we assume that the netpen is unaffected by the waves. Thus, in a dynamic sense it is under the sole influence of floater movement (both horizontally and vertically). If the floater response is small, so is the structural effect of the netpen. Further, we assume that the structural dynamic effect of the netpen can be effectively modeled as linear drag damping. These assumptions are supported by (Lader and Fredheim, 2006) and (Lader et al., 2007a). Among the observations made in (Lader and Fredheim, 2006) is that:

> The floater movement is therefore the main contributor to the forces and tensions in the net, while the forces which are only connected with the fluid/structure interaction on the net are much smaller. This implies the importance of modeling the behavior of the floater accurately in order to obtain good estimates for the structural forces in the net.

In (Lader et al., 2007a) three wave load models are compared against experiments on a fixed, vertical net. Among the conclusions drawn are that a simplified drag load model (i.e. the drag part of Morison's equation) yield comparably good results, and that this load model showed good potential for improvement into a more accurate wave load model.

The uncertainties involved in describing the effect of the netpen is considerable: thread thickness, mesh size, and netpen depth can vary, but are in principle known quantities. More importantly, bio fouling, deflection of the netpen, and the hydrodynamic model are three interconnected factors that introduce considerable uncertainty in the structural analysis. Despite the importance of these factors, their complexity does not allow an elaborate discussion in this context, i.e. bio fouling is neglected, a simplified hydrodynamic model will be assumed, and the netpen is assumed to always be fully stretched.

Vertical drag

As an initial approach we assume that the netpen is always stretched and undeformed, i.e. all threads have the same velocity. Shielding is neglected. The drag is estimated using the drag part of Morison's equation. The total drag is then a function of the vertical velocity of the floater v_f, yarn diameter D_y, yarn drag coefficient $C_{D,y}$, and number of vertical meshes $n = depth/meshsize$:

$$F_{drag,netpen} = 0.5\rho_w D_y C_{D,y} v_f |v_f| n \tag{3.35}$$

Comparing netpen drag with the floater (corresponding to a fully submerged cylinder) drag we get:

$$\frac{F_{drag,np}}{F_{drag,f}} = \frac{0.5\rho_w D_y C_{D,y} v_f |v_f| n}{0.5\rho_w D_f C_{D,f} v_f |v_f|} = \frac{D_y C_{D,y} n}{D_f C_{D,f}} \tag{3.36}$$

To estimate $C_{D,y}$ the KC and Rn-numbers of the yarn are found. Compared with the floater, only the diameter is different (given the above assumptions). Thus, the non-dimensional numbers can be found from the corresponding numbers for the floater:

$$KC_y = KC_f \cdot \frac{D_f}{D_y} = 500 \cdot KC_f \tag{3.37}$$

$$Rn_y = Rn_f \cdot \frac{D_y}{D_f} = \frac{Rn_f}{500} \tag{3.38}$$

Thus, KC-numbers will be bigger than 1000 and Rn numbers are also of the order of 1000.

The Rn numbers are presented in Table 3.16. For very large KC numbers we may expect that the flow for each half period of the motion resembles that experienced in steady current (Sumer and Fredsøe, 2006).

Schlichting (1968) (reproduced in (Fredheim, 2005)) has presented drag coefficients for a circular cylinder at low Reynolds numbers. Based on the average Rn number we get: $C_{D,y} \approx 1.0$. Using netpen dimensions specified in Table 2.8, the netpen drag $F_{drag,np}$ can be expressed as a function of (fully submerged) floater drag $F_{drag,f}$:

$$F_{drag,np} = \frac{0.003m \cdot 1 \cdot 24m}{1m \cdot 1 \cdot 0.045m} F_{drag,f} = 1.60 \cdot F_{drag,f} \tag{3.39}$$

The linearized damping coefficient of the netpen can be found as for a submerged cylinder (cf. Equation 3.17). As discussed in Section 4.3, the perpendicular members of the floater will follow the free surface elevation for very long waves (quasi static response). Thus, the floater (and netpen) velocity is (approximately) the same as the vertical velocity of the free surface, i.e. the free-surface vertical water particle velocity. For wave periods closer to the natural period in heave/pitch/roll the influence of the dynamic response will increase. Thus, the long wavelength assumption is more appropriate for TRW D and H_{max} as opposed to TRW B and C.

Assuming that the netpen vertical motion is equal to the free-surface elevation, we get:

$$F_{drag,np,lin} = \ -\tfrac{1}{2}\,\rho_w\,C_{D,y}\,D_y \cdot n\tfrac{8}{3\pi}\,v_0\,\dot{\eta} = \ -697kg/m^2 \cdot v_0\,\dot{\eta} \tag{3.40}$$

TRW	B	C	D	H_{max}	Avrg.
Rn	$1.8 \cdot 10^3$	$2.4 \cdot 10^3$	$2.6 \cdot 10^3$	$4.0 \cdot 10^3$	$2.7 \cdot 10^3$
$B_{distr,vert}[kNs/m^2]$	0.88	1.1	1.2	1.9	1.3
$B_{distr,hor}[kNs/m^2]$	0.44	0.55	0.62	0.93	0.63

Table 3.16: Reynolds numbers Rn for $2\,mm$ yarn thread. Linearized distributed vertical and horizontal damping coefficient for netpen drag.

For the TRW we can now express the linearized distributed damping coefficient as $B_{np,vert} = 697kg/m^2 \cdot v_0$ for vertical netpen drag. By applying the relevant velocity amplitude for each TWR, we obtain the results in Table 3.16.

Horizontal drag

The horizontal drag of the netpen depends on the (rigid body) horizontal motion of the floater (sway/surge/yaw), whereas the horizontal motion of the floater depends on to which degree the horizontal natural periods are excited. For a traditional stiff mooring the natural periods will be around $2\,s$ (i.e. corresponding to short waves $\approx 6-7m$). As can be seen from Table 4.6, the dynamic amplification factor is low ($DAF \leq 1.5$) and, correspondingly, the maximum horizontal amplitude small ($\Delta_h \leq 0.33m$) even when netpen damping is neglected (except for TRW B).

For short waves close to the natural period (e.g. TRW B) resonance behavior can be experienced (if also wave excitation forces are in phase). In a regime of $\beta \approx 1$ the horizontal movement of the floater will grow and is likely to be limited by the netpen and floater drag damping.

When finding vertical netpen drag, we assumed that the netpen is always stretched and that all threads contribute to the damping. In the horizontal direction all threads are not likely to contribute equally as the horizontal response of the netpen is likely to decay with depth. As an initial approximation we assume that the horizontal perpendicular damping is half the vertical damping, see Table 3.16. However, in (Lader et al., 2007a) it was found that the horizontal forces were much bigger than the vertical forces on a fixed, vertical net. Thus, the vertical vs. horizontal damping effect should be investigated further.

3.3.6 Total damping in heave and sway

Based on the previous sections, estimates of total damping can be found for both heave and sway as a sum of linear (in the case of potential theory) and linearized (in the case of drag) damping, see Table 3.17 and 3.18, respectively. Additionally, critical damping $B_{cr} = 2\sqrt{k \cdot m_{tot}}$ (see Appendix F) and the damping coefficient $\xi = \frac{B}{B_{cr}}$ can be found using added mass values shown in Table 3.11 and 3.12 for heave and sway, respectively. The subscripts *flo* and *np* indicate contributions from the floater and the netpen, respectively.

TRW	B_{cr}	B_{flo}	ξ_{flo}	B_{np}	ξ_{np}	B_{tot}	ξ_{tot}	$\xi_{tot,int}$
B	649	139	21%	105	16%	244	38%	$29-50\%$
C	727	123	17%	131	18%	255	35%	$30-53\%$
D	765	102	13%	149	19%	251	33%	$30-52\%$
H_{max}	795	90	11%	224	28%	314	39%	$37-65\%$
Avrg.	734	113	16%	152	20%	266	36%	$32-55\%$

Table 3.17: Damping parameters for a half submerged cylinder in heave. Damping from linear potential theory and linearized netpen drag. Unit for B: $[kNs/m]$. $k_{distr} = 10.1kN/m^2$, $k_{floater} = 1209kN/m$, $m_{s,distr} = 403kg/m$, $m_{s,floater} = 48.4t$.

TRW	B_{cr}	B_p	ξ_p	B_d	ξ_d	B_{flo}	ξ_{flo}	B_{np}	ξ_{np}	B_{tot}	ξ_{tot}
B	426	30	7%	16	4%	47	11%	26	6%	73	17%
C	419	5	1%	21	5%	25	6%	33	8%	58	14%
D	416	1	0%	21	6%	24	6%	37	9%	61	15%
H_{max}	413	0	0%	35	8%	35	8%	56	14%	91	22%
Avrg.	419	9	2%	24	6%	33	8%	38	9%	71	17%

Table 3.18: Damping parameters for a half submerged cylinder in sway. Damping from linear potential theory, linearized horizontal drag on the floater, and the netpen. Unit for B: $[kNs/m]$. $k_{moor} = 142kN/m$, $k_{moor,tot} = 4 \cdot k_{moor} = 568kN/m$, $m_{struct,distr} = 403kg/m$, $m_{struct,floater} = 48.4t$.

For sway, the floater damping is a sum of (horizontal) drag and potential damping, and the contributions are indicated with the subscripts d and p.

All damping coefficients are given for the total floater. Thus, heave damping is found by multiplying the distributed damping coefficient values with the total length of the four floater members, i.e. $120\,m$. For sway the corresponding value is $60\,m$ as only the sides perpendicular to the wave progagation direction contribute to the damping.

According to linear potential theory, added mass varies with the wave period, see Section 3.3.2. In a realistic (i.e. nonlinear) case the instantaneous added mass will also be a function of submergence. To indicate the effect of a varying added mass on the critical damping and thus the ξ-values, we include the ξ-values resulting from using C_m equal to 0 and 1 in the $\xi_{tot,int}$-column (meaning the interval for ξ_{tot}). The upper limits are found from using $C_m = 0$ (i.e. added mass is zero) and the lower limits from using $C_m = 1$, i.e. the assumed upper limit for added mass.

From the heave table we see that potential and netpen damping each contributes roughly half of the total damping. The decrease in potential damping with TRW-category is offset by a corresponding increase in netpen damping making the damping coefficient in heave almost constant. The total damping is high: ξ_{tot} varies from 33 to 39%. The added mass increases with TRW resulting in an increase in the critical damping and a

corresponding reduction in the damping ratio for TRW B-D.

From the sway/surge table we see that the floater relative damping (i.e. sum of potential and drag damping) varies from 6 to 11% and the average is 8%, i.e. half of the floater average in heave. The estimated netpen damping and thus the total damping is also roughly half the corresponding values for heave: 9% and 17% vs. 20% and 35%.

Finally, it should be emphasized that considerable uncertainties are connected to the damping values. It is thus not unrealistic that the true total damping levels can be half or double those found, i.e. a realistic damping level from 20 to 80% vertically and 10 to 40% horizontally. Thus, the sensitivity to damping in this interval is investigated in Section 7.5.

With linearized damping in the interval 10 to 80%, both heave and sway/surge can be characterized as underdamped with high damping. Thus the linear dynamic amplification factor is limited, and can even be less than 1 (i.e. no amplification). For under-damped systems ($\xi < 100\%$) the damped natural period T_d will be higher than the undamped natural period T_N, see Appendix F.

In Table F.1 Appendix F the values for T_d and T_m for the relevant damping interval are shown. The corresponding maximum dynamic amplification factor DAF_m is also shown. We see that for realistic damping levels both the damped natural period T_d and maximum natural period T_m can be considerably larger than the natural period. For the expected level of damping around 40%, the DAF_m is small. The DAF based on linear potential theory was presented in Figure 3.2. In Figure 3.3 the DAF for increasing damping levels (representing drag damping and netpen damping) are plotted in heave and sway. The increases from linear potential damping are 10%, 20%, and 30%. The figure shows that the level of netpen and floater drag damping are important for both heave and sway response in the relevant wave period range.

3.3.7 Summary of the linear wave loading model

The wave loading effects consist of added mass, damping, water plane stiffness, and excitation forces. Wave loading on the floater has been discussed in Section 3.3 — 3.3.4, whereas wave loading on the netpen has been discussed in Section 3.3.5.

For small amplitude waves, a combination of linear potential theory applied to the floater and linearized drag applied to the floater (only horizontally) and the netpen (horizontally and vertically) is assumed to give a good approximation to the wave loading.

For the wave loading implementation, the members of the BCS are conceptually divided into the same elements and nodes as the model used in the finite element analysis described in the next chapter. This is equivalent to using strip theory. Subdividing long beams is likely to give good results even when hydrodynamic added mass, damping, and exciting forces are considered only for heave and sway DOFs.

The element length is typically $1.5\,m$, i.e. 20 elements per member and a total of 80 elements for the whole BCS.

Each element is given added mass, hydrodynamic damping, and excitation forces in the vertical and (perpendicular) horizontal translation DOFs for both nodes (the values for the two nodes are identical). Additionally, each vertical node is given a vertical stiffness

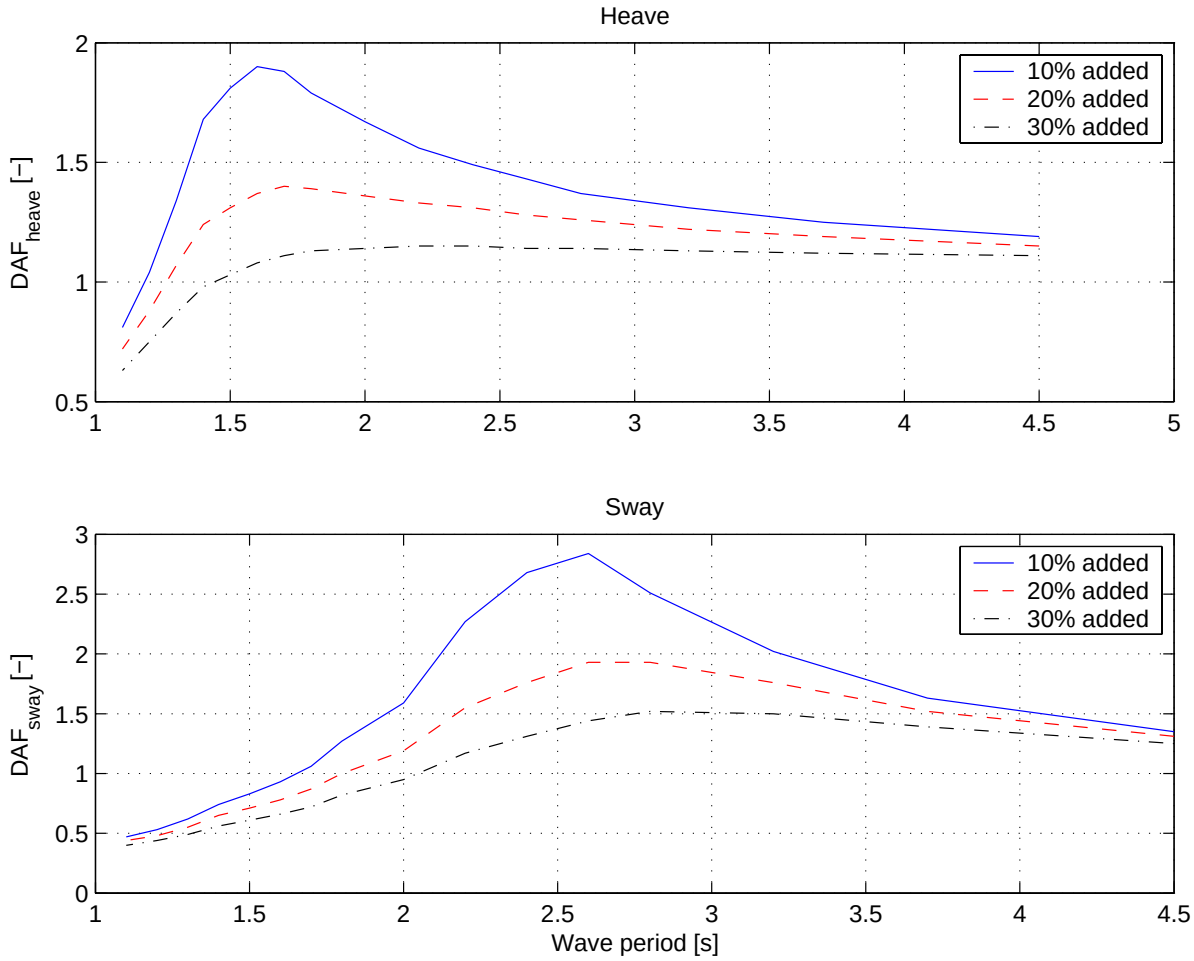

Figure 3.3: DAF for three levels of damping in addition to linear potential damping.

(i.e. a vertical spring) to model the water plane stiffness. Thus, the nodal values are the respective distributed values multiplied with the element length L_{elt} and divided by 2.

The excitation forces are dependent on three wave properties: the free surface elevation as well as the perpendicular components of water particle velocity and acceleration. The different properties are all evaluated at the (initial) location of the midpoint of the relevant element. No account is taken of the free surface inclination over the length (or width) of the element.

The wave load model for linear simulation is summarized in Table 3.19. The first column states the wave effect in question. The second column informs whether it applies to vertical (Vert.) or horizontal (Hor.) DOFs. The third column states which structural part is affected, i.e. floater or netpen. The fourth column states the theory basis, i.e. linear potential theory (LPT) or linearized drag (LD). The fifth, sixth and seventh columns state the equation used, the average values for the coefficients, and the nodal values based on the average values in column six and an element length of $2\,m$. Column eight gives references to the relevant equations and sections of this chapter.

3.4 Nonlinear analysis of the floater

As the wave height increases, nonlinearities are gradually introduced, stemming from both the wave loading effects and the structure.

The most important structural sources of nonlinear behavior are assumed to be:

- Full submergence of the mooring buoys and/or nonconstant water plane area of the mooring buoys.
- Large rotations and deflections of the floater members

In the present thesis we will not implement structural nonlinearity. However, the importance of structural nonlinearities will be investigated in a qualitative way.

For the hydrodynamic effects, linearization has been introduced for potential theory and drag, see Section 3.3. Here, we will not introduce nonlinear drag effects. As has been discussed in previous sections, linearization of drag is a reasonable approach for the BCS. The hydrodynamic damping and loads due to drag will be treated as in the linear analysis. Below, we will discuss the introduction of nonlinear effects in connection with potential theory.

3.4.1 Nonlinear hydrodynamic effects

To evaluate whether linear potential theory is applicable we consider two possible nonlinear hydrodynamic effects:

Steep Waves As the waves get steeper (i.e. H/λ approaches 1/7), a linear wave formulation (Airy wave theory) becomes a poorer approximation and alternative wave theories such as Stokes' can be used. For the TRW the wave steepness varies between 0.07

Wave effect	Dir.	Struc. part	Theory	Expression	Avrg. Coeff.	Nod. val.	Ref.
Added Mass	Vert.	Floater	LPT	$\frac{1}{2}C_{m,eq}\rho_w\frac{\pi D^2}{4}L_{elt}$	$C_{m,eq,avg}=0.66$	$530kg$	Table 3.11
	Hor.				$C_{m,eq,avg}=0.60$	$480kg$	Table 3.12
Damping	Vert.	Floater	LPT	$\frac{1}{2}BL_{elt}$	$B_{avg}=0.9\frac{kNs}{m^2}$	$0.9\frac{kNs}{m}$	Table 3.11
		Netpen	LD		$B_{avg}=1.3\frac{kNs}{m^2}$	$1.3\frac{kNs}{m}$	Table3.16
	Hor.	Floater	LPT		$B_{avg}=0.1\frac{kNs}{m^2}$	$0.1\frac{kNs}{m}$	Table 3.12
			LD		$B_{avg}=0.4\frac{kNs}{m^2}$	$0.4\frac{kNs}{m}$	Table 3.15
		Netpen			$B_{avg}=0.6\frac{kNs}{m^2}$	$0.6\frac{kNs}{m}$	Table 3.16
WPS	Vert.	Floater	LPT	$\frac{1}{2}k_{w,max}L_{elt}$	$k_{w,max}=10.1\frac{kN}{m^2}$	$10.1\frac{kN}{m^2}$	Section 3.2.1
Excit. Force	Vert.	Floater	LPT	$\frac{1}{2}k_{w,max}\zeta L_{elt}$	$\zeta_{avg}=1.5m$	$14.7kN$	Equation 3.33
				$\frac{1}{2}Bv_{\perp}L_{elt}$	$B_{avg}=0.9\frac{kNs}{m^2}$	$1.6\,kN$	Table 3.11
	Hor.			$\frac{1}{2}C_{M,eq}\rho_w\frac{\pi D^2}{4}L_{elt}a_{\perp}$	$C_{M,eq,avg}=1.1$	$2.2kN$	Table 3.14
				$\frac{1}{2}Bv_{\perp}L_{elt}$	$B_{avg}=0.1\frac{kNs}{m^2}$	$0.19\,kN$	Table 3.12
			LD	$\frac{1}{2}Bv_{\perp}L_{elt}$	$B_{avg}=0.4\frac{kNs}{m^2}$	$0.4\frac{kNs}{m}$	Table 3.15

Table 3.19: Summary of linear wave loading regime

and 0.10, i.e. from 48% to 72% of the maximum wave steepness $\zeta_{max} = 1/7 \approx 0.14$, see Table 3.6. The wave steepness is so small that we will not consider nonlinearities due to steep waves.

Large Wave amplitude The H/D-relation varies from 1.0 to 5.7, see Table 3.6, thus the wave height is assumed large enough to introduce considerable non-linearities for all TRW.

To conclude, the most important hydrodynamic nonlinearity is due to relatively high waves.

If the small wave amplitude assumption is not valid, A_{jk}, B_{jk}, C_{jk}, and F_j in Equation 3.18 are all dependent on wave amplitude and response ($\ddot{\eta}_k$, $\dot{\eta}_k$, and η_k). According to structural dynamic analysis methods, a fully nonlinear, incremental formulation is then appropriate together with a time domain analysis, e.g. using the Newton-Raphson method, see (Newton, 1671), (Raphson, 1690), and (Mathworld, 2007). This approach rests on the assumption that an incremental version of Equation 3.18 is still an appropriate description of the physical problem at hand, and all coefficients should be recalculated at the start of each time step. This approach has been briefly described by Journée and Massie (2001). They note that:

> This approach is direct and straightforward in theory, but is often so cumbersome to carry out that it becomes impractical in practice.

Nevertheless, this is the method of choice for this thesis due to its superiority in dealing with nonlinearities and the belief that the ever increasing power of modern computers can render it a realistic and practical approach. However, to reduce complexity and increase feasibility no attempt is made to consider all nonlinearities. Instead, only the expected most important nonlinearity — water plane stiffness (i.e. buoyancy) — will be introduced and compared to linear results. An additional benefit of this approach is that by restricting the considered nonlinearities to the stiffness term, algorithms and even software from (linear) structural dynamics can be used after modifications.

3.4.2 Implementation of nonlinear buoyancy

(Vertical) buoyancy is the only nonlinear effect considered. It is assumed to be the dominating nonlinearity (water plane stiffness in the extreme case may become zero). This nonlinearity is due to the change in water plane stiffness. In the nonlinear dynamic time domain analysis the nonlinear buoyancy will be taken into account by using the instantaneous water plane stiffness for calculation of the instantaneous incremental excitation force (i.e. buoyancy). This nonlinear buoyancy is implemented in the time domain analysis in the form of nonlinear springs.

For element i, the instantaneous draft d_i is found by using the instantaneous vertical response $\eta_i(t)$ of the midpoint of the element and the free surface elevation at the (initial)

midpoint position of the element $\zeta_i(t)$:

$$d_i(t_n) = \zeta_i(t_n) - \eta_i(t_n) + \frac{D}{2} \tag{3.41}$$

The submergence is assumed constant for the whole element, i.e. the inclinations of the element and the free surface are not taken into account. The instantaneous water plane stiffness k_w is then found by using Equation 3.8.

Assuming that k_w is (approximately) constant over time step n the incremental excitation force (i.e. buoyancy) is:

$$\begin{aligned} \Delta F_{vert,i}(t_n) = & \quad F_{vert,i}(t_{n+1}) - F_{vert,i}(t_n) \\ = & \quad k_{w,i}(t_n)[\zeta_i(t_{n+1}) - \zeta_i(t_n)] = k_{w,i}(t_n) \cdot \Delta\zeta_i(t_n) \end{aligned} \tag{3.42}$$

Chapter 4

STATIC ANALYSIS AND NATURAL PERIODS

In this chapter, a linear static analysis and a natural period analysis of the BCS are presented.

A linear static analysis of the BCS is important in order to get a better structural understanding of the BCS. In particular, it will enable a comparison of in-phase vs. out-of-phase loading of two opposite cylinders. The static analysis results will also be a reference for the dynamic results and enable an estimation of the dynamic amplification. The BCS will be analyzed separately for horizontal loads and vertical loads. The load amplitudes are typical values obtained earlier in the present thesis. The shapes of the moment diagrams (and not the magnitudes) are of primary interest.

Quantifying natural periods is of importance for dynamic analysis in general. For the BCS, it is of particular interest to compare the natural periods to the peak period of the wave spectrum T_p. Although nonlinear effects are assumed to be important, emphasis will be on the linear case. In Section 4.3 and 4.4 vertical and horizontal rigid body natural periods, respectively, are investigated. Flexural natural periods are considered in Section 4.5.

4.1 Static analysis

The static analysis is performed using the commercial software *Dr.Frame3D* from Dr. Software LCC (Dr Software LCC, 2007)[8]. The BCS is modeled with the appropriate mooring springs in the corners and one buoyancy spring per $1.5\,m$, i.e. a total of 80 buoyancy springs with stiffness $k = 15.1\,kN/m$.

For waves with a direction perpendicular to the BCS, all members will be loaded. However, since the loading on the members with their axes parallel to the wave direction typically will experience a fluctuating load (for limited wave lengths), this loading has less

[8]The Dr.Frame3D software is based on an earlier version of the framework used for the prototype developed during the present PhD-work, see (Rucki and Miller, 1996) and (Rucki and Miller, 1998)

	Load case	M_1 [kNm]	M_2 [kNm]	M_3 [kNm]	T [kNm]	Δ_1 [mm]	Δ_2 [mm]	Figure
V	# 1	176	78	135	20	-310	60	B.1
	# 2	255	255	255	0	-250	-250	B.2
	# 3	98	98	53	40	-370	370	B.3
H	# 1	184	26	131	0	148		B.4
	# 2	158	158	157	0	296		B.5
	# 3	210	210	105	0	0		B.6

Table 4.1: Static linear analysis of the BCS for vertical (V) and horizontal (H) loading

influence than the uniform loading on the perpendicular members. Thus, the BCS is loaded with a distributed load — vertically or horizontally — on one side or on two opposite sides. The former is called load case # 1. Loads in the same direction on opposite members, i.e. in-phase, is called load case # 2, and loads in opposite directions, i.e. out-of-phase, is called load case # 3. The maximum bending moment of the loaded member is called M_1, the maximum on the opposite member (loaded or not) is called M_2 and the maximum bending moment of the "nonloaded" members is called M_3. The torsion of the "nonloaded" members are called T (the loaded members have no torsion). The displacements of the joints (corners) are also computed. For vertical loading, Δ_1 is the displacement of the joints of the loaded member and Δ_2 is the displacement of the joints of the opposite member. For horizontal loading, all joints have approximately the same displacement: Δ_1.

The vertical distributed load is set to the amplitude of the Froude-Kriloff load for the long wave length limit case of a $1\,m$ wave ($0.5\,m$ amplitude), see Equation 3.25:

$$F_{vert} = k_{w,max} \cdot \frac{H}{2} = 5.0\,kN/m \tag{4.1}$$

The horizontal distributed load is set to the amplitude of the mass load of TRW B, i.e. for $H = 1\,m$ and $C_M = 1.1$ (see Equation 3.32 and Table 3.14):

$$F_{hor} = C_M \cdot a_2 \frac{\pi D^2}{4} \rho_w = 2.8\,kN/m \tag{4.2}$$

The results for vertical (V) and horizontal (H) loading are given in Table 4.1. Screenshots of all load cases together with the loading and the moment distribution are shown in Appendix B. Reference to the relevant figure is given in the table for each load case.

Discussion

Comparing load case # 2 and 3 for vertical loading we see that an in-phase vs. out-of-phase situation is very decisive for the static maximum moment. For the loaded and "nonloaded" members, the ratios are $\frac{255\,kNm}{98\,kNm} \approx 2.6$ and $\frac{255\,kNm}{53\,kNm} \approx 4.8$, respectively. For the vertical case, in-phase loading gives higher moment than out-of-phase loading for all members.

For horizontal loading, this is only the case for the "nonloaded" members. The ratios for maximum moment are $\frac{158\,kNm}{210\,kNm} \approx 0.75$ for loaded members and $\frac{157\,kNm}{105\,kNm} \approx 1.5$ for nonloaded members. For the horizontal case the parallel members have a constant moment distribution for out-of-phase loading and a linear distribution for in-phase loading. Thus, the end points (and not the mid point) have the maximum moments.

For long waves the vertical loading on the members parallel to the wave direction will also be important and superposed to the effects described above. Whereas the vertical loading intensity is constant for the perpendicular members this is not the case for the parallel members (for the linear case it will be sinusoidal).

The effect of in-phase vs. out-of-phase loading is discussed further in Section 7.4 for a linear structure and regular waves, i.e. the sensitivity to wave period. In Section 9.1.1 the sensitivity of wave period for a nonlinear structure is discussed, and, finally, and in Section 9.4 the sensitivity of peak period for a linear as well as a nonlinear structure is discussed.

4.2 Natural periods

The structural model of the BCS has no true rigid body motion in the numerical sense due to the use of horizontal mooring springs and the vertical buoyancy springs. However, the highest six natural periods of the BCS will have no deformation of the floater itself — only the buoyancy and/or mooring springs. We will refer to these natural modes as rigid body motions and use the terms typically used for the rigid body motions of floating structures: heave, sway, surge, roll, pitch, and yaw.

The rigid body natural periods — both vertically and horizontally – are important for several reasons:

- The natural periods can be located within an area of high wave energy.
- Rigid body motions are likely to be the dominant part of the total motion and are thus important to quantify in order to understand the behavior of the structure.
- The (nonlinear) wave loading is dependent on the position, response, and acceleration of the structure in relation to the waves. Load calculations based on the initial location will be increasingly inaccurate with increasing response. Thus, the applicability of a particular wave load model typically depends on the quality of assumptions made in relation to structural response.
- Resonant behavior of the floater can lead to structural problems for other system components, e.g. increased fatigue loading of mooring and netpen. Additionally, it can have a negative impact on the working environment — both for personnel and for equipment.

For small wave heights the response of the floater will be approximately linear. Although realistic wave heights are not likely to be small enough for a linear assumption, it is of interest to investigate the linear characteristics of the system as they will give a good

TRW	Heave			Sway/surge		
	T_N $[s]$	β $[-]$	Δ_{stat} $[m]$	T_N $[s]$	β $[-]$	Δ_{stat} $[m]$
B	1.7	0.67	0.49	2.4	0.94	0.29
C	1.9	0.47	1.0	2.3	0.58	0.22
D	2.0	0.38	1.5	2.3	0.43	0.19
H_{max}	2.1	0.31	2.9	2.3	0.34	0.22
Avrg.	1.9	0.46	1.5	2.3	0.57	0.23

Table 4.2: Natural period T_N, the relative frequency β, and the quasi-static response Δ_{stat} in heave and sway/surge.

Mode	T_N $[s]$			Avrg.
	$C_{m,0}$	$C_{m,1}$	$C_{m,2}$	
Heave/Pitch/Roll	1.3	1.9	2.2	1.8
Sway/Surge	1.8	2.4	2.6	2.3
Yaw	1.5	1.7	1.8	1.7

Table 4.3: Natural period T_N in heave/pitch/roll, sway/surge, and yaw. Three added mass coefficients applied: $C_{m,0} = 0.0$, $C_{m,1} = 0.63$, and $C_{m,2} = 1.0$ (see text for explanation of C_m).

indication also of the nonlinear characteristics and the degree of nonlinear behavior to be expected.

In this and the following sections we will discuss rigid body natural periods and (the degree of) resonant response for vertical (heave/pitch/roll) and horizontal modes (sway/surge/yaw), respectively.

In Table 4.2 fundamental linear dynamic parameters for both heave and sway/surge are shown, i.e. the natural period T_N, the relative frequency β, and the static response Δ_{stat}, see Appendix F. In heave, the amplitude of the force is $F_{vert,a} = k_w\zeta_a$, see Equation 3.33. The force amplitude in sway corresponds to the mass force, see Equation 3.32 and Table 3.14 and 3.15. The natural periods are not constant for the TRW because the added mass varies with wave period.

In Table 4.3 the influence of added mass on the natural period in heave/pitch/roll, sway/surge, and yaw is shown. Three C_m-values are used: $C_{m,0} = 0.0$, $C_{m,1} = 0.63$, and $C_{m,2} = 1.0$. The $C_{m,1}$-value is found by averaging the $C_{m,eq}$-values from Table 3.11 and 3.12. This is assumed to be a likely range of variation for added mass due to varying draft.

The natural periods in heave, pitch, and roll will be identical assuming linear water plane stiffness and constant distributed total mass.

Discussion

The Δ_{stat}-values (see Table 4.2) show that in the quasi static case (i.e. for long waves) the heave response of a perpendicular pipe is approximately equal to the sea elevation amplitude and the phase angle is approximately zero, i.e. it will follow the sea surface elevation. The quasi static response in sway is approximately constant as the increase in wave height is counteracted by a decrease in water particle acceleration.

The TRW periods (as well as the peak periods for irregular waves) are greater than the natural periods in heave giving small β-factors and limited dynamic effects ($\beta \leq 0.67$). The natural period in sway is very close to the wave period of TRW B: $\beta_{TRWB} = 0.94$.

Further, in Table 4.2 we see that the change in added mass dependent on wave period yields a maximum natural period in heave which is 23% larger than the smallest values ($2.1\,s$ vs. $1.7\,s$). The effect in sway is more limited, i.e. a change of only 4% ($2.4\,s$ vs. $2.3\,s$).

The effect of the varying added mass is large, see Table 4.3. The natural period increases with 69% in heave, 44% in sway, and 20% in yaw when going from $C_{m,0} = 0.0$ to $C_{m,2} = 1.0$.

4.3 Vertical resonance

4.3.1 Qualitative evaluation

Perpendicular members of the BCS

For a single pipe floating in very long waves (i.e. very long wave periods) with a wave direction perpendicular to its axis, the excitation period is much greater than the natural period in heave and the pipe will follow the wave elevation as the dynamic effects can be neglected ($\beta \approx 0$, $\phi \approx 0$, $DAF \approx 1$).

As opposed to the members which are oriented in the direction of the waves, the whole length of the perpendicular members of the BCS will experience the same wave action and are therefore likely to dominate the rigid body behavior of the system. Thus, for very long waves the two cage members perpendicular to the wave direction will tend to follow the wave surface elevation in the same way as the single pipe described above. The two members can be excited in-phase, out-of-phase, or anything in between — determining the relative distribution of heave vs. pitch/roll motion. If the excitation of the two perpendicular members is in phase (e.g. $\lambda = L/1, L/2, L/3, L/4 = 30\,m, 20\,m, 10\,m, 7.5\,m$, see Table 7.10) the cage will experience mainly heave response. If the waves are out-of-phase (e.g. $\lambda = L/0.5, L/1.5, L/2.5, L/3.5 = 60\,m, 20\,m, 12\,m, 8.6\,m$, see Table 7.10) the system will experience mainly pitch response.

For shorter waves a single perpendicular pipe can experience dynamic effects ($\beta > 0.3$, $\phi \neq 0$, $DAF > 1$) in heave. For this case the dynamic effects will be superimposed on the wave surface elevation. Damping is caused by potential damping from the floater and drag damping from the netpen. The (total) damping ratio is assumed to be high ($\xi > 20\%$) and will limit the dynamic response significantly.

TRW	Potential damping				Total damping			
	DAF	$\Delta_{v,r,min}$	DAF_m	ϕ	DAF	$\Delta_{v,r,min}$	DAF_m	ϕ
B	1.62	0.29	2.40	28°	1.34	0.16	1.44	43°
C	1.26	0.30	3.00	12°	1.18	0.22	1.52	23°
D	1.16	0.29	3.78	7°	1.12	0.23	1.61	16°
H_{max}	1.10	0.38	4.45	4°	1.07	0.28	1.38	15°

Table 4.4: Dynamic characteristics in heave for a pipe perpendicular to the wave direction. Two levels of damping are considered: only floater ($\xi = 11 - 21\%$) and total damping ($\xi = 33 - 39\%$). See text for explanation of symbols

In case of large response of a pipe relative to the surface elevation its cross section may become completely dry or fully submerged. For both cases, this implies that the water plane stiffness and the natural frequency in heave is zero (the system is inertia controlled since the stiffness will be zero). Typically, for the BCS, different parts will experience different submergence and the effect of changing water plane stiffness is harder to predict.

Parallel members of the BCS

Members in the direction of the waves can experience wave lengths from $\frac{1}{3}$ to $2\frac{1}{3}$-times their own length for the TRW (i.e. $\lambda = 10\,m - 70\,m$ vs. $30\,m$). Thus, the members are too long to follow the wave surface elevation. Although a single parallel member will have the same resonant heave/pitch/roll period as a perpendicular member, it is likely to have smaller response as the wave loading will not be uniform. A parallel pipe is likely to experience larger changes in draft because of the limited wave length. Thus, the change in water plane stiffness can be more important.

4.3.2 Linear heave

In Table 4.4 dynamic characteristics in heave for a pipe perpendicular to the wave direction are shown for two levels of damping: only floater damping and total damping (i.e. $\xi = 11-21\%$ and $\xi = 33-39\%$, respectively, see Table 3.17). In heave, potential damping is the only contribution to floater damping. Total damping also includes netpen damping. For each damping level four different quantities are given: the actual dynamic amplification factor DAF, minimum relative response amplitude[9] $\Delta_{v,r,min} = \Delta_{stat} \cdot DAF - \zeta_a$, the maximum dynamic amplification factor DAF_m (see Equation F.11 in Appendix F), as well as the phase angle between the loading and the response ϕ (see Equation F.7 of Appendix F). The loading in heave is in-phase with the sea surface elevation $\zeta(t)$.

[9]For a phase angle different from zero, the relative response amplitude will be greater than the minimum relative response amplitude.

Discussion

For a pipe perpendicular to the wave direction, Table 4.4 predicts that the response amplitude will be at least 29 cm and 16 cm larger than the wave surface elevation amplitude applying total damping and potential damping, respectively. Further, the phase angle will increase the relative response amplitude. The results imply that the change in draft of a perpendicular pipe can give noticeable nonlinear stiffness effects.

4.3.3 Nonlinear heave

In linear potential theory, added mass coefficients, damping coefficients , and water plane stiffness are assumed to be constant. For waves that are short enough to give dynamic effects (typically $\beta = \omega/\omega_N > 0.3$) the draft will vary and introduce nonlinear effects.

Let us first consider the effect of changing water plane stiffness, assuming added mass and damping are constant. As the draft changes (i.e increases or decreases) relative to half submergence, the water plane stiffness k_w and the critical damping B_{cr} decreases, whereas the damping coefficient ξ, the natural period T_N, as well as the maximum response period T_m increase.

As opposed to the simple relationship between draft and water plane stiffness, added mass is more complex. Increased draft does not necessarily increase added mass or vice versa.

The potential damping B_{pot} will be affected by changing draft. Additionally, the critical damping B_{cr} is affected by changing water plane stiffness and added mass. Here, we will assume that the absolute damping is constant and only investigate the effect of changes in the critical damping. We assume that the relative damping at half submergence is $\xi_{min} = \frac{B}{B_{cr}} = 40\%$ (i.e. approximately the average total damping in heave of 36%, see Table 3.17). This is a minimum value since the critical damping is at its maximum and the absolute damping is assumed constant.

In Table 4.5 resonance characteristics as functions of changing draft (i.e. water plane stiffness) are shown. First, the water plane stiffness k_w is given as a fraction of the maximum water plane stiffness $k_{w,max} = 10.1\,kN/m^2$. Next, we choose to illustrate the influence of added mass fluctuations by applying three different constant values for C_m when calculating the natural period in heave T_N. In the table, natural periods are found for the following added mass coefficients: $C_{m,0} = 0$, $C_{m,1} = 0.63$, and $C_{m,2} = 1.0$ (see p. 60 and Table 4.3), corresponding to total masses per length equal to 404, 888 and 1213 kg/m. A relative damping coefficient is defined as $\frac{\xi}{\xi_{min}} = \frac{B_{cr,max}}{B_{cr}} = \sqrt{\frac{k_{w,max}}{k_w}}$. Using $\xi_{min} = 40\%$ and the established ξ/ξ_{min}-ratio, we get: $\xi = 40\%\sqrt{\frac{k_{w,max}}{k_w}}$. The period which corresponds to maximum response T_m (see Equation F.10 in Appendix F) is then found for the three C_m-values.

Draft	$\frac{k_w}{k_{w,max}}$	T_N $[s]$			$\frac{\xi}{\xi_{min}}$	T_m $[s]$		
$[m]$	[%]	$C_{m,0}$	$C_{m,1}$	$C_{m,2}$	[-]	$C_{m,0}$	$C_{m,1}$	$C_{m,2}$
0.5	100%	1.3	1.9	2.2	1.00	1.5	2.3	2.6
0.4	98%	1.3	1.9	2.2	1.01	1.5	2.3	2.7
0.3	92%	1.3	1.9	2.3	1.04	1.6	2.4	2.8
0.2	80%	1.4	2.1	2.4	1.12	1.8	2.7	3.1
0.1	60%	1.6	2.4	2.8	1.29	2.4	3.5	4.1
0.01	20%	2.8	4.2	4.9	2.24	∞	∞	∞

Table 4.5: Natural period T_N and maximum response period T_m in heave as a function of draft. Three added mass coefficients are applied: $C_{m,0} = 0.0$, $C_{m,1} = 0.63$, and $C_{m,2} = 1.0$.

Discussion

To asses to what degree the wave regime is likely to excite the heave (and pitch/roll) rigid body mode we compare the periods of the TRW ($2.5\,s$, $4.0\,s$, $5.3\,s$, and $6.7\,s$) with the natural periods and maximum response periods. TRW B falls in the T_N-interval of Table 4.5 for $d \leq 10\,cm$. The other TRW fall in the T_N-interval only for very small draft ($d \approx 1cm$).

The T_m are up to 46% higher than the corresponding T_N-values, but still only TRW B falls in the T_m-intervals for $d \geq 10\,cm$.

It is of interest to note that the stiffness reduction and thus the change in natural period is much slower than the draft reduction, i.e. the important interval for natural frequencies is quite narrow. Assuming constant added mass, the natural period increases by approximately 30% when the draft changes from $0.5\,m$ to $0.1\,m$. On the other hand the natural period assuming $C_m = 1.0$ is approxmately 70% higher than for $C_m = 0.0$. For T_m the increase with draft is doubled (from 30% to approximately 60%) whereas the increase with C_m is about the same as for T_N (i.e. $\approx 70\%$).

The critical damping is reduced to $\frac{\xi}{\xi_{min}} = 1/1.29 \approx 77\%$ of the maximum value due to reduction in stiffness to 60%. A reduction in added mass from $C_m = 1.0$ to $C_m = 0.0$ reduces the critical damping to $1/\sqrt{3} = 57\%$. Again, we see that the effect of water plane stiffness and added mass fluctuations are significant and comparable.

It is reasonable to conclude that the fluctuations of stiffness and added mass are of comparable importance. In the numerical analysis a constant C_m-value will be used. Due to the sensitivity of natural period as well as critical damping with respect to C_m this is likely to be a source of inaccuracy for computation of heave response.

4.4 Horizontal resonance

4.4.1 Qualitative evaluation

The horizontal response of the BCS is of particular importance for several reasons:

- A high magnitude of the horizontal response can lead to full submergence of the buoys (on the windward side of the BCS and dry buoys on the leeward side). This may alter the stiffness of the BCS significantly, see Section 2.2.2. This is an undesirable situation and should be considered in design.

- The magnitude of the horizontal response velocity (compared to the water particle velocity) is important for the influence of drag force and drag damping originating from both the floater and the netpen, see Section 3.3.4.

- The wave loads are based on the initial horizontal location of the BCS. The quality of this assumption decreases with increased horizontal response.

We assume that for perpendicular waves, only the two members of the BCS which are perpendicular to the wave direction will be affected by horizontal wave forces.

Typically, the mooring is very stiff giving a relatively small quasi-static deformation and a natural period in sway which is smaller than the maximum wave periods. Thus, the system is stiffness controlled for the longest (i.e. highest) waves and resonant or inertia controlled for shorter waves.

As for vertical resonance, the degree of in-phase loading on the two perpendicular members is also important for horizontal rigid body excitation, see Section 4.1 and 4.3. Out-of-phase loading will yield zero horizontal response. With wave forces acting on the two perpendicular members (close to) in-phase and a wave period close to resonance the response will grow and thus the importance of floater drag, floater potential damping, and netpen drag damping will increase. As for vertical response, the (total) damping ratio is assumed to be large (but smaller than in heave, i.e. $\xi = 10 - 20\%$) yielding a relatively small DAF.

Oblique waves can excite the yaw rigid body mode and twisting/torsional modes that can be important. However, a quantitative assessment will not be attempted.

4.4.2 Linear sway

In Table 4.6 the dynamic characteristics of the TRW are shown for two levels of damping: only floater damping and assumed total damping (i.e. $\xi = 6 - 11\%$ and $\xi = 14 - 22\%$, respectively, see Table 3.18). For each damping level four different quantities are given: the actual dynamic amplification factor DAF, the response amplitude Δ_h, the response amplitude/wave amplitude ratio Δ_h/ζ_a, as well as the phase angle ϕ between the loading and the response ϕ (see Equation F.7 of Appendix F). The loading in sway is in-phase with the horizontal water particle acceleration $a_2(t)$.

TRW	Floater damping				Total damping			
	DAF [-]	Δ_h [m]	Δ_h/ζ_a [%]	ϕ [°]	DAF [-]	Δ_h [m]	Δ_h/ζ_a [%]	ϕ [°]
B	4.24	1.24	247%	62°	2.92	0.85	170%	71°
C	1.50	0.33	33%	6°	1.46	0.32	32%	14°
D	1.23	0.23	15%	4°	1.22	0.23	15%	9°
H_{max}	1.13	0.25	9%	4°	1.12	0.25	9%	10°

Table 4.6: Dynamic characteristics in sway/surge. Two levels of damping are considered: floater damping ($\xi = 6 - 11\%$) and total damping ($\xi = 14 - 22\%$).

Discussion

The intervals of variation for DAF-values is from $1.13 - 4.24$ when only floater damping is included and $1.12 - 2.92$ with total damping. The intervals of variation for the maximum dynamic amplification factor DAF_m (not included in the table) are $4.6 - 8.8$ and $2.3 - 3.7$ for floater damping and total damping, respectively. TRW B ($T = 2.5\,s$) in Table 4.6 stands out from the others because it represents a response close to resonance, i.e. all values are highest for TRW B. The magnitude of the Δ_h/ζ_a-ratio is much higher than for the other waves (170% vs. less than 32%). The assumption of relative small response is justified for TRW D and H_{max} ($\Delta_h/\zeta_a \leq 15\%$) and probably also for TRW C ($\Delta_h/\zeta_a \leq 33\%$). This is not the case for TRW B. When considering wave classes as such, it is important to notice that wave class B, C, and D are all likely to contain seastates that give horizontal resonance, e.g. for wave class C the seastate with $T_p = 2.8\,s$ and $H_s = 0.7\,m$ is quite common, see Table 8.5. In general, a horizontal response velocity that is (at least) comparable with the horizontal water particle velocity can not be excluded as a possibility. If this is the case, the calculation of drag effects in Section 3.3.4 must be reconsidered.

The assumption of linear mooring behavior breaks down when the horizontal response is greater than the elastic limit for the mooring, i.e. $\Delta_{h,max} = 0.35\,m$, see Table 2.7. From Table 4.6 we see that this can be a problem for TRW B, i.e. in general for seastates causing horizontal resonance.

The Δ_h-values that are found are considered to be upper limits as they are based on the assumption that the horizontal forces on the floater are in phase. The possible factor counteracting large horizontal response for irregular waves is the comparison of the peak period T_p to the in-phase/out-of-phase wave periods, see Table 7.10. To estimate the influence of this effect, an $1800\,s$ analysis of the BCS exposed to irregular waves is performed along the lines described in Chapter 9. T_p is set equal to $2.5\,s$ (see Table 7.10), i.e. the in-phase wave period which is closest to the natural period in sway ($2.4\,s$, see Table 4.2), and H_s is set equal to $1\,m$. The analysis gave a maximum horizontal response of $1.21\,m$. For the closest out-of-phase wave period of $2.3\,s$ a corresponding analysis gave a maximum horizontal deflection of $1.11\,m$, i.e. for irregular waves the location of the

peak period compared to the in-phase/out-of-phase periods does not appear to be very important. Thus, for seastates with a peak period close to the resonant period in sway it is likely that the maximum horizontal response velocity and displacement will both be comparable in magnitude to the water particle velocity and larger than the elastic limit for mooring lines, respectively. However, the likely implications of a great horizontal response discussed above, will not be considered further in the present thesis. The focus will instead be on the effect of vertical wave loading.

4.5 Flexural natural periods

The flexural deformations will be much smaller than the rigid body deformation. Nevertheless, they can be important because of their influence on bending and torsion moments.

First, a single beam is analyzed by hand calculations to get an indication of the interval that natural periods are expected to lie within. The natural period for axial and torsional vibration can be found as:

$$T_{N,axial} = 2\pi \cdot \sqrt{\frac{mL^2}{EA}} = 0.05\,s \tag{4.3}$$

$$T_{N,torsional} = 2\pi \cdot \sqrt{\frac{mL^2}{GI_T}} = 0.15\,s \tag{4.4}$$

No added mass is applied for axial and torsional vibrations.

In Table 4.7 the two lowest natural periods for a 2D pinned-pinned beam as well as a 2D free-free beam (the lowest natural period — i.e. # 1 — for the free-free beam is rigid body motion) are found using the following formula, see e.g. (Bergan et al., 1986):

$$\omega_N = \bar{\omega}_N \cdot \sqrt{\frac{EI}{mL^4}} \tag{4.5}$$

To investigate the influence of added mass, the distributed mass m is found using three alternatives for added mass coefficients: $C_m = 0, 0.63, 1.0$, yielding total masses of $m = 407\,kg/m, 912\,kg/m, 1210\,kg/m$.

To find the flexural natural periods of the BCS a linear eigenvalue analysis is performed, i.e. solutions are found to the eigenvalue equation:

$$(\mathbf{K} - \omega^2\mathbf{M})\mathbf{r} = 0 \tag{4.6}$$

For a numerical eigenvalue analysis of the whole structure the MATLAB version 6.5 (MathWorks, 2007) function `eig` (i.e. ${\omega_N}^2$ = `eig(K,M)`) is used. The stiffness and mass matrices are found by using the finite element method. The floater is modeled as beams supported by springs. The pipes are modeled as traditional linear 3D beams, see e.g. (Bergan et al., 1986). A lumped mass approach is chosen. For the translational and

Beam	Mode	$\bar{\omega}_N$	T_N		
		[-]	$C_m = 0$	$C_m = 0.63$	$C_m = 1.0$
Pinned-pinned	# 1	9.87	0.40	0.60	0.69
	# 2	39.48	0.10	0.15	0.17
Free-free	# 2	22.37	0.18	0.29	0.31
	# 3	61.67	0.06	0.11	0.11

Table 4.7: Highest Natural Periods for 2D beams: pinned-pinned and free-free. Three values of added mass coefficient C_m are applied.

Case	$\frac{k_w}{k_{w,max}}$	C_m	Natural periods T_N [s]					
	[%]	[-]	#7	#8	#9	#10	#11	#12
#1	100%	0.63	0.98	0.76	0.60	0.57	0.31	0.31
#2	60%	0.63	1.04	0.76	0.60	0.59	0.32	0.32
#3	100%	0	0.65	0.64	0.40	0.38	0.21	0.21
#4	100%	1	1.13	0.82	0.70	0.66	0.36	0.36

Table 4.8: Natural periods for the BCS for different combinations of k_w and C_m.

torsional DOFs the concentrated masses are found by row-wise summation, i.e. $\frac{1}{2} \cdot mL$ and $\frac{I_p}{2A} \cdot mL \approx 0.13\,m^2 \cdot mL$, respectively. The rotational terms are set to (see e.g. (Cook et al., 2001)) $\frac{17.5L^2}{420} \cdot mL = \frac{L^2}{24} \cdot mL \approx 0.04L^2 \cdot mL$. The added mass coefficient is used for transverse displacements and bending DOFs (and not for axial displacements and torsional bending DOFs). The element length is set to $1\,m$.

The twelve highest natural periods are found for four combinations of water plane stiffness and added mass coefficient in order to investigate the importance of these values for the natural periods. First two different water plane stiffnesses: $k_w = k_{w,max}$ and $k_w = 60\% \cdot k_{w,max}$ (corresponding to $50\,cm$ and $10\,cm$ submergence, respectively) are applied together with the added mass coefficient $C_m = 0.63$. Subsequently, $k_w = k_{w,max}$ is applied with the (assumed) two extreme added mass coefficients $C_m = 0$ and $C_m = 1.0$. The results for the six smallest natural periods are shown in Table 4.8. The highest six natural periods are all rigid body modes and the results are shown in Table 4.3 and 4.5.

To investigate the importance of element length, case # 1 is rerun with $0.5\,m$ element length. The changes in natural periods were negligible, and it is thus assumed that the chosen number of elements does not influence the accuracy of the results.

The twelve natural modes for case # 1 are show in Appendix A.

Discussion

Modes # 7, 8, and 12 are symmetric or anti-symmetric about the diagonal axis and vibrate out of and in the surface plane, respectively. Thus, they are likely to be excited by diagonal waves. Modes 9, 10, and 11 on the other hand are symmetric or anti-symmetric about a perpendicular axis and are likely to be excited by perpendicular waves.

Mode 9 has the closest resemblance to the first mode of the pinned-pinned beam of Table 4.7 and as expected the natural periods are identical.

The dominating seastates will have peak wave periods considerably higher than the natural periods of Table 4.8, see Table 8.3. Thus, the dynamic amplification of the moments will typically be low, but not so low that it is without importance. The peak periods are higher than the natural periods, but the wave spectrum may still contain energy at periods close to the natural periods.

To illustrate the dynamic effects, the DAF (see Equation F.6 in Appendix F) is found for a 1 DOF linear system with a natural period of $0.6\,s$ and excitation periods from $1\,s$ to $4\,s$. Two levels of damping are employed: $\xi = 1\%$ and $\xi = 20\%$. Although the typical structural damping is from 0.5% to 5% (see Section 3.3.5), the high value is chosen to make it possible to differentiate the two curves. We see from Figure 4.1 that the DAF is low for the typical wave period interval and that the level of structural damping is of little importance. Of course, from $T = 1\,s$ towards the natural period of $0.6\,s$ the curves will diverge considerably. The maximum DAF values are: $DAF_m = 2.5$ for $\xi = 20\%$ and $DAF_m = 5$ for $\xi = 1\%$, see Appendix F. A rule of thumb is that dynamic effects can be ignored if $\beta < 0.3$, i.e. $T > 2\,s$ if $T_N = 0.6\,s$. From Figure 4.1 we see that $DAF \approx 1.1$ for $T = 2.0\,s$.

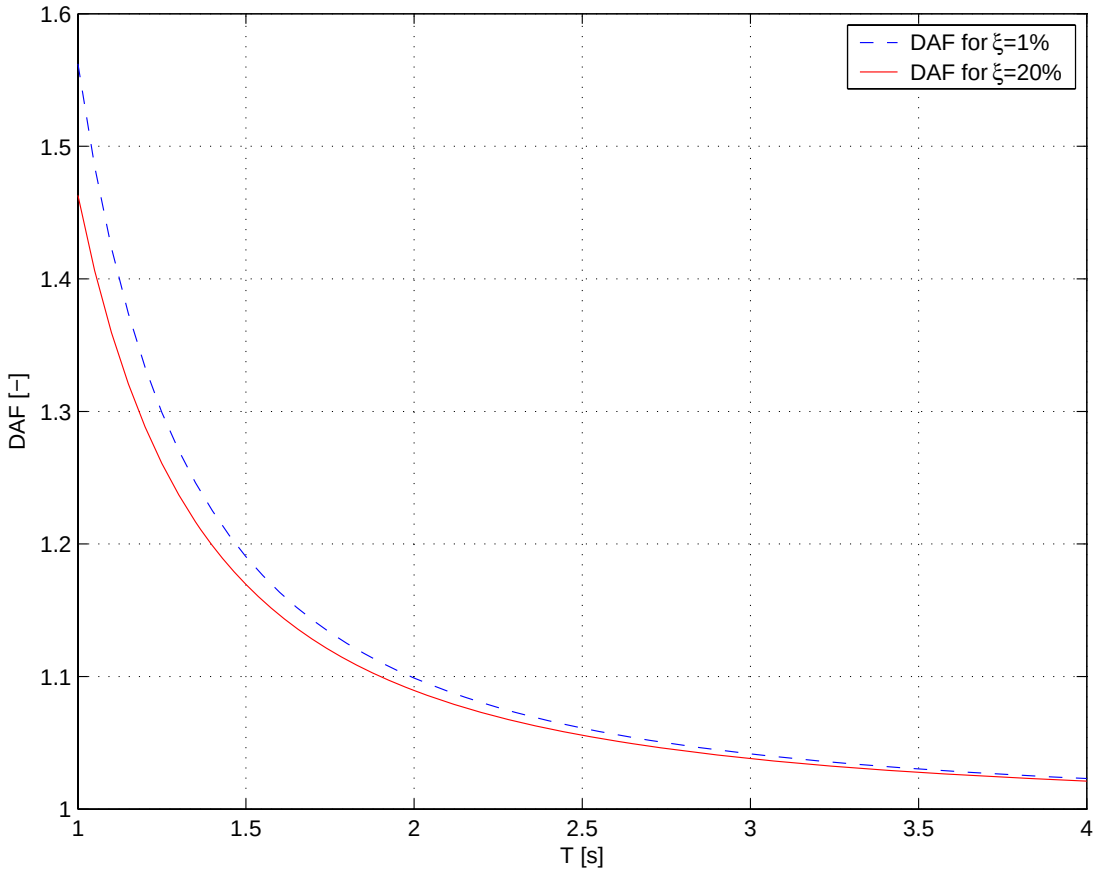

Figure 4.1: DAF for typical wave periods T and natural period $T_N = 0.6\,s$. Two levels of damping: $\xi = 1\%$ and $\xi = 20\%$.

Chapter 5

STRUCTURAL DYNAMIC ANALYSIS

5.1 Nonlinear time domain analysis

Dynamic analysis of marine structures are performed in the frequency domain and/or the time domain. Of the two alternatives, the former is most prevalent in particular due to its superior speed. However, nonlinearities can not be accounted for directly and the results will be increasingly inaccurate as the importance of nonlinearities grow. For a system with important nonlinearities, only a time domain analysis can be trusted. The major drawback associated with nonlinear time domain analysis is the significant computation time typically seen.

For a floating fish farm, nonlinearities are probably important and a nonlinear time domain analysis is therefore the chosen method of approach in the present thesis. It is assumed that a time domain analysis is realistic within an engineering context given the ever increasing speed of computer calculations.

The finite element method (FEM) is today established as the dominant method for performing structural analysis. Due to its proven track record, it was chosen as the tool for discretization of the structure.

5.2 Linear dynamic analysis

5.2.1 Stiffness

The floater

Each pipe is subdivided into beam elements of equal length. The initial element length is set to $1\,m$ and the elements are linear. Assuming linear material behavior (i.e. small strains) is believed to be reasonable as plastic behavior is of no concern in the present work. However, rotations and displacements can possibly be so large that nonlinear elements should be considered at a later stage. This work is limited to considering to what degree the observed

displacements and rotations call for the use of nonlinear elements, see Section 7.2.2 and 7.6.

The mooring

As discussed in Section 2.2.2, the mooring is modeled by means of linear horizontal springs. Each corner node of the BCS has one spring in each principal direction. The stiffness is set to $142.0\,kN/m$, see Section 2.2.2.

The buoyancy springs

The buoyancy is modeled as vertical springs. The springs are nonlinear in the nonlinear analysis. The maximum water plane stiffness is $k_{w,max} = 10.1\,kN/m^2$.

The water plane stiffness of an element is lumped to its two nodes. Each spring of element j has the stiffness: $k_j^{spring} = \frac{1}{2}k_w l_j$. Typically, $k_w = k_{max}$ and $l_j = 1.0\,m$, i.e. $k_j^{spring} = 5.0\,kN/m$. For the BCS all nodes will have two springs with this stiffness as each node is shared by two beam elements.

5.2.2 Mass

Structural mass

The BCS has a total mass giving half submergence as the equilibrium position, i.e. $m_{struct} = 403\,kg/m$. A lumped mass matrix is used with nonzero values only for the translational DOFs.

Hydrodynamic added mass

Each element is given an added mass in the vertical direction equal to $C_{m,vert}\,\rho_w \frac{\pi D^2}{4}$, and correspondingly in the perpendicular, horizontal direction: $C_{m,hor}\,\rho_w \frac{\pi D^2}{4}$. The C_m-values for the TRW are given in Table 3.11 and 3.12. For reference they are repeated in Table 5.1.

The added mass is also lumped. DOFs for translation parallel with the beam axis as well as rotations have no added mass.

The total mass matrix is:

$$\mathbf{m} = \mathbf{m_{struct}} + \mathbf{m_{a,hor}} + \mathbf{m_{a,vert}} \tag{5.1}$$

5.2.3 Damping

Hydrodynamic damping

As for hydrodynamic added mass, hydrodynamic damping is applied only to the vertical and the perpendicular horizontal DOFs. The damping is lumped.

The distributed hydrodynamic damping is found by dividing the B-values in Table 3.17 and 3.18 with $120\,m$ and $60\,m$, respectively. The resulting values are shown in Table 5.1.

TRW	*Heave*			*Sway*			
	B_{flo}	B_{tot}	$C_{m,eq}$	B_{flo}	B_{tot}	$C_{m,eq}$	$C_{M,eq}$
B	1.2	2.0	0.40	0.78	1.2	0.65	1.1
C	1.0	2.1	0.63	0.42	1.0	0.60	1.1
D	0.85	2.1	0.75	0.40	1.0	0.58	1.0
H_{max}	0.75	2.6	0.85	0.58	1.5	0.56	1.0
Avrg.	0.95	2.2	0.66	0.55	1.2	0.60	1.1

Table 5.1: Distributed hydrodynamic damping and equivalent added mass coefficients in heave and sway. For damping, both floater and total (i.e. incl. netpen) values are shown. Unit for damping: $[kNs/m^2]$.

Structural damping

In addition to the hydrodynamic damping discussed previously, there will also be structural damping present. The Rayleigh damping scheme is chosen to represent the structural damping. The damping matrix[10] $\mathbf{B}$ is then expressed as a linear combination of the (total) mass $\mathbf{M}$ and stiffness matrices $\mathbf{K}$:

$$\mathbf{B} = \alpha\mathbf{K} + \gamma\mathbf{M} \tag{5.2}$$

Damping constants[11] α and γ are determined by choosing the fraction of critical damping (ξ_1 and ξ_2) at two different frequencies (ω_1 and ω_2) and solving simultaneous equations for α and γ, see e.g. (Cook et al., 2001). ω_1 is taken as the lowest natural frequency of the structure, and ω_2 is the maximum frequency of interest in relation to the loading. Using the corresponding natural periods, these values are set to the maximum average natural period from Table 4.3, i.e. $2.3\,s$, and the assumed lower limit of the wave spectrum, i.e. $0.1\,s$. In steel piping ξ ranges from 0.5% to 5%. Additionally, for structures with rigid body motion it is important that the γ-value is not excessive; typically $\gamma < 0.1$ is acceptable. Since buoyancy is modelled as springs, the BCS does not have rigid body motion per.se. (the rigid body modes will appear in a natural frequency analysis with a nonzero natural frequency). However, $\gamma < 0.1$ is adhered to since the motion can still be mass governed. In Table 5.2 the chosen T-, ω-, ξ-, α-, and γ-values are shown. To indicate the relative size of the three contributions to the damping (stiffness proportional structural damping, mass proportional structural damping, and hydrodynamic damping), the respective numerical values for the vertical DOF for an element length of $L = 1\,m$ are compared in Table 5.3. Also, the expressions used are shown (abbreviated Exp.). The hydrodynamic

[10] In structural mechanics the damping matrix is usually named $\mathbf{C}$ and the restoring force (i.e. stiffness) $\mathbf{K}$, whereas in hydrodynamics damping is named $\mathbf{B}$ and restoring force $\mathbf{C}$. To avoid misunderstandings $\mathbf{B}$ is used for damping and $\mathbf{K}$ for restoring force.

[11] β is often used instead of γ, but since β has already been used for the frequency ratio γ is chosen here.

T_1	ω_1	ξ_1	T_2	ω_2	ξ_2	α	γ
$2.3s$	$2.7\frac{rad}{s}$	2.0%	$0.1s$	$62.8\frac{rad}{s}$	4%	$0.0012\frac{rad}{s}$	$0.100\frac{rad}{s}$

Table 5.2: Rayleigh damping constants and input values.

Stiffness prop.		Mass prop.		Hydrodynamic	
Exp.	Value	Exp.	Value	Exp.	Value
$\alpha\frac{12EI}{L^3}$	$1.2E07\,Ns/m$	$\gamma\,\frac{1}{2}(m_a+m_s)L$	$47\,Ns/m$	$\frac{1}{2}B_{tot}\,L$	$1100\,Ns/m$

Table 5.3: Contributions to vertical DOF of the element damping stiffness ($Ns/m = kg/s$). $L_{elt} = 1\,m$ and $C_m = 0.6$

damping is found by using $B_{tot} = 2.2\,kNs/m^2$, see Table 5.1, i.e. the average value for total damping in heave[12]. The hydrodynamic contribution is about 20 times greater than the mass proportional, whereas the stiffness proportional is about 10000 times greater than the hydrodynamic one.

The total damping matrix is:

$$\mathbf{B} = \mathbf{B_{struct}} + \mathbf{B_{lin,hyd,hor}} + \mathbf{B_{lin,hyd,vert}} \tag{5.3}$$

5.2.4 Load modeling

The dynamic loading consists of mass loading (i.e. in-phase with water particle acceleration or sea surface elevation) in both directions and drag loading (i.e. in-phase with water particle velocity) in the horizontal direction. Gravity load F_G constitutes the static loading. The buoyancy load F_B is static in the linear analysis, but stepwise updated in the nonlinear analysis. The element loading is lumped to the two nodes of each element. The lumped value for element i is:

$$F_i = \frac{1}{2}q_i(x_{i,0}, y_{i,0}, z_{i,0}) \cdot L_i \tag{5.4}$$

The distributed load $q_{i,j}$ (element i, time step j) is found for the midpoint of the element at its static position $(x_{i,0}, y_{i,0}, z_{i,0})$. The linear vertical load for element i is the sum of gravity, (initial) buoyancy, and $k_w \cdot \zeta(t)$ (see Equation 3.33):

$$q_{vert,i,j} = F_{G,distr} + F_{Buoy,distr} + F_{inrt,distr}(t) = F_{G,distr} + F_{Buoy,distr} + k_w \cdot \zeta(t) \tag{5.5}$$

[12]The hydrodynamic damping generally depends on the wave frequency, but this is not reflected here explicitly.

The horizontal force is the sum of mass force and (linearized) drag force (see Equation 3.30):

$$q_{hor,i,j} = F_{inrt,hor}(t) + F_{v,hor,lin}(t) = C_{M,eq} \cdot \rho_w \frac{\pi D^2}{4} a_\perp(t) + B_{lin,hor} u_\perp(t) \tag{5.6}$$

$a_\perp$ and $u_\perp$ are the component of the horizontal water particle acceleration and velocity, respectively, which are perpendicular to the element axis.

5.2.5 Time integration

The response of a fish farm system is found by time integration of the equation of motion, discretized by means of the finite element method. The Newmark-β method (Newmark, 1959) is used for time integration. The linear algorithm presented by Chopra (2006) is used. The coefficients are set to $\beta = 0.25$ and $\gamma = 0.5$ (i.e. constant average acceleration) thus making the scheme implicit and unconditionally stable.

5.2.6 Choice of time step

The chosen parameters for the Newmark-β integration yield an implicit method — which is always numerically stable (for a linear system). The time step is therefore chosen from accuracy considerations alone. Cook et al. (2001) suggests a time step based on the lowest period of interest in the loading or response of the structure T_u. From Table 4.8 we see that the minimum natural period for the 12 highest natural periods of case #1 is $0.31\,s$. Thus, we set $T_u = 0.31\,s$. A minimum of 20 time steps per period should provide very good accuracy for modes that participate dynamically in the response. A suggested time step is then:

$$\Delta t = \frac{T_u}{20} = 0.015\,s \tag{5.7}$$

5.2.7 Disturbances from initial conditions

Initial conditions can introduce unwanted disturbances in the analysis. To minimize disturbances the wave amplitude will be increased linearly from zero to the intended wave amplitude over a prescribed length of time. The required ramp-up time is determined based on observed response behavior.

5.3 Nonlinear dynamic analysis

Nonlinearities for a floating fish farm can arise both from hydrodynamic effects and structural behavior. As discussed in the previous chapter, the dominating nonlinear effect is assumed to be nonconstant water plane stiffness.

5.3.1 Nonconstant water plane stiffness

As for linear analysis, the buoyancy of an element is lumped to its two nodes, i.e. modeled as two nonlinear springs. The instantaneous spring stiffness for each spring is $k_{i,j}^{spring} = \frac{1}{2}k_w(d_{i,j})l_i$, making it a function of the instantaneous draft $d_{i,j}$. The draft is assumed to be constant for the whole element, i.e. both the element and the free surface are approximated as being horizontal. The draft is found for the midpoint of the element. The deflection is the average of the vertical displacement of the two nodes, whereas the free surface elevation is the elevation for the initial horizontal position of the element. Thus, nonlinearities due to horizontal response of the element are not introduced. The draft $d_{i,j}$ for element i at time t_j is calculated as (c.f. Equation 3.10):

$$d_{i,j} = w_0 + \frac{w_{i,j}^{node1} + w_{i,j}^{node2}}{2} - \zeta(x_{i,0}^{midpoint}, y_{i,0}^{midpoint}, t_j) - r \tag{5.8}$$

$w_{i,0}$ is the initial vertical location of the midpoint of the element, typically $w_{i,0} = 0\,m$. w_i^{node1} and w_i^{node2} are the vertical response of node 1 and 2 of the element, respectively. $\zeta(x_{i,0}^{midpoint}, y_{i,0}^{midpoint}, t_i)$ is the free surface elevation at the initial location of the element midpoint $(x_{i,0}^{midpoint}, y_{i,0}^{midpoint})$ at time t_j. The water plane stiffness k_w as a function of draft is found using Equation 3.8.

5.3.2 Nonlinear load

The vertical load is changed to reflect the nonconstant water plane stiffness. As shown in Section 3.4.2, the distributed, incremental force is:

$$\Delta F_{vert,i,j}(t_i) = k_{w,i} \cdot \Delta\zeta_{i,j}(t_i) \tag{5.9}$$

The incremental distributed vertical load is (cf. Equation 5.5):

$$q_{vert,i,j} = F_{G,distr} + F_{Buoy,distr} + k_{w,i} \cdot \Delta\zeta_i(t_j) \tag{5.10}$$

5.3.3 Modified Newton-Raphson iteration

The algorithm chosen for the nonlinear case of Newmark-β is the well-known modified Newton-Raphson iteration. The Newton-Raphson method was initially proposed by Newton (1671) and Raphson (1690), and is described in (Mathworld, 2007).

The modified version of the method is used where the initial tangent stiffness is used within each time step. The algorithm is e.g. described by Chopra (2006), Belytschko et al. (2000), Langen and Sigbjörnsson (1999).

In the Newton-Raphson scheme, the residual (unbalance) $\Delta R(j+1)$ of the equation of motion of iteration j is used to refine the result $u_{i+1}^{(j)}$ for time step $i+1$ until it reaches the convergence criteria. As the nonlinearity is confined to the buoyancy springs, the

residual can only be nonzero for the vertical DOFs and is calculated one DOF at a time. $\Delta R^{(j+1)}, j \geq 1$ is the residual for iteration $(j+1)$ and DOF k, and is found as:

$$\Delta f^{(j)} = f_S^{(j)} - f_S^{(j-1)} + (\hat{k}_T - k_T)\Delta u^{(j)} \tag{5.11}$$
$$\Delta R^{(j+1)} = \Delta R^{(j)} - \Delta f^{(j)}$$

When finding the solution for time step $(i+1)$, $f_S^{(j)}$ for $j \geq 1$ is the buoyancy force as a function of draft, i.e. the known free surface elevation at time $(i+1)$ and the estimated response for each vertical DOF k, correspondingly

5.3.4 Convergence criteria

A Euclidean norm is chosen as convergence criteria (Remseth, 1978):

$$\epsilon = \sqrt{\frac{1}{N}\sum_{i=1}^{N}\left|\frac{\Delta r_i}{r_{j,ref}}\right|^2} \tag{5.12}$$

In Equation 5.12, Δr_i is the increment of displacement component number i during the iteration cycle, while $r_{j,ref}$ is the reference value used for degrees of freedom of type j. The norm ϵ gives an average measure of the rate of change of displacements.

Termination of iterations according to this norm is based on a predefined limit, $\bar{\epsilon}$. Iterations continue until the relation $\epsilon \leq \bar{\epsilon}$ is fulfilled. In addition, a maximum number of iterations is prescribed to terminate iterations even if the claim on the displacement norm is not met.

The choice of reference value $r_{j,ref}$ and the limit value $\bar{\epsilon}$ must be seen in connection with one another. Since only vertical forces can be nonzero in the residual, the reference value is only set for vertical displacements. Although rotations will also occur, they are assumed to be sufficiently accurate when the vertical displacements converge as the floater sides have relatively many elements. We choose to set:

$$r_{vert,ref} = 0.001m \tag{5.13}$$
$$\bar{\epsilon} = 1 \tag{5.14}$$

Thus, the convergence is loosely defined as when the average incremental vertical displacement is less than $0.001\,m = 1\,mm$. The scheme is terminated after 10 iterations as the maximum limit.

5.3.5 Choice of time step

For the nonlinear case no integration schemes can be proven to be unconditionally stable. As a starting point the time step in Section 5.2.6 is used also for nonlinear analysis. In

general, convergence difficulties might require a shorter time step for nonlinear than for linear analysis. On the other hand, a longer time step is desirable to increase the analysis speed, see Section 7.3.

Chapter 6

SOFTWARE TOOLS AND DEVELPMENT

6.1 FEM software options

Structural analysis and design of a floating fish cage is mathematically and numerically intensive and complex to a degree that suitable computer software is an indispensable remedy. Computer tools are beneficial for several reasons, e.g.:

- The highly complex nature of the structural system and its loading excludes, to a large degree, hand calculations.
- Limited engineering experience, especially in more exposed areas of the sea, gives poor guidance in relation to reliable design.
- Establishing and improving the methods of design in a research context requires computer analysis.
- Employing design methods in a certification/engineering context will also require computer analysis.
- Customized computer tools can be used in the (preliminary) design phase.

The finite element method (FEM) is today the dominating numerical method used for structural analysis. Four general alternative strategies for finite element software intended for the present purpose were identified:

1. Using a general finite element package (typically commercially available)
2. Using and possibly extending a purpose built finite element program
3. Developing a finite element program from scratch
4. Developing a finite element program from a framework available as source code

There is an abundance of general purpose finite element software commercially available, e.g. ABAQUS (Simulia, 2007), ANSYS (Ansys, 2007). Among their advantages are an emphasis on support and documentation, a well tested code, and easy (if not necessarily inexpensive) availability. General purpose FEM software has been used in the analysis of fish farms, see e.g. (Jensen et al., 2007). However, it was found to be hard to identify a program that was particularly well suited for analysis and design of floating fish farms. Existing computer tools typically lack functionality for the special needs of the structural and loading system for a fish farm (i.e. hydrostatic and hydrodynamic loads on floating, slender members) and/or advanced analysis options for marine structures, i.e. irregular waves, and this is typically coupled with limited expandability.

Over the last decade, efforts have been made to establish specialized finite element programs suitable for analysis of floating fish cages, typically based on existing software, e.g. RIFLEX (Ormberg, 1991), AquaFE (Gosz et al., 1996), AquaSim (Berstad and Tronstad, 2005), MOSES (Ultramarine, 2007). These tools aim at amending what the general purpose codes lack in specialized functionality. The price to pay is typically a more poor support, documentation, testing of the code, and a small user base. Similar to their general purpose big brothers, they are typically neither readily available as source code. A Norwegian aquaculture certification company is currently using three different analysis software as they have not found that any single alternative provides the functionality they need for structural analysis of floating fish cages (Roaldsnes, 2007).

Developing a specialized finite element program from scratch was assumed to require an unrealistic amount of resources. Building on a general finite element framework available as source code, however, was assumed to be a realistic approach, depending on the amount of work required to go from a general framework to a specialized application. A number of frameworks have been developed and are mostly in academic use, see e.g. OpenSees (2007), OOFEM (2007). Their main advantage is full source code availability in addition to being developed with expandability in mind.

The author has previous knowledge and experience with an object-oriented (OO) FEM framework specialized for structural mechanics developed at the University of Washington, Seattle, USA, see (Thomassen, 1985). After a (re)evaluation of the latter framework it was chosen[13] without a more thorough assessment of the alternatives. The most recent version of the framework has been developed by Jang (2007) during his PhD work. The source code used as the starting point for the development of the floating fish farm prototype was based on a version of the framework dated February, 2005.

6.2 The framework

The framework is fully object-oriented (OO) and is programmed in C++. The framework follows the lines of OO implementation of structural engineering described in (Miller, 1991), (Miller, 1993).

[13] A decisive factor for the choice was the fact that the framework was under active parallel development and actively supported by the people behind the framework.

Among the strengths of the framework are its joint emphasis on extensibility, user experience and computational efficiency. It also has a focused and limited scope. The area on which the framework (and its predecessors) stands apart from most alternatives is its capabilities for providing live modeling in the following sense:

> ... the prototype supplies a functional and realistic interactive and visual test environment. The prototype implementation is not just a command line based conventional procedural program. It interacts with end-users through a graphical user interface, and enables them to see the results immediately after they change material properties, loading conditions, boundary conditions, topology, and so on. The target range of problems are those that are amenable for quasi-realtime analysis.

6.3 The prototype

The floating fish cage prototype shall be used for time domain analysis of the BCS and shall have two principal features:

- Fully interactive, quasi real-time modeling and investigation of the structure
- High speed analysis to facilitate time domain analyses covering the whole scatter diagram

The first feature takes advantage of the live modeling capabilities of the framework. A screenshot of the prototype graphical user interface (GUI) is shown in Figure 6.1. The GUI is made up of three main parts: the input pane, the visualization pane and the output pane. MFC (Microsoft, 2008) is used to build the GUI, whereas OpenGL (OpenGL, 2008) is used for visualization. The structural model and the wave loading parameters are defined through the input pane and immediately reflected in the visualization pane. The speed of the dynamic (linear or nonlinear) analysis is set as a factor of the real time, i.e. a simulation can progress faster, slower or in real time. The structure is visualized according to the visualization parameters given by the user. In addition to the structural model, the visualization pane of the GUI contains a graph which plots a response quantity chosen by the user, e.g. a moment or displacement component. The output pane contains the maximum values observed and the time of occurrence for a list of response quantities. This mode is intended for preliminary deign and investigation of the floating fish cage. The structure will typically be observed for up to a couple of minutes. One or more input parameters can then be changed before a new simulation is run.

The second feature is intended for design limit state verification. Analysis durations of the order of hours for each seastate are typically required, i.e. tens of hours in total for all necessary seastates. For this kind of analysis, the analysis speed (expressed as the ratio of computer time to real time) is of paramount importance, and real time capabilities are of less interest. The operational requirement in this respect for the prototype was that the necessary results could be generated at an adequate speed. After some optimization

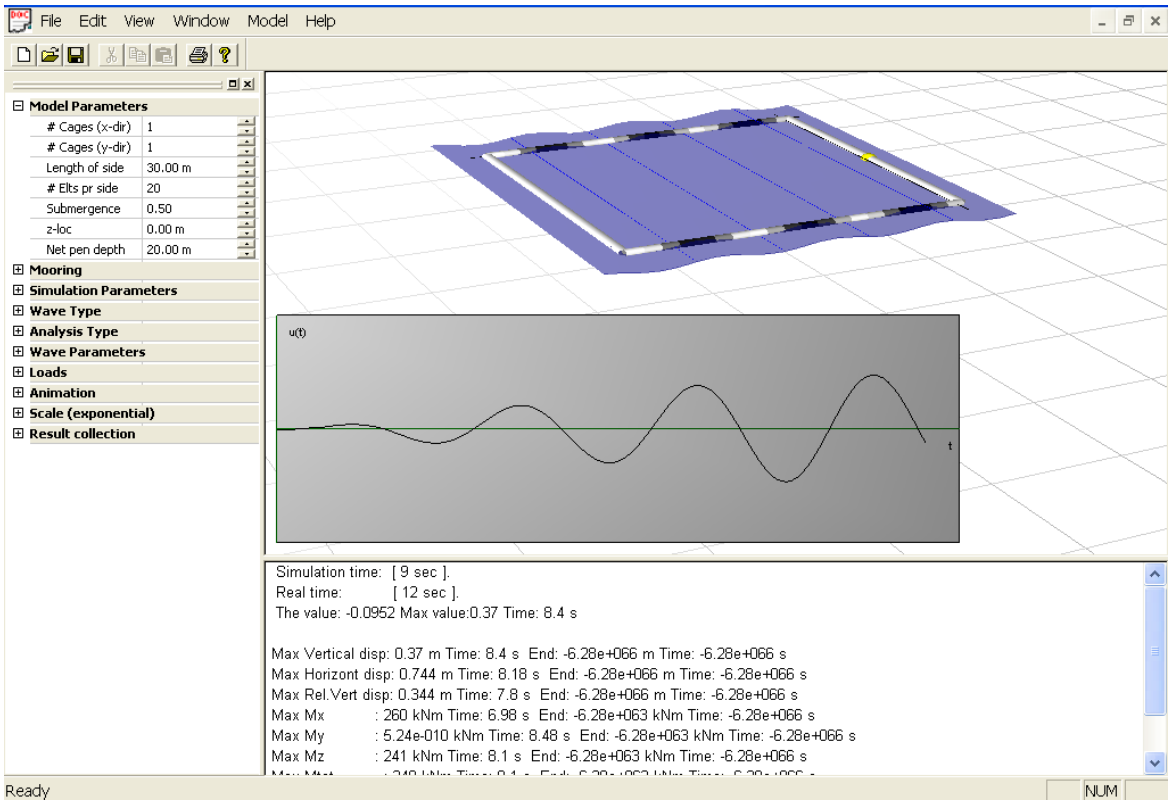

Figure 6.1: Screenshot of the prototype GUI

of the element length and the time step (see Section 7.3), the linear analyses of the BCS were observed to require a computer time approximately equal to the real-time duration, whereas the nonlinear analyses required a computer time six times longer than the real time duration. For the typical (real-time) analysis duration of half an hour, this was considered acceptable. No other optimization (e.g. compiler settings or in the source code) have been introduced to achieve increased computation speed in the prototype. Whereas the focus of the framework used was to investigate and expand the limits for the structure complexity (i.e. number of DOFs) in a real-time environment, the goal for the second feature above is to achieve a computation speed that is acceptable in an engineering sense. However, it is reasonable to assume that the optimization measures will also give a faster solution for each time step in a dynamic analysis with less DOFs. Based on the findings by Jang (2007), there is reason to assume that increase in speed (maybe by orders of magnitude) is possible by optimization of the source code and compiler settings. Additionally, switching to a modern high-performance PC is also likely to give considerable speed gains[14]. In particular, TDA lends itself well to benefit from multiple core processors that are becoming standard in new PCs. Jang (2007) measured that real-time behavior for a linear, static 3D frame structure was possible with more than 18000 DOFs (in comparison, the BCS has 486 DOF). It appears realistic that optimization can lead to significant gains in relation to TDA of floating fish cages along several axes of interest:

- Increase the speed
- Increase the number of DOFs
- Decrease the time step
- Introduce an improved nonlinear model (e.g. with respect to geometry and hydrodynamic coefficients)

6.4 Use and extensions of the framework

The framework had the capabilities of linear, dynamic analysis. Further, although the framework had several solution algorithms, only Gaussian elimination was used as the structure has relatively few DOFs. Extension of the framework was thus foremost needed in the following areas:

The floating fish cage structure A new class defines the structure and loading. A specialized spring has been introduced to represent buoyancy as a linear or nonlinear spring.

Nonlinear dynamic analysis Nonlinear dynamic analysis has been implemented (see Section 5.3).

[14]All analyses in the present thesis have been run on a 4 year old laptop PC with a Pentium 4 2.80GHz processor and 512 MB RAM.

Name	Description
dat2tp	Extracts turning points from data, optionally rainflowfiltered.
tp2rfc	Finds the rainflow cycles from the sequence of turning points.
cc2dam	Calculates the total Palmgren-Miner damage of a cycle count.

Table 6.1: WAFO functions used in the fatigue analysis

Wave model Regular and irregular long-crested waves with arbitrary direction have been implemented. The irregular wave simulation includes horizontal velocity and acceleration.

Hydrodynamic model The hydrodynamic model contains added mass, damping, and coefficients for horizontal wave force.

Visualization Live visualization of the BCS and the waves have been implemented. Loading and moments can also be shown.

Results recording The output of a simulation is the time history of the chosen response parameter for the chosen location. The history is written to a binary file.

6.5 Additional software used

The software prototype described in the previous section is used to produce moment histories for the critical locations. The stress histories are written to file. Based on the moment histories the fatigue analyses are performed using MATLAB (MathWorks, 2007) and the toolbox WAFO, see (Brodtkorb et al., 2000), (WAFO, 2007). The WAFO functions that have been used are listed and briefly described in Table 6.1.

The FFT simulation (see p.115) was performed by means of the FFT libray fftw (FFTW, 2008).

Chapter 7

REGULAR WAVE PARAMETER STUDY

In this chapter we will use both the linear and nonlinear models defined in the previous chapters in a parameter study applying long-crested regular waves. Regular waves analyses are considered to be well-suited for a relative comparison of various effects. The results are also quite transparent with respect to the relation between sea elevation and response magnitudes.

The main objectives of this chapter are three fold:

- Compare results of the linear analysis with the "hand-calculations" presented in Chapter 3. This will verify a correct implementation of the linear model in the software tool.
- Compare results of nonlinear analyses with the linear analyses for small amplitude waves. Again, good consistency will verify a correct implementation of the nonlinear model.
- Investigate when the nonlinear results diverge from the linear results. This will illustrate the importance of the included nonlinear effects.

First, the suggested analysis procedure is investigated. Next, in Section 7.2 a single cylinder is analyzed. The remaining sections of this chapter deals with the BCS.

7.1 Analysis procedure

Steady-state results are the focus of this parameter study. For the linear system, regular waves will cause a periodic loading (i.e. sinusoidal) — both vertically and horizontally. Thus, the steady-state response will be sinusoidal with a period equal to the wave period. A periodic behavior is also expected for the nonlinear system. However, this can not be proven in advance to always be the case. Further, a non-sinusoidal response is expected as

the nonlinear effects increase. Our main interest will be the respective maximum absolute values of the steady state responses.

Linear and nonlinear analyses will be run for both a single cylinder and the BCS. A single cylinder is included to examine the isolated effect of the perpendicular and parallel sections of the BCS, respectively. The single cylinder case will also be compared to the "hand-calculations" of Chapter 3. Accordingly, the single cylinder will be analyzed in waves perpendicular and parallel to its axis. The BCS will be analyzed in perpendicular waves and in 45° oblique waves.

Initially, the analysis will be run with uniform time step and element length: $\Delta t = 0.015\,s$ and $L_{elt} = 1\,m$ (i.e. 30 elements pr. side and 120 elements for the BCS). The time step is chosen in accordance with Section 5.2.6 and 5.3.5. However, in Section 7.3 we will investigate the effects of changing time step and element length for the BCS.

7.1.1 Verification of steady state conditions

As steady-state response is the focus of this parameter study, we want to eliminate the transient effects from our results. Damping will gradually remove transient effects. Thus, maximum values will be collected for a time period (i.e. the recording period) at the end of the analyses. Additionally, the wave amplitude will be gradually increased from zero to its maximum over a given time period (the ramp-up period) to remove transient effects from the presented results.

We start the parameter study by evaluating the lengths of the ramp-up, recording, and analysis periods. (i.e. whether the periods are sufficiently long). Initially, we assume that a ramp-up period equal to the maximum wave period of the TRW is sufficient, i.e. $t_{ramp-up} = 6.7\,s$. Initially, the length of the recording period is set to $t_{rec} = 10\,s$ (i.e. approximately one-and-a-half times the maximum wave period) and the total analysis period is set to $t_{tot} = 30\,s$.

For all the TRW we run linear and nonlinear analyses for a perpendicular cylinder. For each TRW we use the damping and added mass coefficients specified in Table 5.1. The maximum vertical response Δ_v and the maximum relative response $\Delta_{v,r}$ is found for the total analysis period ($30\,s$) and the recording period (last $10\,s$). The former results are labeled *Tot* in the table and the latter *Rec*. Both the maximum values and the corresponding times of occurrence are recorded, see Table 7.1. Linear and nonlinear analyses are performed and labeled L and NL, respectively.

Discussion

Table 7.1 shows very good agreement between corresponding maximum values for the total period and for the recording period. The maxima of the recording period varies from $87\% - 100\%$ of the corresponding maxima of the total analysis period. The differences are due to transient effects. For most cases the total maxima occur approximately within one period after the ramp-up period. This is a good indication that the duration of the ramp-up, the analysis, and the recording intervals are sufficiently long. Only for the nonlinear

TRW		Δ_v				$\Delta_{v,r}$			
		Tot		Rec		Tot		Rec	
		$[m]$	$[s]$	$[m]$	$[s]$	$[m]$	$[s]$	$[m]$	$[s]$
B	L	0.68	8.4	0.68	20.9	0.47	7.5	0.46	21.4
	NL	0.67	9.7	0.67	22.2	0.54	16.4	0.54	20.1
C	L	1.19	7.3	1.19	21.3	0.49	7.8	0.47	21.9
	NL	1.23	25.4	1.23	25.4	0.67	28.1	0.67	28.1
D	L	1.68	12.2	1.68	20.1	0.51	7.6	0.48	21.0
	NL	1.76	12.3	1.76	20.2	0.71	10.8	0.71	21.4
H_{max}	L	3.05	8.6	3.04	22.1	0.82	6.8	0.79	23.3
	NL	2.43	9.4	2.10	23.0	2.83	11.1	2.76	24.5

Table 7.1: Maximum vertical response Δ_v and maximum relative response $\Delta_{v,r}$ for perpendicular cylinder. Maximum values are found for the total analysis period of $30\,s$ (labeled Tot) and for the last $10\,s$ (labeled Rec). Both absolute value and time of occurrence is recorded. The units are meters and seconds for each pair of results, respectively.

analysis applying TRW C, the maximum value occurs close to the end and this indicates that a longer analysis period is appropriate. However, as it is observed that the maximum value is approximately equal to the previous maximum of the time series, the analysis time is not increased.

The initially suggested periods — $t_{ramp-up} = 6.7\,s$, $t_{rec} = 10\,s$, and $t_{tot} = 30\,s$ — will be kept for the rest of this chapter. Also, we will report only the relevant absolute maximum values in the recording period (and not the corresponding time of occurrence).

7.2 Single cylinder

A single floating cylinder is analyzed to investigate the isolated behavior of a perpendicular and a parallel cylinder. The perpendicular cylinder will also be compared to the results of the hand-calculations in Chapter 3 as a verification of the software implementation of linear analysis.

Both cylinder directions will be analyzed linearly and nonlinearly, and the nonlinear results will be compared to linear results.

7.2.1 Perpendicular cylinder

For the perpendicular cylinder (cylinder axis perpendicular to wave direction, see Figure 7.1) we focus on the vertical and horizontal displacement and the moment about the vertical axis.

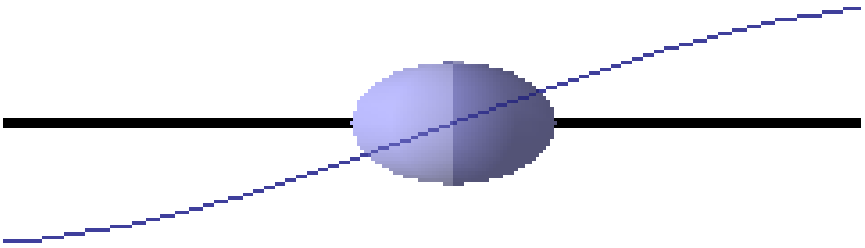

Figure 7.1: Cylinder axis perpendicular to wave direction. Horizontal line is $z = 0\,m$. Screenshot from prototype.

Vertical response

All nodes will have virtually the same vertical loading and displacement, thus moments about the horizontal axes will be negligible. As explained in Section 3.4.1 the only non-linear effect included in the nonlinear analyses is nonconstant water plane stiffness. The importance of this effect will depend on the relative displacement and thus on the wave height and wave period.

Based on the linear results of Table 7.1, we can compare the maximum values Δ_v to the respective wave amplitudes ζ_a, see Table 7.2. In the Table we also compare relative response $\Delta_{v,r}$ to Δ_{full} and find the wave height that gives zero water plane stiffness H_{full} (i.e. full submergence or dry cylinder) for the linear system. Δ_{full} is the relative response required for full submergence or dry cylinder, i.e. $\Delta_{full} = 0.5\,m$. H_{full} is the wave height for a given wave period required for full submergence or dry cylinder, i.e. whereas Δ_{full} is a constant, H_{full} depends wave period. Using a TRW wave height H and the respective linear $\Delta_{v,r}$-value, we get:

$$H_{full} = H \cdot \frac{\Delta_{v,r}}{\Delta_{full}} = H \cdot \frac{\Delta_{v,r}}{0.5\,m} \tag{7.1}$$

Using Equation 3.25 as the vertical load, the maximum static deflection is $\Delta_{stat} = \zeta_a$. Thus, we can find the dynamic amplification factor based on the numerical results DAF_{nu}:

$$DAF_{nu} = \frac{\Delta_v}{\Delta_{stat}} = \frac{\Delta_v}{\zeta_a} \tag{7.2}$$

I.e. DAF_{nu} is equal to $\frac{\Delta_v}{\zeta_a}$ of the first column in Table 7.2 and these numbers can be compared with the DAFs based on hand-calculations of Table 4.4.

In Table 7.3 absolute maximum vertical displacement Δ_v and relative displacement $\Delta_{v,r}$ are recorded for the TRW periods and a nonlinear system. For each period, several wave heights H are applied. The wave heights are chosen as a percentage of the respective TRW wave heights — from 50% to 175%. For TRW B $H = 1.4\,m$ yields maximum steepness,

TRW	$\frac{\Delta_v}{\zeta_a}$	$\frac{\Delta_{v,r}}{\Delta_{full}}$	H_{full}
B	135%	91%	$1.1m$
C	119%	94%	$2.1m$
D	112%	95%	$3.1m$
H_{max}	107%	158%	$3.6m$

Table 7.2: Linear analyses results for a perpendicular cylinder applying the TRW. Vertical response.

and this value is thus used instead of the 150%-value of $1.5\,m$ (and marked with a * in the tables). Correspondingly, the 175% wave height level is not used for TRW B. The purpose is to indicate when and to what degree nonlinear effects become important. In Table G.1 the corresponding differences between linear and nonlinear results are given, i.e.: $\frac{nonlinear-linear}{linear}$. In Figure 7.2 the Δ_v and $\Delta_{v,r}$ results are shown for TRW C — both linear and nonlinear.

Horizontal response

No nonlinearities have been introduced in the horizontal direction. Thus, nonlinear analyses should give identical results to linear analyses in the horizontal direction. This has been verified. Further, it has been verified that the horizontal results are linear with respect to wave height.

We want to compare linear horizontal response from numerical analyses for the perpendicular cylinder with the hand-calculations for the BCS. The equivalent horizontal added mass coefficient is increased to give a total horizontal mass for the pipe of half the total horizontal mass of the BCS. The horizontal $C_{m,eq}$-factors of the TRW are then: $C_{m,eq} = 1.2, 1.1, 1.1, 1.1$, respectively, see Table 7.4. As the (horizontal) mooring stiffness is also half the value of the BCS, the maximum rigid body responses are expected to be the same as in Table 4.6.

The perpendicular horizontal displacement will vary slightly along the length of the cylinder (the rigid body displacement contribution will dominate over the flexural displacement contribution). As explained in Section 3.3.4 the horizontal wave loading is dominated by the mass loading and it is the only loading included for these analyses. The maximum total horizontal response Δ_h (due to mass force) at one end and at the middle is presented in Table 7.4. We also record the maximum bending moment about the vertical axis $M_{b,v}$ at the middle. Δ_h for the end point is compared to the rigid body amplitude $\Delta_{h,hand}$ from hand-calculations in Table 4.6.

	$\frac{H}{H_{ref}}$	50%	75%	100%	125%	150%	175%
B	H [m]	0.50	0.75	1.0	1.25	1.4*	
	Δ_v [m]	0.34	0.51	0.67	0.72	0.73	
	$\Delta_{v,r}$ [m]	0.24	0.37	0.54	0.79	0.91	
C	H [m]	1.00	1.50	2.00	2.50	3.00	3.50
	Δ_v [m]	0.60	0.90	1.23	1.30	1.31	1.32
	$\Delta_{v,r}$ [m]	0.24	0.38	0.67	1.32	1.71	2.04
D	H [m]	1.50	2.25	3.00	3.75	4.50	5.25
	Δ_v [m]	0.84	1.27	1.76	1.86	1.86	1.87
	$\Delta_{v,r}$ [m]	0.25	0.39	0.71	1.81	2.39	2.89
H_{max}	H [m]	2.85	4.28	5.70	7.13	8.55	9.98
	Δ_v [m]	1.54	2.08	2.10	2.10	2.10	2.13
	$\Delta_{v,r}$ [m]	0.45	1.67	2.76	3.64	4.46	5.26

Table 7.3: Maximum vertical response Δ_v and maximum relative response $\Delta_{v,r}$ for nonlinear analysis of perpendicular cylinder.

TRW	$C_{m,eq}$	Mid point		End point	
		Δ_h	$M_{b,v}$	Δ_h	$\frac{\Delta_h}{\Delta_{h,hand}}$
	[-]	[m]	[kNm]	[m]	[%]
B	1.2	0.97	936	0.86	101
C	1.1	0.39	384	0.35	109
D	1.1	0.26	266	0.22	97
H_{max}	1.1	0.27	334	0.24	97

Table 7.4: Linear analyses results for a perpendicular cylinder applying the TRW. Horizontal responses.

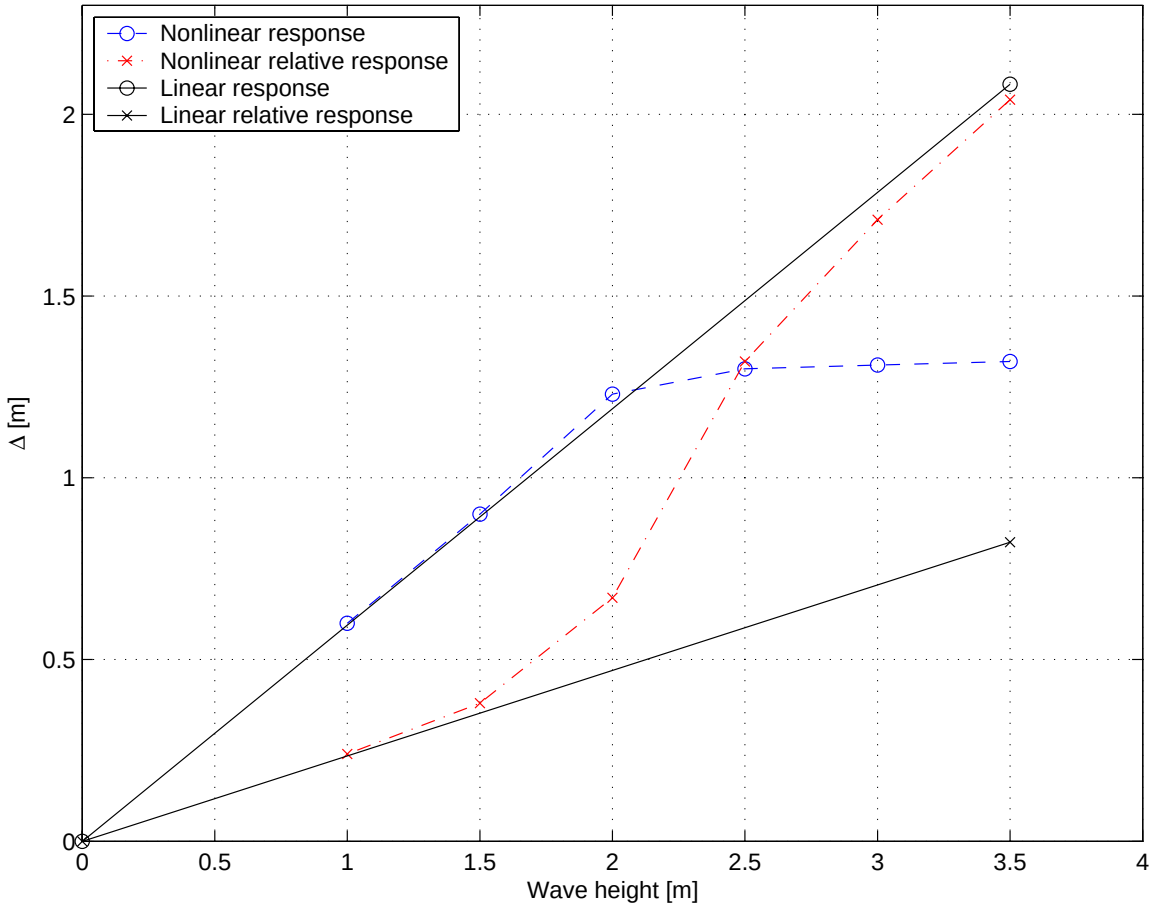

Figure 7.2: Wave height H vs. Δ_v and $\Delta_{v,r}$ for TRW C

Figure 7.3: Wave direction parallel to the pipe axis. Screenshot from prototype.

Discussion

From Table 7.2 we see that the maximum vertical displacements from linear analyses vary from 107% to 135% of the corresponding TRW wave amplitudes. As expected the percentage decrease with increasing wave period as the natural period is short ($\approx 2\,s$). The relative displacement $\Delta_{v,r}$ varies from 91% to 95% of Δ_{full} for TRW B-D and is considerably higher for TRW H_{max}: 158%. This shows that full submergence is to be expected for all TRW. Thus, the nonlinear effects are expected to be considerable. The comparison of dynamic amplification factors show very good agreement. This is a good indication of correct software implementation of the linear analysis.

The nonlinear analysis (see Table 7.3 and Figure 7.2) show that the vertical response increases approximately until the cylinder becomes fully submerged. Increased wave height after this point will not increase the vertical response. This is as expected because the vertical load (i.e. buoyancy) will not increase after full submergence. Figure 7.2 shows that the relative response $\Delta_{v,r}$ approaches the linear (absolute) response curve after full submergence.

Nonlinear effects are more pronounced for $\Delta_{v,r}$ than for Δ_v. The likely reason for this is that nonlinearity also leads to a non-sinusoidal response and this is only reflected for $\Delta_{v,r}$. From Table G.1 we see that nonlinear effects can be of importance even for wave height of 50% of the TRW wave height.

From Table 7.4 we see that the horizontal displacement and moment $M_{b,v}$ are biggest for TRW B as its wave period is closest to the natural periods, see Table 7.4. The maximum moment is 33% of the M_{el}.

Δ_h of the end point show good correspondence with the hand-calculations of Table 4.6: $\frac{\Delta_h}{\Delta_{h,hand}}$ varies from 97 to 109%. Again, this is a good indication of correct software implementation of the linear analysis.

7.2.2 Parallel cylinder

For a parallel cylinder (cylinder axis is parallel to the wave direction, see Figure 7.3) we focus on pitch angle θ, bending moment $M_{b,h}$ (b stands for bending) about the perpendicular horizontal axis at the midpoint, and vertical deflection of the mid- and endpoint. There is no horizontal response as there are no horizontal forces. Likewise, moments about the vertical axis and horizontal parallel axis (i.e. torsion) are zero. In Table 7.5 maximum values for pitch angle θ, moment $M_{b,h}$, vertical deflection Δ_v, and relative vertical deflection $\Delta_{v,r}$ of the midpoint of the cylinder are presented for the linear system. As for Table 7.2 $\frac{\Delta_v}{\zeta_a}$, $\frac{\Delta_{v,r}}{\Delta_{full}}$, and H_{full} are also included. In Table 7.6 the same results are shown for an end

TRW	Δ_v [m]	$\frac{\Delta_v}{\zeta_a}$ [-]	$\Delta_{v,r}$ [m]	$\frac{\Delta_{v,r}}{\Delta_{full}}$ [-]	H_{full} [m]	$M_{b,h}$ [kNm]	θ [°]
B	0.02	3%	0.51	102%	1.0	37	0.5
C	0.17	17%	1.16	232%	0.9	458	1.5
D	0.67	45%	0.87	174%	1.7	466	5.2
H_{max}	2.22	78%	0.91	181%	3.1	421	8.1

Table 7.5: Mid point of parallel cylinder. Linear analyses.

TRW	Δ_v [m]	$\frac{\Delta_v}{\zeta_a}$ [-]	$\Delta_{v,r}$ [m]	$\frac{\Delta_{v,r}}{\Delta_{full}}$ [-]	H_{full} [m]
B	0.20	41%	0.67	134%	0.7
C	0.64	64%	1.49	298%	0.7
D	2.34	156%	2.16	336%	0.7
H_{max}	4.03	141%	2.35	26%	1.2

Table 7.6: End point of parallel cylinder. Linear analyses.

point, except for the moment (which is zero) and pitch angle (which is the same as for the midpoint).

The results from the nonlinear analyses are presented in Table 7.8 and G.2 for the midpoint and Table 7.9 and G.3 for the endpoint. The presentation of the results follows the lines described for Table 7.3 and G.1 except that $M_{b,h}$ and θ are included for the midpoint. The units used are listed in Table 7.7.

Discussion

From Table 7.5 we see that for the mid point both Δ_v and $\frac{\Delta_v}{\zeta_a}$ increase sharply with TRW. The pitch angle also increases, whereas pitch angle normalized with wave height ($\frac{\theta}{H}$) has its maximum for TRW D. As expected, short wave lengths give small (relative) vertical displacement and pitch angle. The highest values are found for wavelengths around twice the cylinder length (i.e. TRW D and H_{max}). The maximum moment normalized with wave height occurs for TRW C, see Table 7.5. This is probably due to the TRW C wave period

Symbol	H	Δ_v	$\Delta_{v,r}$	$M_{b,h}$	Pitch
Unit	[m]	[m]	[m]	[kNm]	[°]

Table 7.7: Units for the following tables.

$\frac{H}{H_{ref}}$		50%	75%	100%	125%	150%	175%
B	H	0.50	0.75	1.00	1.25	1.40*	
	Δ_v	0.01	0.01	0.02	0.02	0.02	
	$\Delta_{v,r}$	0.26	0.38	0.51	0.63	0.71	
	$M_{b,h}$	18	24	28	33	34	
	Pitch	0.4	0.6	0.9	1.0	1.0	
C	H	1.00	1.50	2.00	2.50	3.00	3.50
	Δ_v	0.04	0.09	0.11	0.18	0.20	0.22
	$\Delta_{v,r}$	0.56	0.79	1.04	1.29	1.52	1.74
	$M_{b,h}$	178	177	190	207	214	215
	Pitch	2.9	3.2	3.4	3.4	1.0	4.6
D	H	1.50	2.25	3.00	3.75	4.5	5.25
	Δ_v	0.45	0.82	1.01	1.10	1.00	0.90
	$\Delta_{v,r}$	0.36	0.68	0.87	1.09	1.31	1.52
	$M_{b,h}$	139	148	141	121	114	120
	Pitch	4.2	5.5	6.6	7.1	8.4	8.8
H_{max}	H	2.85	4.28	5.70	7.13	8.55	9.98
	Δ_v	1.26	1.63	1.49	1.45	1.44	1.43
	$\Delta_{v,r}$	0.64	1.75	2.84	3.69	4.49	5.26
	$M_{b,h}$	120	109	112	114	114	116
	Pitch	5.5	5.8	7.0	7.3	7.5	7.7

Table 7.8: Parallel cylinder. Nonlinear analyses. Mid point

$\frac{H}{H_{ref}}$		50%	75%	100%	125%	150%	175%
B	H	0.50	0.75	1.0	1.25	1.4*	
	Δ_v	0.10	0.16	0.22	0.26	0.26	
	$\Delta_{v,r}$	0.34	0.52	0.72	0.88	0.95	
C	H	1.00	1.50	2.00	2.50	3.00	3.50
	Δ_v	0.38	0.60	0.71	0.77	0.78	0.77
	$\Delta_{v,r}$	0.84	1.35	1.68	1.94	2.15	2.37
D	H	1.50	2.25	3.00	3.75	4.50	5.25
	Δ_v	1.29	1.77	1.86	1.95	2.13	2.21
	$\Delta_{v,r}$	1.28	2.36	2.90	3.36	3.96	4.49
H_{max}	H	2.85	4.28	5.70	7.13	8.55	9.98
	Δ_v	2.05	2.22	2.36	2.43	2.48	2.51
	$\Delta_{v,r}$	1.68	2.77	3.85	4.73	5.54	6.34

Table 7.9: Parallel cylinder. Nonlinear analyses. End point

being closer to the natural periods in bending than TRW D and H_{max}.

For the nonlinear analysis we see the same pattern as for the perpendicular cylinder: the response levels off around a wave height close to the respective TRW wave heights. TRW C has the highest maximum moment of approximately $215\,kNm$, i.e. $7\% \cdot M_{el}$, whereas TRW D has the highest pitch angle of approximately 8°. The maximum pitch angle is so small that nonlinearities due to rotations are expected to be of minor importance (cp. Section 5.2.1).

7.3 Sensitivity to time step and element length

For the single cylinder, nonlinear analysis can be performed in real time on the PC used in the present work, whereas the linear analysis can be performed approximately three times faster than real time. Thus, the chosen time step and element length do not cause inconvenient analysis durations for the parameter study. However, for the BCS the nonlinear analysis speed is decreased to approximately a sixth of the speed for the single cylinder, and it is of practical interest to consider increasing the time step and/or increasing the element length to reduce the computation time.

From a theoretical point of view it is also of interest to investigate the sensitivity of both time step and element length. The results should have converged with respect to both time step and element length to be reliable. The chosen method for time integration — Newmark-β, see Section 5.2.5 — is unconditional stable (i.e. for a linear analysis increased

time step can only cause inaccuracy and not instability[15]).

To investigate the sensitivity of the time step we will look at the effect of increasing the time step ten times (from $0.015\,s$ to $0.15\,s$) for the midpoint of a parallel member. The TRW B wave period of $2.5\,s$ is chosen, and will be combined with two wave heights: $H = 1.0\,m$ and $H = 1.4\,m$, i.e. the TRW B and maximum wave heights, respectively. For $H = 1.0\,m$ the difference between using $\Delta t = 0.015\,s$ and $\Delta t = 0.15\,s$ is less than 1%. Likewise, the differences for the linear anlyses for $H = 1.4\,m$ are less than 1%. For the nonlinear analyses the differences are less than 3% except for the torsional moment which is 16% bigger for $\Delta t = 0.15\,s$ than for $\Delta t = 0.015\,s$. It is also observed that the plot of the torsional moment is clearly more jagged for the greater time step. Based on the above, a nonlinear analysis with a time step of five times the original time step is run for $H = 1.4\,m$, i.e. $\Delta t = 0.075\,s$. This yields negligible difference also for the moments (less than 3%).

To investigate the sensitivity of the element length we consider the effect of increasing the element length from $1\,m$ to $3\,m$. A time step of $0.015\,s$, the TRW B wave period of $2.5\,s$ together with the maximum wave height of $H = 1.4\,m$ are used for both cases. For the linear analyses the differences are negligible except for torsional moment and pitch angle where the longer element length yields 9% higher and 14% smaller results than for the reference length, respectively. For the nonlinear analyses the longer element yields approximately 15% bigger moments about both horizontal axes (the other differences are negligible). Based on these results an element length of $1.5\,m$ is tested. The maximum difference is 3%. Finally, an analysis using $\Delta t = 0.075\,s$ and $L_{elt} = 1.5\,m$ also yields a maximum difference of 3%. Thus, we choose to perform the regular wave BCS analyses with $\Delta t = 0.075\,s$ and $L_{elt} = 1.5\,m$. This combination gives approximately real time speed for the nonlinear analysis.

7.4 Sensitivity to wave period in a linear analysis

As discussed in Section 4.1 (static analysis), the response of the BCS exposed to a perpendicular regular wave is very sensitive to the wave period. We will continue the discussion by looking at linear analysis results for regular waves. However, first we will identify the points of expected min/max values. In-phase loading occurs when the ratio of the member length and the wave length is close to an integer, whereas out-of-phase loading occurs when the ratio is half-way between two integers. The wave lengths and wave periods of the expected max/min points (in-phase/out-of-phase) are given in Table 7.10.

For vertical loading, in-phase loading yield maximum moments at the midpoints for all members, see Section 4.1 and Figure B.2. On the other hand, out-of-phase loading also results in maximum moments at the midpoints for the perpendicular members, but at the quarter points for the parallel members, see Figure B.3. In Figure 7.4, the maximum linear bending moment about the horizontal axis $M_{b,h}$ (i.e. the amplitude) for the midpoints of the perpendicular and parallel members are shown as a function of wave period. The ratios

[15]For a nonlinear analysis stability is not guaranteed.

$\frac{30\,m}{\lambda}$	[-]	1	2	3	4	5	6	7	8	9	10
λ	[m]	30.0	15.0	10.0	7.5	6.0	5.0	4.3	3.8	3.3	3.0
T	[s]	4.4	3.1	2.5	2.2	2.0	1.8	1.7	1.5	1.5	1.4
$\frac{30\,m}{\lambda}$	[-]	0.5	1.5	2.5	3.5	4.5	5.5	6.5	7.5	8.5	9.5
λ	[m]	60.0	20.0	12.0	8.6	6.7	5.5	4.6	4.0	3.5	3.2
T	[s]	6.2	3.6	2.8	2.3	2.1	1.9	1.7	1.6	1.5	1.4

Table 7.10: Wave lengths and wave periods for in-phase (upper half) and out-of-phase (lower half) loading

of maximum and minimum values are $\frac{280\,MPa}{97\,MPa} = 2.9$ and $\frac{483\,MPa}{15\,MPa} = 32.2$ for perpendicular and parallel members, respectively.

Discussion

Comparing Figure 7.4 to Table 7.10, we see that the max/min points of the figure correspond very closely to the predicted max/min points of the tables. The max points are approximately 10% higher than the static maxima of Table 4.1, and this is probably due to dynamic amplification. The minimum values for the perpendicular cylinder are also very close to the static values. The minimum points of the parallel cylinder are even smaller than the static results. This is because the static results apply to the end points of the parallel members.

As the wave length approaches $30\,m$ (i.e. a wave period of $4.4\,s$) and beyond, the loading on the parallel members becomes more uniform and thus more important. The pattern for $T < 4\,s$ is broken. In particular for the parallel members themselves the superposition of loading results in a maximum moment almost twice the previous maxima. When the wave length continues to increase the loading of the whole BCS becomes more uniform and the moments decrease. For very long waves the moments will be zero.

In Section 9.1.1, nonlinear analyses are compared to linear results for regular waves.

7.5 Sensitivity to damping

As noted previously (see Section 3.3.6), the damping levels are considered to be very uncertain. It is therefore of interest to investigate the effect of increased and decreased levels of damping as compared with the levels assumed. With reference to the linear TRW B analysis, see Table 7.13, we double and halve both the vertical and the horizontal linear damping levels, see Table 7.11. The total vertical (heave) and horizontal (sway) damping levels of TRW B are $B_v = 2.0\,kNs/m^2$ and $B_h = 1.2\,kNs/m^2$, respectively, see Table 5.1. This is case # 1 in Table 7.11. The maximum vertical response Δ_v, the maximum horizontal response Δ_h, the maximum relative vertical response $\Delta_{v,r}$, the maximum bending

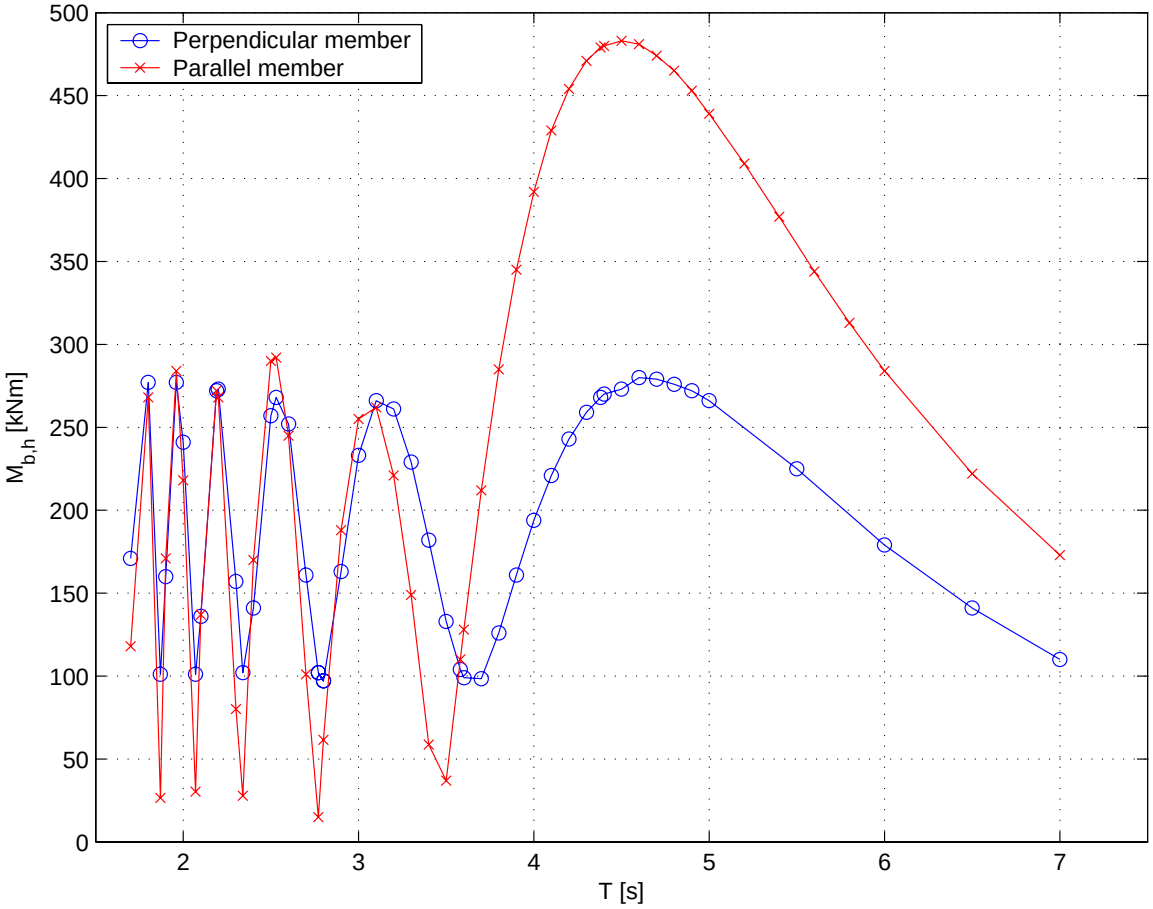

Figure 7.4: The amplitude of bending moments about the horizontal axis $M_{b,h}$ for mid points of the perpendicular and parallel members as a function of wave period T. Wave height: $H = 1\,m$. Linear analysis.

Case	B_v $[\frac{kNs}{m^2}]$	B_h $[\frac{kNs}{m^2}]$	Δ_v [m]	Δ_h [m]	$\Delta_{v,r}$ [m]	$M_{b,h}$ [kNm]	$M_{b,v}$ [kNm]
# 1	2.0	1.2	0.37	0.88	0.34	260	291
# 2	1.0	1.2	0.45	0.88	0.22	262	291
# 3	4.0	1.2	0.24	0.88	0.43	256	291
# 4	2.0	0.6	0.37	1.6	0.34	257	565
# 5	2.0	2.4	0.37	0.45	0.34	257	123

Table 7.11: Sensitivity of linear damping. Linear analysis. Midpoint of perpendicular BCS member.

moment about the horizontal axis $M_{b,h}$, and finally the maximum bending moment about the vertical axis $M_{b,v}$ are included in Table 7.11. The results are for the midpoint of the perpendicular cylinder.

Discussion

We see from Table 7.11 that the vertical damping has a strong influence on the vertical displacements (Δ_v and $\Delta_{v,r}$), but not on the bending moment about the horizontal axis $M_{b,h}$. The horizontal damping has a strong influence on both the horizontal displacement Δ_h *and* the bending moment about the vertical axis $M_{b,v}$. Thus, the level of damping can influence the moment values both directly (as was the case for vertical damping) and indirectly through the translational response. For a nonlinear analysis, the translational response will change the hydrodynamic load effects. Results from nonlinear analyses with double and half the vertical damping are shown in Table 7.12. $M_{b,h}$ is influenced, but not significantly. Further, both increasing and decreasing the damping reduces the moment, which shows that it is harder to predict the effect of changing parameters in a nonlinear analysis.

The difference of influence on the moment is assumed to be due to the difference in the horizontal vs. the vertical spring supports. Whereas the horizontal springs are concentrated at the corners, the vertical springs are distributed.

7.6 Perpendicular wave direction

For waves acting perpendicular to the BCS we will collect the same results as for the single cylinder. Additionally, for the member perpendicular to the wave direction, moment values will be collected. The linear results for the perpendicular and parallel members of the BCS are presented in Table 7.13 and 7.14, respectively. The nonlinear analysis results

Case	B_v $[\frac{kNs}{m^2}]$	B_h $[\frac{kNs}{m^2}]$	Δ_v [m]	$\Delta_{v,r}$ [m]	$M_{b,h}$ [kNm]
# 1	2.0	1.2	0.39	0.44	220
# 2	1.0	1.2	0.59	0.40	205
# 3	4.0	1.2	0.22	0.47	215

Table 7.12: Sensitivity of linear damping. Nonlinear analysis. Midpoint of perpendicular BCS member.

TRW	Δ_v	Δ_h	$\Delta_{v,r}$	$M_{b,h}$	$M_{b,v}$	M_{tot}	$\frac{\Delta_v}{\zeta_a}$	$\frac{\Delta_{v,r}}{\Delta_{full}}$	H_{full}
B	0.37	0.88	0.34	260	291	390	74	68	1.5
C	0.73	0.29	0.47	392	149	394	73	94	2.1
D	1.58	0.14	1.09	732	143	745	105	218	1.4
H_{max}	3.33	0.07	1.47	732	188	740	117	294	1.9

Table 7.13: Midpoint of perpendicular BCS member. Linear analyses. Maximum values for the TRW.

are presented in Table 7.15 and G.4 for the perpendicular member and in Table 7.16 and G.5 for the parallel member.

Discussion

From the linear results (see Table 7.13 and 7.14) we see that the wave length is decisive for the importance of heave vs. pitch response. Inspecting the θ and $\frac{\Delta_v}{\zeta_a}$ parameters of the parallel member (see Table 7.14) we can conclude that TRW B and C give rise to much heave and little pitch. TRW D gives rise to little heave and much pitch, whereas

TRW	Δ_v	Δ_h	$\Delta_{v,r}$	M_t	$M_{b,h}$	$M_{b,v}$	M_{tot}	θ	$\frac{\Delta_v}{\zeta_a}$	$\frac{\Delta_{v,r}}{\Delta_{full}}$
B	0.32	0.85	0.75	23	292	27	293	0.2	63	151
C	0.51	0.28	1.48	89	795	52	797	1.4	51	296
D	0.03	0.13	1.51	56	1180	60	1180	6.2	2	302
H_{max}	1.55	0.07	1.39	31	1150	96	1150	11.8	54	278

Table 7.14: Midpoint of parallel BCS member. Linear analyses. Maximum values for the TRW.

TRW	$\frac{H}{H_{ref}}$	25%	50%	75%	100%	125%	150%	175%
B	H	0.25	0.50	0.75	1.00	1.25	1.40*	
	Δ_v	0.09	0.19	0.29	0.39	0.44	0.45	
	$\Delta_{v,r}$	0.09	0.18	0.29	0.44	0.63	0.74	
	$M_{b,h}$	64	125	179	220	249	259	
	M_{tot}	96	190	280	362	429	462	
C	H	0.50	1.00	1.50	2.00	2.50	3.00	3.50
	Δ_v	0.19	0.40	0.63	0.81	0.83	0.82	0.81
	$\Delta_{v,r}$	0.12	0.26	0.44	0.76	1.22	1.58	1.89
	$M_{b,h}$	94	168	231	246	273	294	313
	M_{tot}	95	172	241	256	309	330	349
D	H	0.75	1.50	2.25	3.00	3.75	4.50	5.25
	Δ_v	0.40	0.84	1.26	1.45	1.57	1.63	1.63
	$\Delta_{v,r}$	0.28	0.64	1.52	2.15	2.66	3.22	3.67
	$M_{b,h}$	172	239	284	337	352	461	478
	M_{tot}	176	246	290	350	375	491	522
H_{max}	H	1.43	2.85	4.28	5.70	7.13	8.55	9.98
	Δ_v	0.84	1.70	1.92	2.00	2.05	2.09	2.13
	$\Delta_{v,r}$	0.39	1.32	2.40	3.38	4.23	5.03	5.81
	$M_{b,h}$	167	248	304	284	308	330	351
	M_{tot}	169	248	308	302	341	381	421

Table 7.15: BCS, midpoint of perpendicular member. Nonlinear analyses. H_{ref} is the wave height of the corresponding TRW (first column), i.e. $1.0\,m$, $2.0\,m$, $3.0\,m$, and $5.7\,m$, see Table 3.3.

TRW	$\frac{H}{H_{ref}}$	25%	50%	75%	100%	125%	150%	175%
B	H	0.25	0.50	0.75	1.00	1.25	1.40*	
	Δ_v	0.08	0.16	0.27	0.37	0.43	0.44	
	$\Delta_{v,r}$	0.19	0.38	0.57	0.74	0.82	0.83	
	M_t	5	10	13	14	18	22	
	$M_{b,h}$	72	140	200	248	281	285	
	M_{tot}	72	141	201	249	283	288	
	θ	0.1	0.1	0.2	0.3	0.3	0.3	
C	H	0.50	1.00	1.50	2.00	2.50	3.00	3.50
	Δ_v	0.13	0.32	0.54	0.64	0.65	0.65	0.65
	$\Delta_{v,r}$	0.37	0.79	1.21	1.45	1.55	1.66	1.81
	M_t	21	34	36	41	48	53	55
	$M_{b,h}$	187	284	347	412	446	458	463
	M_{tot}	187	285	348	414	450	464	471
	θ	0.4	0.8	1.4	1.7	1.6	1.5	1.4
D	H	0.75	1.50	2.25	3.00	3.75	4.50	5.25
	Δ_v	0.01	0.06	0.18	0.34	0.46	0.26	0.22
	$\Delta_{v,r}$	0.38	0.77	0.99	1.39	1.91	2.46	2.84
	M_t	14	28	40	39	36	34	38
	$M_{b,h}$	275	368	361	410	409	584	638
	M_{tot}	276	368	363	410	410	586	640
	θ	1.5	3.2	4.9	6.0	7.0	7.3	7.2
H_{max}	H	1.43	2.85	4.28	5.70	7.13	8.55	9.98
	Δ_v	0.39	0.92	1.20	1.00	0.95	0.93	0.92
	$\Delta_{v,r}$	0.35	0.70	1.76	2.79	3.64	4.43	5.19
	M_t	8	20	25	33	32	29	31
	$M_{b,h}$	263	310	347	337	329	344	366
	M_{tot}	264	310	350	344	342	364	393
	θ	3.0	5.3	6.3	7.2	7.4	7.5	7.6

Table 7.16: BCS, midpoint of parallel member. Nonlinear analyses. H_{ref} is the wave height of the corresponding TRW (first column), i.e. $1.0\,m$, $2.0\,m$, $3.0\,m$, and $5.7\,m$, see Table 3.3.

TRW H_{max} results in much heave and much pitch. There is no clear connection between the relative importance of heave vs. pitch and the magnitudes of the bending moments.

The maximum pitch angle of 11.8° is slightly greater than for the single cylinder (see Section 7.2.2), but it is still so small that nonlinearities due to rotations are expected to be of minor importance.

The perpendicular members have no torsion whereas its two bending components are both of importance. From Table 7.13 we see that bending about the vertical axis $M_{b,v}$ show a decreasing trend, whereas bending about the horizontal axis $M_{b,h}$, and the total moment M_{tot} show an increasing trend with TRW. The maximum magnitudes are $291\,kNm$, $732\,kNm$, and $745\,kNm$, respectively.

For the parallel member, bending about the horizontal axis $M_{b,h}$ is the dominating moment component. From Table 7.14 we see that its maximum value of $1180\,kNm$ is found for TRW D (i.e. $41\% \cdot M_{el}$). The maximum torsion M_t and bending about the vertical axis $M_{b,v}$ are $89\,kNm$ (TRW C) and $96\,kNm$ (TRW H_{max}), respectively.

As for the single cylinder, the nonlinear analyses of the BCS (see Table 7.15 and 7.16) show that the responses reach finite limits when parts of the structure are fully submerged/dry. Full submergence is first observed over a large interval: between 25% and 125% of the TRW wave height. The effect of submergence is not as predictable as for the single cylinder. The levels can be stable, reach a maximum and (slowly) decrease, or have a slow rate of increase. In Figure 7.5 the linear and nonlinear bending moments about the horizontal axis $M_{b,h}$ are shown for the TRW C wave period. Both the perpendicular and the parallel members are included. As in Figure 7.2 the response magnitudes "saturate" at approximately the TRW waveheight (i.e. $2\,m$). We see that the linear moment for the parallel cylinder is about twice the linear moment for the perpendicular moment. The difference for the nonlinear case is smaller — the moment at the midpont of the parallel cylinder is approximately 50% higher.

The most important nonlinear moment component — bending about the horizontal axis — has maximum nonlinear magnitudes of $468\,kNm$ for the perpendicular member and $640\,kNm$ for the parallel member (both for TRW D). The maximum values are highest for the parallel member for all TRW.

7.7 Oblique wave direction

Oblique waves are likely to introduce different loading patterns and will therefore be investigated separately in this section. It is assumed that the effect of oblique waves will reach its maximum for waves with a 45° direction. Thus, this is the only direction considered here. In the subsequent chapters we will only consider perpendicular waves, and therefore the presented results for oblique waves will be less elaborate than for perpendicular waves in the previous section. Only TRW D will be considered, and only for the TRW wave height. Further, only the moment components are investigated.

As all members are expected to experience similar response histories (due to symmetry) only one member will be considered. However, we will look at five points from the corner

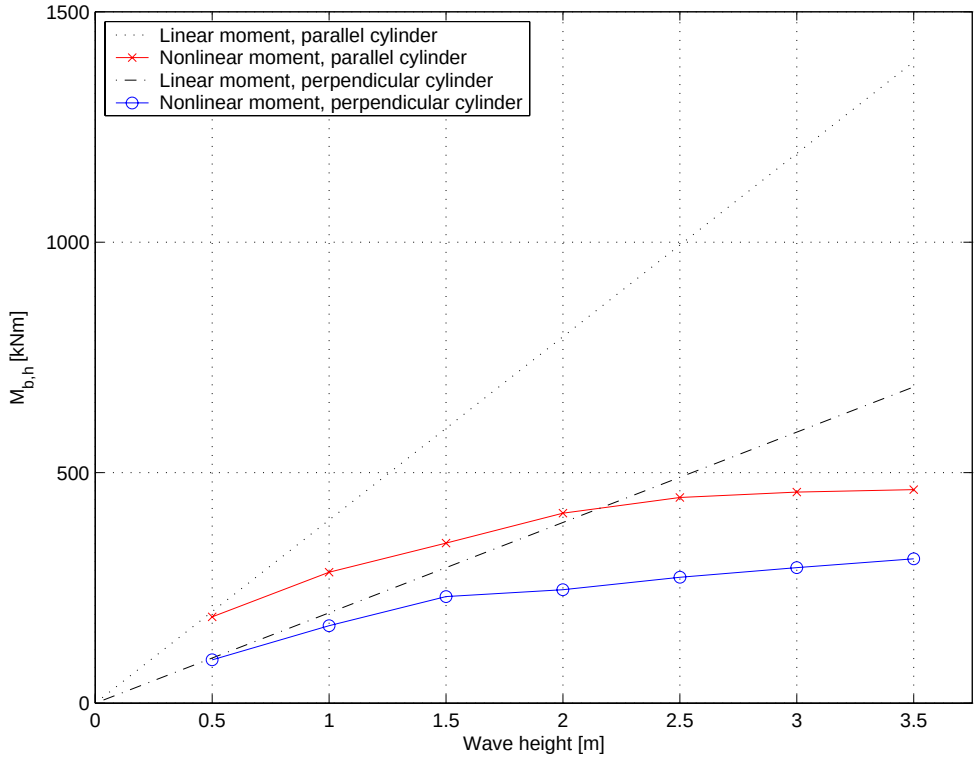

Figure 7.5: Bending moment about the horizontal axis $M_{b,h}$ for the midpoint of the perpendicular and the parallel cylinder. TRW C wave period: $T = 4.0\,s$.

Dist	0%	5%	10%	25%	50%
$M_{b,h,lin}$ [kNm]	1020	1010	971	734	386
$M_{b,h,nlin}$ [kNm]	382	378	366	279	143

Table 7.17: BCS, TRW D, and 45°-waves. Bending about the horizontal axis at different distances from the corner. Linear and nonlinear analysis.

to the midpoint. The distances from the corner are the following fractions of the member length: 0%, 5%,10%, 25%, 50%. The maximum torsional moment is the same for all points — for both linear and nonlinear analysis. The respective magnitudes are: $1020\,kNm$ for linear analysis and $382\,kNm$ for nonlinear analysis. The bending about the vertical axis is linear and has a maximum value of $71\,kNm$ observed at the corner. The bending about the horizontal axis $M_{b,h}$ varies along the length of the member. The variation is shown in Table 7.17.

Discussion

45° oblique waves will increase the maximum level of torsion considerably for the whole BCS, whereas the bending maximum moments will be smaller. As opposed to perpendicular waves the corners have the highest total moment. The maximum torsion is the same for the whole length of the member whereas the bending moment about the horizontal axis will have a maximum at the corners and a minimum at the midpoint. The magnitudes at the corners are the same for the two moment components of importance. The bending about the vertical axis is small for the whole length of the member.

Chapter 8

FATIGUE ANALYSIS PROCEDURE

The fatigue phenomenon is characterized by the growth of cracks exposed to cyclic stresses, which over time can lead to structural failure. The definition of fatigue as stated by ASTM (2000), follows:

> The process of progressive localized permanent structural change occurring in a material subjected to conditions that produce fluctuating stresses and strains at some point or points and that may culminate in cracks or complete fracture after a sufficient number of fluctuations.

Fatigue analysis and design of marine steel structures has been performed for many years and is an area of continuing research. For references on fatigue design of marine structures see e.g. (Almar-Naess, 1999), (Berge, 2004a), (Berge, 2004b), (Etube, 2001), (Moan, 2001). For references on metal fatigue in general see e.g. (Bannantine, 1989), (Larsen, 1990), (Schijve, 2001), (Stephens, 2001), and (Wirsching et al., 2006).

Norwegian offshore petroleum activities have been known to be particularly vulnerable to fatigue due to the severe winter storms of the North Sea (Almar-Naess, 1999). Despite this knowledge the disastrous collapse of the Alexander Kielland oil platform in the North Sea in 1981 is believed to have been caused by fatigue failure, see e.g. (Accident commision, 1981) and (Moan et al., 1981).

Also for floating fish farms made of steel, fatigue is believed to be a serious problem. Ormberg (1991) found very low fatigue life when performing a simplified fatigue analysis for a steel fish farm that collapsed in 1989. Ormberg notes that his findings were in line with the results from inspection and metallurgical analysis, but also suggests that a stochastic wave approach would give better estimates of fatigue life (i.e. less conservative).[16] 15 years later, in an overview report of the research status in aquaculture from the Norwegian Research Council, Lien et al. (2006) concluded that fatigue problems are probably the reason behind many structural failures of steel plants.

[16] A stochastic wave approach is a part of the methodology which is suggested and implemented in this thesis.

It is not surprising that a floating fish farm is vulnerable to fatigue. Marine structures in general are exposed to the perpetual action of the waves. With a wave climate of shorter wave lengths and wave periods, the typical number of stress fluctuations for fish farms can be even larger than for traditional open ocean marine structures, thus increasing the number of stress fluctuations (though not necessarily the stress range level). As a contrary effect, expected longer periods of calm weather in sheltered waters will contribute to fewer stress fluctuations than for open ocean conditions. Assuming a constant wave period of $2.5\,s$ (as for TRW B) during one year yields $1.26 \cdot 10^7$ wave fluctuations (and during 20 years yields $2.52 \cdot 10^8$ wave fluctuations). As the nonlinear response is generally not sinusoidal, the frequency of stress fluctuations can be even higher than this (i.e. possibly more than one maximum/minimum per wave period).

Fatigue cracks of a steel structure normally originates at welds due to weaknesses such as notches and initial defects. It is typically expected that (micro) cracks always exist in a (welded) steel structure and that cracks *will* grow. Due to the high uncertainties (still) involved in fatigue design, a numerical approach is often (and should be according to (Standard Norge, 2004)) complemented with inspection and maintenance requirements.

Fatigue design of marine structures can be described as first identifying the critical details of the structure and then ensuring that the critical details will survive the expected stress history (yielding a stress range distribution) throughout the structure's planned lifetime. It is *not* our goal to present a fatigue design procedure that is fundamentally new, but rather to suggest how important aspects of state-of-the-art fatigue design can be introduced for floating fish cages in steel, show an example of such an analysis, and demonstrate that with a customized software tool the analysis procedure is realistic on a modern PC with respect to computation time.

This chapter will be used to first give an outline of a fatigue design methodology of particular relevance for this thesis. Then, we will describe how the methodology is applied for the BCS in the parameter study. The parameter study itself is presented in Chapter 9.

8.1 Loading

8.1.1 The stress range history

The loading in fatigue design is the stress history over the lifetime of the critical detail — often expressed in terms of an (approximated) standard long-term distribution of stress ranges (e.g. the Weibull distribution). However, the stress history in combination with a cycle counting algorithm can be used directly, see Section 8.4.1. The latter approach is the more accurate as it forms the basis for the standardized long-term distribution. In (Moan, 2001) three alternatives for establishing load histories are listed with increasing accuracy and complexity:

- Assume that stress ranges follow a two-parameter Weibull distribution (see Section 8.3.3).

- Frequency Domain Analysis (FDA) for each sea state to determine response variance and assume narrow-band response, implying Rayleigh distribution of stress ranges.
- Time Domain Analysis (TDA) combined with rainflow counting of cycles for a representative set of sea states that are found to contribute most to the fatigue damage.

Further, Moan (2001) notes that stochastic approaches (i.e. irregular waves) should be applied to dynamically sensitive structures, and finally:

> More complete time domain approaches may especially be necessary in case of strong nonlinearities (e.g. associated with local splash zone behavior), at least to calibrate simpler methods.

For a linear analysis, the FDA and the TDA give the same results (if the response is narrow banded, see above). Typically, the FDA is more convenient. However, in the present thesis such analysis is not included because a TDA was used for the nonlinear case and hence the stress range distribution is investigated explicitly. The main advantage of including FDA in this thesis would have been as a check of the linear TDA results.

8.1.2 Irregular waves

Although we will perform simplified fatigue analyses based on regular waves (see Section 9.1), the emphasis in this chapter is on irregular waves. Irregular waves based on linear theory is commonly used as a more realistic description of ocean waves. The use of irregular waves has been described by many authors, see e.g. (Faltinsen, 1990), (Goda, 2000), (Hudspeth, 2006), (Myrhaug, 2003), and (Ochi, 2005). Simulation of linear irregular waves is typically based on a wave spectrum together with a scatter diagram. The former gives a statistical description of each seastate, and the latter gives the relative occurrence of seastates. The use of a scatter diagram in the fatigue design criteria is described in Section 8.3.2, and the use of irregular waves for fatigue analysis of the BCS is described in Section 8.4.1.

8.1.3 The relevant stress component

The location of the stresses of interest in a fatigue analysis is that of the identified critical detail. However, the stress situations encountered are often so complex that it is not obvious which stress component and direction that should be used. Most often the maximum principal stress range is used as a basis for both the amplitude and the direction (Almar-Naess, 1999).

When using an SN approach (see the next section), it is of importance which factors that shall be taken into consideration when calculating the stress range. In general, the SN-curves include the effect of local stress concentration due to the joints (i.e. welds) themselves and the weld profile. Other effects, such as local stress concentration and fabrication misalignment, must be considered explicitly, see (Almar-Naess, 1999), (DNV, 2005). This is typically done by finding a stress concentration factor (SCF).

8.2 Resistance

Two methods are prevalent for deciding and describing the resistance of a critical detail:

- SN approach
- Fracture mechanics (see e.g. (Almar-Naess, 1999))

In this thesis only the SN approach will be considered. This is the simpler approach and is most common in use, see (Moan, 2001), (Almar-Naess, 1999), (DNV, 2005).

SN approach

In the SN approach fatigue tests of structural details are used to define relationships between the number of fluctuations N that a specimen can endure at a stress level S, and this relationship is called an SN curve. The SN curve is assumed to be (bi-)linear in a log-log plot, typically with $\log S$ ($S = \Delta\sigma$) on the vertical axis and $\log N$ on the horizontal. In DNV-RP-C203 (DNV, 2005) the basic design SN curve is given as:

$$\log N = \log \bar{a} - m \log \Delta\sigma \tag{8.1}$$

N = predicted number of cycles to failure for stress range $\Delta\sigma$
$\Delta\sigma$ = stress range
m = negative inverse slope of SN-curve
$\log \bar{a}$ = intercept of log N-axis for SN-curve

Equation 8.1 can also be expressed on the following two forms:

$$N \cdot (\Delta\sigma)^m = \bar{a} \tag{8.2}$$

$$\log \Delta\sigma = -\frac{1}{m} \log N + \frac{1}{m} \log \bar{a} \tag{8.3}$$

To classify different structural details, families of SN curves are defined, see e.g. Table 8.6. It is common that an SN curve is bilinear with a higher m-factor for the high cycle region. Typically, the family of SN curves have the transition point at the same number of cycles (e.g. $N = 10^7$) and thus at different levels of stress range. SN curves can even be horizontal beyond the transition point, i.e. stress ranges below the corresponding level do not contribute to the fatigue damage.

8.3 Design criteria

8.3.1 Miner-Palmgren law

The design criteria for fatigue design using SN curves is based on the assumption of linear cumulative damage, known as the Miner-Palmgren law (or Palmgren-Miner), see (Palmgren, 1924) and (Miner, 1945). The fatigue damage D is then typically expressed as (see (DNV, 2005)):

$$D = \sum_{i=1}^{k} \frac{n_i}{N_i} = \frac{1}{\bar{a}} \sum_{i=1}^{k} n_i \cdot (\Delta\sigma_i)^m \leq \eta \tag{8.4}$$

D = accumulated fatigue damage

$\bar{a}$ = intercept of the design SN curve with the log N axis, see Table 8.6

m = negative inverse slope of the SN curve, see Table 8.6

k = number of stress blocks

n_i = number of stress cycles in stress block i

N_i = number of cycles to failure at constant stress range $\Delta\sigma_i$

η = usage factor

= 1/ Design Fatigue Factor (DFF) from OS-C101 Section 6

DFF=1, 2, or 3.

From Equation 8.4 we see that the damage for one cycle $D_{N=1}$ with stress range $\Delta\sigma$ is:

$$D_{N=1} = \frac{(\Delta\sigma)^m}{\bar{a}} \tag{8.5}$$

Moan (2001) writes that a usage factor in the range of 0.1 to 1.0 is typically used together with the Miner-Palmgren rule. The section discussing the design fatigue factor in DNV-OS-C101 (DNV, 2004) is quoted in Appendix C, and according to this the floater should be given a DFF of 2 or 3, i.e. $\eta = \frac{1}{2}$ or $\eta = \frac{1}{3}$, respectively. NS 3472 (Standard Norge, 2001) specifies that $\eta = 1.0$ is the typical value to be used, but that other values can be specified in relevant codes and rules.

The fatigue life L is the ratio of the duration for which the stress ranges are referred to (typically the design fatigue life L_0) and the corresponding fatigue damage D_{L_0}:

$$L = \frac{L_0}{D_{L_0}} \tag{8.6}$$

8.3.2 Fatigue analysis using a scatter diagram

For a linear structural system in a regular wave (with a given wave period T and wave height H), the stress range $\Delta\sigma$ will be constant and there will be one stress range per wave

period. The number of seconds per year t_{1y} and cycles per year n_{1y} are:

$$t_{1y} = 365\,d/y \cdot 24\,h/d \cdot 3600\,s/h = 3.1536 \cdot 10^7\,s \tag{8.7}$$

$$n_{1y} = \frac{t_{1y}}{T} \tag{8.8}$$

The damage for 1 year $D_{sc,1y}$ and the corresponding fatigue life L_{sc} is then:

$$D_{sc,1y} = \frac{n_{1y}}{N} = \frac{n_{1y}}{10^{\log \bar{a} - m \log \Delta\sigma}} \tag{8.9}$$

$$L_{sc} = \frac{1y \cdot \eta}{D_{sc,1y}} = \frac{N \cdot \eta}{n_{1y}} \cdot 1y = \frac{10^{\log \bar{a} - m \log \Delta\sigma} \cdot T \cdot \eta}{t_{1y}} \cdot 1y \tag{8.10}$$

For a nonlinear system, the response will typically be periodic with a period equal to the wave period (as was observed for all nonlinear analyses in Chapter 7), but there can be more than one stress cycle over a wave period, and the damage $D_{N=1}$ must be found for each stress range.

For irregular waves the stress fluctuation will be non-periodic — for a nonlinear as well as for a linear system. Fatigue analysis based on irregular waves typically uses a sea elevation spectrum in conjunction with a scatter diagram describing the relative occurrence of seastates, see Section 8.1.2.

A stress history is found by a time domain analysis for one seastate *sc* (see Table 8.5 for the BCS scatter diagram) of duration t. The irregular stress history is transformed to a stress range distribution using a cycle-counting technique — e.g. rainflow counting, see p. 122 — to allow for the use of the Miner-Palmgren rule. The damage $D_{sc,t}$ caused by a stress history from a TDA of seastate *sc* and duration t resulting in $n_{sc,t}$ (cycle counted) stress ranges $\Delta\sigma_i$ can then be found by summing the damage of the individual cycles:

$$D_{sc,t} = \sum_{i=1}^{n_{sc,t}} \frac{(\Delta\sigma_i)^m}{\bar{a}} \tag{8.11}$$

The corresponding fatigue life L_{sc} (assuming only seastate *sc*) is:

$$L_{sc} = \frac{t \cdot \eta}{D_{sc,t}} \tag{8.12}$$

With p_{sc} being the percentage of occurrence of the seastate *sc*, we can now find the damage D_{sc,L_0}caused by seastate *sc* over the design fatigue life L_0:

$$D_{sc,L_0} = \frac{p_{sc} \cdot L_0}{L_{sc}} = p_{sc} \cdot D_{sc,t} \cdot \frac{L_0}{t \cdot \eta} \tag{8.13}$$

The total D_{L_0} damage over the design fatigue life L_0 and the corresponding fatigue life L are then:

$$D_{L_0} = \sum_{sc} D_{sc,L_0} \tag{8.14}$$

$$L = \frac{L_0 \cdot \eta}{D_{L_0}} \tag{8.15}$$

8.3.3 Simplified fatigue analysis

The Weibull distribution has been used to model the long-term distribution of stress ranges of offshore structures as well as the basis for simplified methods. The 2-parameter Weibull probability density function of stress ranges $\Delta\sigma$ can be expressed as:

$$p(\Delta\sigma) = \frac{h}{q} \cdot \left[\frac{\Delta\sigma}{q}\right]^{h-1} \cdot \exp\left[\left(-\frac{\Delta\sigma}{q}\right)^{h}\right] \tag{8.16}$$

where q is the scale parameter and h is the shape parameter. A damage calculation based on application of the Weibull distribution is often used as the basis for a simplified fatigue analysis, see e.g. (Almar-Naess, 1999), (Moan, 2001), (DNV, 2005). The fatigue damage D can then be expressed as:

$$D = \frac{n_0}{\bar{a}} \cdot q^m \cdot \Gamma(1 + \frac{m}{h}) \tag{8.17}$$

where $\bar{a}$ and m are the SN parameters. n_0 is the number of cycles (during the period that is being considered). The scale parameter q can be replaced by the maximum stress range $\Delta\sigma_0$ (i.e. the level expected to be exceeded once for a total of n_0 cycles) by:

$$q = \frac{\Delta\sigma_0}{(\ln n_0)^{1/h}} \tag{8.18}$$

Correspondingly, $\Delta\sigma_0$ can be found as:

$$\Delta\sigma_0 = q \cdot (\ln n_0)^{1/h} \tag{8.19}$$

We then get the following expression for the damage:

$$D = \frac{n_0}{\bar{a}} \cdot \frac{(\Delta\sigma_0)^m}{(\ln n_0)^{m/h}} \cdot \Gamma(1 + \frac{m}{h}) \tag{8.20}$$

Using Equation 8.15 we can then express the fatigue life L as:

$$L = \frac{L_0 \cdot \bar{a} \cdot (\ln n_0)^{m/h} \cdot \eta}{n_0 \cdot \Delta\sigma_0^m \cdot \Gamma(1 + \frac{m}{h})} \tag{8.21}$$

The fatigue damage is very sensitive to the shape parameter h and it should be estimated from TDA procedures, see Figure 9.20 and e.g. (Moan, 2003). The fatigue damage can then be found based on the maximum stress range and the number of cycles for the structure in question. The short- and long-term distribution of stress ranges and the application of the simplified method are investigated in Section 9.8.

The equivalent stress range $\Delta\sigma_{eq}$ is defined as the constant stress range that yields the same fatigue damage as a given stress range distribution. Using Equation 8.4 and 8.20 we get the following expression for $\Delta\sigma_{eq}$:

$$\Delta\sigma_{eq} = \frac{\Delta\sigma_0}{(\ln n_0)^{1/h}} \cdot \left[\Gamma(1+\frac{m}{h})\right]^{\frac{1}{m}} \tag{8.22}$$

8.4 Fatigue design of the BCS

Based on the general outline of fatigue design given in the previous sections, the details of the fatigue design performed for the BCS are given in the present section.

The design working life — and thus the design fatigue life — is set to 20 years. This is consistent with both NS 9415 (Standard Norge, 2003) (minimum 10 years) and NS-EN 1990 (Standard Norge, 2002b) (minimum 15 years), see Appendix C in the present thesis.

8.4.1 Loading

Long-crested uni-directional waves

We assume that the BCS geographical location has a wave climate with a single dominating wave direction and that the BCS has an orientation perpendicular to this direction. Thus, long-crested (i.e. one-dimensional) waves simulated from a wave (elevation) spectrum $S(\omega)$ will be used in the TDA. We assume that this can be realistic for a Norwegian fjord with a principal direction. Thus, it is a reasonable first implementation of irregular waves, although a short-crested (two-dimensional) approach is more general and should be implemented at a later stage.

Wave elevation spectrum: JONSWAP

The (modified) Pierson-Moskowitz spectrum and the JONSWAP spectrum (Hasselmann et al., 1973) are commonly used for fully developed seas and for limited fetch, respectively. As waves in a Norwegian fjord typically will have limited fetch and not be fully developed, the JONSWAP spectrum will be used in this thesis.

The (five parameter) JONSWAP spectrum is given as (see e.g. (Holthuijsen, 2007), (Young, 1999)):

$$S(\omega) = \alpha\frac{g^2}{\omega^5}\exp\left[-\frac{5}{4}\left(\frac{\omega_p}{\omega}\right)^4\right]\gamma^{\exp\left[-\frac{1}{2}\left(\frac{\omega-\omega_p}{\sigma\omega_p}\right)^2\right]} \tag{8.23}$$

$$\sigma = \sigma_a \; for \; \omega \leq \omega_p$$

$$= \sigma_b \; for \; \omega > \omega_p$$

where ω_p and α are scale parameters, and the other three parameters γ, σ_a, and σ_b are related to the shape of the spectrum. ω_p is the peak frequency. The peakedness parameter

γ is the ratio of the maximum value of the JONSWAP spectrum to the maximum value of the corresponding PM spectrum, i.e. for $\gamma = 1$ the JONSWAP spectrum is equal to the PM spectrum.

The ITTC version of the JONSWAP spectrum

As the parameters of the JONSWAP spectrum depends on the seastate (i.e. H_s and T_p) Equation 8.23 is not easily applicable within an engineering context.

In this thesis we choose to use the one-dimensional JONSWAP spectrum recommended by the 17th ITTC, given as (Faltinsen, 1990):

$$S(\omega) = 155\frac{H_{\frac{1}{3}}^2}{T_1^4\omega^5}\exp\left(\frac{-944}{T_1^4\omega^4}\right)3.3^Y \tag{8.24}$$

where

$$Y = \exp\left(-\left(\frac{0.191\omega T_1 - 1}{2^{\frac{1}{2}}\sigma}\right)^2\right) \tag{8.25}$$

and

$$\begin{aligned}\sigma &= 0.07 \; for \; \omega \leq 5.24/T_1 \\ &= 0.09 \; for \; \omega > 5.24/T_1\end{aligned} \tag{8.26}$$

T_1 is the mean wave period: $T_1 = 2\pi\frac{m_0}{m_1}$. The peakedness factor γ in Equation 8.24 is set to 3.3, which is its mean value. For $\gamma = 3.3$ the relation between mean wave period T_1 and spectral peak period T_p is: $\frac{T_1}{T_p} = 0.834$.

The use of the JONSWAP spectrum with peakedness factor $\gamma = 2.5$ is recommended in Section 5.11.4 of NS 9415 (Standard Norge, 2003) (see also Appendix C.1 in the present thesis). However, a peakedness factor according to Equation C.1 is prescribed in Section 5.4.2 of NS 9415, see Appendix C.1 of the present thesis. Equation C.1 yields an interval of γ-values from 2.4 to 4.8 for the H_s and T_p combinations of the scatter diagram that will be used in the fatigue analysis, see Table 8.5. Due to the conflicting γ-values of NS 9415 and its lack of references, we choose to use the ITTC recommendation ($\gamma = 3.3$). On a general level it is noted that it is probably possible to make a better estimate for the parameterization of the JONSWAP spectrum, but this is not investigated further in this thesis.

Wave component simulation

Surface elevation as well as wave particle velocity and acceleration for linear irregular waves can be simulated using the surface elevation spectrum. The simulation method used in this work is based on the work by Rice (1944), Rice (1945) which is the so called Deterministic Spectral Amplitude model (DSA). The simulation is most effectively done using FFT, see e.g. (Cooley and Tukey, 1965), (Cooley et al., 1969). Ocean wave simulation is discussed e.g. by (Borgman, 1967) and (Morooka and Yokoo, 1997).

The minimum frequency component can for a PM spectrum be set to $\omega_{min} = \frac{\pi}{T_2}$, i.e. $T_{max} = 1.42 \cdot T_p$ (Faltinsen, 1990). As a JONSWAP spectrum is more peaked than a PM spectrum, this provides a conservative value for a JONSWAP spectrum. In the FFT simulation, the minimum frequency is 0 (i.e the maximum period is ∞).

The maximum frequency (i.e. minimum period) is harder to establish as the wave energy drops off more slowly for larger frequencies. The time step Δt used in the simulation determines the cut-off level (maximum frequency) for the spectrum:

$$\omega_{max} = \frac{\pi}{\Delta t} \tag{8.27}$$

$$T_{min} = 2 \cdot \Delta t \tag{8.28}$$

The simulations will be done with a time step equal to the time step of the numerical integration of the equation of motion: $\Delta t = 0.075\,s$, i.e. the cut-off level for the spectrum is: $\omega_{max} = 41.9\,rad/s$, correspondingly $T_{min} = 0.15\,s$.

Horizontal wave particle velocity and acceleration in addition to wave surface elevation are simulated according to the wave load model presented in Chapter 3. For velocity and acceleration the simulation is valid for a particular depth (as opposed to surface elevation). However, as explained in Section 3.2.4, velocity and acceleration are simulated at only one depth: $z = 0\,m$ (i.e. the surface). Simulations are made for each nodal position in the wave direction, i.e. typically for 21 points along the wave direction.

H_s/T_p-scatter diagram based on wind speed distribution

Establishing a wave scatter diagram requires in general a significant effort in terms of time and resources, and this is also the case for relevant fish farm locations. Thus, using a scatter diagram is not customary procedure in the design and certification of floating fish farms. A simplified method applying regular maximum waves is the dominating (if not the only?) approach used in practice.[17] Undoubtedly, generating a scatter diagram based on measurements at or near the location in question is the most trustworthy and accurate approach in order to establish a scatter diagram to be used in design. In the absence of on-site measurements there are several numerical approaches to estimate a scatter diagram. However, no methodology for generating a scatter diagram is given in NS 9415.

Here, we will suggest and describe a simplified method based on wind speed distribution together with fetch F and the significant wave height/peak period relationships.

The suggested approach in effect assumes that the wind always blows in the direction of the assumed principal direction of the fjord (perpendicular to the BCS).

Distribution of wind speed

The 10 minutes mean wind at $10\,m$ above the sea surface/ground $\bar{U}_{10}$ is often assumed to be (2-parameter) Weibull distributed, see e.g. (Myrhaug, 2006), (Børresen, 1987), (DWIA,

[17] The author is not aware of structural analysis based on a scatter diagram for a floating fish farm.

Description	Symbol	Value
Scale parameter	q	9.985
Shape parameter	h	1.926
Mean wind speed	$\bar{U}_{10,mean}$	$8.85\,m/s$
Median wind speed	$\bar{U}_{10,med}$	$8.3\,m/s$

Table 8.1: 2-parameter Weibull distribution assuming a 6 hour observation interval, 50-year wind speed of $\bar{U}_{10} = 35\,m/s$, and 1-year wind speed $\bar{U}_{10} = 28\,m/s$.

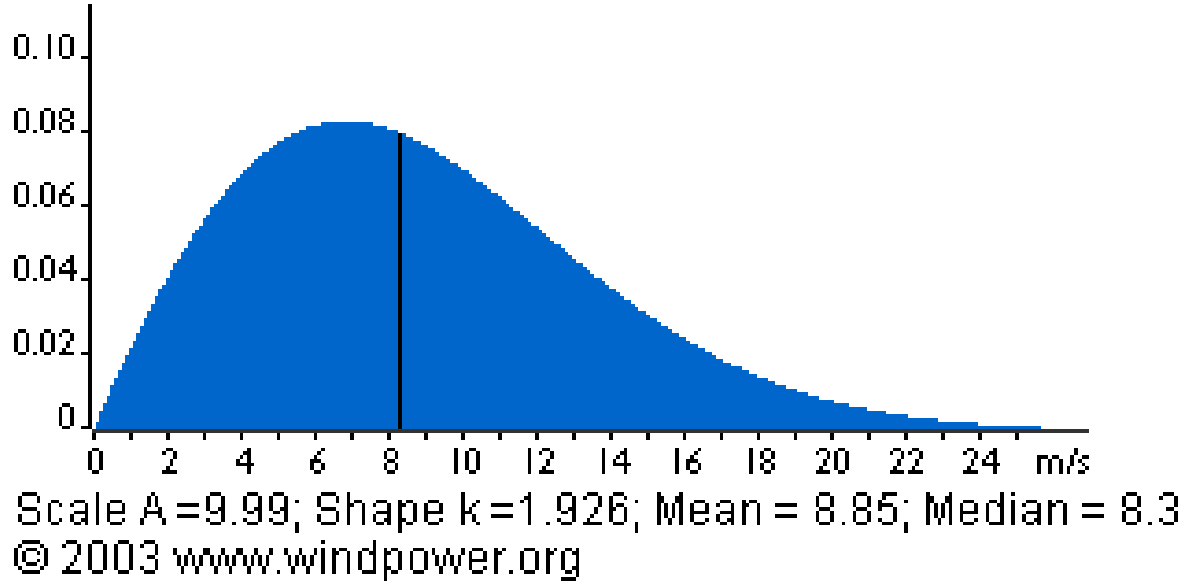

Figure 8.1: Weibull distribution of the mean wind velocity

2007). In NS 9415 (Section 5.5.2 and Appendix A) the 50-year and 1-year wind speeds are given as $35\,m/s$ and $28\,m/s$, see Appendix C.1.1 in the present thesis.

Combining the conservative (as most fish farm locations are somewhat sheltered) 1- and 50-year values with a 2-parameter Weibull distribution and an assumed observation interval of $6\,h$ we can find the shape and scale parameters of the assumed Weibull distribution, see Table 8.1. Using DWIA (2007) we can plot the distribution, see Figure 8.1, and find the mean and median wind speed, see Table 8.1.

To generate a wave scatter diagram from the wind speed distribution we start by making a wind speed scatter diagram. We divide the wind speed in nine intervals, see Table 8.2. The midpoints of the inner seven intervals are $5\,m/s$ apart: 5, 10, 15, 20, 25, 30 and $35\,m/s$. An alternative approach to arrive at wind speed intervals would have been to use the 12 intervals of the Beaufort scale, giving a finer "grid" and direct Beaufort scale

Sc.#	Interval	p_{sc}	Num	Return Period
0	≤ 2.5	6.7%	1959	$4d$
1	$\langle 2.5, 7.5]$	37.1%	10831	$16h$
2	$\langle 7.5, 12.5]$	34.8%	10159	$17h$
3	$\langle 12.5, 17.5]$	16.2%	4718	$37h$
4	$\langle 17.5, 22.5]$	4.4%	1288	$6d$
5	$\langle 22.5, 27.5]$	0.8%	219	$33d$
6	$\langle 27.5, 32.5]$	0.08%	24	$305d$
7	$\langle 32.5, 37.5]$	0.006%	2	$12y$
8	> 37.5	0.0003%	0.1	$246y$

Table 8.2: Relative occurrence of the nine wind speed intervals.

correspondence[18]. A discretization even finer than the Beaufort scale could also have been considered. As an initial approach the coarse discretization was chosen as it is the least comprehensive and thus a good starting point.

Using the Weibull distribution we can find the relative frequency of occurrence for the respective wind speed intervals, see Table 8.2. The number of occurrences assuming a 6 hours observation interval over a 20 year period (totally 29200 observations) are also included.

The distribution of wind speed has a typical shape. In DWIA (2007) a general description is given:

> If you measure wind speeds throughout a year, you will notice that in most areas strong gale force winds are rare, while moderate and fresh winds are quite common[19].

The distribution described in table 8.2 comply with the description of general wind speed distribution cited above: the moderate and fresh breeze interval (i.e. $[5.5\,m/s, 10.7\,m/s]$) appears to be common whereas the strong gale interval (i.e. $[20.8\,m/s, \infty\rangle$) is rare.

From Wind Speed Distribution to 1D Scatter Diagram

Using Equation 3.3 and 3.4 we have found H_s and T_p for the wind speed midpoints of Table 8.2. Midpoint wind speeds $\bar{U}_{10}$ and corresponding H_s/T_p-values are shown in Table 8.3 for wave classes B, C, and D. The fetch values for the three wave classes are taken from Table 3.3 and are $1.2\,km$, $4.8\,km$, and $10.9\,km$, respectively. The frequency of occurrence for the H_s/T_p-pairs is assumed to be the frequency of occurrence for the corresponding

[18]The complete Beaufort scale is given in Appendix E.

[19]In Appendix E and Table 8.3 of the present thesis the term breeze is used instead of wind and violent severe gale instead of strong gale.

$\bar{U}_{10}$-values of Table 8.3. The Beaufort number and Beaufort description for the interval in which the respective wind speeds fall are also given in Table 8.3.

Effectively, we get a one dimensional scatter diagram since there is a one-to-one relationship between H_s and T_p. A typical, full-scale scatter diagram is two dimensional, i.e. there are many seastates with the same H_s, but different T_p and vice versa. Looking at the scatter diagram example in Appendix D for the North Sea, we can observe a clear difference in the distribution of observations between the H_s vs. the T_p interval. All T_p-values have the maximum number of observations for low H_s-values: $1 - 3\,m$, whereas the maximum number of observations for H_s-values occurs for increasing values of T_p. This gives rise to the typical triangular shape of the scatter diagram. Further, it can be observed that for any given H_s-value, the T_p-value with maximum number of observations has approximately the same number of observations for larger as for smaller T_p-values, i.e. symmetry. E.g. for $H_s = 6\,m$, the maximum number of observations has occurred for $T_p = 12\,s$ and there were 1770 observations for lower T_p values vs. 2000 observations for higher T_p values. For a given T_p-value, there are much more observations for H_s-values which are larger than the H_s-value with the maximum number of observations. E.g. for $T_p = 12\,s$, the maximum number of observations occurred for $H_s = 3\,m$ and there were 2053 observations for lower H_s values vs. 5720 observations for higher H_s values.

Finding a 1D scatter diagram as described above is assumed to be similar to summing all observations for each H_s value and connecting it to the T_p-value with the maximum number of observations[20]. This is a special case of a procedure (often called blocking) to simplify the scatter diagram where its cells are grouped into blocks. The cells of each block have similar response characteristics. This procedure is described and used e.g. in (Karunakaran, 1993). Using this approach, a scatter diagram as given in Appendix D is changed (i.e. "blocked) into the 1D scatter diagram showed in Table 8.4. Based on visual assessment of the histogram of H_s it appears to be similar to a Rayleigh distribution. When fitting the H_s-histogram to a Weibull distribution a shape parameter of 2.41 was found. In example studies from (Karunakaran, 1993) each block typically contains the whole T_p interval (the interval is divided in two for low H_s values due to resonant contributions), whereas the H_s interval (from $1\,m$ to $18\,m$) is divided into eight blocks.

We want to compare the two approaches to get to a 1D scatter diagram: directly from the wind distribution vs. by blocking a 2D scatter diagram as described above. In Figure 8.2, first the normalized significant wave height is plotted against the normalized number of observations. Then, the H_s values are normalized with the corresponding maximum H_s.

We see from the plots that the shape of the corresponding normalized plots (in the lower part of the figure) are similar. It is thus assumed that the two approaches lead to similar 1D scatter diagrams and that constructing a 1D scatter diagram from the wind distribution is a reasonable simplified approach if resonant contributions are not important. In the next chapter we investigate the fatigue lifetime sensitivity to H_s and T_p at different levels. In

[20]It is noted that the opposite approach would not give a usable result as the maximum number of observations all occur for the smallest H_s-values.

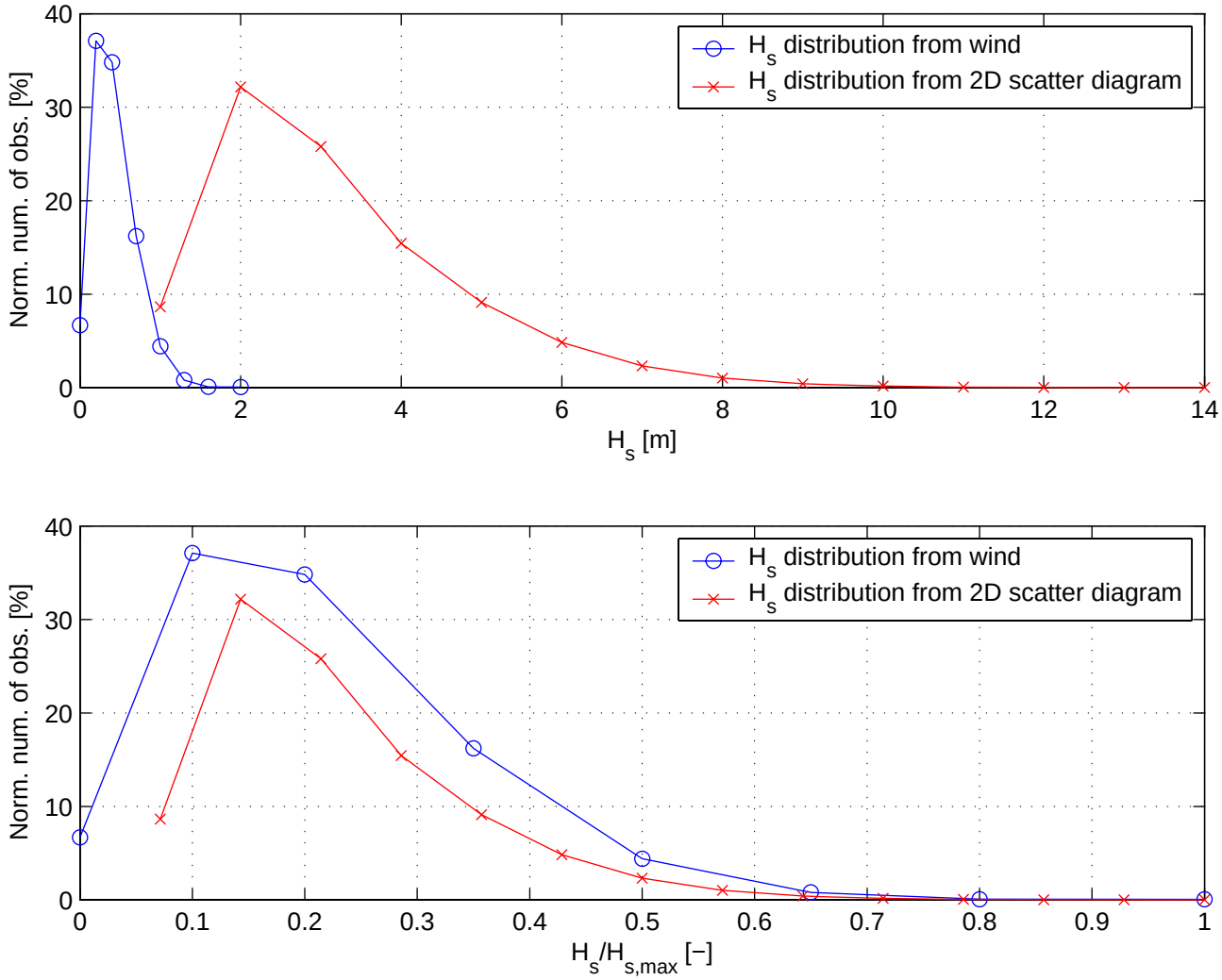

Figure 8.2: Distribution of H_s from wind vs. from 2D scatter diagram.

$\bar{U}_{10}$ [m/s]		5	10	15	20	25	30	35
Beaufort #		3	5	7	8	10	11	12
Wave class	Description	Gentle breeze	Fresh breeze	Near gale	Gale	Storm	Violent storm	Hurricane
B	H_s	0.1	0.2	0.4	0.5	0.7	0.8	1.0
	T_p	1.1	1.5	1.8	2.0	2.2	2.4	2.5
C	H_s	0.2	0.4	0.7	1.0	1.3	1.6	2.0
	T_p	1.8	2.4	2.8	3.2	3.5	3.8	4.0
D	H_s	0.3	0.6	1.1	1.5	2.0	2.5	3.0
	T_p	2.4	3.2	3.7	4.2	4.6	5.0	5.3

Table 8.3: H_s and T_p values for wave classes B, C, and D. Units for T_p and H_s are [s] and [m], respectively.

H_s [m]	1	2	3	4	5	6	7
T_p [s]	7	8	9	10	11	12	13
# obs.	8636	32155	25792	15442	9118	4839	2329
H_s [m]	8	9	10	11	12	13	14
T_p [s]	13	13	14	14	15	15	16
# obs.	1028	419	160	57	19	6	1

Table 8.4: H_s and T_p values for a 1D scatter diagram resulting from transforming the 2D scatter diagram of Appendix D (from the Northern North Sea).

particular, if the sensitivity of T_p is low the 1D scatter diagram is assumed to give results comparable to the 2D scatter diagram.

Wave class C

The analyses from here on are restricted to wave class C in order to limit the extent of the analyses required as well as the results presented.

The wave scatter diagram for wave class C is shown in Table 8.5. The wave length λ corresponding to a regular wave period $T = T_p$ is included (see Section 3.1.3). The minimum wave length is $5.1\,m$, i.e. $\frac{\lambda}{D} > 5$ and it is reasonable to neglect wave diffraction effects for all relevant seastates, see Section 3.2.3 and Equation 3.11. The ratio between the BCS length and the wave length ($\frac{30m}{\lambda}$) are also included because the extent to which the loading of the perpendicular members are in-phase is very important for the reaction forces, see Section 7.4 and 9.4. Finally, the peakedness parameter γ-values according to Equation

Sc. #		1	2	3	4	5	6	7
H_s	[m]	0.2	0.4	0.7	1.0	1.3	1.6	2.0
T_p	[s]	1.8	2.4	2.8	3.2	3.5	3.8	4.0
p_{sc}	[%]	37.1	34.8	16.2	4.4	0.8	0.08	0.006
λ	[m]	5.1	9.0	12.2	16.0	19.1	22.5	25.0
$\frac{30m}{\lambda}$	[-]	5.93	3.34	2.46	1.88	1.57	1.33	1.20
$\gamma_{5.4.2}$	[-]	2.4	3.1	3.5	3.9	4.2	4.5	4.8

Table 8.5: 1D scatter diagram. H_s and T_p values corresponding to a fetch of $4.8\,km$ (wave class C).

C.1 are also given (see previous discussion in this section). The variance of the surface elevation σ_ζ^2 has been found by integrating the spectrum using the MATLAB (MathWorks, 2007) function `quadl`. The standard deviation $\sigma_\zeta = \sqrt{\sigma_\zeta^2}$ was as expected found to be 25% of the significant wave height H_s (independent of T_p), see e.g. (Faltinsen, 1990).

Cycle Counting: Rainflow

In this thesis rainflow counting will be used for cycle counting. The rainflow counting algorithm was developed by Matsuishi and Endo (1968) and is still a very popular cycle counting algorithm for fatigue analysis. Details of the rainflow counting algorithm can be found in (Brodtkorb et al., 2000) and in Section 6.5.

8.4.2 Resistance

Classifying the identified critical details according to the correct SN curve is an important task when using the SN approach in design. However, in the present thesis we will not try to categorize actual details of the BCS to particular SN curves. Instead, a critical location is assumed, and fatigue design is performed using a selection of SN-curves for the obtained stress histories at this structural location. The reasons for this approach are threefold. Firstly, we have neither defined the BCS to the necessary structural detail level nor gained access to the details of an actual fish farm of the BCS-type. Secondly, and more importantly, this approach gives a more clear picture of the interval of fatigue design life given by the family of SN curves. Finally, the principal goal is to present a methodology for fatigue design and give an example of application rather than to evaluate particular structural details.

We will refer to the structural codes NS 3472 (Standard Norge, 2001) and DNV-RP-C203 (DNV, 2005), published in 2001 and 2005, respectively, for fatigue design. SN curves are given for details in air, in seawater with cathodic protection, and in seawater with free corrosion (i.e. without cathodic protection). As floating fish farms with steel in direct

contact with seawater typically have cathodic protection, the curves for cathodic protection are used. The NS 3472 and DNV-RP-C203 curves are identical except for the B1 and B2 curves. In the current version of DNV-RP-C203 the slope has been changed to $m = 4.0$ to be more in line with fatigue test data for the base material.

In both codes curves for details in air and in seawater with cathodic protection are bilinear. The transition points are 10^7 cycles in air and 10^6 cycles in seawater with cathodic protection. The m-factor for high cycle fatigue is 5 in either case. The SN curves for seawater without cathodic protection are *not* bilinear. In both codes a fatigue stress range limit Δf_D is given for the curves in air and in seawater with cathodic protection. For variable amplitude loading the fatigue capacity can be assumed to be sufficient if the maximum stress range is smaller than the fatigue stress range limit: $\Delta\sigma_0 < \Delta f_D$. The Δf_D-values for details in air and in seawater with cathodic protection are the same for corresponding curves. The values are found by using $N = 10^7$ in Equation 8.3 and the m and $\log \bar{a}$-values for details in *air* (i.e. the curve parameters for air are also used to find Δf_D for details in seawater with cathodic protection):

$$\log \Delta f_D = \frac{\log \bar{a}_{air} - 7}{m_{air}} \tag{8.29}$$

The m-, $\log \bar{a}$-, and Δf_D-values of DNV-RP-C203 are listed in Table 8.6. We have also included $\Delta\sigma_{N=10^6}$, the fatigue limit at $N = 10^6$ which is the transition point, i.e. the crossing point between the curve with $m = 3$ or 4 and the curve with $m = 5$.

C2 and F

In order to get a more perspicuous and compact presentation we will restrict the results from the numerical parameter study to two SN curves. Using additional curves are assumed not to yield further insight or understanding at this point. The chosen curves are: C2 and F, i.e. the fifth and eighth curve from the "top", respectively. The curves are chosen with the intention to represent a surviving detail and a failing detail, respectively, and thus approximately represent the limits of a realistic interval of curves.

Assuming a constant stress range over the lifetime of a structure we can find the stress range capacity for the selected SN curves, see Table 8.7. We find the number of stress cycles assuming that the period of the stress fluctuations is the peak period corresponding to the median wind speed (see Table 8.1), i.e. $T = 2.2\,s$, combined with lifetimes of 1, 10, and 20 years (i.e. $3.15 \cdot 10^7\,s$, $3.15 \cdot 10^8\,s$, and $6.31 \cdot 10^8\,s$, respectively).

Stress ranges below the respective values must dominate the stress range distribution in order for the fatigue strength to be sufficient. The stress ranges are very small compared to the yield stress. Further, the Δf_D-values of Table 8.6 (58 and $42\,MPa$) are much higher than the corresponding stress ranges for 10 and 20 years and very close to the values for 1 year. This is as expected as the Δf_D-values are based on $N = 10^7$, which is approximately the number of stress cycles in one year. A wave period of $3.15\,s$ gives exactly 10^7 fluctuations during 1 year (and for a constant stress range the corresponding capacities are the Δf_D-values of Table 8.6).

#	SN-curve	$N \leq 10^6$		$N > 10^6$	Δf_D	$\Delta\sigma_{N=10^6}$
		m_1	$\log \bar{a}_1$	$\log \bar{a}_2$	[MPa]	[MPa]
#1	B1	4.0	14.917	17.146	107	170
#2	B2	4.0	14.684	16.856	94	148
#3	C	3.0	12.192	16.320	73	116
#4	C1	3.0	12.049	16.081	66	104
#5	C2	3.0	11.901	15.835	58	93
#6	D	3.0	11.764	15.606	53	83
#7	E	3.0	11.610	15.350	47	74
#8	F	3.0	11.455	15.091	42	66
#9	F1	3.0	11.299	14.832	37	58
#10	F3	3.0	11.146	14.576	33	52
#11	G	3.0	10.998	14.330	29	46
#12	W1	3.0	10.861	14.101	26	42
#13	W2	3.0	10.707	13.845	23	37
#14	W3	3.0	10.570	13.617	21	33

Table 8.6: SN-curves in seawater with cathodic protection (DNV, 2005). $m_2 = 5.0$.

Lifetime	1 year		10 years		20 years	
SN-curve	C2	F	C2	F	C2	F
$\Delta\sigma$ [MPa]	54	39	34	24	30	21

Table 8.7: Stress range capacities for SN-curves C2 and F assuming wave period $T = 2.2\,s$ and varying lifetimes: 1 year, 10 years , and 20 years.

$\Delta\sigma$ [MPa]	10	20	30	40	50	60	70	80	90	100
C2	4771y	149y	20y	4.7y	1.5y	224d	104d	53d	29d	20d
F	860y	27y	3.5y	307d	100d	40d	21d	14d	10d	7d

Table 8.8: Fatigue lives for SN curves C2 and F assuming fluctuation period $T = 2.2\,s$.

For a design fatigue life of 20 years the stress range capacities are approximately one third of the $\Delta\sigma_{N=10^6}$-values of Table 8.6. Thus, very few stress cycles are expected to be above the $\Delta\sigma_{N=10^6}$-values over a 20-year period and only considering the extrapolated high cycle fatigue curve (with m=5) will be acceptable in most cases (considering only one of the two fatigue curves will aways be conservative).

Table 8.8 gives the fatigue lives for the two SN curves and realistic stress range levels: $\Delta\sigma = 10\,MPa$ to $100\,MPa$ assuming a constant stress range. Again, a period of $2.2\,s$ is assumed. The ratio of fatigue life is 5.5 for the $N > 10^6$ curves and 2.8 for the $N \leq 10^6$ curves (i.e. the C2 curve yields 5.5 times and 2.8 times longer fatigue life than curve F, respectively). We see that the fatigue lives in the right half of Table 8.8 are very short, and this indicates that the details can endure very short durations of stresses at these levels. The table also illustrates that for an SN curve with $m = 5$, doubling the stress level $\Delta\sigma$ e.g. from 40 to $80\,MPa$ will reduce the life time by a factor of $2^5 = 32$: $\frac{4.7\,y}{53\,d} \approx 32$.

Critical structural locations

Stress histories are of relevance for positions with maximum moments for perpendicular waves, i.e. at the mid-section of the perpendicular and parallel members. This implies that we assume that critical details are located at these positions. With maximum moment fluctuations, these are locations where one would strive not to place weak details. However, it is not unrealistic that a weld is placed at or close to these locations e.g. for design or production related reasons. Additionally, these locations will probably provide a conservative fatigue life estimate for other locations along the members.

When computing the principal stress, only bending stress will be considered. It is reasonable to assume that the stresses due to shear and axial forces will be of considerably less importance as this is a typical beam structure. Also, torsion stresses are neglected as we have shown previously that stresses due to torsion moments are considerably smaller than due to bending moments for perpendicular waves. Further, we assume that the detail in question is located at the top point of the cross section, i.e. at the point of maximum bending stress for bending moment about the horizontal axis. We focus on this moment component because it exhibits nonlinear effects. The mid sections of the BCS and the top point of the cross section are shown in Figure 8.3. This figure is based on Figure 2.7.

No stress concentration factor (SCF) is applied, although it might be appropriate to apply a SCF depending on the local design. Not applying a SCF (> 1) can be nonconcervative.

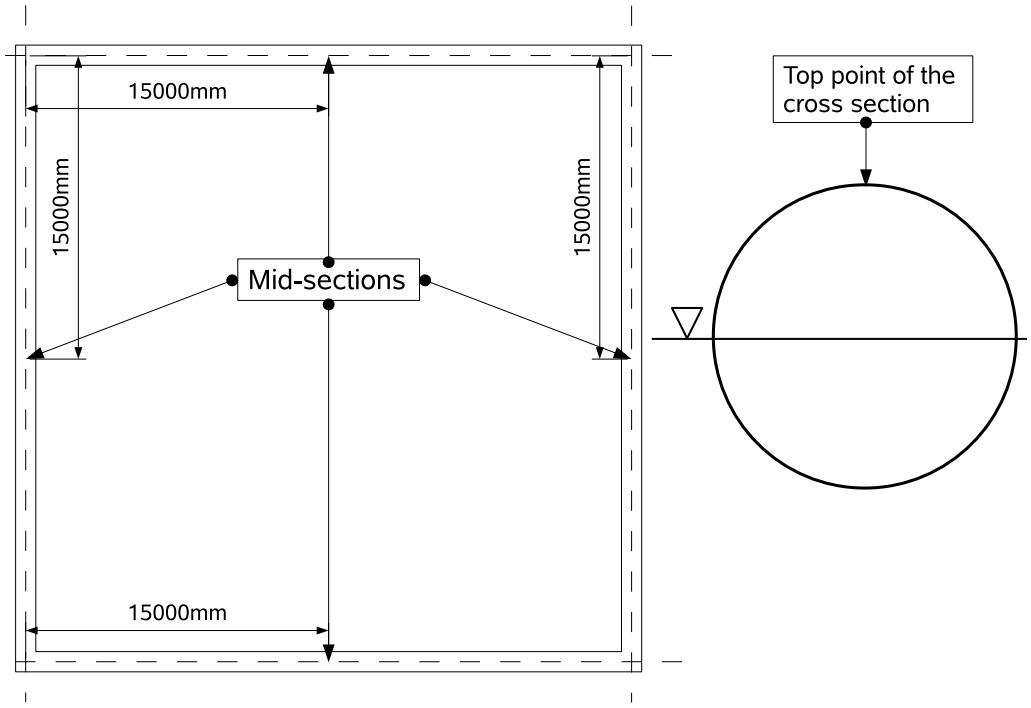

Figure 8.3: Left: Mid-sections of the BCS. Right: Top point of cross section.

#	Description	Reference
1	Critical details (with respect to fatigue life) and the appropriate SN curves are identified.	Section 8.4.2
2	A scatter diagram and wave spectrum is established for the relevant geographical location.	Section 8.4.1
3	TDAs are performed for all sea states of importance.	Chapter 5
4	Time histories are recorded for relevant reaction forces of the cross section at the identified critical points and transformed to stress histories.	Section 8.4.1 Section 8.1.3
5	Damage per seastate is established for all seastates by using the relevant SN curves and rainflow counting.	Section 8.3.2
6	Summation of damage for all seastates of the scatter diagram whereby the fatigue life can be estimated.	Section 8.3.2

Table 8.9: The principal steps for fatigue design of a floating fish cage.

8.5 Summary: Suggested methodology

In the previous chapter it was demonstrated that a floating fish farm can be dynamically sensitive and is expected to be influenced by nonlinearities. Thus, a TDA is the appropriate approach for fatigue design of floating fish farms (see Section 8.1). The TDA is described in Chapter 5. Although generally accepted as the most accurate methodology, TDA with a nonlinear system and applying irregular waves has gained limited ground in practice. The primary reason for this is the computer resources required — both software and hardware. Nevertheless, this is the preferred method in the present thesis based on the belief that the advances in computer technology will merit such a computationally demanding approach.

The six principal steps suggested for fatigue design of a floating fish farm are listed in Table 8.9.

Application of this procedure will be further illustrated in relation to the parameter study for the BCS presented in the next chapter.

Chapter 9

FATIGUE ANALYSIS PARAMETER STUDY

As noted in the previous chapter we will perform the parameter study for a fish farm in a wave class C location (see p.121) and for SN-curves C2 and F (see p.123). The waves are assumed to be long-crested and perpendicular to the BCS. The critical details are assumed to be at the top points of the mid-sections of the members. In the regular wave parameter study in Chapter 7, added mass and damping coefficients determined as functions of wave period (see Section 3.3.2) for the TRW were used. For irregular waves it is common to base the coefficients on the peak period T_p of the spectrum. As a simplification the hydrodynamic coefficients are kept constant for all seastates in this chapter, and the coefficients of TRW B are used (i.e. for $T = 2.5\,s$, see Table 5.1). $T = 2.5\,s$ was chosen because it is close to the middle of the wave period interval for a wave class C location (i.e. from $1.8\,s$ to $4\,s$, see Table 8.5). From Figure 3.2 we see that a constant value appears to be a good approximation for added mass in sway and damping in heave, and not as good for damping in sway and added mass in heave.

9.1 Regular waves

First, we will perform a simplified fatigue analysis based on regular waves. The two main objectives of starting with regular waves is to be able to compare results using the MATLAB library WAFO (see Section 6.5) with fatigue analysis performed by hand calculations (i.e. not using WAFO) as well as to illustrate the sensitivity of the wave period and wave height when using regular waves in a fatigue analysis. Thus, the hand calculations are used as a verification of correct use of the WAFO functions and of the fatigue life calculations implemented in the MATLAB m-file.

The procedure for deterministic (i.e. regular wave) fatigue analysis presented here is not intended or recommended to be used for design. More elaborate and accurate approaches have been presented by other authors, see e.g. (Sheehan et al., 2006). As opposed to the *single* height/period combination for each seastate used in the present work, Sheehan et al.

	Constant H_s		*Constant* T_p	
Sc. #	H_s [m]	T_p [s]	H_s [m]	T_p [s]
2	0.4	1.8-2.8	0.2-0.7	2.4
3	0.7	2.4-3.2	0.4-1.0	2.8
4	1.0	2.8-3.5	0.7-1.3	3.2
5	1.3	3.2-3.8	1.0-1.6	3.5

Table 9.1: Wave period and wave height combinations used to investigate sensitivity of peak period and significant wave heigth.

(2006) employed 20 or more wave height/wave period combinations for *each* seastate. The (single) wave height used to represent a particular seastate is set equal to the significant wave height of the corresponding seastate. This choice can both over- and under predict the reference fatigue life (found from irregular wave analysis), see Figure 9.6. Using the estimate for maximum wave height ($H = 1.9 \cdot H_s$, see Equation 3.1) instead of $H = H_s$ is relevant for an ultimate limit state, but is likely to underestimate the fatigue life, see Section 9.4. In an example given by Sheehan et al. (2006) less than half a percent of the regular wave fluctuations are for regular waves with wave heights higher than the corresponding significant wave height interval. (However, the fatigue damage caused by these waves will be greater.)

9.1.1 Sensitivity to wave period in a nonlinear analysis.

In Section 7.4 a strong sensitivity to wave period for the response obtained from linear analyses was demonstrated. Now, we continue to pursue this effect by looking at the wave period sensitivity for a nonlinear analysis as compared to a linear analysis. We look at different wave heights since the nonlinear effects in general will increase with wave height. The analyses are restricted to the critical point of the perpendicular member and are related to seastates assumed to have the greatest influence: *sc.* # 2,3,4, and 5, see Table 8.5. For each seastate the (regular wave) wave height H is set equal to the significant wave height H_s (see above) and we consider the corresponding wave period interval ranging from the peak period value of the seastate below to the peak period value of the seastate above, see columns for *Constant* H_s in Table 9.1. Although H_s and T_p are used as symbols in Table 9.1, the values are used for regular wave height H and period T

In Figure 9.1 the stress ranges $\Delta\sigma$ are plotted versus the wave period T for each of the four wave period intervals with their respective (constant) wave height H. The pair of graphs for linear and nonlinear analysis have similar shape, but they move apart with increasing wave height (i.e. increasing nonlinear effect). The wave height for the four pairs of linear/nonlinear curves are $0.4\,m$, $0.7\,m$, $1.0\,m$, and $1.3\,m$, see Table 9.1. The numerical values are given in Table G.6 to G.9 of Appendix G.

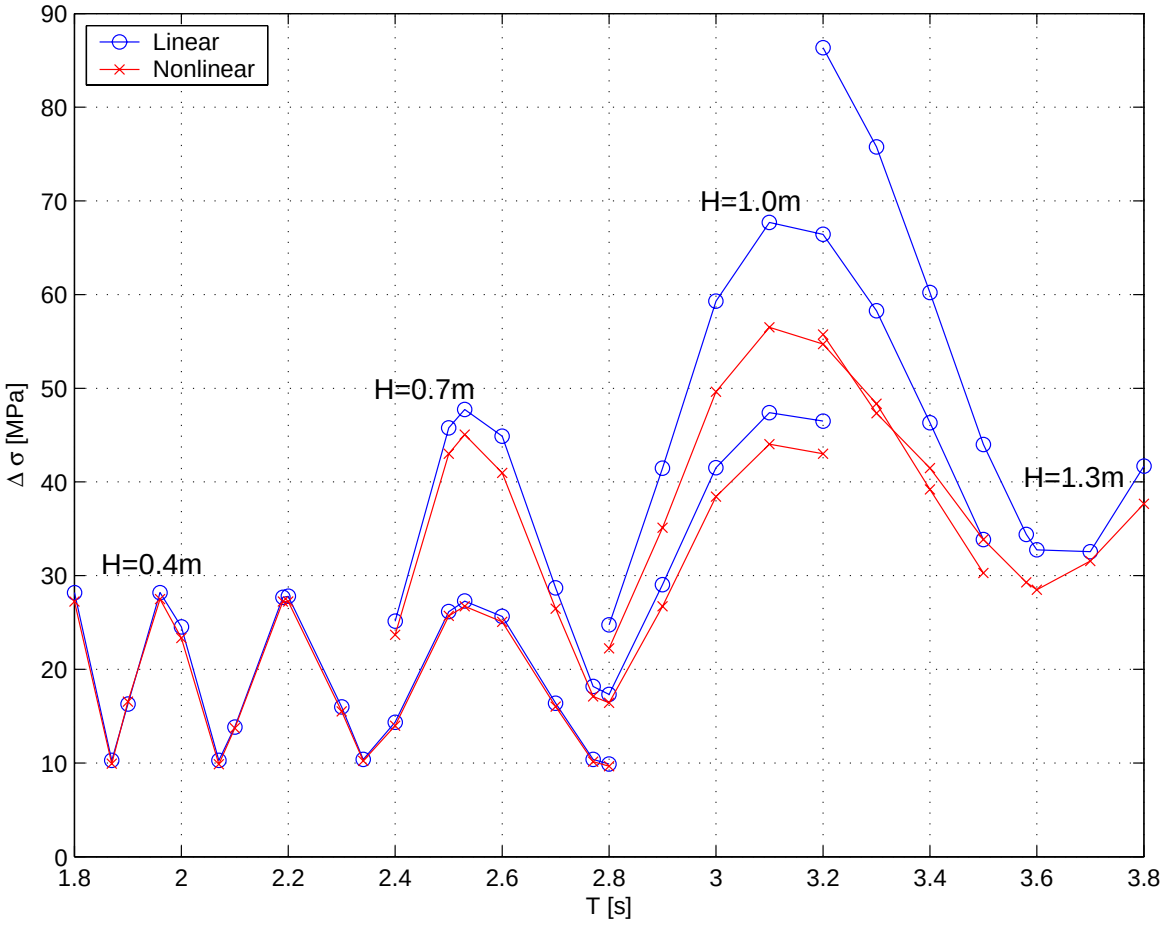

Figure 9.1: Linear and nonlinear stress ranges $\Delta\sigma$ for the wave period interval and wave height combinations of Table 9.1, columns for *Constant* H_s.

Discussion

From Figure 9.1 we see that the nonlinear and linear results are very similar for the lower two wave heights, i.e. the nonlinear effects are minor. For the largest two wave heights variation with wave period is very similar for the linear and nonlinear analysis, but the nonlinear stress range seems to reach a limit — i.e. increasing the wave height from $1\,m$ to $1.3\,m$ does not seem to increase the stress range (in the $T = 3.2\,s$ to $3.5\,s$ interval the graphs overlap and are hard to tell apart in the figure). As the nonlinear effect is stronger for the in-phase intervals than for the out-of-phase intervals, the sensitivity for a nonlinear analysis is lower than for a linear analysis. E.g. for $H = 1.3\,m$ and $T = 3.2\,s - 3.8\,s$, the ratios of the maximum value and the minimum value are $\frac{86\,MPa}{33\,MPa} = 2.6$ and $\frac{56\,MPa}{29\,MPa} = 1.9$. Thus, when using the above ratios (2.6 and 1.9) as a measure of sensitivity, we conclude that the sensitivity to wave height is significant also when nonlinear effects become important. However, the sensitivity is a bit smaller than for linear analysis. The sensitivity of fatigue life, L_{sc}, based on stress range will be significantly increased due to the logarithmic nature of the SN curve, see Figure 9.6 and Table G.6 to G.9.

We conclude that the strong sensitivity of wave period renders regular waves (i.e. a deterministic approach) less suitable for structural design in general and fatigue design in particular for the present class of structures.

The sensitivity to peak period T_p for irregular waves is investigated in Section 9.4.

9.1.2 Analysis based on scatter diagram

Fatigue analysis based on irregular waves and a scatter diagram was presented in Section 8.3.2. For regular waves we will simplify this procedure by assuming a constant stress range $\Delta\sigma$. For the hand calculations, the moment amplitude M_a at the critical point about the horizontal, perpendicular axis is found. The constant stress range $\Delta\sigma$ is then:

$$\Delta\sigma = 2 \cdot \frac{M_a}{W_{el}} \tag{9.1}$$

The stress range frequency for the hand calculations was set equal to the wave frequency. To find M_a-values to be used in the the hand calculations, time domain analysis with $30\,s$ duration were run, whereas $120\,s$ time series were used as input for the WAFO analysis. The longer durations were chosen to diminish start and end effects. As expected, the WAFO results were very similar to those from the hand calculations: the differences were less than 5%. Thus, the WAFO results are not presented.

We will use seven wave height/wave period combinations corresponding to the H_s/T_p-pairs of the scatter diagram established previously, see Table 8.5. The wave height is set equal to the significant wave height: $H = H_s$, and the wave period is set equal to the peak period: $T = T_p$.

The results for the assumed critical detail at the midpoint of the perpendicular cylinder are shown in Table 9.2. The fatigue life L_{sc} (in years) and damage over the design fatigue life D_{sc,L_0} for each "seastate" sc (i.e. each of the seven H/T-combinations in Table 8.5) are

	Sc. #		1	2	3	4	5	6	7
L	$\Delta\sigma_L$ [MPa]		14	15	18	68	45	53	100
	$\frac{\Delta\sigma}{H}$ [MPa/m]		70	38	36	68	35	33	50
	C2	L_{sc}	714	641	306	0.48	4.11	2.03	0.10
		D_{sc,L_0}	0.01	0.01	0.01	1.83	0.04	0.01	0.01
	F	L_{sc}	129	116	55	0.09	0.74	0.37	0.04
		D_{sc,L_0}	0.06	0.06	0.06	9.5	0.20	0.04	0.03
NL	$\Delta\sigma_{NL}$ [MPa]		14	15	17	54	33	46	63
	$\frac{\Delta\sigma_{NL}}{\Delta\sigma_L}$ [%]		100	100	94	79	73	87	63
	C2	L_{sc}	2367	2491	1537	5	59	9	3
		D_{sc,L_0}	0.01	0.01	0.01	0.58	0.01	0.00	0.00
	F	L_{sc}	140	147	91	0.3	3.5	0.8	0.2
		D_{sc,L_0}	0.05	0.05	0.04	3.21	0.04	0.02	0.01

Table 9.2: Fatigue life time and damage for critical point on perpendicular cylinder. Regular waves. SN-curves C2 and F.

presented for SN curve C2 and F. The D_{sc,L_0}-values are found taking the relative frequency of occurence for the respective seastates into account, see Table 8.2. Both linear (L) and nonlinear (NL) analyses are performed. For the nonlinear results the ratio between $\Delta\sigma$ and the wave height is also included to indicate the "power" of the wave height. For the linear results the ratio between the nonlinear and the linear $\Delta\sigma$ is included to indicate the degree of nonlinear effects.

The corresponding results for the assumed critical location at the midpoint of the parallel cylinder are shown in Table 9.3. The presentation of results follows the lines described for the perpendicular cylinder above.

In Table 9.4 the results from Table 9.2 and 9.3 are summarized: the total damage over the design life of the structure, i.e. D_{sc,L_0}, and the fatigue life L are presented for both of the SN curves as well as for the linear and nonlinear case.

Discussion

The stress levels arising from a regular wave are strongly dependent on degree of in-phase loading of the perpendicular members of the BCS (see Section 7.4 and 9.1.1), and this is the reason that fatigue damage in Table 9.2 is dominated by one H/T combination: *sc.* # 4: $H = 1.0\,m$, $T = 3.2\,s$.

From the $\Delta\sigma/H$-rows of Table 9.2 and 9.3 we see that the relative stress level is relatively high for *sc.* # 4, and this is combined with a high frequency of occurrence.

	Sc. #		1	2	3	4	5	6	7
L	$\Delta\sigma_L$ [MPa]		13	18	12	57	11	117	202
	$\frac{\Delta\sigma}{H}$ [MPa/m]		72	42	17	57	9	71	101
	C2	L_{sc}	1049	266	2665	1.13	3958	0.06	0.01
		D_{sc,L_0}	0.01	0.03	0.00	0.78	0.00	0.28	0.10
	F	L_{sc}	189	48	480	0.20	714	0.02	0.00
		D_{sc,L_0}	0.04	0.14	0.01	4.32	0.00	0.77	0.27
NL	$\Delta\sigma_{NL}$ [MPa]		13	17	8	44	10	62	103
	$\frac{\Delta\sigma_{NL}}{\Delta\sigma_L}$ [%]		98	93	70	76	86	53	51
	C2	L_{sc}	1147	383	16225	4.3	8335	0.9	0.1
		D_{sc,L_0}	0.01	0.02	0.00	0.20	0.00	0.02	0.01
	F	L_{sc}	207	69	2925	0.78	1503	0.16	0.03
		D_{sc,L_0}	0.04	0.10	0.00	1.13	0.00	0.10	0.04

Table 9.3: Fatigue life time and damage for critical point on parallel cylinder. Regular waves. SN-curves C2 and F.

SN		Perpendicular		Parallel	
		L [year]	D_{20y} [-]	L [year]	D_{20y} [-]
C2	Linear	10	1.9	17	1.2
	Nonlinear	32	0.62	77	0.26
F	Linear	1.9	11	3.6	5.6
	Nonlinear	5.9	3.4	14	1.4

Table 9.4: Resulting fatigue life L and fatigue damage over 20 years D_{20y} for critical point on perpendicular cylinder. Regular waves. SN-curves C2 and F.

9.1.3 Maximum stress range

The most common simplified method for fatigue design is based on an estimate of the maximum stress range and an assumed Weibull shape parameter, see Section 8.3.3 and Equation 8.20. It is therefore of interest to make an estimate of the long-term maximum stress range $\Delta\sigma_0$. In Section 9.1.1 it was shown that there is a very strong sensitivity to the (regular) wave period. This is the case for both linear and nonlinear analysis, but for increasing wave heights the sensitivity is strongest for the linear analysis.

To estimate the 20-year maximum stress range we use the 20-year significant wave height based on the 20-year wind speed $\bar{U}_{10,20y}$. From Table 8.2, $\bar{U}_{10,20y}$ is approximated to $32.5\,m/s$. $\bar{U}_{10,20y} = 32.5\,m/s$ yields $H_{s,20y} = 1.8\,m$ and $T_{p,20y} = 3.9\,s$ using Equation 3.3 and 3.4. According to NS 9415 the maximum wave height is then $H_{max,20y} = 1.9 \cdot 1.8\,m = 3.4\,m$, see Equation 3.1. This wave height is used for linear and nonlinear analyses for the whole wave period interval of wave class C (see Table 3.1): $T_p = [2.5\,s, 5.1\,s]$. To investigate the trend for higher wave periods the upper limit of the interval is increased to $7\,s$. In Figure 9.2 the maximum stress ranges $\Delta\sigma_0$ for the linear and nonlinear analyses are plotted against wave period for $H = 3.4\,m$. The nonlinear results have a trend which is similar in shape to the linear, but at a level of approximately half the linear one. The nonlinear maximum stress range varies from 30 to 80% of the linear case. The nonlinear results are also more irregular for the lower wave periods.

Although the nonlinear time series appears to be quite broad banded (see Figure 9.3), hand-calculations based on Section 9.1.2 give the same results for fatigue life and maximum stress range as WAFO analyses of the time series. Thus, the maximum stress range has the same period as the waves and completely dominates the fatigue damage.

The largest and smallest maximum stress range for the various analyses are given in Table 9.5. Additionally, the ratios of the maximum value to the minimum value $\frac{\Delta\sigma_{0,max}}{\Delta\sigma_{0,min}}$ and the linear value to the nonlinear value $\frac{\Delta\sigma_{0,L}}{\Delta\sigma_{0,NL}}$ are given. We see from the table that the maximum stress range is approximately three times the minimum, and that the linear stress range is 2.1 and 2.4 times the nonlinear. Thus, for both linear and nonlinear analyses the maximum stress range is very sensitive to the wave period. Increasing the stress range by a factor of three will — assuming constant stress range — decrease the fatigue life by a factor of $3^5 = 243$, assuming $m = 5$. The difference of maximum stress range of a linear and a nonlinear analyses is roughly a factor of two corresponding to a factor of $2^5 = 32$ for the fatigue damage, see Equation 8.20.

9.2 The irregular wave implementation

In Section 7.2.1 we performed a check of the implementation of the linear structure and regular waves. Here, the irregular wave implementation is scrutinized by calculating the variance of vertical and horizontal response and comparing it to the direct integration of the response spectrum. As in Section 7.2.1, a single cylinder perpendicular to the wave direction is used because it can be modeled as a 1 DOF system, vertically or horizontally.

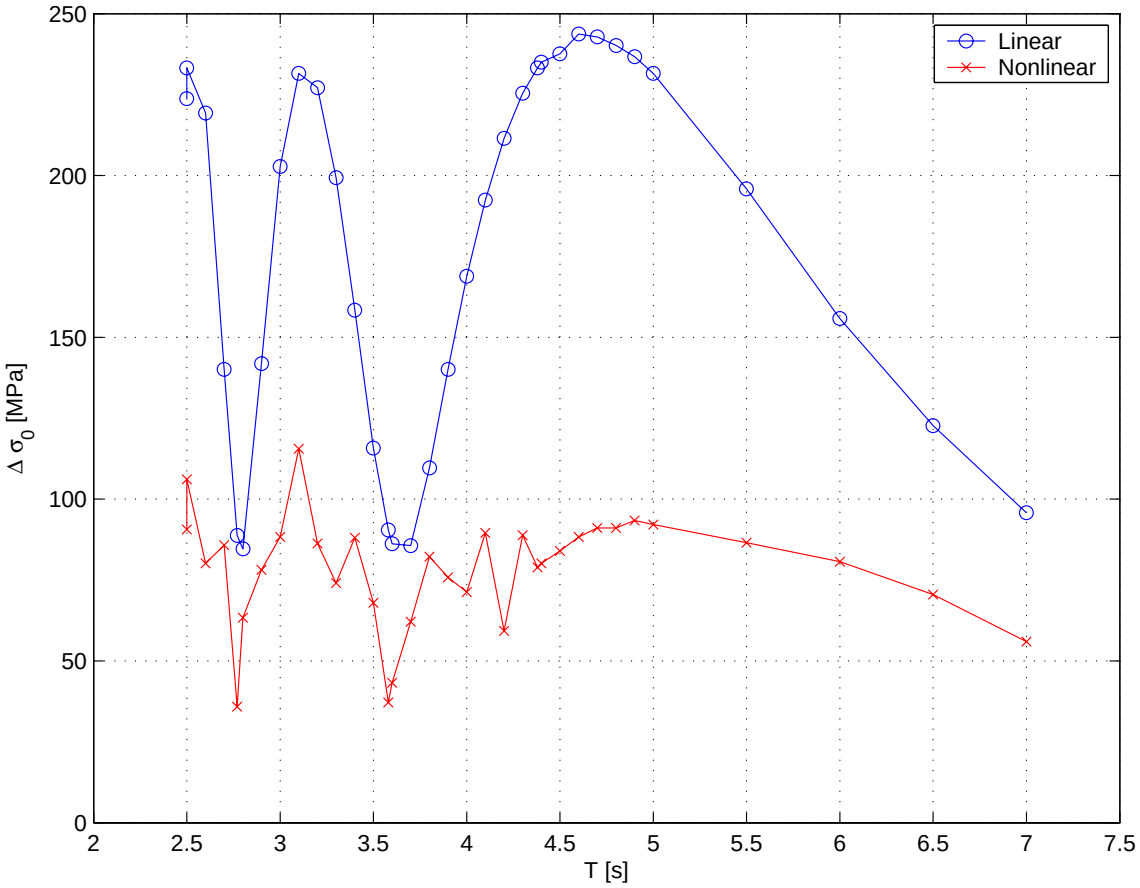

Figure 9.2: $\Delta\sigma_0$ for linear and nonlinear analyses using regular waves with $H = 3.4\,m$.

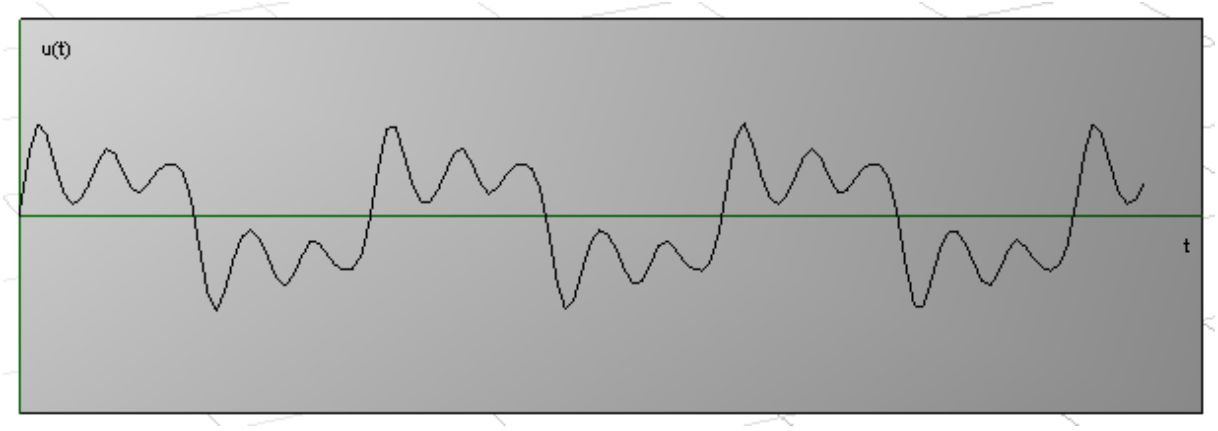

Figure 9.3: Time history of bending moment about the horizontal axis for midpoint of perpendicular member. Nonlinear analysis, regular waves with $H = 3.4\,m$ and $T = 3.1\,s$.

	$\Delta\sigma_{0,max}$	$\Delta\sigma_{0,min}$	$\frac{\Delta\sigma_{0,max}}{\Delta\sigma_{0,min}}$
Linear	$244\,MPa$	$85\,MPa$	2.9
Nonlinear	$116\,MPa$	$36\,MPa$	3.2
$\frac{\Delta\sigma_{0,L}}{\Delta\sigma_{0,NL}}$	2.1	2.4	X

Table 9.5: Largest and smallest maximum stress range $\Delta\sigma_0$ for linear and nonlinear analyses. Regular waves: wave height $H = 3.4\,m$, wave period $T = 2.5\,s\ -\ 7\,s$.

	$\sigma_{\eta_{vert}}$	$\sigma_{\eta_{hor}}$
Analytical	$0.226\,m$	$0.230\,m$
TDA	$0.219\,m$	$0.227\,m$
Diff.	-3%	-1%

Table 9.6: Comparison of standard deviations for vertical and horizontal displacement from analytical analyses and TDA.

From e.g. Newland (2005) we know that for a linear system the integral of a spectrum is equal to the variance:

$$\sigma_x{}^2 = \int_0^\infty S_x(\omega)d\omega \tag{9.2}$$

The response spectrum $S_x(\omega)$ can be found by using the wave elevation spectrum and the relevant transfer functions. We use the hydrodynamic coefficients of TRW C[21] and an H_s/T_p-pair corresponding to $\bar{U}_{10} = 15\,m/s$, i.e. $H_s = 0.7\,m$, $T_p = 2.8\,s$, see Table 8.5. In Table 9.6 the standard deviation for vertical and horizontal displacement (i.e. $\sigma_{\eta_{vert}}$ and $\sigma_{\eta_{hor}}$) are found analytically and from a TDA. The TDA has a total duration of $900\,s$, and as before the first $20\,s$ are discarded. The correspondence between the analytical and numerical results are very good, and this indicates that irregular waves have been implemented properly.

9.3 Sensitivity to analysis duration

In this section we will investigate the required analysis duration for convergence of (the stochastic variable) fatigue life L_{sc}. Since regular waves yield a periodic response with a period equal to the wave period, only the maximum stress over a wave period is typically[22]

[21] This is the only section where the coefficients for TRW C are used, otherwise the coefficients for TRW B are used

[22] Nonlinear analysis can have more than one pair of extreme points over a wave period.

of interest and can be found by a short analysis (e.g. $30\,s$ as previously). For irregular waves the response will not be periodic, and a much longer analysis must be performed for the results to converge. However, since fatigue life is typically less dependent on the very rare maximum stress ranges and more dependent on the medium-to-high stress ranges that occur often, the required duration is expected to be shorter than what would be required in order to find a reliable extreme value.

To evaluate the required analysis duration we have performed three sets of eight TDAs with a duration of $1800\,s = \frac{1}{2}\,h$, $3600\,s = 1\,h$, and $7200\,s = 2\,h$. Each stress time history is first rainflow counted (to obtain a list of stress ranges $\Delta\sigma$). Fatigue life L_{sc} and seven different statistical parameters are found based on each list. These eight parameters are: fatigue life for a C2 detail $L_{sc,C2}$, median stress range $\widetilde{\Delta\sigma}$, mean stress range $\mu_{\Delta\sigma}$, coefficient of variation for the stress range $COV_{\Delta\sigma}$, maximum stress range $\Delta\sigma_0$, average stress range period $T_{\Delta\sigma}$, and finally the scale and shape parameters for a fitted Weibull distribution, i.e. q and h, respectively. ($T_{\Delta\sigma}$ is the ratio of TDA duration and the number of stress ranges observed.) For each time duration we then have eight sets of these parameters, and for each parameter the expected value E and the COV are found based on the eight values, see Table 9.7.

The analysis is performed for the H_s/T_p combination of sc. #3 (corresponding to a wind speed of $15\,m/s$), i.e. $H_s = 0.7\,m$ and $T_p = 2.8\,s$. The stress histories are generated for the critical point of the perpendicular cylinder. Both linear and nonlinear analysis are performed.

A number of half-hour analyses are also performed for the critical point of the parallel cylinder, see Table 9.8.

Discussion

Based on the results presented above, the following conclusions are drawn:

- The coefficient of variation is considerably higher for fatigue life L_{sc} and maximum stress range $\Delta\sigma_0$ than for the other parameters presented.
- Doubling the analysis duration leads to a reduction of COV for fatigue life of roughly one third.
- For the perpendicular cylinder the COV for linear analysis are typically higher than for the nonlinear analysis. The opposite is the case for the parallel cylinder.
- The perpendicular and the parallel cylinders give very similar results, both in terms of expected values and coefficients of variation.
- The COV of the fatigue life and maximum stress range are sufficiently low for the shortest analysis duration (i.e. $1800\,s$) to be used in the subsequent fatigue analyses.

t [h]			$L_{sc,C2}$ [year]	$\widetilde{\Delta\sigma}$ [MPa]	$\mu_{\Delta\sigma}$ [MPa]	$COV_{\Delta\sigma}$ [%]	$\Delta\sigma_0$ [MPa]	$T_{\Delta\sigma}$ [s]	q [-]	h [-]
$\frac{1}{2}$	L	E	11.2	4.2	11.1	120	70.4	0.88	8.47	0.685
		COV	8.3	3.3	0.8	0.9	8.9	0.8	2.0	1.7
	N	E	15.7	4.0	10.6	118	62.1	0.86	8.13	0.686
		COV	6.5	3.9	0.9	0.9	6.1	1.2	1.2	0.9
1	L	E	11.4	4.1	11.0	120	71.8	0.88	8.47	0.688
		COV	6.1	3.1	1.1	0.7	3.3	1.1	1.5	0.4
	N	E	16.1	4.0	10.5	119	67.0	0.86	8.08	0.692
		COV	4.4	3.7	0.9	0.9	2.6	1.1	1.8	1.1
2	L	E	11.3	4.1	11.0	120	73.8	0.87	8.44	0.683
		COV	4.8	1.4	1.1	0.3	6.3	0.8	1.2	0.5
	N	E	16.3	4.1	10.5	118	67.4	0.86	8.12	0.692
		COV	2.9	1.8	0.6	0.6	3.0	0.6	0.7	0.8

Table 9.7: Expected value E and COV found for eight parameters based on eight rainflow counted stress time histories for each duration t. Perpendicular cylinder. Sc. # 3: $H_s = 0.7\,m$, $T_p = 2.8\,s$.

		$L_{sc,C2}$ [year]	$\widetilde{\Delta\sigma}$ [MPa]	$\mu_{\Delta\sigma}$ [MPa]	$COV_{\Delta\sigma}$ [%]	$\Delta\sigma_0$ [MPa]	$T_{\Delta\sigma}$ [s]	q [-]	h [-]
L	E	14.0	4.8	11.2	114	66.7	0.93	9.12	0.707
	COV	8.5	2.0	1.6	0.9	6.2	1.0	1.4	2.3
NL	E	17.3	4.4	10.6	116	63.5	0.89	8.40	0.693
	COV	11.1	4.4	1.7	1.3	8.3	1.3	2.7	2.2

Table 9.8: Expected value E and COV found for eight parameters based on eight rainflow counted stress time histories. Parallel cylinder. Sc. # 3: $H_s = 0.7\,m$, $T_p = 2.8\,s$. Analysis duration $t = 1800\,s$.

9.4 Sensitivity to peak period

In Section 9.1.1 we found that the response to regular waves was extremely sensitive to the wave period. Now, we investigate the dependence of peak period T_p for the perpendicular member and the irregular wave analyses. The stronger the dependence on the peak period T_p is, the finer the T_p-axis of the scatter diagram should be subdivided. Sc. # 2-5 are the entries of the scatter diagram which are most important for the fatigue damage, see Table 9.12 (sc. # 1, 6, and 7 could also have been included for completeness). Similar to regular waves, for each seastate we consider the peak period interval from the value which applies for the seastate below to the value which applies for the seastate above, see Table 9.1. A subdivision of $0.1\,s$ is used. Additionally the max/min points of Table 7.10 are included. The results can be found in Appendix G, Table G.10 to G.13. The maximum stress range $\Delta\sigma_{0,sc}$, fatigue life L_{sc} are included for linear and nonlinear analyses. Additionally, the ratios of nonlinear and linear results are presented.

The results from the tables are shown in Figure 9.4 and 9.5. The plots show that the relationship between T_p and fatigue life is approximately linear. Thus, linear curve fitting is performed for all curves using the least squares method. The resulting lines $L_{sc} = a \cdot T_p + b$ are included in the plots and the linear coefficients a and b are presented in Table 9.9. The ratios of the slope parameter a to the reference fatigue life $L_{sc,ref}$ of the respective seastate are also included. This percentage tells how much the fatigue life L_{sc} is expected to increase with an increase in the peak period of $0.1\,s$ (thus the multiplication by $0.1\,s$). $0.1\,s$ is chosen as it is considered to be a convenient level of granularity when discussing the peak period and because it gives manageable $\frac{a \cdot 0.1\,s}{L_{sc}}$-values. The linear and nonlinear $L_{sc,ref}$-values for sc. # 2-5 used when calculating the $\frac{a \cdot 0.1\,s}{L_{sc,ref}}$-values are (see Table G.10 to G.13):

- $L_{sc,L,ref}$ $= 117.6\,y$, $11.4\,y$, $1.5\,y$, and $0.92\,y$
- $L_{sc,NL,ref} = 138.0\,y$, $16.1\,y$, $4.3\,y$, and $2.4\,y$

Alternatively, the linear and nonlinear $L_{sc,ref}$-values based on linear regression could have been used (see the diagonals of Table 9.10 and 9.11):

- $L_{sc,L,ref}$ $= 125\,y$, $10.1\,y$, $2.2\,y$,and $0.79\,y$
- $L_{sc,NL,ref} = 150\,y$, $14.2\,y$, $4.9\,y$, and $2.5\,y$

The corresponding sets of values are very similar (this can also be seen from Figure 9.4 and 9.5). Thus, the choice of which set to use is of relatively little importance.

The following is given as an example of the interpretation of Table 9.9. For sc. # 4 ($H_s = 1.0\,m$ and $T_p = 3.2\,m$) an increase in peak period from to 3.2 to $3.3\,m$ is expected to increase the fatigue lifetime L_{sc} with 7.5% for linear analyses, i.e. from $1.5\,y$ to $1.6\,y$.

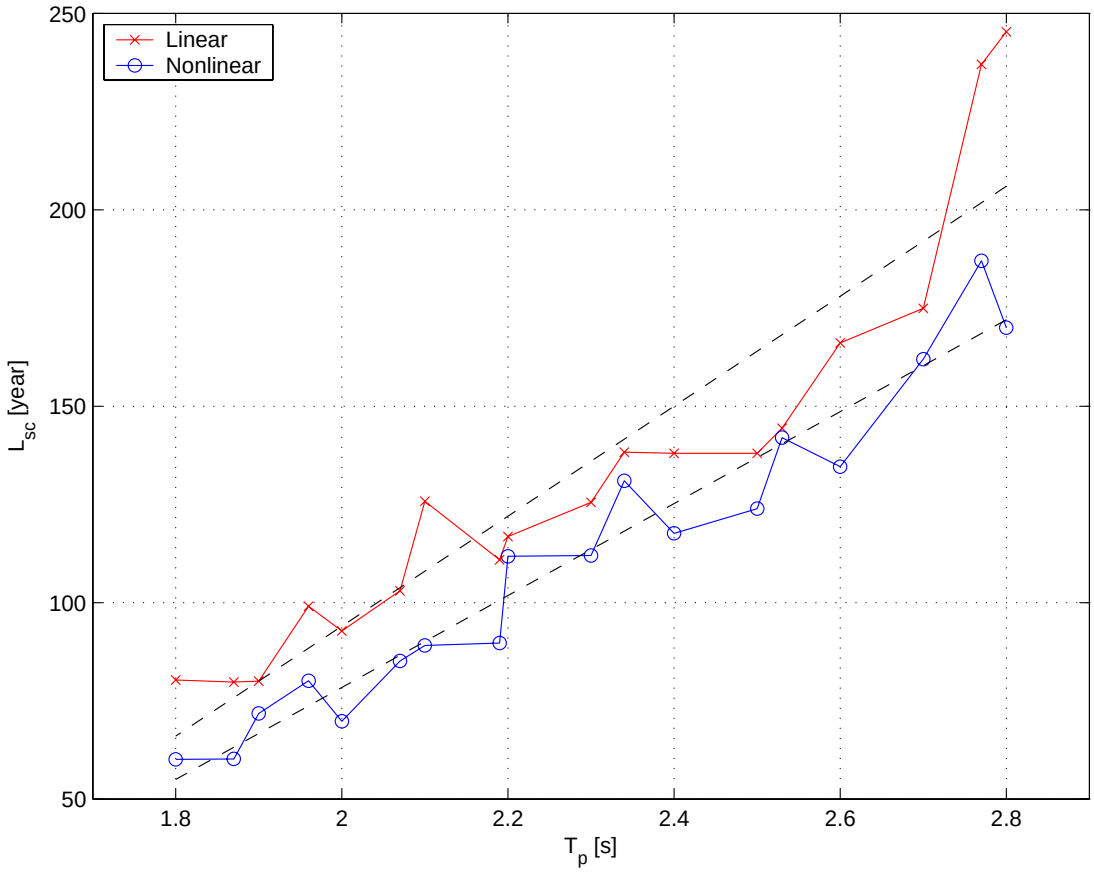

Figure 9.4: Peak period T_p vs. fatigue life L_{sc} for significant wave height $H_s = 0.4\,m$. Broken line is a linear regression fit, see Table 9.9

Sc.#	T_p [s]	Linear a [year/s]	Linear b [year]	Linear $\frac{a \cdot 0.1\,s}{L_{sc,ref}}$ [%]	Nonlinear a [year/s]	Nonlinear b [year]	Nonlinear $\frac{a \cdot 0.1\,s}{L_{sc,ref}}$ [%]
2	$1.8 - 2.8$	117	-155	9.9	140	-186	10
3	$2.4 - 3.2$	5.3	-4.6	4.6	9.9	-13.5	6.1
4	$2.8 - 3.5$	1.2	-1.5	7.5	3.7	-7.1	8.7
5	$3.2 - 3.8$	1.1	-3.0	12	2.6	-6.5	11

Table 9.9: Linear regression parameters a and b for lifetime L_{sc} of SN-curve C2 as a function of peak period T_p ($L_{sc} = a \cdot T_p + b$) and ratio of slope parameter a to the reference lifetime $L_{sc,ref}$. Results for both linear and nonlinear analyses are included.

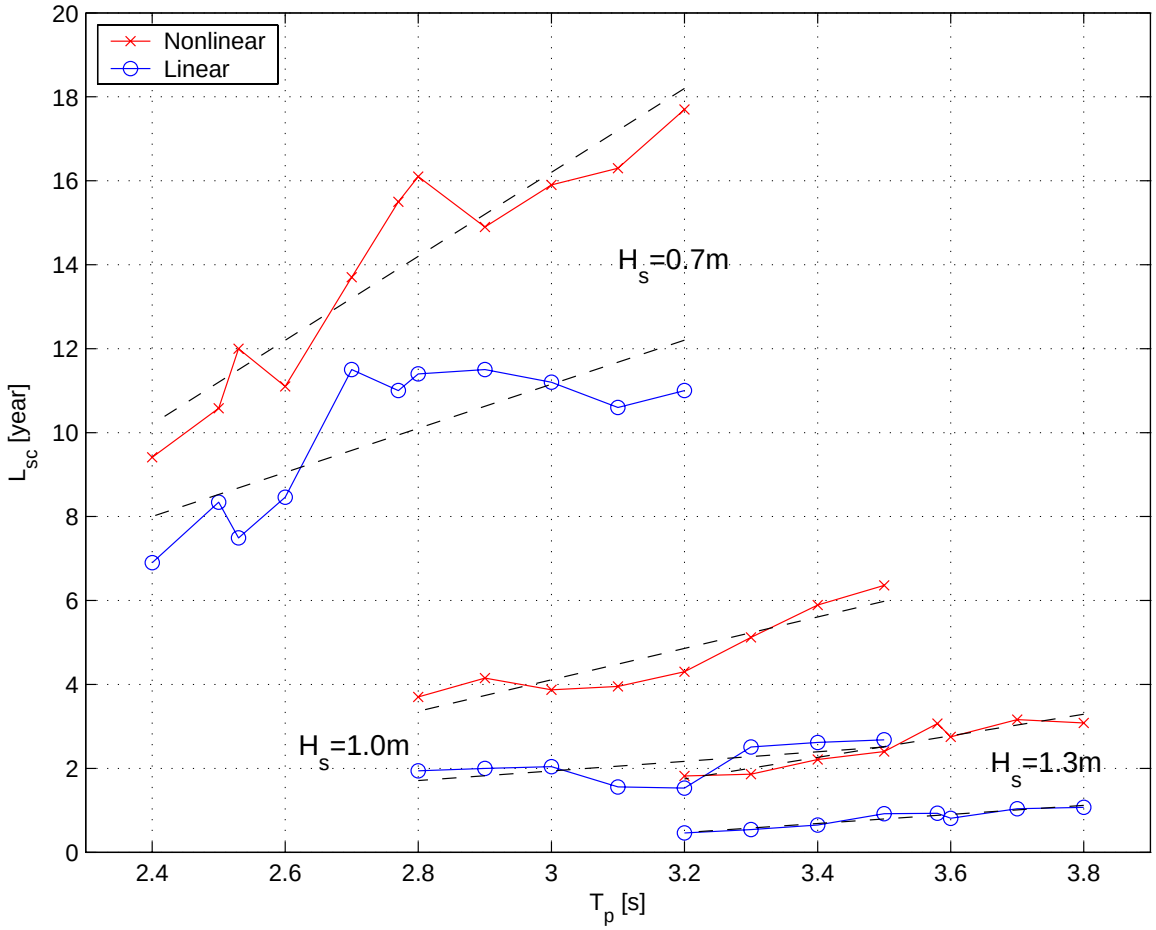

Figure 9.5: Peak period T_p vs. fatigue life L_{sc} for three levels of H_s: $0.7\,m$, $1.0\,m$, and $1.3\,m$. Broken lines are linear regression fits, see Table 9.9.

Discussion

The sensitivity to peak period T_p for irregular waves is much weaker than the sensitivity to wave period T for regular waves, see Section 9.1.1. Instead of being determined by the degree of in-phase loading, irregular waves exhibit a systematic linear increase in fatigue life with peak period. However, it seems like the increase in fatigue life is slower when approaching an in-phase period (e.g. in the $2.8\,s - 3.1\,s$ interval) as compared to the opposite case (e.g. in the $2.5\,s - 2.8\,s$ interval). This is probably because the increase of in-phase loading is counteracting the effect of increasing period.

We can now compare the results for regular waves (see Section 9.1.1) and irregular waves (this section) to illustrate the difference in effect on fatigue life due to wave period T of regular waves vs. peak period T_p for irregular waves. As an example, we look at regular waves with a wave height of $H = 0.7\,m$ and wave period T in the interval from $2.4\,s$ to $3.2\,s$ (see Figure 9.1 and Table G.7 in Appendix G). This is compared to irregular waves with significant wave height $H_s = 0.7\,m$ and peak period T_p in the interval from $2.4\,s$ to $3.2\,s$ (see Figure 9.5 and Table G.11 in Appendix G). The fatigue life times are shown in Figure 9.6. Due to the large variation of lifetimes for regular waves compared to irregular waves, the logarithmic value of the fatigue life L_{sc} is plotted. The figure illustrates the large variation in fatigue life values from a regular wave analysis compared to an irregular wave analysis. The latter appears by comparison to be virtually independent of the peak period (although Figure 9.5 shows that the fatigue life approximately doubles over the interval $T_p = 2.4\,s - 3.2\,s$). As indicated on p.129, using one regular wave to represent one seastate can not be expected to give a good estimate of fatigue life.

The equivalent stress range, see Equation 8.22, is the value that a regular wave stress range should have to yield the same fatigue damage as the irregular wave approach. Assuming $2\,s$ period of fluctuation (i.e. $n_0 = 3.15 \cdot 10^8$), and a Rayleigh stress range distribution (i.e. $h = 2$) the ratio of equivalent stress range $\Delta\sigma_{eq}$ to maximum stress range $\Delta\sigma_0$ is: $\frac{\Delta\sigma_{eq}}{\Delta\sigma_0} = 29\%$. Looking at Figure 9.6 we see that regular and irregular analyses yield the same damage between $T = 2.6\,s$ and $2.7\,s$. The ratios of regular wave stress range and irregular wave maximum stress range for these periods are (see Table G.7 and G.11): $\frac{44.9\,MPa}{69\,MPa} = 65\%$ and $\frac{28.7\,MPa}{66\,MPa} = 43\%$, respectively. The ratio found above falls slightly outside this interval. This can be due to several factors, e.g. there are more fluctuations in the irregular analysis and that the stress ranges are not (perfectly) Rayleigh distributed.

If a wave height of $H = H_{max} = 1.9 \cdot H_s = 1.3m$ were used instead of $H = H_s$, the maximum and minimum stress ranges on the $2.4\,s - 3.2\,s$ interval for the linear analysis would be $47.7\,MPa$ and $90.6\,MPa$. These values yield fatigue lives of approximately 2 years and less than 0.1 year, i.e. an underestimated fatigue life for all wave periods.

9.5 Sensitivity to significant wave height

As Figure 9.4 and 9.5 indicate a strong sensitivity to significant wave height, this is further investigated in the present section. As in the previous section, sc. # 2-5 are considered,

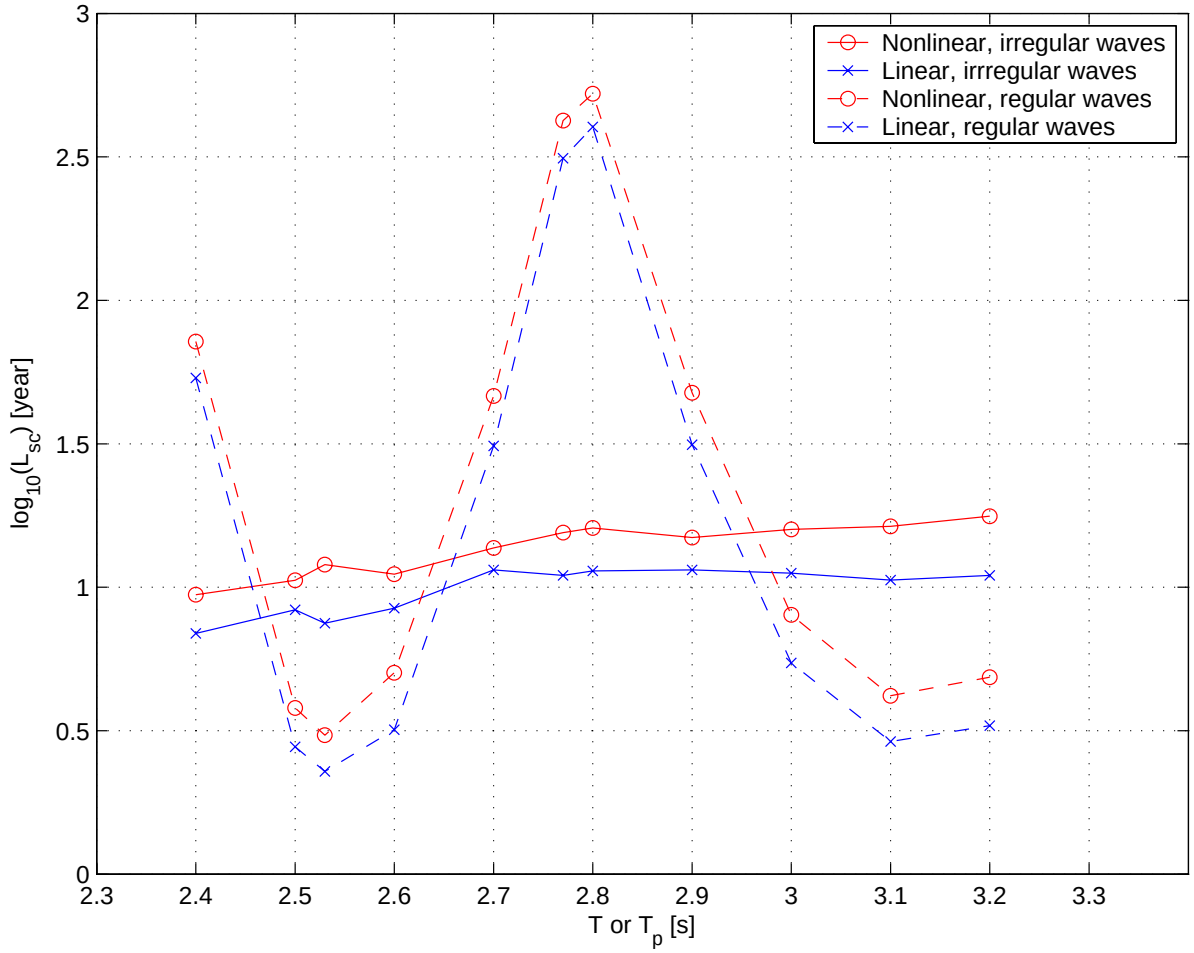

Figure 9.6: Wave period T or peak period T_p vs. the logarithm of fatigue life L_{sc} for $H = 0.7\,m$ and $H_s = 0.7\,m$, respectively. Results for both linear and nonlinear analyses are shown.

H_s	T_p [s]					
$[m]$	1.8	2.4	2.8	3.2	3.5	3.8
0.2	X	4441	X	X	X	X
0.4	55	125	172	X	X	X
0.7	X	8.0	10.1	12.2	X	X
1.0	X	X	1.7	2.2	2.5	X
1.3	X	X	X	0.47	0.79	1.12
1.6	X	X	X	X	0.29	X

Table 9.10: Fatigue life L_{sc} found by means of linear regression. Linear structural analysis. X designates no analysis performed.

but now T_p is kept constant. H_s varies from the H_s-value of the scatter entry below to the H_s-value of the scatter entry above, see Table 9.1, e.g. from $0.2\,m$ to $0.7\,m$ for sc. #2.

The maximum stress range $\Delta\sigma_{0,sc}$, the fatigue life L_{sc} for linear and nonlinear analyses as well as the ratio of nonlinear to linear results for either category are included in Table G.14 - G.17 in Appendix G. The fatigue life is plotted in Figure 9.7.

Discussion

As opposed to the linear behavior observed for constant H_s (see Figure 9.4 and 9.5), the curves for constant T_p are visually assessed to be parabolic. The fitted linear relationship between peak period and fatigue life causes the relative reduction in fatigue life to decrease with increasing peak period. The (approximate) parabolic relationship between H_s and fatigue life causes the relative reduction in fatigue life with increasing H_s to decrease, e.g. for $T_p = 3.2\,s$ the reduction per $0.1\,m$ increase goes from $\frac{9.6\,y - 17.7\,y}{17.7\,y} = -46\%$ for $H_s = 0.7\,m$ to $\frac{1.8\,y - 2.3\,y}{2.3\,y} = -22\%$ for $H_s = 1.2\,m$, see Table G.16.

9.6 Peak period vs. significant wave height sensitivity

The linear and nonlinear results in Table G.10 to G.13 (Appendix G) are summarized in Table 9.10 and 9.11, respectively. The fatigue lifetimes for SN-curve C2 are presented for the T_p-values of the scatter diagram, and the respective significant wave heights H_s. The values for the linear regression are used (see Table 9.9 and the broken linear lines of Figure 9.4 and 9.5), except for the two extreme combinations $H_s = 0.2\,m / T_p = 2.4\,s$ and $H_s = 1.6\,m / T_p = 3.5\,s$ for which the analysis results are presented directly, as these are the only analyses for the respective H_s-levels. An X in the tables indicates that no analysis has been performed for this H_s/T_p-combination. These combinations are considered very unlikely.

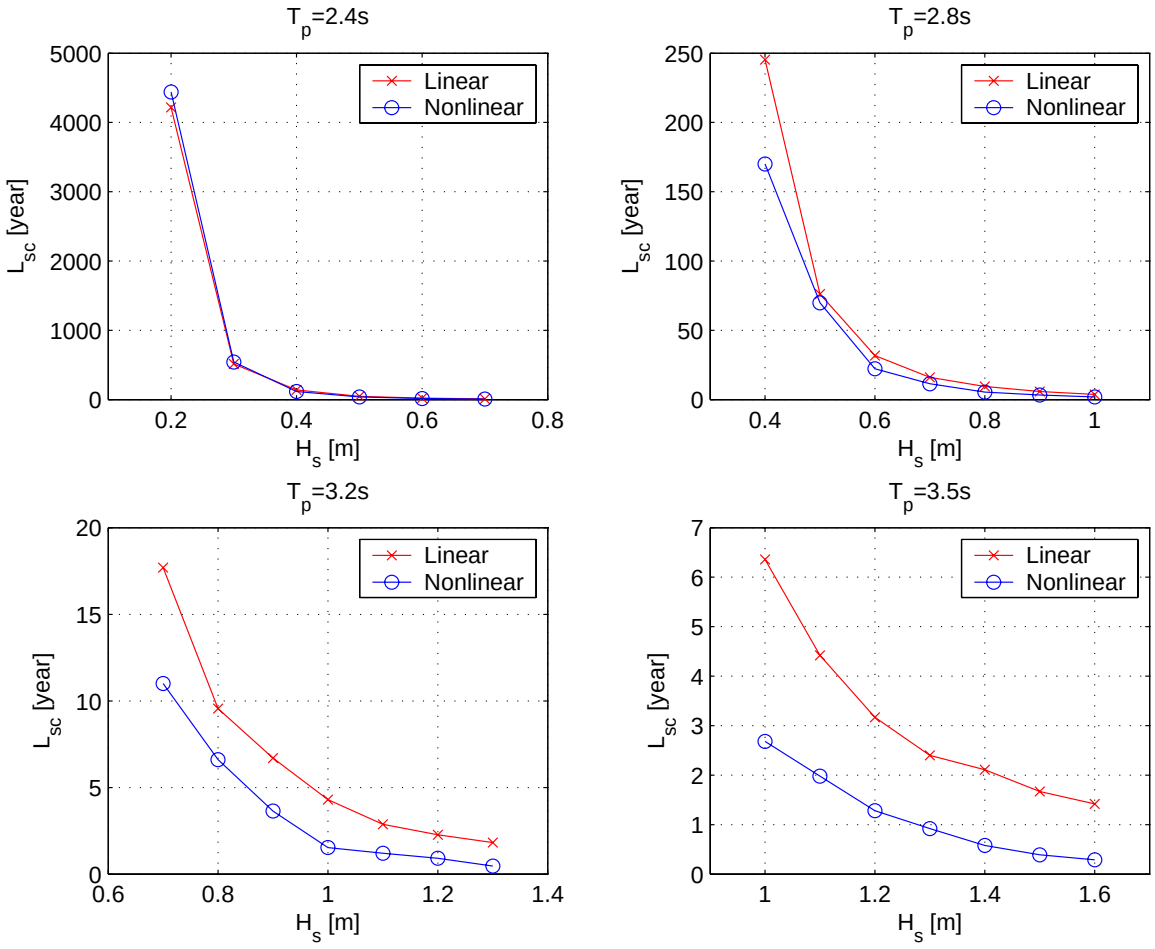

Figure 9.7: H_s vs. fatigue life L_{sc} for four different values of T_p

H_s	T_p [s]					
$[m]$	1.8	2.4	2.8	3.2	3.5	3.8
0.2	X	4217	X	X	X	X
0.4	66	150	206	X	X	X
0.7	X	10.2	14.2	18.2	X	X
1.0	X	X	3.4	4.9	6.0	X
1.3	X	X	X	1.8	2.5	3.3
1.6	X	X	X	X	1.4	X

Table 9.11: Fatigue life L_{sc} found by means of linear regression. Nonlinear structural analysis. X designates no analysis performed.

For both the linear and nonlinear case we see that for a given H_s the fatigue life increases with peak period. The increase is typically between 30 and 100% from one level to the next. The increase in fatigue life with *decreasing* H_s is stronger for both the linear and the nonlinear analyses. The effect is strongest from 0.7 to $0.4\,m$ with a 15-fold increase. Comparing the linear to the nonlinear results, we observe that there is a clear difference between the results for $H_s = 0.4\,m$ and $0.7\,m$ on one side and $H_s = 1.0\,m$ and $1.3\,m$ on the other. For the former interval the nonlinear fatigue lifetimes are roughly 50% higher than the linear. For the latter interval the differences are roughly between 200% and 300%. These results are probably due to the increase in nonlinear effects with increasing wave height and conform to previous results.

Discussion

The investigation of the sensitivity of fatigue life to peak period and significant wave height, respectively, leads to the following conclusions:

- The sensitivity to H_s is more important than the sensitivity to T_p, thus a subdivision of the H_s axis in the scatter diagram is most important.
- As the sensitivity to H_s is more important than the sensitivity to T_p, the 1D scatter diagram approach based on H_s, see Section 8.4.1, is likely to be a better approximation than if a 1D approach based on T_p was applied.
- The results indicate that a further subdivision of the scatter diagram should be considered for H_s (and in particular for the interval from $0.7\,m$ to $1.0\,m$). The same interval would be identified also based only on the D/D_{tot}-ratios of Table 9.12 because sc. # 3 and 4 yield the highest relative damage.

9.7 Analysis based on scatter diagram

Fatigue analyses according to Section 8.5 are performed here for irregular waves, see Table 9.12 and 9.13. The presentation follows the lines for regular waves, see Table 9.2 and 9.3, but $\frac{\Delta\sigma}{H}$ and $\frac{\Delta\sigma_{NL}}{\Delta\sigma_L}$ have been replaced with $\frac{L_{sc,NL}}{L_{sc,L}}$, i.e. the ratio of nonlinear and linear fatigue life of the respective seastates.

In Table 9.14 the results from Table 9.12 and 9.13 are summarized, cf. Table 9.4. Additionally, the maximum stress range $\Delta\sigma_0$ (over the design fatigue life, typically 20 years) is presented for the linear and nonlinear case. $\Delta\sigma_0$ is conservatively set as the maximum stress range of the sc. #7 ($H_s = 2.0\,m$ and $T_p = 4.0\,s$) simulation, i.e. the 50-year storm.

Discussion

As opposed to the regular wave analyses (see Table 9.2 and 9.3), the fatigue life has a continuous reduction with increasing seastate, and is thus probably a more realistic result.

The reduction in fatigue life is by a factor approximately varying from 2 to 15, with the highest factor for the lowest seastates. For higher seastates the decrease in fatigue life from one seastate to the higher is smaller for nonlinear analysis than for linear analysis. This is in accordance with previous observations.

For the perpendicular cylinder, the fatigue damage is highest for sc. # 3 and 4, but sc. # 2, 5 and 6 also have noticeable contributions. For linear analyses the fatigue damage is more skewed towards the higher seastates than for nonlinear analysis.

For the parallel cylinder the damage for both linear and nonlinear analysis are more skewed towards the higher seastates than the respective analysis for the perpendicular cylinder. Comparing $\Delta\sigma_{0,sc}$ and fatigue life, we see that the perpendicular cylinder has the highest $\Delta\sigma_{0,sc}$ and lowest L_{sc} for sc. # 1-3, whereas the opposite is the case for sc. # 5-6. This confirms the observation from Figure 7.4 that the parallel members have a strong increase in the moment about the horizontal axis for high seastates (i.e. wave lengths over $20\,m$ for the regular wave case).

Table 9.14 shows that the fatigue life is similar for the perpendicular and the parallel members: the fatigue life of the perpendicular cylinder is approximately 20-30% higher than for the parallel cylinder. The fatigue life of the nonlinear approach is approximately twice the fatigue life of the linear approach. For the C2 detail, the fatigue life is sufficient (i.e. more than $20\,years$) according to the nonlinear approach, but not sufficent for the linear approach. For the F detail, neither the linear nor the nonlinear approach gives a sufficent fatigue life.

Comparing the summary Tables 9.4 and 9.14 we see that the results are relatively similar. However, whereas the regular wave approach predicts lower fatigue life for the perpendicular cylinder, it predicts higher fatigue life for the parallel cylinder. As concluded in Section 9.1.2, the simplified regular wave approach is very sensitive to the wave period and it is a coincidence whether the agreement with the irregular wave approach is good or if the results are higher or lower.

9.8 Statistical properties of stress range distributions

As stated in Section 8.1.1, the state-of-the-art of the SN approach to fatigue life analysis is a TDA combined with cycle counting. Thus, this was the basis of the analyses of Section 9.7. Nevertheless, it is of interest to investigate the statistical properties of the stress range distributions, e.g. in order to:

- Estimate the short- and/or long term distribution that can be used for simplified methods, and evaluate the applicability of simplified methods.

- Get a better understanding of the underlying processes that cause the stress range distributions and thus the fatigue damage.

- Evaluate the quality and plausibility of the generated stress range histories.

	Sc. #		1	2	3	4	5	6	7
L	$\Delta\sigma_{0,sc}$ [MPa]		24	46	72	106	115	150	190
	C2	L_{sc}	1709	119	14	1.5	0.86	0.35	0.08
		D_{sc,L_0}	0.00	0.06	0.28	0.58	0.18	0.05	0.01
	F	L_{sc}	308	22	2.5	0.28	0.15	0.06	0.01
		D_{sc,L_0}	0.02	0.32	1.31	3.15	0.97	0.26	0.08
	$\frac{D_{sc,L_0}}{D_{tot}}$ [%]		0	5	21	51	16	4	1
NL	$\Delta\sigma_{0,sc}$ [MPa]		24	40	67	76	85	94	104
	C2	L_{sc}	1991	138	16	4.3	2.4	1.7	0.90
		D_{sc,L_0}	0.00	0.05	0.20	0.20	0.06	0.01	0.00
	F	L_s	359	25	2.8	0.8	0.4	0.3	0.2
		D_{sc,L_0}	0.02	0.28	1.16	1.14	0.35	0.05	0.01
	$\frac{L_{sc,NL}}{L_{sc,L}}$ [-]		1.2	1.2	1.2	2.8	2.8	4.9	10.5
	$\frac{D_{sc,L_0}}{D_{tot}}$ [%]		1	9	39	38	11	2	0

Table 9.12: Fatigue life time for critical point on perpendicular cylinder. Irregular waves. SN-curves C2 and F

	Sc. #		1	2	3	4	5	6	7
L	$\Delta\sigma_{0,sc}$ [MPa]		23	39	69	98	163	201	296
	C2	L_{sc}	2236	147	14	1.9	0.49	0.07	0.01
		D_{sc,L_0}	0.00	0.05	0.24	0.47	0.31	0.25	0.10
	F	L_s	403	26	2.5	0.34	0.09	0.01	0.00
		D_{sc,L_0}	0.02	0.26	1.31	2.63	1.71	1.37	0.53
	$\frac{D_{sc,L_0}}{D_{tot}}$ [%]		0	3	17	34	22	18	7
NL	$\Delta\sigma_{0,sc}$ [MPa]		22	37	62	81	102	124	128
	C2	L_{sc}	2622	177	16	3.7	1.3	0.43	0.22
		D_{sc,L_0}	0.00	0.04	0.20	0.24	0.12	0.04	0.01
	F	L_s	473	32	2.9	0.67	0.23	0.08	0.04
		D_{sc,L_0}	0.02	0.22	1.12	1.32	0.65	0.21	0.03
	$\frac{L_{sc,NL}}{L_{sc,L}}$ [-]		1.2	1.2	1.2	2.0	2.6	6.5	17.8
	$\frac{D_{sc,L_0}}{D_{tot}}$ [%]		0	6	31	37	18	6	1

Table 9.13: Fatigue life time for critical point on parallel cylinder. Irregular waves. SN-curves C2 and F

SN		Perpendicular			Parallel		
		L [year]	D_{20y} [-]	$\Delta\sigma_0$ [MPa]	L [year]	D_{20y} [-]	$\Delta\sigma_0$ [MPa]
C2	Linear	18	1.1	190	14	1.4	296
	Nonlinear	38	0.53	104	31	0.64	128
F	Linear	3.3	6.1	X	2.6	7.8	X
	Nonlinear	6.7	3.0	X	5.6	3.6	X

Table 9.14: Fatigue life L, fatigue damage over 20 years D_{20y}, and maximum stress range $\Delta\sigma_0$ for critical point on perpendicular and parallel cylinder. Irregular waves. SN-curves C2 and F.

#	Linear					Nonlinear				
	t [h]	L_{sc} [year]	$\Delta\sigma_{0,sc}$ [MPa]	q [-]	h [-]	t [h]	L_{sc} [year]	$\Delta\sigma_{0,sc}$ [MPa]	q [-]	h [-]
1	0.5	10.6	79	8.51	0.698	0.5	16.5	65	8.23	0.682
2	2	10.8	78	8.55	0.685	2	16.7	66	8.08	0.696
3	10	11.3	82	8.39	0.687	10	15.6	69	8.18	0.693

Table 9.15: Properties of three linear and three nonlinear stress range histories/distributions used for initial statistical evaluation. Sc. #3: $H_s = 0.7\,m$, $T_p = 2.8\,s$. Perpendicular cylinder. SN curve C2.

In this section we investigate the statistical properties of the stress range histories through Weibull plots, histograms, damage plots, and finally estimation of short- and long term distributions and evaluation of its applicability in relation to simplified methods.

As a basis for evaluation we will first use the stress range histories of three different analysis durations: $\frac{1}{2}\,h$, $2\,h$ and $10\,h$ for a linear structure and $\frac{1}{2}\,h$, $2\,h$ and $6\,h$ for a nonlinear structure. The fatigue life L_{sc}, the maximum stress range $\Delta\sigma_{0,sc}$, and the Weibull parameters q and h of the six stress range histories/distributions are shown in Table 9.15. The results apply to a perpendicular cylinder and the SN curve C2.

9.8.1 Weibull probability paper

The stress range corresponding to a narrow-band Gaussian response in a single seastate can be described by a Rayleigh distribution when this stress range is taken to be twice the amplitude, see e.g. (Moan, 2001). Figure 9.8 and 9.9 show 10 seconds plots[23] of time vs. bending moment resulting from linear and nonlinear analysis, respectively, for the present structure. The irregular wave histories both correspond to sc. # 3, but they

[23]The figures are screenshots from the prototype software.

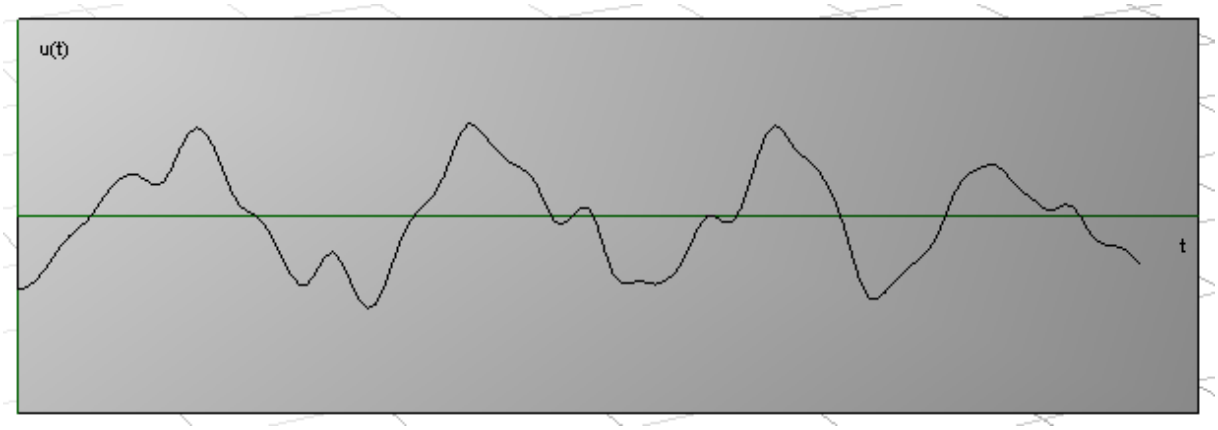

Figure 9.8: 10 seconds of the time vs. bending moment history for a linear analysis in sc. # 3 waves.

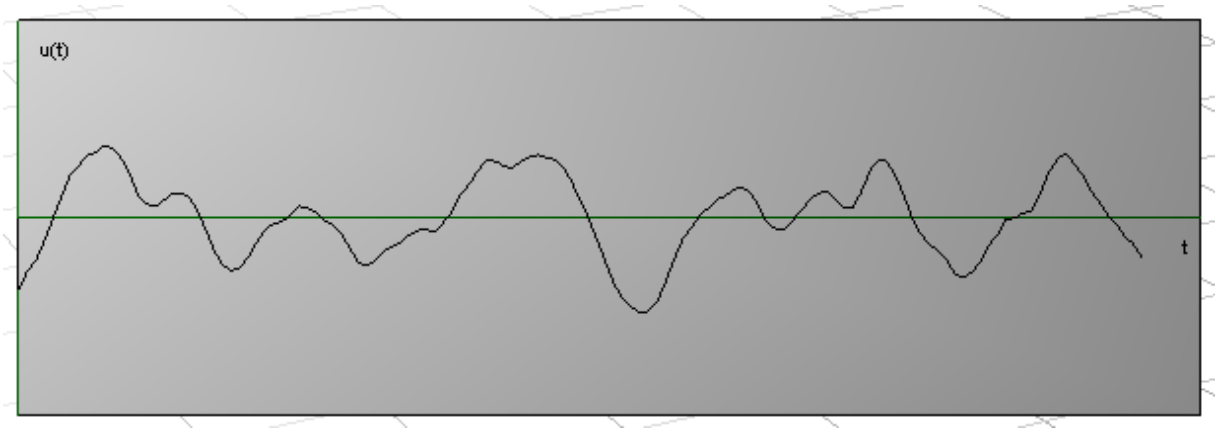

Figure 9.9: 10 seconds of the time vs. bending moment history for a nonlinear analysis in sc. # 3 waves.

are not identical. The figures illustrate that the response is not narrow-banded: high-frequency small amplitude stress fluctuations seem to be superimposed on the dominating low-frequency response. Thus, the short term distribution is not expected to be Rayleigh distributed. The Rayleigh distribution can be seen as a special case of the empirical (2- or 3-parameter) Weibull distribution, see e.g. (Walpole et al., 2006), (Leira, 2000). In particular, the Weibull distribution has been used to model the long-term distribution of stress ranges of offshore structures as well as the basis for simplified methods, see Section 8.3.3. Probability paper is often used to visually evaluate the degree of fit to a particular distribution. The six stress range histories described in Table 9.15 have been plotted in Weibull probability paper, see Figure 9.10.

Visual inspection of the plots indicate a fairly good fit, i.e. based on Weibull paper the Weibull distribution appears to be reasonable. The points representing the smallest and greatest stress ranges deviate most from the fitted linear line. The points to the far

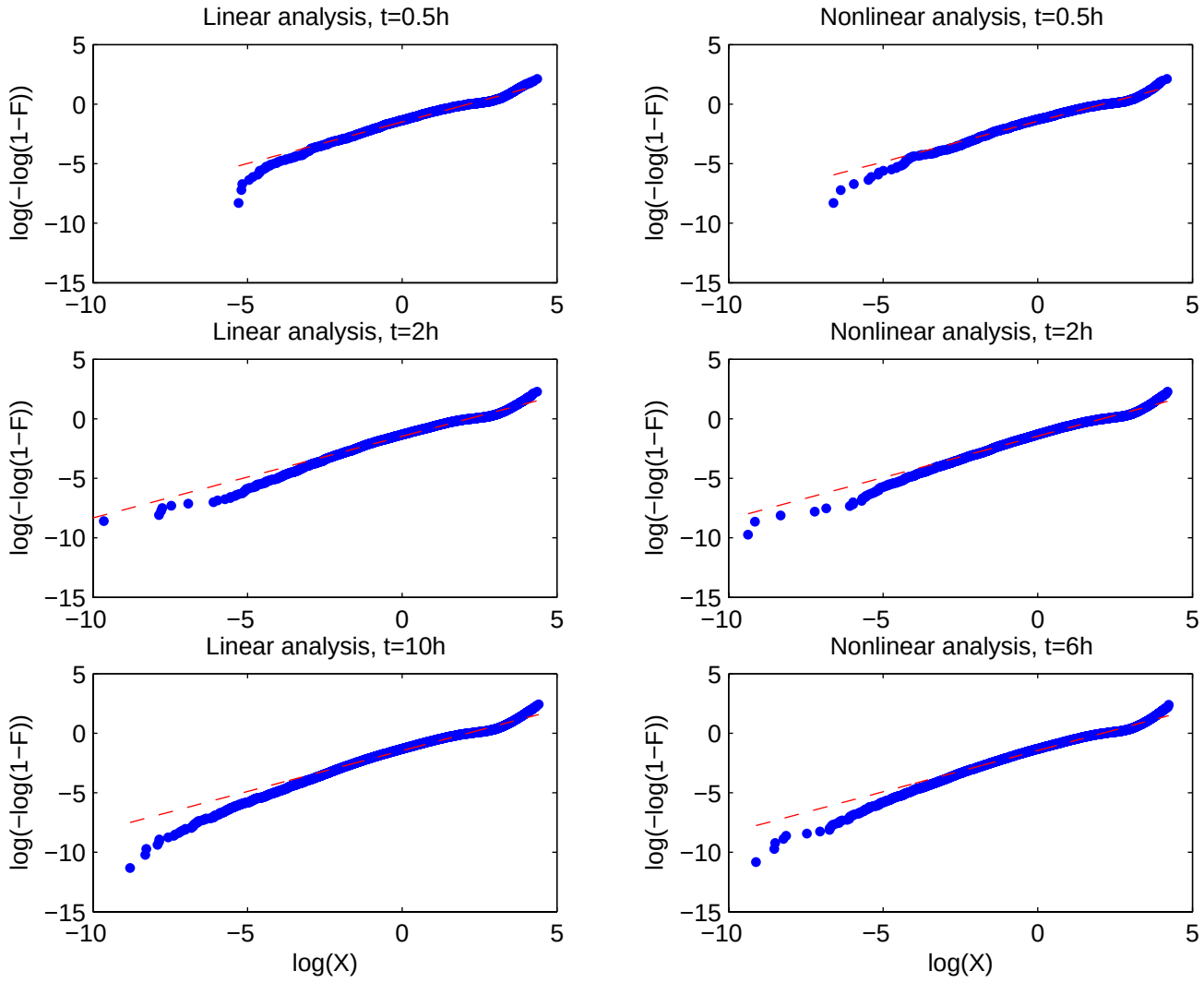

Figure 9.10: Weibull plots of the stress range histories described in Table 9.15

left (representing the smallest stress ranges) are below the fitted linear line, whereas the points to the far right (representing the greatest stress ranges) are above the line. The shape of the corresponding linear and nonlinear plots are very similar. Increasing analysis duration gives smaller minimum values. (However, in spite of the good fit we will see in Section 9.8.3 that the Weibull distribution gives poor results for estimation of fatigue life as well as maximum stress range.)

9.8.2 Stress range histograms and damage plots

Investigating the histograms of the stress range histories will indicate which (if any) probablity distributions that can be expected to fit. Histograms are shown for the six analyses of Table 9.15 on the left side in Figure 9.11 and 9.12. The intervals of the histograms have equal length and the number of intervals are the value of the maximum stress range $\Delta\sigma_0$ (measured inn [MPa]), i.e. each interval has a width of approximately $1\,MPa$ and there are approximately $70 - 80$ intervals.

Based on the total number of observations n and the SN curve for detail C2, the fatigue damage due to each interval is found, see Equation 8.4 and 8.5. The damage is normalize to a one year duration (by multiplying with $24\,h/day$ and $365\,days/year$ and dividing by the duration in hours). The damage per year for all intervals of the histograms are plotted and titled "Damage plots" on the right hand side of the corresponding histograms in Figure 9.11 and 9.12.

Discussion

At first glance the histograms seem to be similar to a Weibull distribution dominated by very small stress ranges ($< 5\,MPa$) and with a shape parameter smaller than 1 (i.e. no peaks). However, at closer inspection, a local minimum for stress ranges in the $5-20\,MPa$ interval and a subsequent local maximum — not in accordance with a Weibull distribution — can be observed. In Figure 9.13 the stress ranges smaller than $7\,MPa$ are removed from the $10\,h$ linear histogram (i.e. # 3, see Table 9.15), and we see that the transition from the sharply decreasing trend of the stress range to the slowly increasing trend is rather clearly defined (at approximately $12\,MPa$). By visual inspection of the distribution from the transition point onwards ($\approx 12\,MPa - 80\,MPa$) they appear to be consistent with Weibull distributions with a shape parameter h greater than 1 (possibly close to a Rayleigh shape with $h = 2$). Thus, it is hypothesized that the stress range distribution is a superposition of two processes: a high frequency Weibull process with shape parameter smaller than one and small stress ranges and a low frequencies Weibull process with shape parameter h greater than one. In the preceding section, first, Weibull distributions are fitted to the complete histograms. Secondly, parts of the histograms (with the lowest stress range levels removed) are fitted to Rayleigh distributions, see Figure 9.14 to 9.17.

The damage plots of Figure 9.11 and 9.12 showed that for the C2-curve stress ranges below $20\,MPa$ gave very little damage. Thus, the small stress ranges of the high-frequency process is probably of limited importance for the fatigue damage.

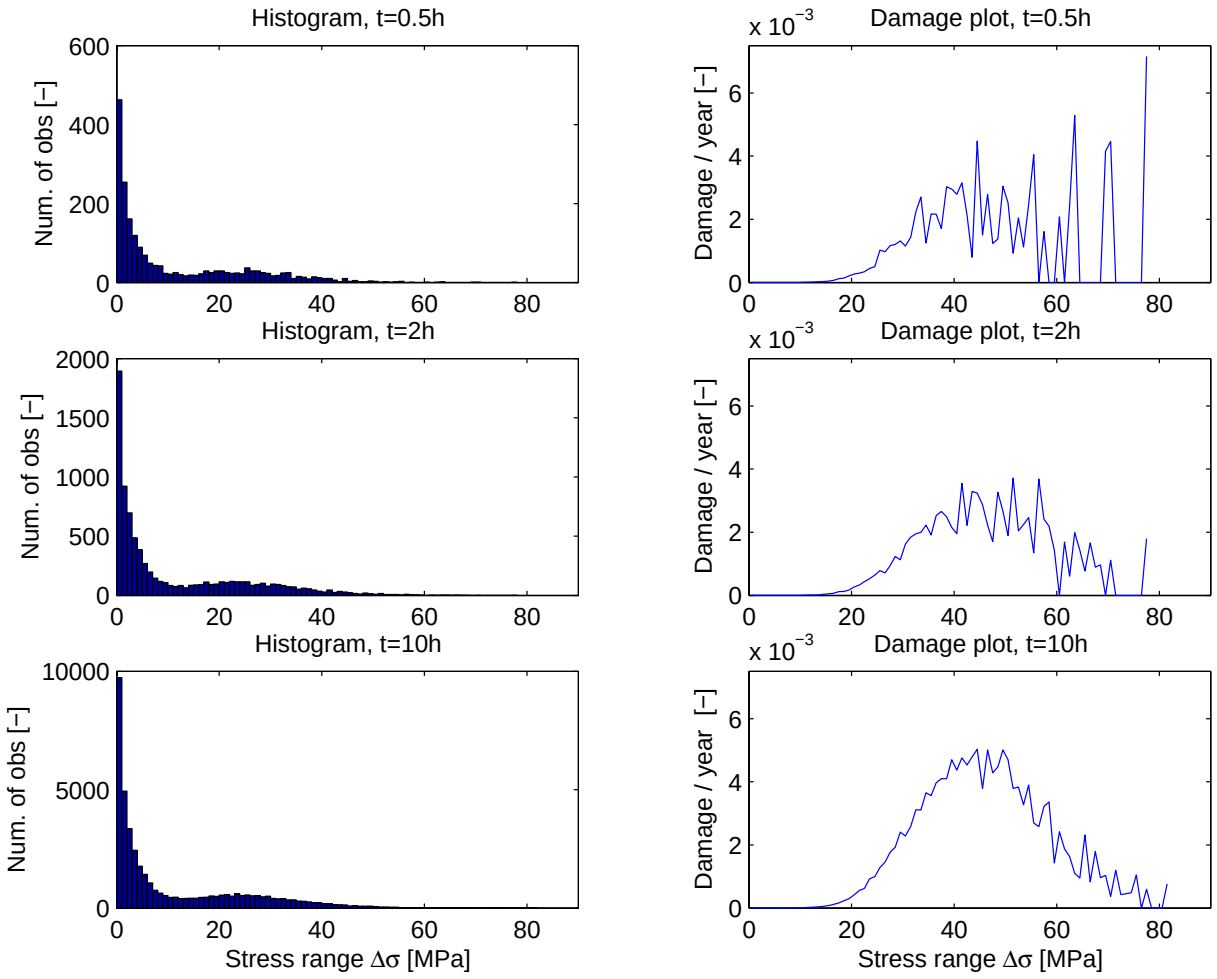

Figure 9.11: Histograms and damage plots for linear analysis

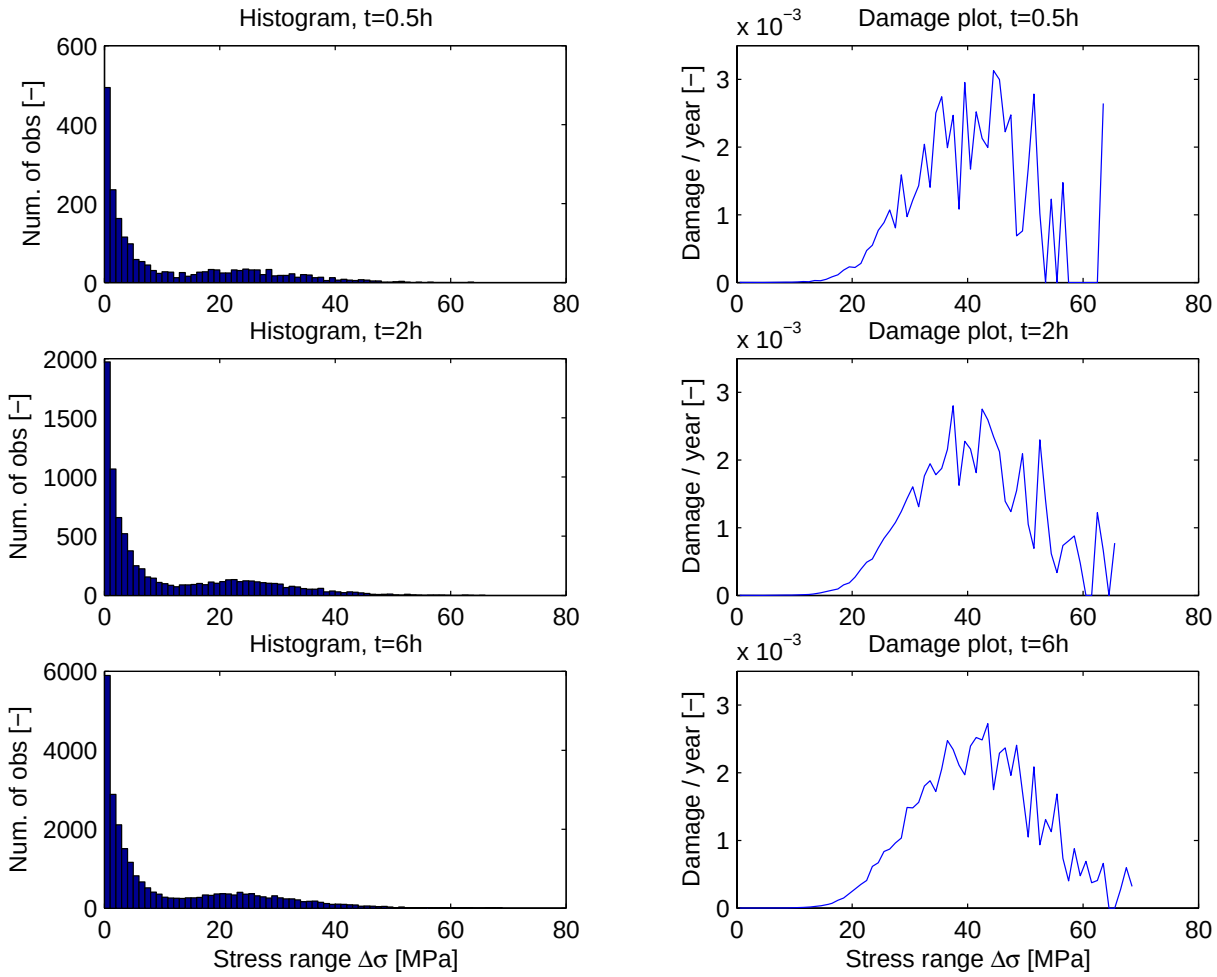

Figure 9.12: Histograms and damage plots for nonlinear analysis

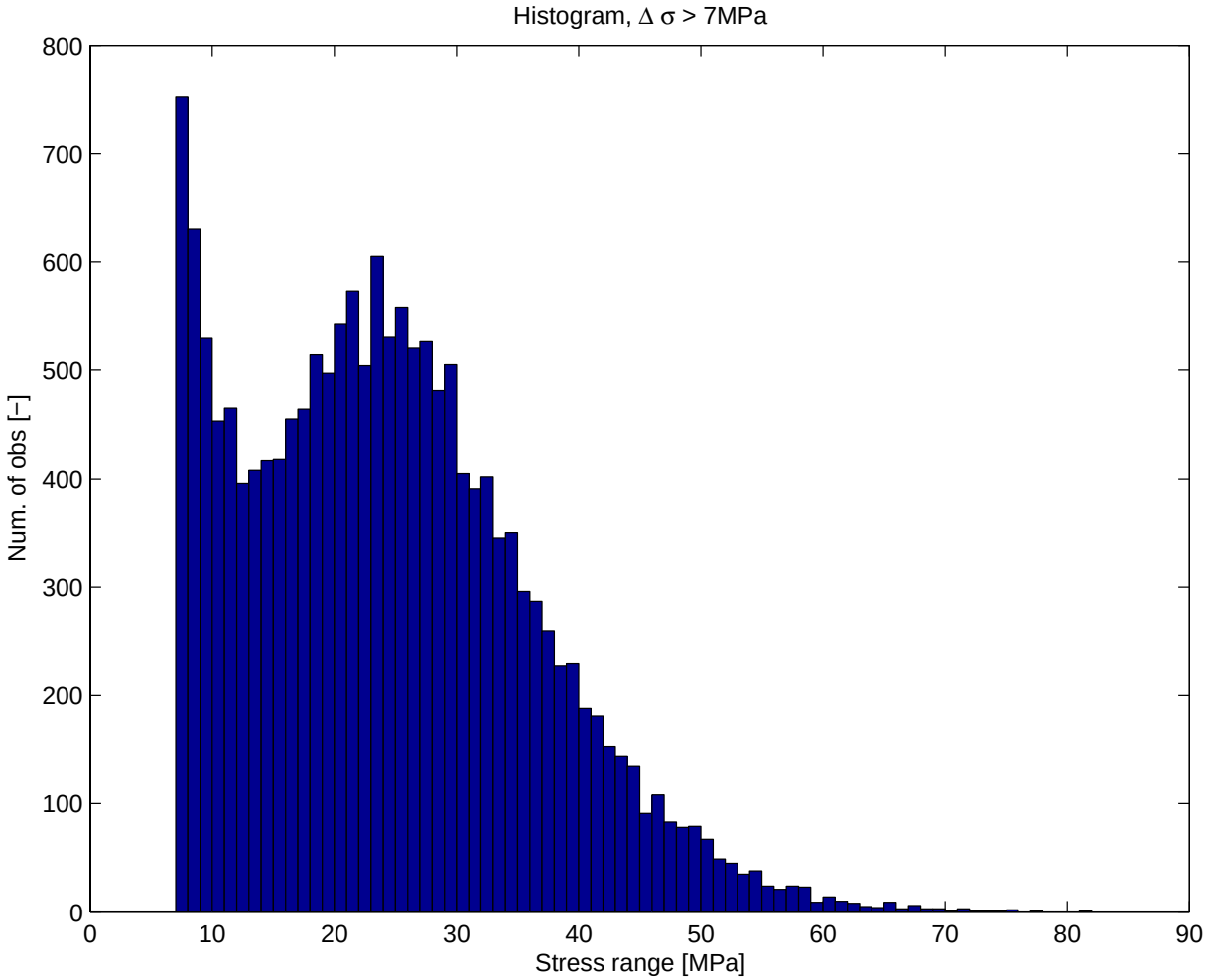

Figure 9.13: Histogram for $\Delta\sigma > 7\,MPa$ for linear analysis of $10\,h$ duration.

The fatigue damage plots display a clear peak around $30 - 50\,MPa$. On the lower side of this peak the plot is very smooth. However, for the higher stress range intervals the damage plot is very jagged. This is because the number of observations in each interval of the histogram gets very low and a neighboring interval can be doubled or halved. As each observation at these stress range levels gives a noticeable fatigue damage, the jaggedness is more visible in the damage plot than in the histograms.

By increasing the analysis duration the jaggedness is reduced and it is assumed that results will converge towards a smooth curve for very long durations. Despite the observed jaggedness of the shortest duration, it was found in Section 9.3 that the total fatigue damage is relatively stable, i.e. even the considerable jaggedness of a $\frac{1}{2}\,h$ analysis duration is likely to produce reasonable results for fatigue life. The jaggedness of the linear analyses seem to be more pronounced that for the nonlinear analyses. This is in agreement with the observation of higher fatigue life COV for linear analyses, see Table 9.7.

	t [h]	$T_{\Delta\sigma}$ [s]	$L_{sc,W}$ [year]	$\Delta\sigma_{0,W}$ [MPa]	$\Delta\sigma_c$ [MPa]	$L_{sc,R}$ [year]	$\Delta\sigma_{0,R}$ [MPa]
L	10	0.87	0.51	262	5.4	11.8	80
N	6	0.86	0.65	249	5.2	15.3	76

Table 9.16: Properties of estimated Weibull and Rayleigh distributions for the # 3 time histories of Table 9.15.

9.8.3 Short-term distributions

To investigate the effect of alternative approaches for computation of short-term distributions, we start by using all stress ranges and fitting a Weibull distribution using WAFO, i.e. the same basis as for the Weibull plots in Section 9.8.1. The # 3 stress range histories of Table 9.15 (i.e. longest analysis durations and thus smoothest histograms) are used in a case study, i.e. $q = 8.39$ and $h = 0.687$ for the linear case and $q = 8.18$ and $h = 0.693$ for the nonlinear case. The estimated fatigue life $L_{sc,W}$ and maximum stress range $\Delta\sigma_{0,W}$ based on these Weibull distribution are shown in Table 9.16. The estimated Weibull distribution is plotted together with the histogram curve in Figure 9.14 for the linear case. In the upper half, the whole curve is plotted. In the lower half, only the high stress range part is plotted in order to magnify the interval most important for fatigue damage. The Weibull curve is obtained by finding the probability of each interval value (i.e. $0.5\,MPa$, $1.5\,MPa$ etc.) using Equation 8.16. The probability is then multiplied by the width of the category (i.e. $1\,MPa$) and the total number of observations of the histogram. The corresponding plots for the $6\,h$ nonlinear stress history are shown in Figure 9.15.

From the figures we see that the Weibull distributions underestimates the histogram for the stress range interval approximately from 20 to $50\,MPa$, whereas the lower and higher intervals are overestimated. The corresponding underestimation of the reference fatigue life found in Table 9.14, seems reasonable as the high stress range is most important for fatigue damage (i.e. the overestimation for the upper stress range interval is more important than the underestimation for the middle interval for the fatigue life).

To find a distribution more suitable for estimating fatigue life, we try to approximate the assumed Rayleigh process for high stress ranges, see Section 9.8.2. By removing stress ranges below a cut-off limit $\Delta\sigma_c$, the shape parameter of the estimated Weibull distribution will increase. The cut-off limit that yields a shape parameter of $h \approx 2$, i.e. a Rayleigh distribution, is identified. The cut-off level increases with seastate. The cut-off limits of the stress range histories are given in Table 9.16. Plots for the Rayleigh distribution corresponding to Figure 9.14 and 9.15 are shown in Figure 9.16 and 9.17. This time the estimated distribution shows a very close fit to the histogram for $\Delta\sigma > 20\,MPa$, i.e. the interval that gives fatigue damage. Not surprisingly, the calculated fatigue life $L_{sc,R}$ and maximum stress range $\Delta\sigma_{0,R}$ (see Table 9.16) are also very close to the reference values in Table 9.15 (based on rainflow counting).

The same analyses that were performed for the long duration analyses of sc. # 3 are

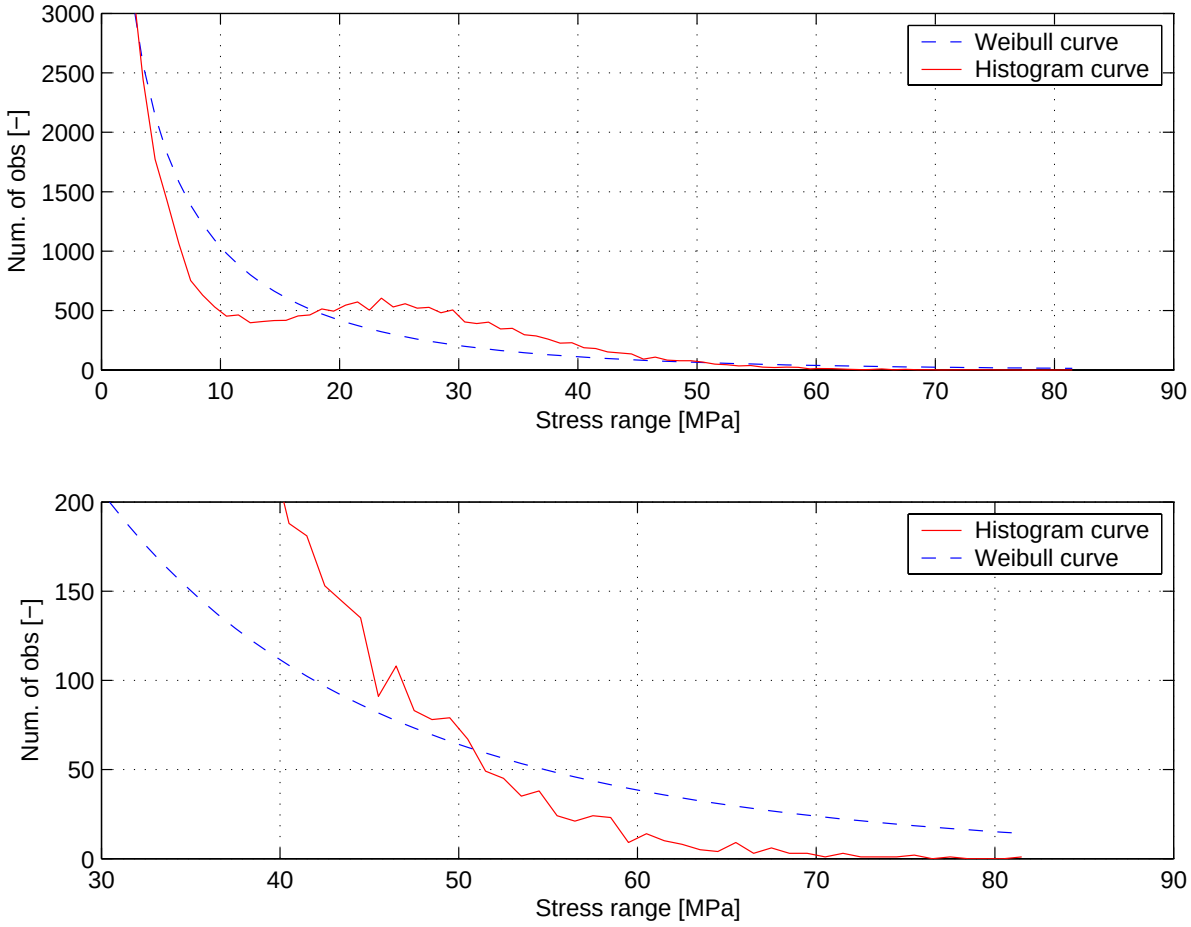

Figure 9.14: Histogram plots and Weibull plots for stress range distributions from linear analyses. Sc. # 3 ($H_s = 0.7\,m$, $T_p = 2.8\,s$). Analysis duration $10\,h$. The lower figure is an expansion of the high stress range interval ($30\,MPa - 90\,MPa$) of the upper figure.

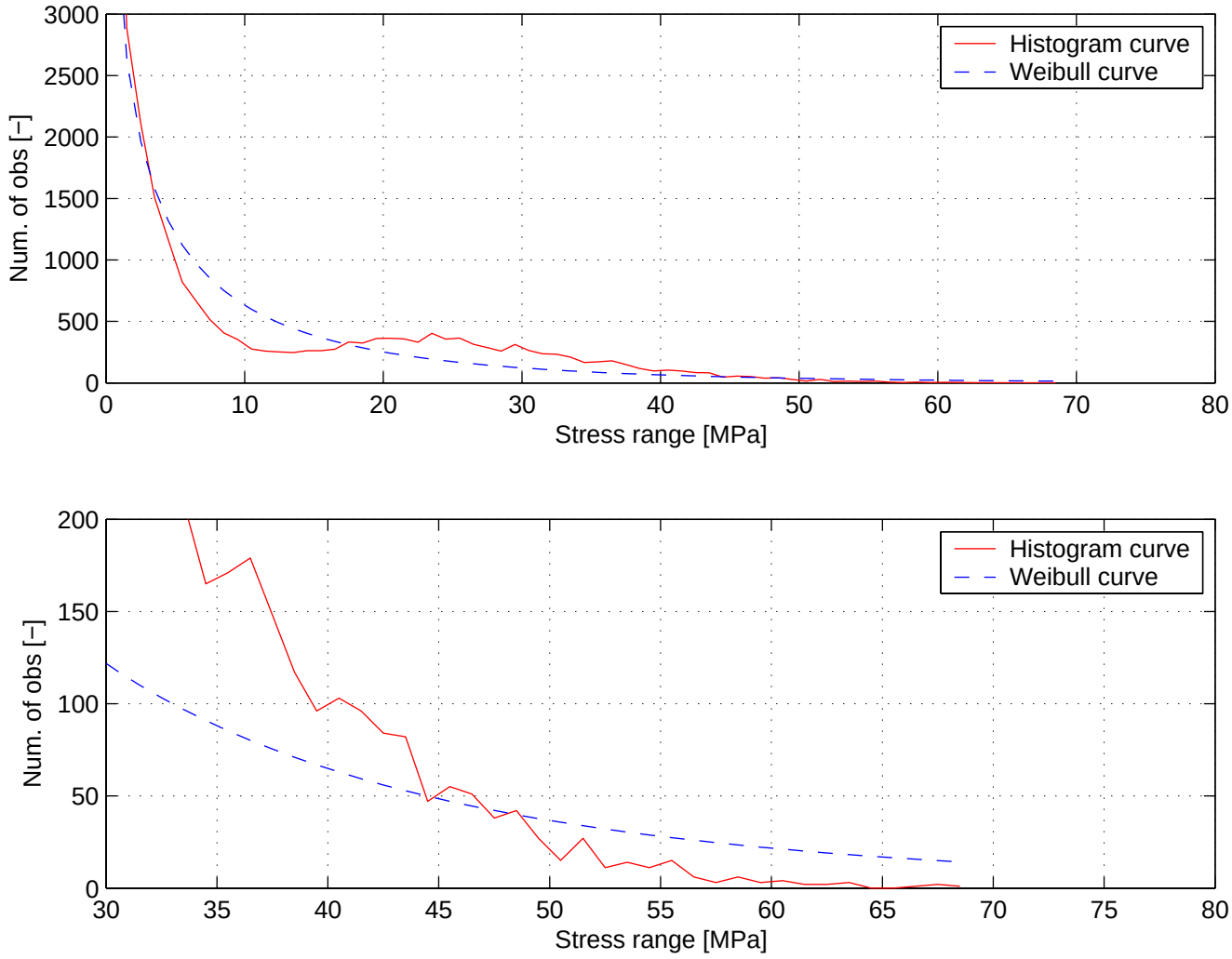

Figure 9.15: Histogram plots and Weibull plots for for stress range distributions from nonlinear analyses. Sc. # 3 ($H_s = 0.7\,m$, $T_p = 2.8\,s$). Analysis duration $6\,h$. The lower figure is an expansion of the high stress range interval ($30\,MPa - 80\,MPa$) of the upper figure.

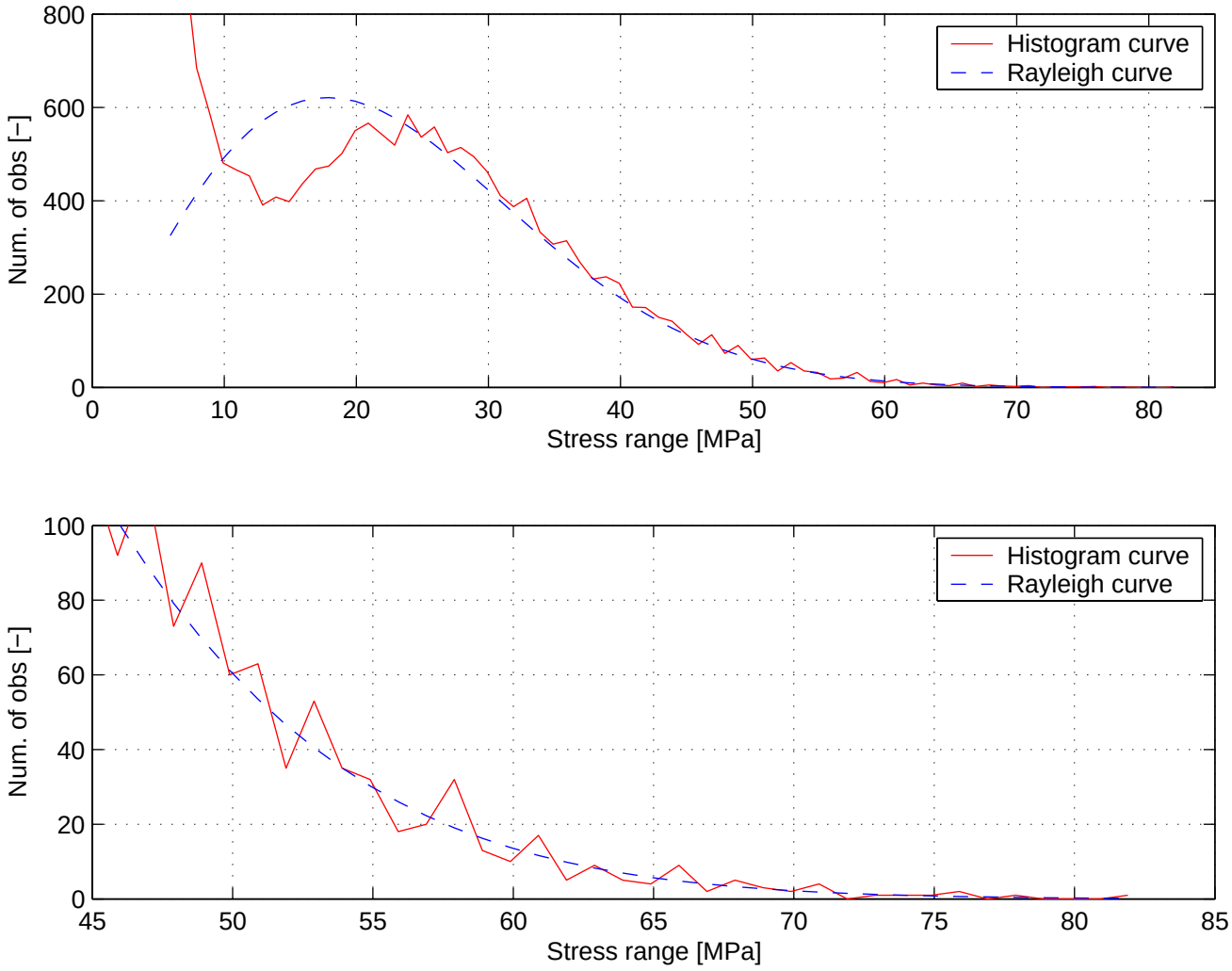

Figure 9.16: Histogram plots and Rayleigh plots for stress range distribution from linear analysis (corresponding to Figure 9.15). Cut-off limit $\Delta\sigma_c = 5.2\,MPa$, see Table 9.16.

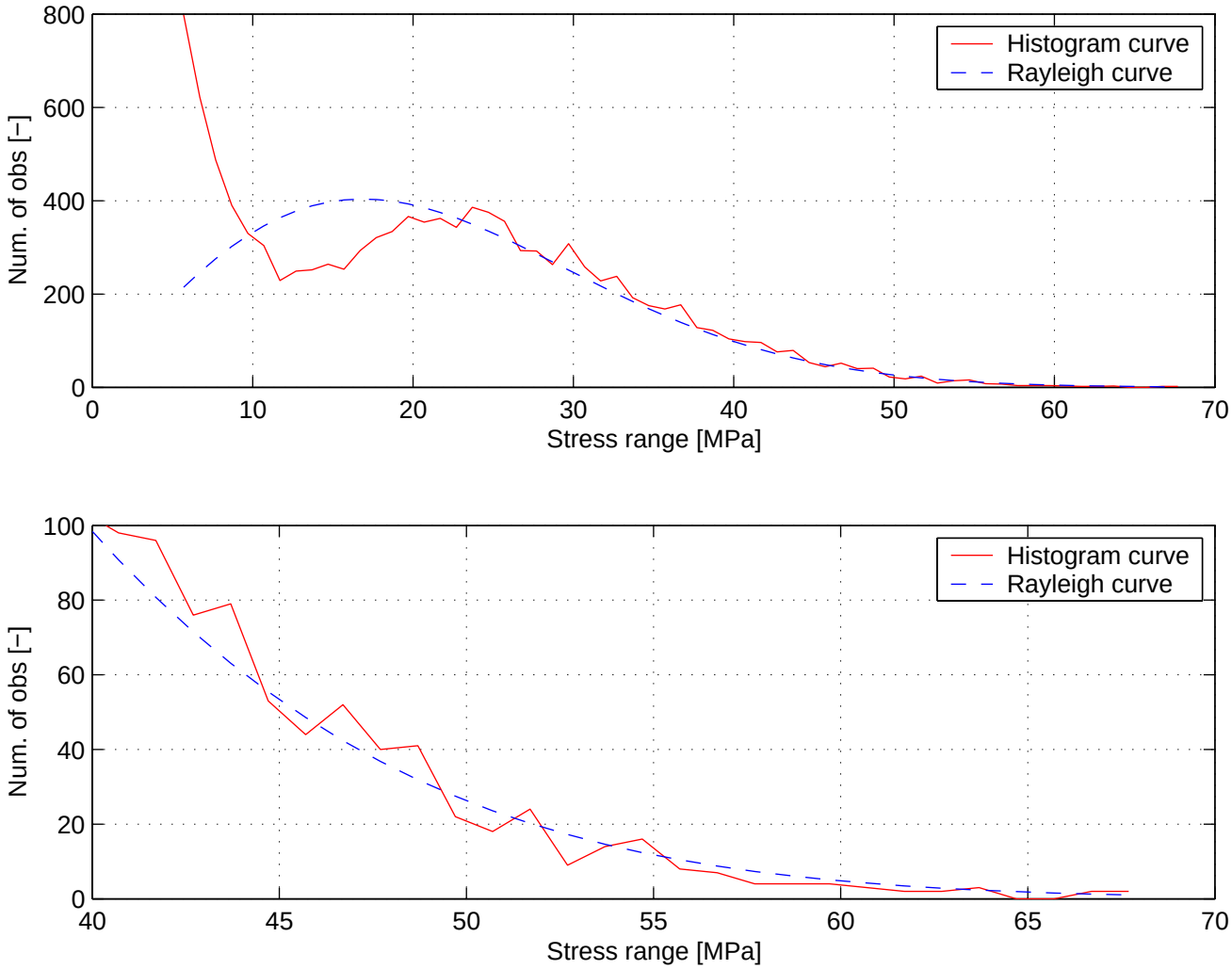

Figure 9.17: Histogram plots and Rayleigh plots for stress range distribution from nonlinear analysis (corresponding to Figure 9.14). Cut-off limit $\Delta\sigma_c = 5.4\,MPa$, see Table 9.16.

now performed for the 1800 s duration stress histories that were the basis for Table 9.12. These results are given in Table 9.17. Based on the shape and scale parameters together with the average period we estimate the maximum stress range $\Delta\sigma_{0,sc,W}$ and the fatigue life $L_{sc,W}$ for each of the seven seastates using Equation 8.19 and 8.20. The ratios of $\Delta\sigma_{0,sc,W}$ and $L_{sc,W}$ to $\Delta\sigma_{0,sc}$ and L_{sc} from Table 9.12 are then found. Based on the estimated Rayleigh distribution, the maximum stress range $\Delta\sigma_{0,sc,R}$ and fatigue life $L_{sc,R}$ are also estimated. The results are summarized in Table 9.18.

The observations made for the long analysis durations for sc. # 3 above also hold for the 1800 s duration.

We see that the maximum stress ranges based on the Weibull distributions are approximately twice the reference values (directly from rainflow counting, see Table 9.12) and the fatigue life are from 4 to 20% of the reference values. This means both the maximum stress range and the fatigue damage are vastly overestimated using the short term Weibull distributions. Thus, the estimated short term Weibull distributions are not well suited for a fatigue life analysis, despite an apparently good fit on Weibull paper (see Figure 9.10).

For the Rayleigh distribution, the results are very close to the reference values which are obtained by cycle counting: both $\Delta\sigma_{0,sc,R}$ and fatigue life $L_{sc,R}$ are within 10% of the simulation results.

In Table 9.18 the fatigue life and damage based on the Rayleigh and Weibull short-term distributions are given, cf. Table 9.14. The ratio of the fatigue life to the respective reference values are also included. The fatigue life based on Rayleigh distributions are estimated as 35 and 19 years, for nonlinear and linear analyses, respectively. These values correspond to 93% and 113% of the fatigue life found directly from the rainflow count. The fatigue lives based on Weibull distributions are vastly underestimated.

9.8.4 Long-term distribution

The long-term stress range distributions for a fatigue analysis of marine structures are often assumed to be Weibull distributed, see Section 8.3.3. Here, we will combine the stress histories of the different seastates to estimate the Weibull parameters of the long term distribution. From the wind scatter diagram (Table 8.2), we see that 93.2% of the probability of occurence is caused by sc. 1-5. the first five intervals. Correspondingly, the relative damage of the first five seastates, see Table 9.12, are 95% and 98% of the total damage for the linear and nonlinear analysis, respectively Thus, we neglect the influence of seastate sc. 0, 6 and 7 (see Table 8.5) when estimating stress range distributions. Their 6.8% of the probability of occurence is assumed not to give any fatigue damage. The cycle counts of the 1800 s stress histories (also used as the basis for Table 9.12) are then combined with their respective relative frequency of occurrence. I.e. the cycle counting (using the rainflow method) is — as before — first performed for each stress time history to obtain the stress range distribution. The stress range distributions (*not* the stress time histories) are then concatenated. The frequencies are normalized with the lowest frequency of occurence, i.e. 0.8% for sc. # 5. The relative occurence is shown in Table 9.19.

The parameters resulting from fitting a Weibull distribution to the complete stress

	Sc. #		1	2	3	4	5	6	7
L	q	[-]	4.69	5.99	8.47	10.5	11.7	13.2	14.8
	h	[-]	0.825	0.732	0.688	0.647	0.635	0.624	0.587
	$\Delta\sigma_{0,sc,W}$	[MPa]	57	98	162	238	279	328	445
	$T_{\Delta\sigma}$	[s]	0.70	0.80	0.88	0.99	1.00	1.06	1.12
	$\frac{\Delta\sigma_{0,sc,W}}{\Delta\sigma_{0,sc}}$	[-]	2.4	2.1	2.3	2.3	2.4	2.2	2.3
	$L_{sc,W}$	[y]	83	6.3	0.50	0.07	0.03	0.01	0.00
	$\frac{L_{sc}}{L_{sc,W}}$	[-]	21	19	27	21	27	25	29
	$\Delta\sigma_c$	[MPa]	1.8	3.4	5.4	7.8	9.0	10.6	14.8
	q_R	[-]	8.15	15.1	25.0	38.7	45.3	56.4	77.1
	$\Delta\sigma_{0,sc,R}$	[MPa]	22	40	65	100	116	143	194
	$\frac{\Delta\sigma_{0,sc,R}}{\Delta\sigma_{0,sc}}$	[-]	0.94	0.85	0.90	0.94	1.01	0.96	1.02
	$L_{sc,R}$	[y]	2014	139	13	1.8	0.87	0.32	0.08
	$\frac{L_{sc}}{L_{sc,R}}$	[-]	1.2	1.2	1.0	1.2	1.0	0.9	1.0
NL	q	[-]	4.49	5.84	8.08	9.60	10.21	10.5	12.9
	h	[-]	0.814	0.733	0.692	0.679	0.680	0.688	0.750
	$\Delta\sigma_{0,sc,W}$	[MPa]	56	95	153	190	202	202	196
	$T_{\Delta\sigma}$	[s]	0.70	0.80	0.85	0.90	0.88	0.84	0.80
	$\frac{\Delta\sigma_{0,sc,W}}{\Delta\sigma_{0,sc}}$	[-]	2.4	2.4	2.3	2.5	2.4	2.1	1.9
	$L_{sc,W}$	[y]	88	7	0.68	0.23	0.17	0.17	0.19
	$\frac{L_{sc}}{L_{sc,W}}$	[-]	23	19	24	19	15	10	4
	$\Delta\sigma_c$	[MPa]	1.8	3.5	5.2	7.3	8.8	9.7	12.2
	q_R	[-]	8.07	15.0	24.2	33.0	37.3	38.5	45.0
	$\Delta\sigma_{0,sc,R}$	[MPa]	22	39	62	85	95	99	115
	$\frac{\Delta\sigma_{0,sc,R}}{\Delta\sigma_{0,sc}}$	[-]	0.9	1.0	0.9	1.1	1.1	1.1	1.1
	$L_{sc,R}$	[y]	2244	143	16	3.8	2.2	1.8	0.83
	$\frac{L_{sc}}{L_{sc,R}}$	[-]	1.1	1.0	1.0	0.9	0.9	1.1	1.0

Table 9.17: Parameters from fit of Weibull and Rayleigh distributions to the stress range distributions resulting from 1800 s analyses of seastates sc. # 1-7. Perpendicular cylinder. SN curve C2.

	Rayleigh			Weibull		
	L_R [year]	D_{20y} [-]	$\frac{L_R}{L}$ [%]	L_W [year]	D_{20y} [-]	$\frac{L_W}{L}$ [%]
Linear	19	1.03	113	0.77	26.0	4
Nonlinear	35	0.57	93	1.9	10.7	5

Table 9.18: Fatigue life time L and damage over 20 years D_{20y} calculated from short term Rayleigh and Weibull distributions. Critical point on perpendicular cylinder. Irregular waves. SN curve C2.

Sc.#	1	2	3	4	5
Freq.	49.4	46.4	21.5	5.9	1

Table 9.19: Relative frequency for scatter diagram entries #1 to 5.

range distributions, are shown in Table 9.20 as case # 1a for both the linear and nonlinear structure. The stress range period $T_{\Delta\sigma}$, the maximum 20-years stress range $\Delta\sigma_0$, and the fatigue life L_W are also presented. $T_{\Delta\sigma}$ is found by taking the relative probability of occurrence for the five seastates into account (t is the analysis duration and $n_{\Delta\sigma}$ is the number of stress ranges during this interval):

$$T_{\Delta\sigma} = \frac{t}{n_{\Delta\sigma} \cdot 93.2\%} \tag{9.3}$$

L_W and $\Delta\sigma_0$ can then be found using Equation 8.21 and 8.19, respectively. Finally, the ratio of fatigue life estimated from the long term distributions to the reference fatigue life values $\frac{L_W}{L_{ref}}$ and the corresponding ratio for maximum stress range $\Delta\sigma_0$ (i.e. $\frac{\Delta\sigma_{0,W}}{\Delta\sigma_{0,ref}}$) are also included in Table 9.20. The reference values are found directly from rainflow counting and are different for linear and nonlinear analysis, see Table 9.14).

The distributions are compared to the corresponding histogram plots in Figure 9.18 and 9.19. As for Figure 9.14 and 9.15, the high stress range intervals are expanded to illustrate the fit in the area most important for fatigue damage.

Figure 9.18 and 9.19 show a quite good fit by visual inspection for the estimated Weibull distribution (the 1a-curves) to the histograms. Also for the high stress range interval the fit seems to be good, although the Weibull distribution seems to be overestimating the histogram in the high stress range area. The estimated fatigue lives are lower than the reference values: 64% and 35% for linear and nonlinear analyses, respectively, see Table 9.20. The maximum 20-years stress range $\Delta\sigma_0$ is considerably higher than the reference values: 1.9 times and 3.2 times greater for linear and nonlinear analyses, respectively. These numbers are consistent with the observed slight overestimation for high stress ranges.

As an alternative to approach to finding a long term distribution, we use the cut-off values $\Delta\sigma_c$ identified in the previous section. Thus, all stress ranges below the respective

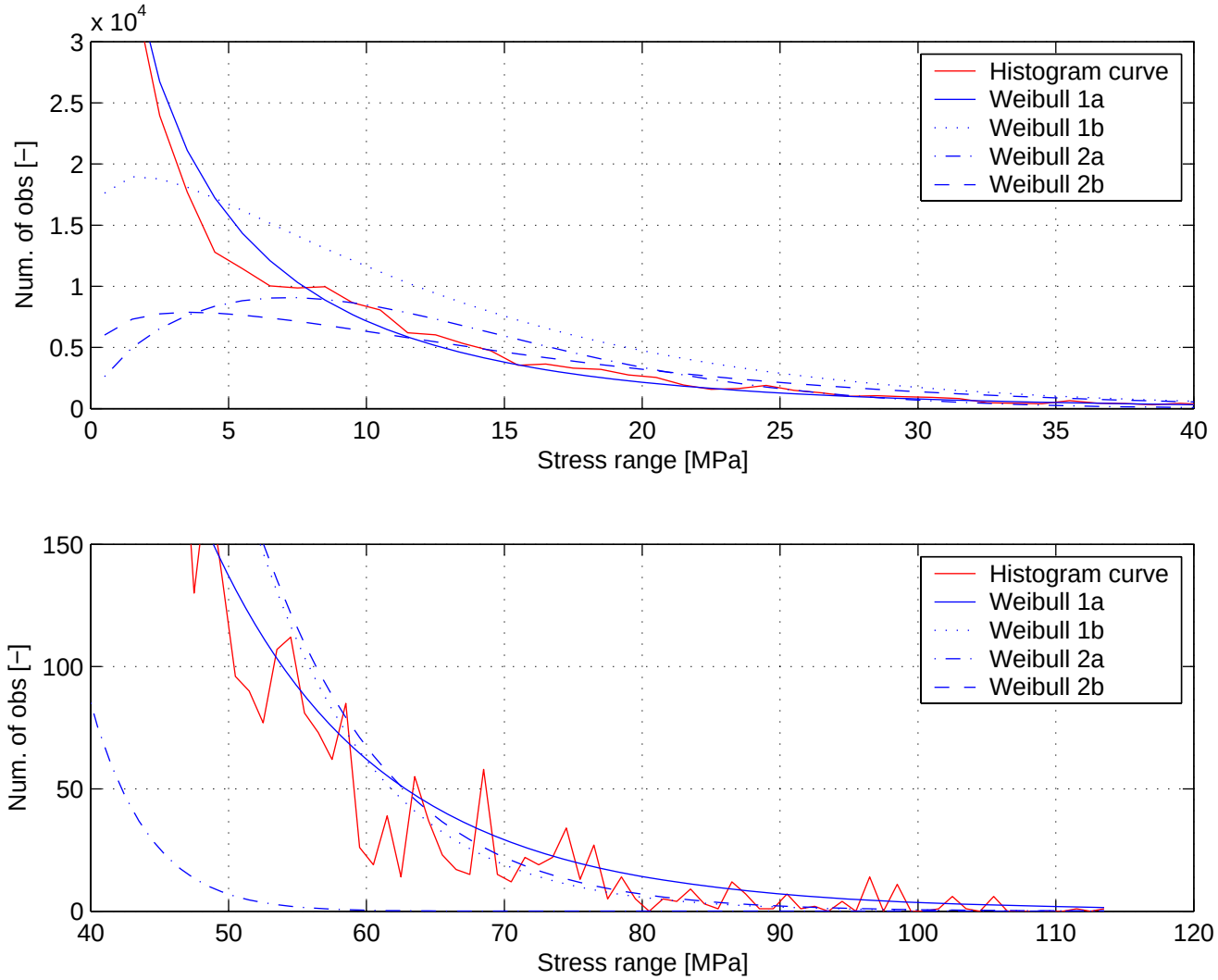

Figure 9.18: Histogram curve and four Weibull curves for the long-term distribution. Linear analysis. The stress range distribution is split in two figures. Upper figure: $0 - 40\,MPa$, lower figure: $40 - 120\,MPa$. Cases 1a-2b are explained in text and in Table 9.20.

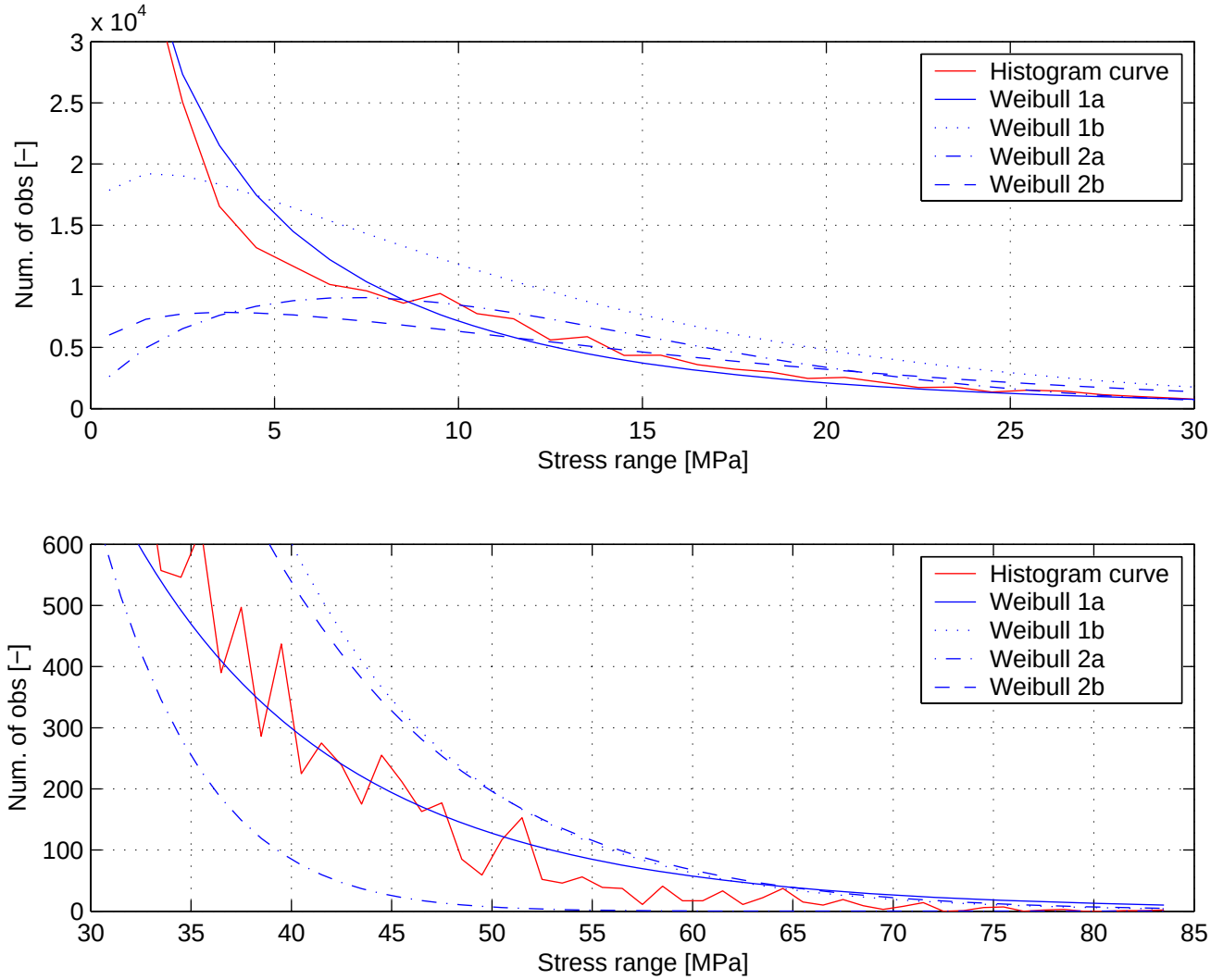

Figure 9.19: Histogram curve and four Weibull curves for the long-term distribution. Non-linear analysis. Upper figure: $0 - 30\,MPa$, lower figure: $30 - 85\,MPa$. Cases 1a-2b are explained in text and in Table 9.20.

	#	$T_{\Delta\sigma}$	q	h	$\Delta\sigma_{0,W}$	L_W	$\frac{L_W}{L_{ref}}$	$\frac{\Delta\sigma_{0,W}}{\Delta\sigma_{0,ref}}$
L	1a	0.83	5.82	0.753	320	11	0.64	1.9
	1b	0.83	11.8	1.13	X	X	X	X
	2a	1.53	13.0	1.61	83	131	7.7	0.49
	2b	1.53	14.7	1.22	X	X	X	X
NL	1a	0.82	5.63	0.752	312	13	0.35	3.2
	1b	0.82	17.6	1.73	X	X	X	X
	2a	1.53	12.8	1.64	79	152	4.1	0.80
	2b	1.53	14.5	1.57	X	X	X	X

Table 9.20: Parameters for estimated long-term stress range distributions.

cut-off stress ranges are removed before the Weibull fit is performed. The results are designated by # 2a in Table 9.20.

From Figure 9.18 and 9.19 we see that 2a shows a good fit for medium stress ranges: $5-30\,MPa$, but the histogram is underestimated in the high stress range interval. Accordingly, the fatigue life is overestimated and the maximum stress range is underestimated. We can conclude that the direct Weibull fit (1a) gives better results (i.e. closer to the reference values) than the approach with stress ranges below the cut-off levels removed (2a).

For a given maximum stress range $\Delta\sigma_0$, fatigue life L, and stress range period $T_{\Delta\sigma}$, the shape h and the scale q parameters of a Weibull distribution can be found by iterating. By assuming a shape factor h, the scale factor q is found from Equation 8.18 and the fatigue life from Equation 8.21. Using this approach, q and h corresponding to the reference values of Table 9.14 and the stress range periods $T_{\Delta\sigma}$ of 1a and 2a, respectively, in Table 9.20 are found. The results are designated by # 1b and 2b in Table 9.20. The last four columns in Table 9.20 are not used for # 1b and 2b because they give perfect fit to the reference values: $\frac{L_W}{L_{ref}} = 1$ and $\frac{\Delta\sigma_{0,W}}{\Delta\sigma_{0,ref}} = 1$. The distributions are also shown in Figure 9.18 and 9.19.

The estimated Weibull distributions 1b and 2b give good fits (comparable to 1a) relative to the histogram for the high stress range interval $(40-115\,MPa)$. Further, they are both steeper than 1a in this interval yielding the low $\Delta\sigma_0$ values. For the low and medium stress ranges they show poor fits relative to the histogram.

The Weibull distributions which are "forced" to yield the reference values for fatigue life L and maximum stress range $\Delta\sigma_0$ have a good fit only for the high stress range interval. Thus, they do not give a good statistical description of the stress range distribution in general.

9.8.5 Applicability of the simplified method

Based on the above results, it is concluded that a fitted Weibull distribution based on all stress ranges gives a good description of the distribution of stress range in general, but not

	Regular waves sim.	Irregular waves		
		Sim.	1a	2a
Reference	Table 9.5	Table 9.12	Table 9.20	Table 9.20
Linear	244	190	320	83
Nonlinear	116	104	312	79

Table 9.21: Summary of maximum stress ranges $\Delta\sigma_0$. Units: [MPa].

for the maximum stress range $\Delta\sigma_0$. Correspondingly, the fatigue life estimated from the Weibull parameters L_W is a better approximation than the maximum stress range $\Delta\sigma_{0,W}$. In Table 9.21 the maximum stress ranges from regular and irregular waves simulations are summarized. Additionally, estimates from distributions are included for irregular waves.

The simplified method for fatigue design is based on an estimate of the maximum stress range $\Delta\sigma_0$ and a shape parameter h based on previous experience. Thus, the method used to finding $\Delta\sigma_0$ and the experience based h must be calibrated against each other. From the paragraph above, we conclude that the Weibull parameters ($h \approx 0.7 - 0.8$) and the maximum stress ranges ($\Delta\sigma_0 \approx 100 - 190\,MPa$) found from analyses described in the present thesis can not be used together in a simplified method, this would yield too long a fatigue life. For the linear and nonlinear cases we get a fatigue life of 152 years and 3119 years, respectively. However, due to the high sensitivity of fatigue life due to both shape parameter and maximum stress range, relatively small changes can bring the fatigue life close to the reference values (20-40 years). For example, using the maximum stress range of regular waves analysis $\Delta\sigma_0 = 244\,MPa$, we get a fatigue life of 44 years.

Alternatively, the shape parameter h can be increased to yield the reference values for fatigue life when used in conjunction with the maximum stress range values from the analyses (see Table 9.20). The results so far support the use of different shape factors for linear and nonlinear analysis. Using the average of 1b and 2b we get $h_{linear} = 1.2$ and $h_{nonlinear} = 1.7$.

The sensitivity of shape factor h and maximum stress range $\Delta\sigma_0$ when using Equation 8.21 to calculate fatigue life L is illustrated in Figure 9.20. Fatigue life is found for three levels of $\Delta\sigma_0$: 100, 200, and $300\,MPa$. The stress range period is set to $1\,s$.

Both the alternatives presented above are artificial in the sense that they are not based on the actual stress range distributions, but instead construct distributions that yield the desired result for fatigue life. Additionally, the results are very sensitive to the input parameters h and $\Delta\sigma_0$. Thus, the use of a simplified method is not recommended. However, further research may nevertheless substantiate the use of these "artificial" distributions for simplified design.

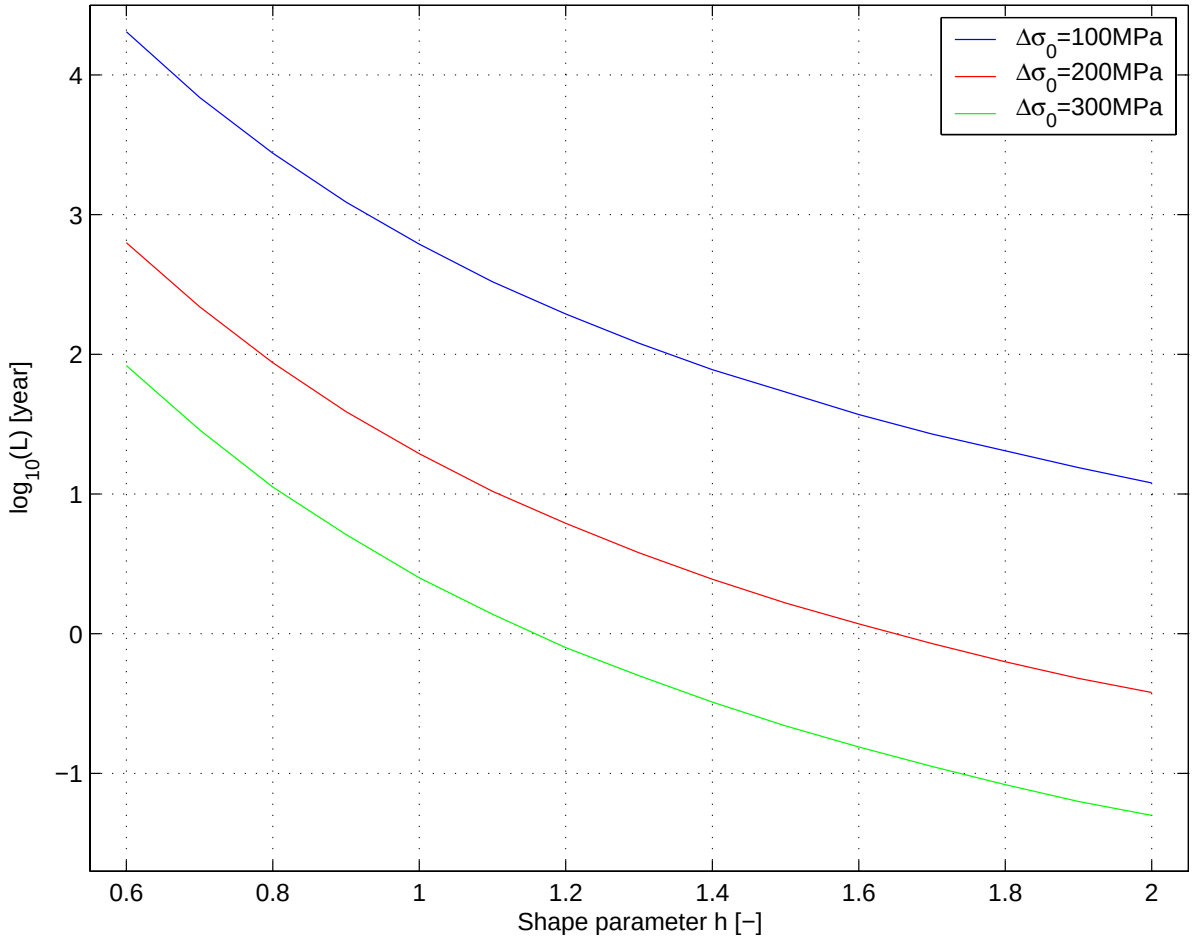

Figure 9.20: Fatigue life as a function of Weibull shape parameter h. Three levels of maximum stress range $\Delta\sigma_0$: 100, 200, and 300 MPa.

9.9 Implications for the Ultimate Limit State

The focus in the present thesis has been on the fatigue limit state design. However, the implication of the results for the ultimate limit state is here briefly evaluated. Of particular importance is the maximum stress range $\Delta\sigma_0$, see Table 9.21. It is assumed that the maximum stress σ_{max} is approximated as half the maximum stress range $\Delta\sigma_0$.

The maximum stress range for a nonlinear structure in irregular waves is considered to represent the best estimate for $\Delta\sigma_0$, i.e. $\Delta\sigma_0 = 104\,MPa$ and thus $\sigma_{max} = \frac{\Delta\sigma_0}{2} = 52\,MPa$. Using the yield strength from Table 2.2: $f_y = 360\,MPa$, this implies only a 14% utilization. Applying appropriate load and resistance factors will increase the degree of utilization, but it will still be low. As the fatigue limit state resulted in a fatigue life of 38 years (see Table 9.14), it is concluded that a steel floater designed for the fatigue limit state is likely also to satisfy the ultimate limit state requirements.

Chapter 10

CONCLUSIONS AND FURTHER WORK

A prototype software tool for dynamic, nonlinear FEM analysis of a floating fish farm in waves has successfully been developed employing relevant state-of-the-art elements of marine structural analysis. This applies in particular to time domain analysis of a nonlinear structure in irregular waves. This has allowed a fatigue design parameter study of a steel floater. The principal conclusions are:

- It is realistic to design a steel floater for a 20-year fatigue life.
- A linear analysis yields a more conservative result than a nonlinear analysis (as well as a less adequate description of the physics).
- The high response sensitivity to the wave period for regular waves implies that they should not be applied for design purposes.
- Regarding computer time, it is realistic to perform a time domain fatigue analysis based on a scatter diagram within an engineering context. This applies even for a nonlinear structure.
- It proved effective and realistic to base the software prototype tool on a general object-oriented FEM framework for structural analysis run on a PC.
- A steel floater designed for the Fatigue Limit State is likely also to satisfy the Ultimate Limit State requirements.

10.1 Fatigue analysis and irregular waves

It has been shown that using an irregular wave formulation is very advantageous compared to using regular waves. The main reason for this is the very strong sensitivity to the wave period for the structural response to regular waves.

Further, it has been shown that a nonlinear formulation yields considerably smaller load effects compared to a linear formulation for higher waves. The nonlinear effects become important as the cross section (of parts of the BCS) approaches full submergence or an out-of-water situation. Increasing wave height beyond this level has little to no effect for a nonlinear formulation.

For a fatigue life analysis, the nonlinear formulation gives approximately twice the fatigue life of a linear formulation. For a constant stress range, doubling the life time corresponds to approximately a 15% reduction of the (constant) stress range.

For fatigue analysis a (real-time) duration of $\frac{1}{2}\,h$ was found to give sufficiently low coefficient of variation for the fatigue life estimate (less than 10%).

Increasing the duration gives slow convergence of fatigue life estimates. The effect of increased duration has also been evaluated by considering plots of relative fatigue damage for different stress range levels. The damage plot has a peaked shape with a smooth lower side and a jagged upper side. The peak is roughly at a stress range half the maximum stress range. The jaggedness decreases with increased analysis duration, but even for a 12 hours duration some jaggedness can still be observed. It is interesting to notice that even though the damage plot for short durations is very jagged this does not transform to high COVs for fatigue life. The jaggedness of linear vs. nonlinear analyses are not very different, as judged by visual inspection.

The typical wave climate for floating fish farms has both smaller peak periods and lower significant wave heights than would be the case for the open ocean. The smaller wave periods lead to a higher number of stress fluctuations and — seen in isolation — lower acceptable stress range levels. On the other hand, a sheltered location will typically have longer periods of calm seastates lowering the number of stress fluctuations (which give fatigue damage). The fatigue analyses resulted in stress ranges dominated by levels below the intersection point of the SN curves, thus a slope of m=5 was typically used. This slope gives a very strong dependency of stress range — doubling the stress range reduces the fatigue life to 3% of the original value (i.e. $\frac{1}{2^5}$). This implies that even for seastates with seemingly small nonlinear influence, the effect on fatigue life can be important. The maximum stress ranges are at a very low level compared to the yield stress. Thus, it is reasonable to assume that the fatigue limit state is more important than the ultimate limit state and will be decisive for design. Extreme (Ultimate Limit State) stress levels close to the yield stress are likely to be accompanied with a stress range history giving very low fatigue life.

10.2 Statistical distribution of stress range

The stress range histories have been plotted on Weibull paper and the two-parameter Weibull parameters have been estimated. A visual inspection of the short-term Weibull plots indicates a quite good fit, and the shape parameter is typically between 0.6 and 0.8. However, a closer inspection of the histograms shows that the process seems to be a combination of a high frequency/low stress range level process with a Weibull shape

parameter $h < 1$ and a low frequency/high stress range level process with a Weibull shape parameter $h > 1$ (possibly $h \approx 2$, i.e. a Rayleigh distribution). By visual inspection of the histograms and the accompanying fatigue damage plots, it is found that the stress range levels of the $h < 1$ Weibull process are so small that they give virtually no fatigue damage.

Calculating fatigue life and maximum stress range based on the estimated Weibull parameters yields overestimation of the stress range and underestimation of the fatigue life.

An assumed Rayleigh process is estimated by filtering out the smaller stress ranges until a Weibull fit yields a shape parameter of $h = 2$. Calculating maximum stress range and fatigue life for the individual seastates gives a very good fit to results from the direct calculations.

The long-term distribution was estimated by combining the lower five seastates based on the frequencies of occurrence given by the scatter diagram. A Weibull fit resulted in a shape parameter of approximately 0.7. As for short-term distributions, based on the estimated parameters the maximum stress range and fatigue life were over and under estimated, respectively. Due to the poor fit, two alternative methods for long-term estimation were investigated, but the results were not significantly better. Based on the maximum stress ranges and fatigue life estimated from the stress history directly, corresponding combinations of the shape and scale parameters were found. The shape parameter was generally very high: $h \approx 1.2$ for the linear analysis and $h \approx 1.7$ for the nonlinear analysis. Based on the poor fit using a Weibull distribution, a simplified method based on this distribution is hence not recommended.

For floating fish farms made of steel it is recommended that fatigue design be based on time domain analysis of a nonlinear system in irregular waves. Given appropriate software this is an effective procedure — also within an engineering context.

10.3 Recommendations for further work

The biggest drawback of this work is the lack of comparison with and verification against model tests. Unfortunately, on this issue we have to echo what Ormberg (1991) suggested:

> Further verification against model tests is also recommended, not with fully integrated systems, but with simple cross sections subjected to well defined waves.

Being even more specific, it is suggested that model test should start with a floating, half submerged, circular cylinder in perpendicular and parallel regular waves and with linear, horizontal mooring. This should be followed by investigating the same model with a netpen included.

In the present work, several simplifications of the hydrodynamic and structural models have been introduced. The importance of nonlinear effects not yet considered should be investigated and taken into account if appropriate. These include hydrodynamic phenomena related to:

- Added mass
- Potential damping
- Drag loading and damping of the floater
- Large structural rotations

The importance of the netpen and the mooring for the design of the floater should be investigated more thoroughly and implemented accordingly

The generality of the software should be increased to facilitate analysis of a wider range of structures. This includes:

- Modeling of a grid of interconnected floaters
- Modeling of walkway-type steel floaters with buoys
- Modeling of plastic floaters

The generation of wave spectrum and scatter diagram should be further investigated and verified. In particular, the introduction of a 3D wave spectrum should be considered. The verification process should include on-site measurements of wave height and direction distributions for relevant fish farm locations.

References

Aarsnes, J. V., Rudi, H., and Løland, G. (1990). *Current forces on cage, net deflection*. Thomas Telford, London.

Accident commision (1981). *The "Alexander L. Kielland"-accident*. [s.n.], [Oslo]. NOU 1981:11. Report of a Norwegian public commission appointed by royal decree of March 28, 1980, presented to the Ministry of Justice and Police March, 1981.

Almar-Naess, A. (1999). *Fatigue Handbook: Offshore Steel Structures*. Tapir Forlag, 3rev ed edition.

Ansys (2007). http://ansys.com/products/default.asp. [Online. Accessed 29-December-2007].

ASTM (2000). *Standard Terminology Relating to Fatigue and Fracture*, vol. 03.01 edition. Testing ASTM Designation E1823.

Bai, K. J. and Yeung, R. W. (1974). Numerical solutions to free-surface flow problems. Technical report, 10th Naval Hydrodynamics Symposium, Session VII, Technical Report.

Bannantine, J. A. (1989). *Fundamentals of Metal Fatigue Analysis*. Prentice Hall, 1st edition.

Bellona (2007). http://www.bellona.no/havbruksweb. [Online. Accessed 29-December-2007].

Belytschko, T., Liu, W. K., and Moran, B. (2000). *Nonlinear Finite Elements for Continua and Structures*. Wiley, 1 edition.

Bergan, P. G., Larsen, P. K., and Mollestad, E. (1986). *Svingning av konstruksjoner*. Tapir, Trondheim.

Berge, S. (2004a). Fatigue and fracture design of marine structures 1. NTNU, Dept. of Marine Technology. UK-2004-93.

Berge, S. (2004b). Fatigue and fracture design of marine structures 2. NTNU, Dept. of Marine Technology. UK-2004-94.

Berstad, A. and Tronstad, H. (2005). Response from current and regular/irregular waves on a typical polyethylene fish farm. In *In proceedings from Maritime Transportation and Exploitation of Ocean and Coastal Resources (IMAM)*.

Berstad, A. J., Sivertsen, S.-A., Tronstad, H., and Leite, E. (2005). Enhancement of

design criteria for fish farm facilities including operations. volume 2 of *Proceedings of the International Conference on Offshore Mechanics and Arctic Engineering - OMAE*, pages 825–832, Halkidiki, Greece. American Society of Mechanical Engineers, New York, NY 10016-5990, United States.

Berstad, A. J., Tronstad, H., and Ytterland, A. (2004). Design rules for marine fish farms in norway. calculation of the structural response of such flexible structures to verify structural integrity. volume 3 of *Proceedings of the International Conference on Offshore Mechanics and Arctic Engineering - OMAE*, pages 867–874, Vancouver, BC, Canada. American Society of Mechanical Engineers, New York, NY 10016-5990, United States.

Bishop, C. T., Donelan, M. A., and Kahma, K. K. (1992). Shore protection manual's wave prediction reviewed. *Coastal Engineering*, 17:25–48.

Bømlo Construction (2007). www.bc.no. [Online; accessed 10-November-2007].

Bonnemaire, B. and Jensen, A. (2006). Modelling fish farms using riflex. *DNV Software News*, (01).

Borgman, L. E. (1967). Ocean wave simulation for engineering design.

Børresen, J. A. (1987). *Vindatlas for Nordsjøen og Norskehavet*. Universitetsforlaget : Det norske meteorologiske institut, Oslo. In Norwegian.

Brodtkorb, P., Johannesson, P., Lindgren, G., Rychlik, I., Rydén, J., and Sjö, E. (2000). WAFO - a Matlab toolbox for the analysis of random waves and loads. In *Proc. 10'th Int. Offshore and Polar Eng. Conf., ISOPE, Seattle, USA*, volume 3, pages 343–350.

Cairns, J. and Linfoot, B. T. (1990). Some considerations in the structural engineering of sea-cages for aquaculture. In *Proceedings of the Conference Engineering for Offshore Fish Farming*.

Chopra, A. K. (2006). *Dynamics of Structures (3rd Edition)*. Prentice Hall, 3 edition.

Cook, R. D., Malkus, D. S., Plesha, M. E., and Witt, R. J. (2001). *Concepts and Applications of Finite Element Analysis, 4th Edition*. Wiley, 44 edition.

Cooley, J., Lewis, P., and Welch, P. (1969). Fast fourier transform and its applications. *IEEE Transactions on Education*, E-12:27–34.

Cooley, J. W. and Tukey, J. W. (1965). An algorithm for the machine calculation of complex fourier series. *Mathematics of Computation*, 19:297–301.

Dahl, E. (2007). *Kyst og havbruk 2007*, volume 2-2007. Havforskningsinstituttet, Bergen.

DNV (1988). *Tentative regler for sertifisering av flytende fiskeoppdrettsanlegg*. DNV, [Høvik].

DNV (2004). Design of offshore steel structures, general (lrfd method). Offshore standard DNV-OS-C101.

DNV (2005). Fatigue design of offshore structures. Recommended practice DNV-RP-C203.

Dr Software LCC (2007). http:
www.drsoftware-home.com. [Online; accessed 20-November-2007].

DWIA (2007). http://www.windpower.org/en/tour/wres/weibull.htm. Danish wind industry association [Online; accessed 22-November-2007].

Etube, L. (2001). *Fatigue and Fracture Mechanics of Offshore Structures (Engineering Research Series*. Wiley.

Faltinsen, O. (1990). *Sea Loads on Ships and Offshore Structures*. Cambridge Press.

FFTW (2008). http://fftw.org/. [Online. Acessed 03-January-2008].

Fiskeridirektoratet (2007). http://www.fiskeridir.no. [Online; accessed 28-December-2007].

Frank, W. (1967). Oscillation of cylinders in or below the free surface of deep fluids. Technical Report Report 2375, Naval Ship Research and Development Center, Washington DC.

Fredheim, A. (2005). *Current forces on net structures*. PhD thesis, Norwegian University of Science and Technology, Faculty of Engineering Science and Technology, Department of Marine Technology.

Fredriksson, D. W. (2001). *Open ocean fish cage and mooring system dynamics*. PhD thesis, University of New Hampshire.

Fredriksson, D. W., DeCew, J., Swift, M. R., Tsukrov, I., Chambers, M. D., and Celikkol, B. (2004). The design and analysis of a four-cage grid mooring for open ocean aquaculture. *Aquacultural Engineering*, 32:77–94.

Fredriksson, D. W., DeCew, J. C., and Tsukrov, I. (2007a). Development of structural modeling techniques for evaluating hdpe plastic net pens used in marine aquaculture. *Ocean Engineering*, 34:2124–2137.

Fredriksson, D. W., DeCew, J. C., Tsukrov, I., Swift, M., and Irish, J. D. (2007b). Development of large fish farm numerical modeling techniques with in situ mooring tension comparisons. *Aquacultural Engineering*, 36:137–148.

Fredriksson, D. W., Swift, M. R., Eroshkin, O., Tsukrov, I., Irish, J. D., and Celikkol, B. (2005). Moored fish cage dynamics in waves and currents. *IEEE Journal of Oceanic Engineering*, 30:28–36.

Fredriksson, D. W., Swift, M. R., Irish, J. D., Tsukrov, I., and Celikkol, B. (2003). Fish cage and mooring system dynamics using physical and numerical models with field measurements. *Aquacultural Engineering*, 27:117–146.

Goda, Y. (2000). *Random Seas and Design of Maritime Structures*. World Scientific Publishing Company, 2nd edition.

Gosz, M., Kestler, K., Swift, M., and Cellikol, B. (1996). Finite element modeling of submerged aquaculture net-pen systems. In *Proceedings on an International Conference on Open Ocean Aquaculture*, Portland, Maine.

Gui, F., Li, Y., Dong, G., and Guan, C. (2006). Application of ccd image scanning to

sea-cage motion response analysis. *Aquacultural Engineering*, 35:179–190.

Hasselmann, K., Barnett, T., , E. B., , H. C., Cartwright, D., Enke, K., Ewing, J., Gienapp, H., Hasselmann, D., Kruseman, P., Meerburg, A., Meller, P., Olbers, D., Richter, K., and W. Sell, H. W. (1973). Measurements of wind-wave growth and swell decay during the joint north sea wave project (jonswap). *Dtsch. Hydrogr. Z.*

Holthuijsen, L. H. (2007). *Waves in Oceanic and Coastal Waters*. Cambridge University Press.

Hudspeth, R. T. (2006). *Waves and Wave Forces on Coastal and Ocean Structures*. World Scientific Publishing Company.

Jang, J. W. (2007). *Characterization of Live Modeling Performance Boundaries for Computational Structural Mechanics*. PhD thesis, Univesity of Washington.

Jensen, O., Wroldsen, A. S., Lader, P. F., Fredheim, A., and Heide, M. (2007). Finite element analysis of tensegrity structures in offshore aquaculture installations. *Aquacultural Engineering*, 36:272–284.

Journée, J. and Massie, W. (2001). *Offshore hydromechanics*. Delft University of Technology.

Karunakaran, D. N. (1993). *Nonlinear dynamic response and reliability analysis of drag-dominated offshore platforms*. PhD thesis, Department of Marine Structures, Norwegian Institute of Technology, University of Trondheim.

Kishev, R., Rakitin, V., and Yovev, Y. (2006). Model investigation of dynamic behaviour and wave loads on a fish farm cage. In *Proceedings of the Fourth International Conference on Hydroelasticity in Marine Technology*, Wuxi, China.

Kishev, R., Rakitin, V., Yovev, Y., and Nachev, R. (2004). Hydrodynamic model tests of fish farm cage system. In *7th International Conference on Marine Science and Technology. Varna, Bulgaria.*

Kristiansen, D. (2008). *Preliminary title: Wave loads on floaters of aquaculture plants*. PhD thesis, Norwegian University of Science and Technology.

Krolikowski, L. P. and Gay, T. A. (1980). An improved linearization technique for frequency domain riser analysis. *Offshore Technology Conference, OTC*, 3777:341?353.

Lader, P., Dempster, T., Fredheim, A., and Jensen, O. (2008). Current induced net deformations in full-scale sea-cages for atlantic salmon (salmo salar). *Aquacultural Engineering*, 38:52–65.

Lader, P., Jensen, A., Sveen, J. K., Fredheim, A., Enerhaug, B., and Fredriksson, D. (2007a). Experimental investigation of wave forces on net structures. *Applied Ocean Research*, 29:112–127.

Lader, P. F. and Fredheim, A. (2006). Dynamic properties of a flexible net sheet in waves and current-a numerical approach. *Aquacultural Engineering*, 35:228–238.

Lader, P. F., Olsen, A., Jensen, A., Sveen, J. K., Fredheim, A., and Enerhaug, B. (2007b).

Experimental investigation of the interaction between waves and net structures-damping mechanism. *Aquacultural Engineering*, 37:100–114.

Langen, I. and Sigbjörnsson, R. (1999). *Dynamisk analyse av konstruksjoner*. [s.n.], [S.l.].

Larsen, P. K. (1990). *Dimensjonering av stålkonstruksjoner*. Tapir, [Trondheim]. In Norwegian.

Lee, C.-W., Kim, H.-S., Lee, G.-H., and Koo, K.-Y. (2005a). Dynamic simulation for a fish cage system. volume 2 of *Proceedings of the International Conference on Offshore Mechanics and Arctic Engineering - OMAE*, pages 507–516, Halkidiki, Greece. American Society of Mechanical Engineers, New York, NY 10016-5990, United States.

Lee, C.-W., Lee, J.-H., Cha, B.-J., Kim, H.-Y., and Lee, J.-H. (2004). Modeling of underwater flexible structures and its application to the fishing gear system simulation. volume 3 of *Proceedings of the International Conference on Offshore Mechanics and Arctic Engineering - OMAE*, pages 685–690, Vancouver, BC, Canada. American Society of Mechanical Engineers, New York, NY 10016-5990, United States.

Lee, C.-W., Lee, J.-H., Cha, B.-J., Kim, H.-Y., and Lee, J.-H. (2005b). Physical modeling for underwater flexible systems dynamic simulation. *Ocean Engineering*, 32:331–347.

Leira, B. J. (1987). Multidimensional stochastic linearisation of drag forces. *Applied Ocean Research*, 9:150–162.

Leira, B. J. (2000). Stochastic theory of sealoads. NTNU, Dept. of Marine Technolog. UK-2000-72.

Lekang, O.-I. (2007). *Aquaculture Engineering*. Wiley-Blackwell.

Li, Y., Gui, F., and Teng, B. (2007). Hydrodynamic behavior of a straight floating pipe under wave conditions. *Ocean Engineering*, 34:552–559.

Li, Y., Zhao, Y., Gui, F., Teng, B., and Guan, C. (2006). Numerical analysis of the effects of sinker weight on the hydrodynamics behaviour of gravity cage net in uniform flow. *Journal of Hydrodynamics*, 18:77–83.

Lien, E., Sunde, L. M., and Midling, K. (2006). *Havbruksforskning: fra merd til mat : havbruk - produksjon av akvatiske organismer (2000-2005)*, chapter Havbruksteknologi, pages 288–305. Norges forsknigsrad.

Løland, G. (1991). *Current forces on and flow through fish farms*. PhD thesis, Division of Marine Hydrodynamics, Norwegian Institute of Technology.

Marine Harvest (2006). *2006 Annual Report*. Marine Harvest.

MathWorks (2007). www.mathworks.com. [Online; accessed 10-November-2007].

Mathworld (2007). Newton's method. [Online; accessed 10-November-2007] http://mathworld.wolfram.com/NewtonsMethod.html.

Matsuishi, M. and Endo, T. (1968). Fatigue of metals subjected to varying stress. *Japan Society of Mechanical Engineers, Jukvoka, Japan*.

Microsoft (2008). Mfc reference. [Online. Accessed 03-January2008] http://msdn2.microsoft.com/en-us/library/d06h2x6e(VS.71).aspx.

Miller, G. (1991). Object-oriented approach to structural analysis and design. *Computers and Structures*, 40:75–82.

Miller, G. (1993). Coordinate-free isoparametric elements. *Computers and Structures*, 49:1027–1035.

Miner, M. (1945). Cumulative damage in fatigue. *American Society of Mechanical Engineers – Journal of Applied Mechanics*, 12:–159—164.

Moan, T. (2001). *Dynamic Loading and Design of Structures*, chapter 5. Wave loading, pages 175–230. Taylor & Francis. In Norwegian.

Moan, T. (2003). Design of offshore structures, vol. 1. NTNU, Dept. of Marine Technology. UK-01-84.

Moan, T., Berge, S., and Holthe, K. (1981). *Analysis of the fatigue failure of the "Alexander L. Kielland"*.

Moe, H., Olsen, A., Hopperstad, O. S., Jensen, Ø., and Fredheim, A. (2007). Tensile properties for netting materials used in aquaculture net cages. *Aquacultural Engineering*, 37:252–265.

Morison, J., O'Brien, M., Johnson, J., and Schaaf, S. (1950). Force exerted by surface waves on piles. *American Institute of Mining and Metallurgical Engineers – Journal of Petroleum Technology*, 2:149–154.

Morooka, C. K. and Yokoo, I. H. (1997). Numerical simulation and spectral analysis of irregular sea waves. *International Journal of Offshore and Polar Engineering*, 7:189–196.

Myrhaug, D. (2003). Uregelmessig sjø. NTNU, Dept. of Marine Technology. UK-2003-77.

Myrhaug, D. (2006). *Oceanography: wind, waves*, volume UK-2006-78. Institutt for marin teknikk, Trondheim.

Newland, D. E. (2005). *An Introduction to Random Vibrations, Spectral & Wavelet Analysis: Third Edition*. Dover Publications, 3 edition.

Newman, J. N. (1977). *Marine Hydrodynamics*. The MIT Press.

Newmark, N. (1959). Method of computation for structural dynamics. *ASCE – Proceedings – Journal of the Engineering Mechanics Division*, 85:67–94.

Newton, I. (1664-1671). *Methodus fluxionum et serierum infinitarum*.

Norsk Akkreditering (2007). http: www.akkreditert.no. [Online, accessed 28-December-2007].

Ochi, M. K. (2005). *Ocean Waves: The Stochastic Approach*. Cambridge University Press, new ed edition.

OOFEM (2007). http://www.oofem.org/. [Online. Accessed 29-December-2007].

OpenGL (2008). http://opengl.org/. [Online. Accessed 03-January-2008].

OpenSees (2007). http://opensees.berkeley.edu/index.php. [Online. Accessed 29-December-2007].

Ormberg, H. (1991). *Non-linear response analysis of floating fish farm systems*. PhD thesis, Division of Marine Structures, Norwegian Institute of Technology, University of Trondheim.

Palmgren, A. (1924). Die lebensdauer von kugellagern. *Zeitschrift des Vereines Deutscher Ingenieure*, 68:339–341.

Raphson, J. (1690). *Analysis aequationum universalis.* London.

Regjeringen (2007). http://www.regjeringen.no/nb/dep/fkd/tema/akvakultur/romming.html?id=446992. [Online; accessed 28-December-2007] In Norwegian.

Remseth, S. N. (1978). *Nonlinear static and dynamic analysis of space structures*, volume 78-2. Division of Structural Mechanics, The Norwegian Institute of Technology, Trondheim.

Rice, S. (1944). Mathematical analysis of random noise. *Bell System Technical Journal*, 23:282–332.

Rice, S. (1945). Mathematical analysis of random noise. *Bell System Technical Journal*, 24:46–156.

Roaldsnes, K. (2007). Personal communication.

Rømmingskommisjonen for akvakultur (2007). http://www.rommingskommisjonen.no. [Online; accessed 23-November-2007].

Rucki, M. and Miller, G. (1996). Algorithmic framework for flexible finite element-based structural modeling. *Computer Methods in Applied Mechanics and Engineering*, 136:363–384.

Rucki, M. and Miller, G. (1998). Adaptable finite element modelling kernel. *Computers and Structures*, 69:399–409.

Schijve, J. (2001). *Fatigue of Structures and Materials*. Springer, 1 edition.

Schlichting, H. (1968). *Boundary-Layer Theory*. Mcgraw-hill Book Company.

Sheehan, J. M., Grealish, F. W., Harte, A. M., and Smith, R. J. (2006). Characterizing the wave environment in the fatigue analysis of flexible risers. *Journal of Offshore Mechanics and Arctic Engineering*, 128:108–118.

Simulia (2007). http://www.simulia.com/products/unified_fea.html. [Online. Accessed 29-December-2007].

SINTEF (1987). Riflex — flexible riser system analysis program, theory manual. Technical report, MARINTEK and SINTEF, Division of Structural Engineering.

Standard Norge (2001). Steel structures - design rules. Norsk standard NS 3471. In Norwegian.

Standard Norge (2002a). Design of structures- design actions - part 4: Wind loads. Norsk

standard NS 3491-4. In Norwegian.

Standard Norge (2002b). Eurocode - basis of structural design. NS-EN 1990.

Standard Norge (2003). Marine fish farms - requirements for design, dimensioning, production, installation and operation. Norsk Standard NS 9415.

Standard Norge (2004). Design of structures . requirements to reliability. Norsk Standard NS 3490. In Norwegian.

Stephens, R. I. (2001). *Metal Fatigue in Engineering*. Wiley-IEEE.

Sumer, B. M. and Fredsøe, J. (2006). *Hydrodynamics Around Cylindrical Structures*. World Scientific.

Swift, M., Palczynski, M., Kestler, K., Michelin, D., Cellikol, B., and Gosz, M. (1997). Fish cage physical modeling for software development and design applications. In *Symposium on Marine Finfish and Shellfish Aquaculture*.

Swift, M. R., Fredriksson, D. W., Unrein, A., Fullerton, B., Patursson, O., and Baldwin, K. (2006). Drag force acting on biofouled net panels. *Aquacultural Engineering*, 35:292–299.

Thomassen, M. S. (2006). *Havbruksforskning: fra merd til mat : havbruk - produksjon av akvatiske organismer (2000-2005)*. Norges forskningsråd, Oslo.

Thomassen, P. E. (1985). Development of a direct manipulation, two-dimensional finite element analysis tool. Master's thesis, University of Washington.

Thomassen, P. E. and Leira, B. (2005). A prototype tool for analysis and design of floating fish cages. In *Proceedings of the International Conference on Offshore Mechanics and Arctic Engineering - OMAE*, volume 2, pages 787–792, Halkidiki, Greece. American Society of Mechanical Engineers, New York, NY 10016-5990, United States.

Thomassen, P. E. and Leira, B. J. (2006). Fatigue design of floating fish farms based on load and response interaction. In *Proceedings of the Fourth International Conference on Hydroelasticity in Marine Technology*, Wuxi, China.

Tsukrov, I., Eroshkin, O., Fredriksson, D., Swift, M., and Celikkol, B. (2003). Finite element modeling of net panels using a consistent net element. *Ocean Engineering*, 30:251–270.

Tsukrov, I. I., Ozbay, M., Fredriksson, D. W., Swift, M. R., Baldwin, K., and Celikkol, B. (2000). Open ocean aquaculture engineering: numerical modeling. *Marine Technology Society Journal*, 34:29–40.

Ultramarine (2007). http://www.ultramarine.com/. [Online. Accessed 30-December-2007].

US. Army Coastal Engineering Research (1984). *Shore protection manual*.

WAFO (2007). Wave analysis for fatigue and oceanography. [Online; accessed 23-November-2007] http://www.maths.lth.se/matstat/wafo/.

Walpole, R. E., Myers, R. H., Myers, S. L., and Ye, K. (2006). *Probability & Statistics for Engineers & Scientists*. Prentice Hall, 8 edition.

Wheeler, J. D. (1970). Method for calculating forces produced by irregular waves. *Jour. of Petro. Techn.*, 22:359–67.

Wikipedia (2007). http://en.wikipedia.org/wiki/computational_fluid_dynamics. [Online; accessed 18-November-2007].

Wikipedia (2008a). http://en.wikipedia.org/wiki/beaufort_scale. [Accessed online. 04-January-2008].

Wikipedia (2008b). http://en.wikipedia.org/wiki/frequency_scaling. [Accessed online. 25-April-2008].

Wikipedia (2008c). http://en.wikipedia.org/wiki/multi_core. [Accessed online. 25-April-2008.

Wirsching, P. H., Thomas L, P., and Ortiz, K. (2006). *Random Vibrations: Theory and Practice*. Dover Publications.

Wroldsen, A. S., Johansen, V., Skelton, R. E., and Sorensen, A. J. (2006). Hydrodynamic loading of tensegrity structures. Proceedings of SPIE - The International Society for Optical Engineering, San Diego, CA, United States. International Society for Optical Engineering, Bellingham WA, WA 98227-0010, United States.

WWF Norge (2006). Innspill til Regjeringens stortingsproposisjon om vern av villaksen fra WWF, Norges Jeger- og Fiskerforbund og Norske Lakseelver.

Yang, R.-Y., Hwung, H.-H., Jan, S.-J., Teng, C.-L., Capart, H., and Kuo, L.-A. (2007). Experimental study on the interaction between flow current and cage structure. Proceedings of the International Offshore and Polar Engineering Conference, pages 2269–2274, Lisbon, Portugal. International Society of Offshore and Polar Engineers, Cupertino, CA 95015-0189, United States.

Young, I. (1999). *Wind Generated Ocean Waves*. Elsevier Science.

Appendix A

Natural modes

In this appendix the twelve first natural modes of the BCS with the corresponding natural periods T_p are shown, c.f. section 4.5. The result corresponds to case# 1 of Table 4.8, i.e. $\frac{k_w}{k_{w,max}} = 100\%$ and $C_m = 0.63$.

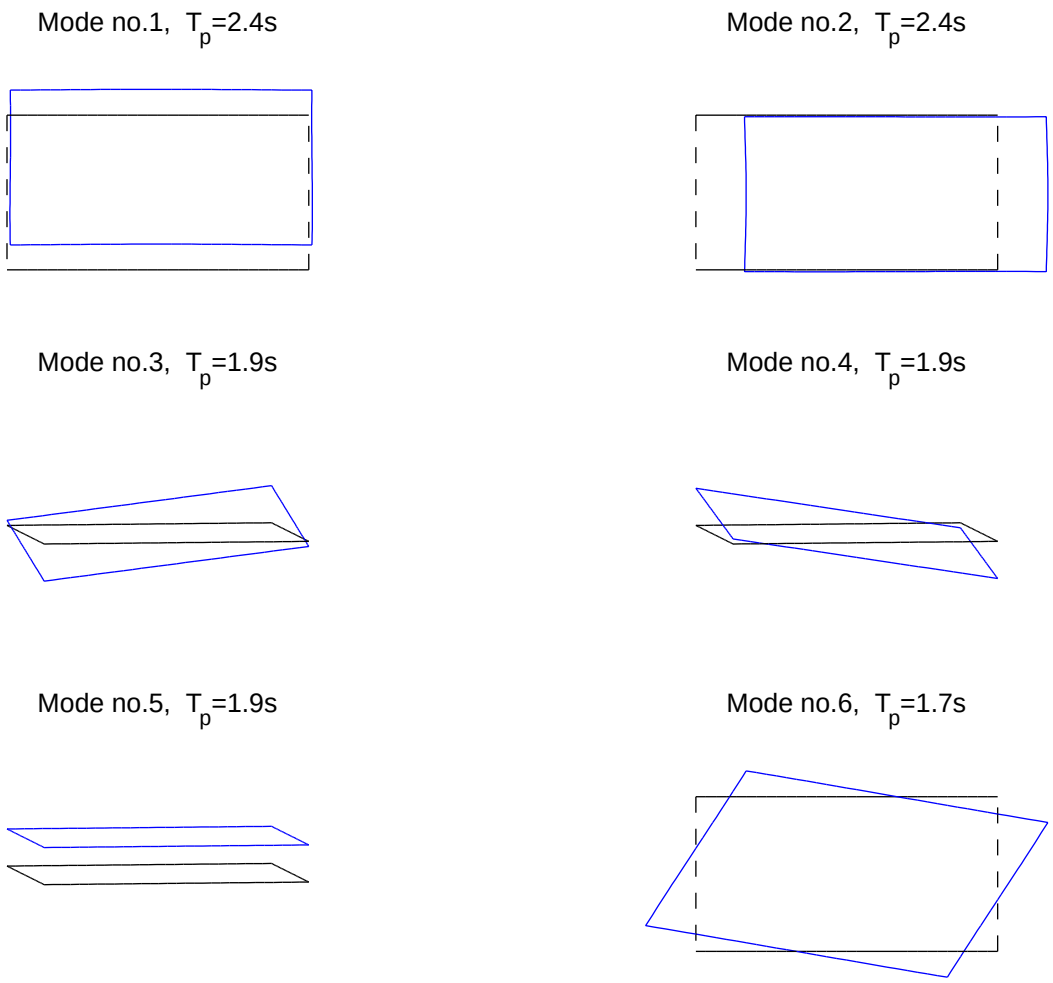

Figure A.1: Natural modes no. 1 to 6

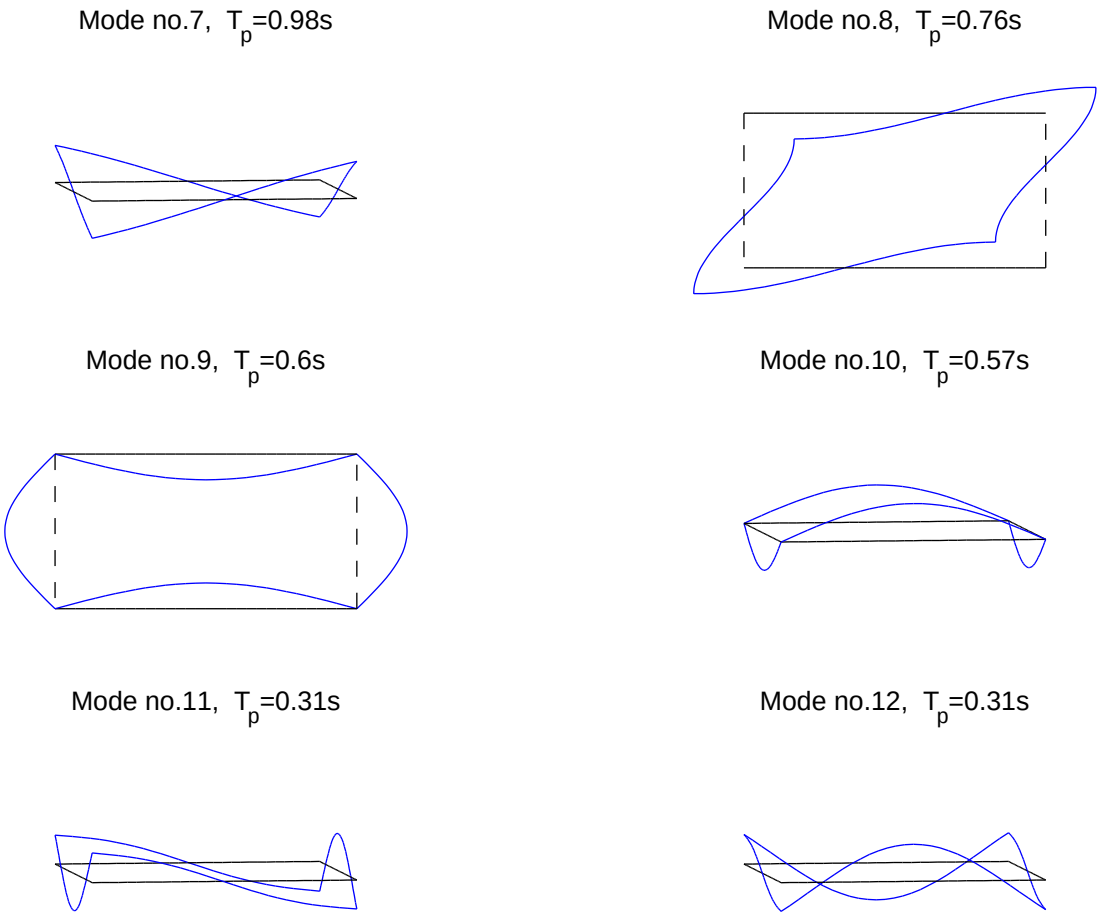

Figure A.2: Natural modes no. 7 to 12

Appendix B

Screenshots from Dr.Frame3D

Screenshots from linear, static analysis of the BCS using the software Dr.Frame3D (Dr Software LCC, 2007) is presented. The analysis and results are explained in Section 4.1.

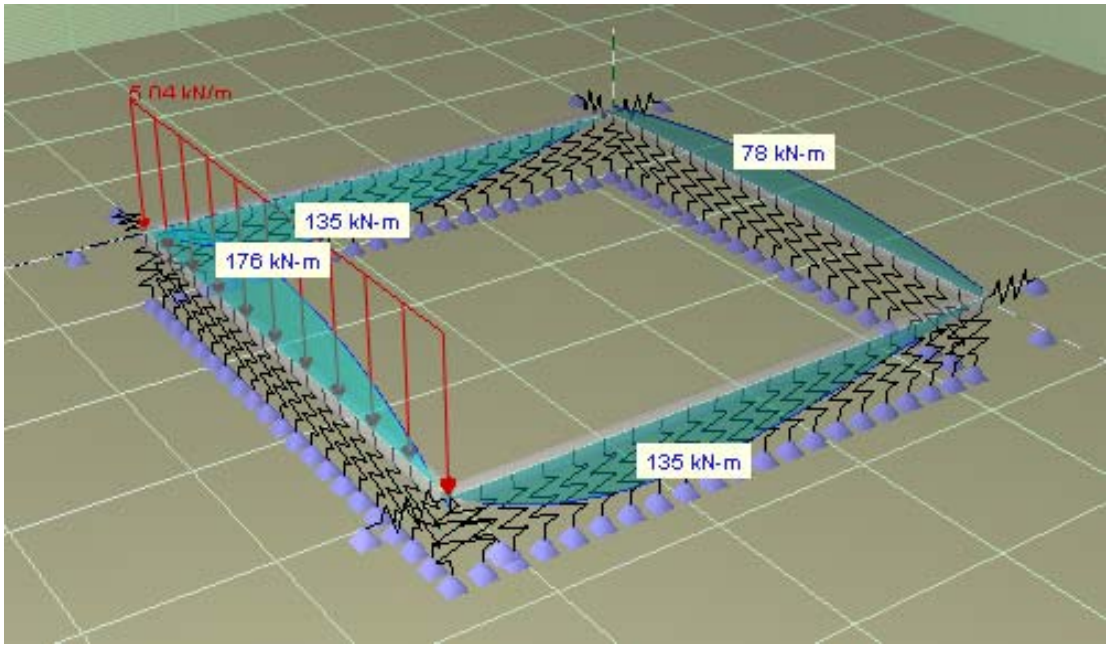

Figure B.1: Vertical loading, load case # 1: Bending moments of the BCS with vertical load on one member, $q = 5.0\,kN/m$.

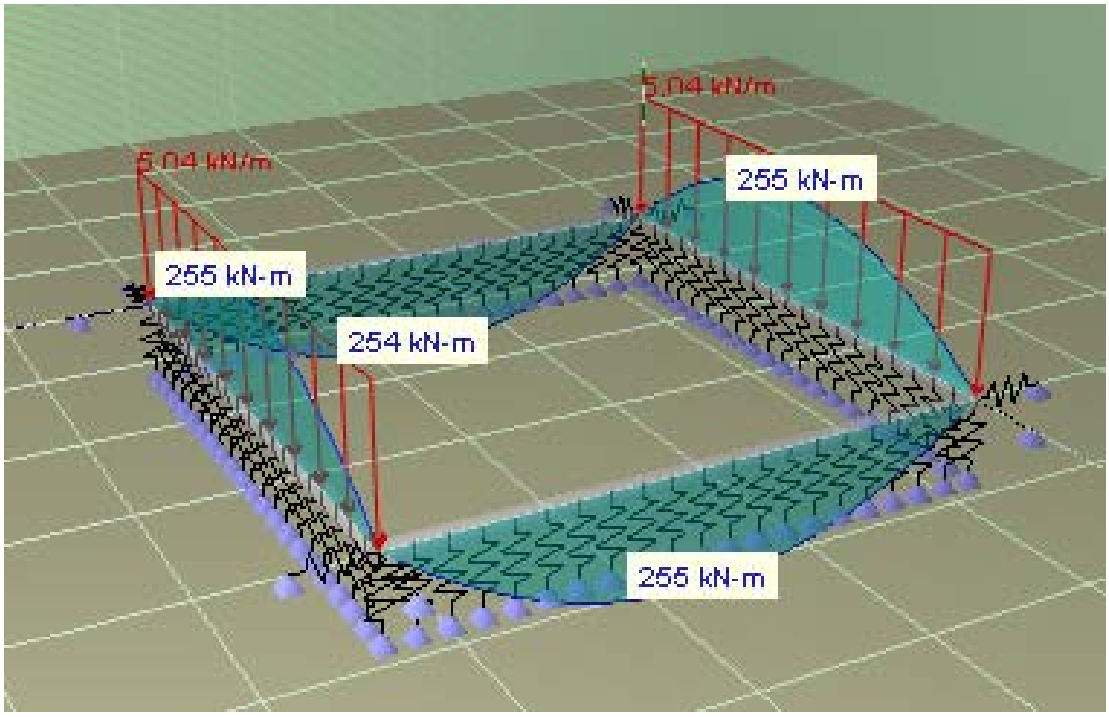

Figure B.2: Vertical loading, load case # 2: Bending moments of BCS with opposite members loaded with vertical loads in the same direction (i.e. in-phase loading)

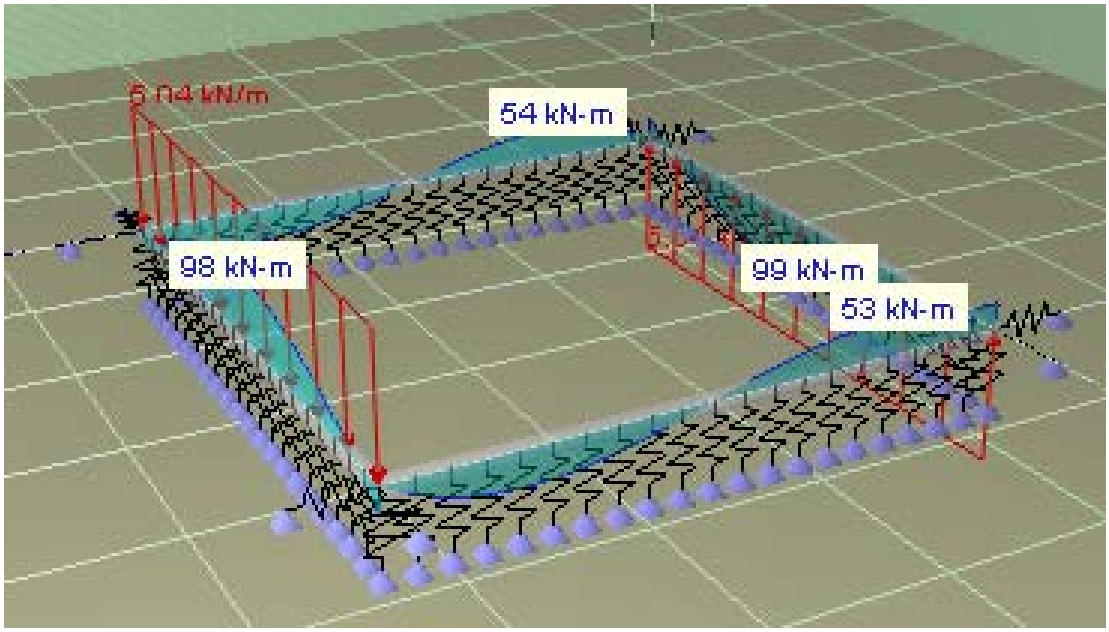

Figure B.3: Vertical loading, load case # 3: Bending moments of BCS with opposite members loaded with vertical loads in opposite directions (i.e. out-of-phase loading).

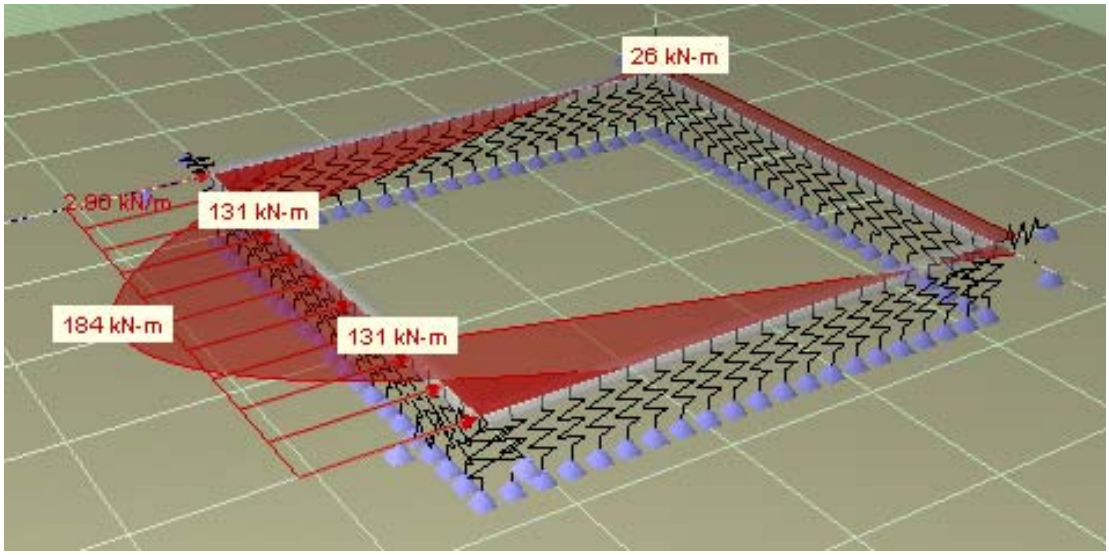

Figure B.4: Horizontal loading, load case # 1: Bending moments of the BCS with horizontal loading of one member, $q = 2.8\,kN/m$

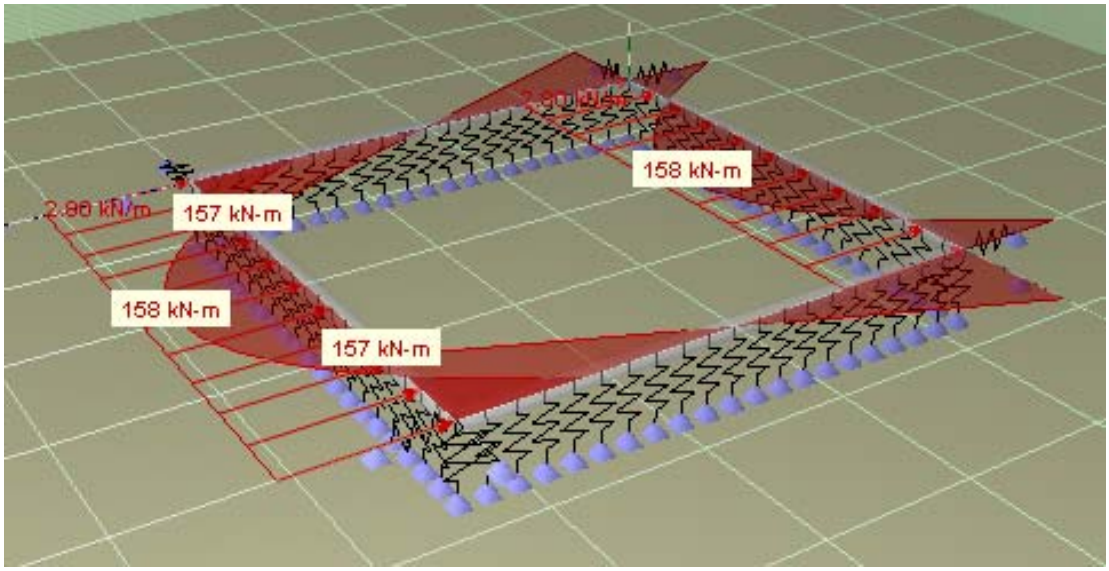

Figure B.5: Horizontal loading, load case # 2: Bending moments with opposite members loaded with horizontal loads in the same direction (i.e. in-phase loading)

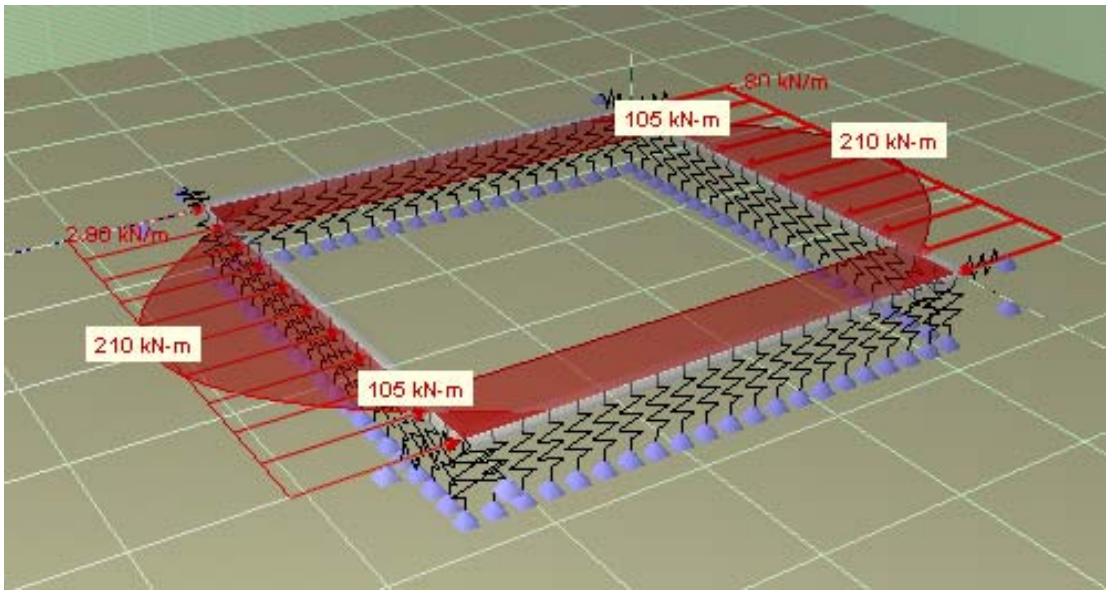

Figure B.6: Horizontal loading, load case # 3: Bending moments of BCS with opposite members loaded with horizontal loads in opposite directions (i.e. out-of-phase loading).

Appendix C

Quotes from relevant codes

In this appendix, quotes from relevant codes are presented and commented.

C.1 Parts of NS 9415 relevant for fatigue design

C.1.1 Wind

> **5.5.2 Use of fixed values for wind**
> In the planning of main components and complete installation, the starting point shall be 50-year wind determined at $35\,m/s$ (see also Annex A) as the dimensioning wind load if there is no empirical wind data for the locality in question. (...)

In Appendix A also the 1-year wind speed for expected extreme wind is given:

> Expected extreme wind is virtually the same along the coast from Lindesnes to North Cape[24] (NS3491-4. Figure A.1 (Standard Norge, 2002a)). Typically, the 1-year wind blows at $28\,m/s$ and the 50-year wind at about $35m/s$ outermost at the coast. In towards the land from the coast, the wind abates.(...) This means that the 50-year wind in the coastal zone will typically vary between $25\,m/s$ and $35\,m/s$. (...) Since the wind varies relatively little along the coast, there is little purpose in classifying localities according to the wind climate.

C.1.2 Peakedness factor

The clause in NS 9415 regulating regular waves was cited in Section 3.1.1. The use of irregular waves are regulated in the Section **5.11 Classification of locality**:

[24]The author assumes that the intention of NS 9415 here was to include the whole western and northern Norwegian coastline, i.e. from Lindesnes to *Grense Jakobselv*

5.11.4 Irregular waves

In irregular waves the jonswap-spectrum with $\gamma = 2.5$ for wind waves and $\gamma = 6.0$ for swell. The duration of a short-term wave load shall be set at $3h$.

However, a seemingly conflicting rule is found in sec. **5.4 Setting of wave parameters**:

5.4.2 Calculation of waves based on fetch

(...)

In the calculation of wave forces on fish farming installations it is usual to model for wave conditions with the aid of a jonswap-spectrum. This spectrum is determined by three parameters: Significant wave height, peak period and peak-shape parameter γ. The peak-shape parameter can be calculated based on:

$$\gamma = 44(H_s/F)^{2/7} \tag{C.1}$$

C.1.3 Design working life

In Section 6.1.2 the dimensioning useful life and the return period of natural loads are given:

6.1.2 Dimensioning useful life and return period

Dimensioning useful life, that is to say, the dimensioning useful life of the floater, shall be defined. The same shall be done with a return period for natural loads. Dimensioning useful life shall not be set at less than 10 years, and the return period shall be at least 2,5 times larger than the dimensioning useful life.

The term"dimensioning useful life" (*dimensjonerende brukstid* in the Norwegian original) is not consistent with NS-EN 1990 (Standard Norge, 2002b) and it is suggested that the term *design working life* should be used instead. Likewise, it is suggested that environmental actions (or loads) are used instead of the term natural loads.

In NS-EN 1990 (Standard Norge, 2002b) the design working life is regulated according to the kind of structure in question, see Section C.2. Design working life category 2 — with an indicative design working life between 15 and 30 years — seems most relevant for floating fish cages as it also covers agricultural structures, see Figure C.1. Also, the design working life is directly connected to time dependent effects, such as fatigue, see quote of NS-EN 1990 (Standard Norge, 2002b), Section 3.1. in Appendix C.2.

C.1.4 Fatigue design

Fatigue design of the floater is required in NS 9415. The following quote is the subsection which describes fatigue design:

6.7.3 Strength calculation

Strength calculation of the installation shall be documented. The calculation program utilized shall be validated.

Based on information regarding the loads, the following calculations shall be done:

- global construction strength analysis, including output from the moorings;
- local construction strength analysis;
- simplified fatigue analysis.

A simplified fatigue analysis shall be undertaken, where the Weibull factor is set at 1.0. For catamaran installations it is reduced to 0.8 provided that the tension in the prevailing direction is at least 20% lower than the tension applied in the fatigue analysis.

A load factor of 1.0 and a material factor of 1.0 are given in table 6 and 7, respectively, of Section 6.7.4 in NS 9415.

C.2 Design working life in NS-EN 1990

The following quotes shows the definition of the term design working life and how it is related to fatigue.

1.5.2. Special terms related to design in general

1.5.2.4 persistent design situation

design situation that is relevant during a period of the same order as the design working life of the structure

1.5.2.8 design working life

assumed period for which a structure or part of it is to be used for its intended purpose with anticipated maintenance but without major repair being necessary.

Section 3 Principles of limit state design

3.1. General

(...)

(5) Verifications of limit states that are concerned with time dependent effects (e.g. fatigue) should be related to the design working life of the construction.

2.3 Design working life

(1) The design working life should be specified.

NOTE Indicative categories are given in Table 2.1. The values given in Table 2.1 may also be used for determining time-dependent performance (*e.g.* fatigue-related calculations). See also Annex A.

Table 2.1 - Indicative design working life

Design working life category	Indicative design working life (years)	Examples
1	10	Temporary structures (1)
2	10 to 25	Replaceable structural parts, e.g. gantry girders, bearings
3	15 to 30	Agricultural and similar structures
4	50	Building structures and other common structures
5	100	Monumental building structures, bridges, and other civil engineering structures
(1) Structures or parts of structures that can be dismantled with a view to being re-used should not be considered as temporary.		

Figure C.1: Section 2.3 of NS-EU 1990

C.3 DFF in DNV-OS-C101 Design of offshore steel structures

The following quote from *DNV-OS-C101, Section 6 Fatigue limit states* (DNV, 2004) explains the use and rationale behind the DFF values:

A200 Design fatigue factors

201 Design fatigue factors (DFF) shall be applied to increase the probability for avoiding fatigue failures.

202 The DFFs are dependent on the significance of the structural component with respect to structural integrity and availability for inspection and repairs.

203 DFFs shall be applied to design fatigue life. The calculated fatigue life shall be longer than the design fatigue life times the DFF.

204 The design requirement can alternatively be expressed as the cumulative damage ratio for the number of load cycles of the defined design fatigue life multiplied with the DFF shall be less or equal to 1.0.

205 The design fatigue factors in Table A1 are valid for units with low consequence of failure and where it can be demonstrated that

Table A1 Design Fatigue Factors (DFF)	
DFF	*Structural element*
1	Internal structure, accessible and not welded directly to the submerged part.
1	External structure, accessible for regular inspection and repair in dry and clean conditions.
2	Internal structure, accessible and welded directly to the submerged part.
2	External structure not accessible for inspection and repair in dry and clean conditions.
3	Non-accessible areas, areas not planned to be accessible for inspection and repair during operation.

```
the structure satisfies the requirements to damaged condition according
to the ALS with failure in the actual joint as the defined damage.
```

Appendix D

SCATTER DIAGRAM

Table 2.2. *Joint frequency of significant wave height and spectral peak period. Representative data for the northern North Sea*

Significant wave height (m) (upper limit of interval)	Spectral peak period (s)																					Sum
	3	4	5	6	7	8	9	10	11	12	13	14	15	16	17	18	19	21	22			
1	59	403	1061	1569	1634	1362	982	643	395	232	132	74	41	22	12	7	4	2	2			8636
2	9	212	1233	3223	5106	5814	5284	4102	2846	1821	1098	634	355	194	105	56	30	16	17			32 155
3	0	8	146	831	2295	3896	4707	4456	3531	2452	1543	901	497	263	135	67	33	16	15			25 792
4	0	0	6	85	481	1371	2406	2960	2796	2163	1437	849	458	231	110	50	22	10	7			15 442
5	0	0	0	4	57	315	898	1564	1879	1696	1228	748	398	191	84	35	13	5	3			9118
6	0	0	0	0	3	39	207	571	950	1069	885	575	309	142	58	21	7	2	1			4839
7	0	0	0	0	0	2	27	136	347	528	533	387	217	98	37	12	4	1	0			2329
8	0	0	0	0	0	0	2	20	88	197	261	226	138	64	23	7	2	0	0			1028
9	0	0	0	0	0	0	0	2	15	54	101	111	78	39	14	4	1	0	0			419
10	0	0	0	0	0	0	0	0	2	11	30	45	39	22	8	2	1	0	0			160
11	0	0	0	0	0	0	0	0	0	2	7	15	16	11	5	1	0	0	0			57
12	0	0	0	0	0	0	0	0	0	0	1	4	6	5	2	1	0	0	0			19
13	0	0	0	0	0	0	0	0	0	0	0	1	2	2	1	0	0	0	0			6
14	0	0	0	0	0	0	0	0	0	0	0	0	0	1	0	0	0	0	0			1
15	0	0	0	0	0	0	0	0	0	0	0	0	0	0	0	0	0	0	0			0
Sum	68	623	2446	5712	9576	12 799	14 513	14 454	12 849	10 225	7256	4570	2554	1285	594	263	117	52	45			100 001

Figure D.1: Scatter diagram reproduced from (Faltinsen, 1990).

Appendix E

THE BEAUFORT WIND SCALE

The Beaufort wind scale is presented din Table E.1, see e.g. (Wikipedia, 2008a), (Børresen, 1987). The wave heigh given is the most probable maximum wave height.

Beaufort number	Wind speed [m/s]	Description	Wave height [m]	Sea conditions
0	0-0.2	Calm	0	Flat.
1	0.3-1.5	Light air	0.1	Ripples without crests.
2	1.6-3.3	Light breeze	0.3	Small wavelets. Crests of glassy appearance, not breaking
3	3.4-5.4	Gentle breeze	1.0	Large wavelets. Crests begin to break; scattered whitecaps.
4	5.5-7.9	Moderate breeze	1.5	Small waves.
5	8.0-10.7	Fresh breeze	2.5	Moderate longer waves. Some foam and spray.
6	10.8-13.8	Strong breeze	4.0	Large waves with foam crests and some spray.
7	13.9-17.1	Moderate gale	5.5	Sea heaps up and foam begins to streak.
8	17.2-20.7	Fresh gale	7.5	Moderately high waves with breaking crests forming spindrift. Streaks of foam.
9	20.8-24.4	Strong gale	10.0	High waves with dense foam. Wave crests start to roll over. Considerable spray.
10	24.5-28.4	Storm	12.5	Very high waves. The sea surface is white and there is considerable tumbling. Visibility is reduced.
11	28.5-32.6	Violent storm	16.0	Exceptionally high waves.
12	32.7-40.8	Hurricane		Huge waves. Air filled with foam and spray. Sea completely white with driving spray. Visibility greatly reduced.

Table E.1: The Beaufort scale. The wave height column presents the most probable maximum wave height on open ocean.

Appendix F

LINEAR SYSTEM

The fundamental equations for a 1 DOF linear dynamic system are summarized in this appendix. For a broader description of the topic, see e.g. (Bergan et al., 1986).

The differential equation for a linear system excited by a sinusoidal load is typically given as:

$$M \cdot \ddot{\eta} + B \cdot \dot{\eta} + K \cdot \eta = F_0 \cdot \sin(\omega\, t) \tag{F.1}$$

M is the mass, B is the (linearized) damping, K is the stiffness, F_0 is the amplitude of the load, and $\omega = \frac{2\pi}{T}$ is the loading frequency (for an explanation of the use of symbols B for damping as opposed to C, see Section 3.3.1). $\ddot{\eta}$, $\dot{\eta}$, and η are acceleration, velocity, and deflection of the body.

The critical damping B_{cr} and the relative damping coefficient ξ are given as:

$$B_{cr} = 2\sqrt{K \cdot M} \tag{F.2}$$

$$\xi = \frac{B}{B_{cr}} = \frac{B}{2\sqrt{K \cdot M}} \tag{F.3}$$

The relevant damping category for a floating fish farm is *under damped system*, i.e. $B < B_{cr}$ and $\xi < 100\%$. The natural frequency ω_N and natural period T_N are given as:

$$\omega_N = \sqrt{\frac{K}{M}}\,,\; T_N = 2\pi\sqrt{\frac{M}{K}} \tag{F.4}$$

The relative frequency β is the ratio of the exciting frequency and the natural frequency:

$$\beta = \frac{\omega}{\omega_N} = \frac{T_N}{T} \tag{F.5}$$

The dynamic amplification factor DAF and the phase angle ϕ is then given as:

$$DAF = \frac{1}{\sqrt{(1-\beta^2)^2 + (2\xi\beta)^2}} \tag{F.6}$$

ξ	$\frac{T_d}{T_N}$	$\frac{T_m}{T_N}$	DAF_m
1%	1.00	1.00	50.0
5%	1.00	1.00	10.0
10%	1.01	1.01	5.03
20%	1.02	1.04	2.55
30%	1.05	1.10	1.75
40%	1.09	1.21	1.36
50%	1.15	1.41	1.15
60%	1.25	1.89	1.04
70%	1.40	7.07	1.00

Table F.1: Damped natural period T_d and period for maximum response T_m as a fraction of natural period T_N. Maximum dynamic amplification factor DAF_m.

$$\tan\phi = -\frac{2\xi\beta}{1-\beta^2} \tag{F.7}$$

The static response Δ_{stat} is :

$$\Delta_{stat} = \frac{F_0}{K} \tag{F.8}$$

For an under damped system ($\xi < 100\%$) the damped natural period T_d will be higher than the undamped natural period, and the period for maximum response T_m is higher yet:

$$T_d = T_N\beta_d = \frac{T_N}{\sqrt{1-\xi^2}}\ ,\ \beta_d = \frac{T_d}{T_N} = \frac{1}{\sqrt{1-\xi^2}} \tag{F.9}$$

$$T_m = T_N\beta_m = \frac{T_N}{\sqrt{1-2\xi^2}}\ ,\ \beta_m = \frac{T_m}{T_N} = \frac{1}{\sqrt{1-2\xi^2}} \tag{F.10}$$

From Equation F.10 we see that $T_m \to \infty$ as $\xi \to \frac{1}{\sqrt{2}} \approx 71\%$. The maximum dynamic amplification factor DAF_m is found by using $\beta = \beta_m = \frac{1}{\sqrt{1-2\xi^2}}$ in Equation F.6:

$$DAF_m = \frac{1}{\sqrt{(1-\beta_m^2)^2 + (2\xi\beta_m)^2}} \tag{F.11}$$

In Table F.1 the values for T_d and T_m for 1% to 70% damping is shown. The corresponding maximum dynamic amplification factor (DAF_m) is also included. We see that for realistic damping levels both the damped and maximum periods can be considerably larger than the natural period.

Appendix G

TABLES

Tables of secondary interest are presented in this appendix.

Table G.1 to G.5 are versions in percentage of tables previously given with absolute values. The correspondence is given in the table titles.

Table G.6 to G.9 are results for regular wave analysis of four different levels of wave height H over a wave period interval. The waves are applied to both a linear and a nonlinear system. The maximum stress range $\Delta\sigma_{0,sc}$, fatigue life L_{sc}, as well as the ratios of nonlinear stress range to linear stress range and nonlinear to linear fatigue life are given. SN curve C2 is used. The critical point is the top point at the middle of a member perpendicular to the wave direction. The tables are related to the discussion in Section 9.1.1.

Table G.10 to G.13 are results for irregular wave analysis of four different levels of significant wave height H_s over a peak period interval. The waves are applied to both a linear and a nonlinear system. The maximum stress range $\Delta\sigma_{0,sc}$, fatigue life L_{sc}, as well as the ratios of nonlinear stress range to linear stress range and nonlinear to linear fatigue life are given. SN curve C2 is used. The critical point is the top point at the middle of a member perpendicular to the wave direction. The tables are related to the discussion in Section 9.4.

Table G.14 to G.17 are results for irregular wave analysis of four different levels of peak period over a significant wave height interval. The waves are applied to both a linear and a nonlinear system. The maximum stress range $\Delta\sigma_{0,sc}$, fatigue life L_{sc}, as well as the ratios of nonlinear stress range to linear stress range and nonlinear to linear fatigue life are given. SN curve C2 is used. The critical point is the top point at the middle of a member perpendicular to the wave direction. The tables are related to the discussion in Section 9.5.

	$\frac{H}{H_{ref}}$	50%	75%	100%	125%	150%	175%
B	H [m]	0.50	0.75	1.0	1.25	1.4*	
	Δ_z	0%	0%	−2%	−15%	−23%	
	$\Delta_{z,r}$	3%	7%	19%	38%	42%	
C	H [m]	1.00	1.50	2.00	2.50	3.00	3.50
	Δ_z	1%	1%	3%	−12%	−26%	−37%
	$\Delta_{z,r}$	3%	8%	43%	125%	143%	148%
D	H [m]	1.50	2.25	3.00	3.75	4.50	5.25
	Δ_z	0%	1%	5%	−11%	−26%	−36%
	$\Delta_{z,r}$	3%	8%	48%	204%	234%	247%
H_{max}	H [m]	2.85	4.28	5.70	7.13	8.55	9.98
	Δ_z	0%	−9%	−31%	−45%	−54%	−60%
	$\Delta_{z,r}$	13%	181%	249%	268%	275%	281%

Table G.1: Mid point, perpendicular cylinder, nonlinear analysis. Comparison of results from Table 7.3 with the corresponding linear results.

$\frac{H}{H_{ref}}$		50%	75%	100%	125%	150%	175%
B	H	0.50	0.75	1.00	1.25	1.40*	
	Δ_z	3%	6%	1%	−9%	−15%	
	$\Delta_{z,r}$	0%	0%	0%	−1%	−2%	
	M_y	−5%	−13%	−25%	−30%	−34%	
	Pitch	3%	6%	10%	4%	−5%	
C	H	1.00	1.50	2.00	2.50	3.00	3.50
	Δ_z	1%	−17%	−24%	−18%	−20%	−28%
	$\Delta_{z,r}$	−4%	−9%	−10%	−11%	−13%	−14%
	M_y	−22%	−49%	−59%	−64%	−69%	−73%
	Pitch	142%	81%	43%	14%	−72%	12%
D	H	1.50	2.25	3.00	3.75	4.5	5.25
	Δ_z	33%	63%	50%	31%	−1%	−23%
	$\Delta_{z,r}$	−17%	4%	42%	65%	82%	88%
	M_y	−40%	−58%	−70%	−79%	−84%	−85%
	Pitch	5%	−13%	−21%	−32%	−33%	−40%
H_{max}	H	2.85	4.28	5.70	7.13	8.55	9.98
	Δ_z	14%	−2%	−33%	−52%	−57%	−63%
	$\Delta_{z,r}$	40%	158%	214%	200%	230%	233%
	M_y	−43%	−66%	−73%	−80%	−82%	−84%
	Pitch	−15%	−41%	−46%	−59%	−62%	−67%

Table G.2: Mid point, parallel cylinder, nonlinear analysis. Comparison of results from Table 7.8 with the corresponding linear results.

$\frac{H}{H_{ref}}$		50%	75%	100%	125%	150%	175%
B	H	0.50	0.75	1.0	1.25	1.4*	
	Δ_z	2%	6%	9%	1%	−8%	
	$\Delta_{z,r}$	2%	4%	7%	5%	1%	
C	H	1.00	1.50	2.00	2.50	3.00	3.50
	Δ_z	18%	25%	11%	−4%	−19%	−31%
	$\Delta_{z,r}$	12%	21%	13%	4%	−4%	−10%
D	H	1.50	2.25	3.00	3.75	4.50	5.25
	Δ_z	12%	3%	−21%	−32%	−38%	−44%
	$\Delta_{z,r}$	19%	46%	34%	24%	24%	20%
H_{max}	H	2.85	4.28	5.70	7.13	8.55	9.98
	Δ_z	2%	−26%	−41%	−52%	−59%	−64%
	$\Delta_{z,r}$	44%	57%	64%	61%	57%	54%

Table G.3: End point, parallel cylinder, nonlinear analysis. Comparison of results from Table 7.9 with the corresponding linear results.

TRW	$\frac{H}{H_{ref}}$	25%	50%	75%	100%	125%	150%	175%
B	H	0.25	0.50	0.75	1.00	1.25	1.40*	
	Δ_z	1	2	5	6	-4	-13	
	$\Delta_{z,r}$	1	5	15	30	48	57	
	M_b	-2	-4	-8	-15	-23	-29	
	M_{tot}	-2	-3	-4	-7	-12	-15	
C	H	0.50	1.00	1.50	2.00	2.50	3.00	3.50
	Δ_z	2	9	15	11	-10	-20	-37
	$\Delta_{z,r}$	1	11	25	63	108	141	130
	M_b	-4	-14	-21	-37	-44	-46	-54
	M_{tot}	-3	-13	-18	-35	-37	-40	-49
D	H	0.75	1.50	2.25	3.00	3.75	4.50	5.25
	Δ_z	1	7	6	-8	-21	-26	-41
	$\Delta_{z,r}$	2	17	86	97	95	111	92
	M_b	-6	-35	-48	-54	-62	-55	-63
	M_{tot}	-6	-34	-48	-53	-60	-53	-60
H_{max}	H	1.43	2.85	4.28	5.70	7.13	8.55	9.98
	Δ_z	1	2	-23	-40	-51	-55	-63
	$\Delta_{z,r}$	6	80	118	130	130	128	126
	M_b	-9	-32	-45	-61	-66	-70	-73
	M_{tot}	-9	-33	-45	-59	-63	-66	-67

Table G.4: BCS, midpoint of perpendicular member. Comparison of results from Table 7.15 with the corresponding linear results.

TRW	$\frac{H}{H_{ref}}$	25%	50%	75%	100%	125%	150%	175%
B	H	0.25	0.50	0.75	1.00	1.25	1.40*	
	Δ_z	1	4	13	19	10	0	
	$\Delta_{z,r}$	0	0	1	-2	-13	-21	
	M_t	-8	-12	-26	-38	-37	-32	
	M_b	-2	-4	-9	-15	-23	-30	
	M_{tot}	-1	-4	-9	-15	-23	-30	
	θ	1	5	17	30	15	-3	
C	H	0.50	1.00	1.50	2.00	2.50	3.00	3.50
	Δ_z	4	27	42	25	2	-9	-27
	$\Delta_{z,r}$	1	7	9	-2	-16	-20	-30
	M_t	-4	-24	-45	-54	-56	-58	-64
	M_b	-6	-29	-42	-48	-55	-59	-67
	M_{tot}	-6	-28	-42	-48	-55	-58	-66
	θ	3	19	33	26	-9	-24	-41
D	H	0.75	1.50	2.25	3.00	3.75	4.50	5.25
	Δ_z	55	234	582	889	967	423	263
	$\Delta_{z,r}$	1	2	-13	-8	1	16	7
	M_t	1	-2	-5	-31	-49	-57	-61
	M_b	-7	-38	-59	-65	-72	-65	-69
	M_{tot}	-6	-38	-59	-65	-72	-65	-69
	θ	0	4	6	-3	-9	-15	-33
H_{max}	H	1.43	2.85	4.28	5.70	7.13	8.55	9.98
	Δ_z	1	19	3	-35	-51	-57	-66
	$\Delta_{z,r}$	2	0	69	101	109	128	113
	M_t	4	27	6	7	-19	-33	-43
	M_b	-9	-46	-60	-71	-77	-79	-826
	M_{tot}	-8	-46	-59	-70	-76	-77	-80
	θ	1	-10	-29	-39	-50	-55	-63

Table G.5: BCS, midpoint of parallel member. Comparison of results from Table 7.16 with the corresponding linear results.

T	Linear (L)		Nonlinear (NL)		$\frac{\Delta\sigma_{0,sc,NL}}{\Delta\sigma_{0,sc,L}}$	$\frac{L_{sc,NL}}{L_{sc,L}}$
	$\Delta\sigma_{0,sc}$	L_{sc}	$\Delta\sigma_{0,sc}$	L_{sc}		
$[s]$	[MPa]	[year]	[MPa]	[year]	[%]	[%]
1.80	28.2	23	27.2	27	97	119
1.87	10.3	3639	9.9	4341	97	119
1.90	16.3	371	16.5	343	102	93
1.96	28.2	25	27.5	28	97	114
2.00	24.5	50	23.3	65	95	128
2.07	10.3	4028	9.9	4930	96	122
2.10	13.8	923	13.7	967	99	105
2.19	27.7	30	27.2	33	98	109
2.20	27.8	30	27.2	33	98	111
2.30	16.0	493	15.5	575	97	117
2.34	10.4	4335	10.2	4668	99	108
2.40	14.4	881	14.0	1008	97	114
2.50	26.2	46	25.7	50	98	109
2.53	27.3	37	26.7	42	98	111
2.60	25.7	52	25.1	59	98	112
2.70	16.4	510	16.0	574	98	113
2.77	10.4	5131	10.2	5737	98	112
2.80	9.9	6600	9.6	7499	97	114

Table G.6: Stress range $\Delta\sigma_{0,sc}$ and fatigue life time L_{sc} for regular waves with $H = 0.4\,m$ and $T = 1.8 - 2.8\,s$. SN curve C2 is used. The critical point is the top point at the middle of a member perpendicular to the wave direction.

T	Linear (L)		Nonlinear (NL)		$\frac{\Delta\sigma_{0,sc,NL}}{\Delta\sigma_{0,sc,L}}$	$\frac{L_{sc,NL}}{L_{sc,L}}$
	$\Delta\sigma_{0,sc}$	L_{sc}	$\Delta\sigma_{0,sc}$	L_{sc}		
$[s]$	[MPa]	[year]	[MPa]	[year]	[%]	[%]
2.40	25.1	54	23.7	72	94	134
2.50	45.8	3	43.0	4	94	137
2.53	47.7	2	45.0	3	94	134
2.60	44.9	3	41.0	5	91	158
2.70	28.7	31	26.5	46	92	149
2.77	18.2	313	17.1	423	94	135
2.80	17.3	402	16.4	525	95	131
2.90	29.0	31	26.7	48	92	152
3.00	41.5	5	38.4	8	93	147
3.10	47.4	3	44.0	4	93	144
3.20	46.5	3	43.0	5	93	148

Table G.7: Stress range $\Delta\sigma_{0,sc}$ and fatigue life time L_{sc} for regular waves with $H = 0.7\,m$ and $T = 2.4 - 3.2\,s$. SN curve C2 is used. The critical point is the top point at the middle of a member perpendicular to the wave direction.

T	Linear (L)		Nonlinear (NL)		$\frac{\Delta\sigma_{0,sc,NL}}{\Delta\sigma_{0,sc,L}}$	$\frac{L_{sc,NL}}{L_{sc,L}}$
	$\Delta\sigma_{0,sc}$	L_{sc}	$\Delta\sigma_{0,sc}$	L_{sc}		
$[s]$	[MPa]	[year]	[MPa]	[year]	[%]	[%]
2.80	24.7	68	22.2	115	90	170
2.90	41.5	5.3	35.1	12	85	230
3.00	59.3	0.9	49.6	2.2	84	244
3.10	67.7	0.5	56.5	1.2	83	247
3.20	66.4	0.6	54.7	1.5	82	264
3.30	58.3	1.1	48.4	2.8	83	254
3.40	46.3	3.6	39.2	8.2	85	231
3.50	33.8	18	30.3	31	89	174

Table G.8: Stress range $\Delta\sigma_{0,sc}$ and fatigue life time L_{sc} for regular waves with $H = 1.0\,m$ and $T = 2.8 - 3.5\,s$. SN curve C2 is used. The critical point is the top point at the middle of a member perpendicular to the wave direction.

T	Linear (L)		Nonlinear (NL)		$\frac{\Delta\sigma_{0,sc,NL}}{\Delta\sigma_{0,sc,L}}$	$\frac{L_{sc,NL}}{L_{sc,L}}$
$[s]$	$\Delta\sigma_{0,sc}$ [MPa]	L_{sc} [year]	$\Delta\sigma_{0,sc}$ [MPa]	L_{sc} [year]	[%]	[%]
3.20	86.4	0.1	55.7	1.3	65	893
3.30	75.8	0.3	47.3	3.1	62	1050
3.40	60.2	1.0	41.5	6.2	69	644
3.50	44.0	4.7	33.8	18	77	371
3.58	34.4	17	29.3	37	85	225
3.60	32.8	21	28.5	43	87	200
3.70	32.6	23	31.6	26	97	117
3.80	41.7	6.7	37.7	11	90	166

Table G.9: Maximum stress range $\Delta\sigma_{0,sc}$ and fatigue life time L_{sc} for regular waves with $H = 1.3\,m$ and $T = 3.2\,s - 3.8\,s$. SN curve C2 is used. The critical point is the top point at the middle of a member perpendicular to the wave direction.

	Linear (L)		Nonlinear (NL)			
T_p	$\Delta\sigma_{0,sc}$	L_{sc}	$\Delta\sigma_{0,sc}$	L_{sc}	$\frac{\Delta\sigma_{0,sc,NL}}{\Delta\sigma_{0,sc,L}}$	$\frac{L_{sc,NL}}{L_{sc,L}}$
$[s]$	[MPa]	[year]	[MPa]	[year]	[%]	[%]
1.80	44	60.1	41	80.3	94	134
1.87	47	60.2	42	79.8	89	133
1.90	45	71.8	43	80.0	96	111
1.96	46	80.1	44	99.1	96	124
2.00	49	69.8	43	92.8	87	133
2.07	44	85.1	44	103.0	100	121
2.10	41	89.1	39	125.8	95	141
2.19	43	89.7	40	110.9	92	124
2.20	42	111.8	45	116.8	106	104
2.30	47	112.0	42	125.5	88	112
2.34	44	131.0	41	138.3	93	106
2.40	45	117.6	41	138.0	90	117
2.50	44	123.9	41	138.0	91	111
2.53	41	142.0	38	144.4	93	102
2.60	42	134.6	37	166.1	90	123
2.70	40	162.0	41	174.9	105	108
2.77	39	187.0	35	237.0	90	127
2.80	45	170.0	39	245.3	87	144

Table G.10: Maximum stress range $\Delta\sigma_{0,sc}$ and fatigue life time L_{sc} for irregular waves with $H_s = 0.4\,m$ and $T_p = 1.8\,s - 2.8\,s$. SN curve C2 is used. The critical point is the top point at the middle of a member perpendicular to the wave direction.

T_p	Linear (L)		Nonlinear (NL)		$\frac{\Delta\sigma_{0,sc,NL}}{\Delta\sigma_{0,sc,L}}$	$\frac{L_{sc,NL}}{L_{sc,L}}$
	$\Delta\sigma_{0,sc}$	L_{sc}	$\Delta\sigma_{0,sc}$	L_{sc}		
$[s]$	[MPa]	[year]	[MPa]	[year]	[%]	[%]
2.40	81	6.9	66	9.4	82	136
2.50	69	8.3	65	10.6	95	127
2.53	73	7.5	64	12.0	88	160
2.60	69	8.5	65	11.1	95	131
2.70	66	11.5	59	13.7	89	119
2.77	67	11.0	63	15.5	94	141
2.80	72	11.4	67	16.1	93	141
2.90	68	11.5	67	14.9	98	130
3.00	75	11.2	66	15.9	87	142
3.10	73	10.6	61	16.3	84	154
3.20	75	11.0	59	17.7	79	161

Table G.11: Maximum stress range $\Delta\sigma_{0,sc}$ and fatigue life time L_{sc} for irregular waves with $H_s = 0.7\,m$ and $T_p = 2.4\,s - 3.2\,s$. SN curve C2 is used. The critical point is the top point at the middle of a member perpendicular to the wave direction.

T_p	Linear (L)		Nonlinear (NL)		$\frac{\Delta\sigma_{0,sc,NL}}{\Delta\sigma_{0,sc,L}}$	$\frac{L_{sc,NL}}{L_{sc,L}}$
	$\Delta\sigma_{0,sc}$	L_{sc}	$\Delta\sigma_{0,sc}$	L_{sc}		
$[s]$	[MPa]	[year]	[MPa]	[year]	[%]	[%]
2.80	100	1.9	77	3.7	77	191
2.90	98	2.0	77	4.2	79	208
3.00	98	2.0	78	3.9	80	190
3.10	101	1.6	76	4.0	75	253
3.20	106	1.5	76	4.3	72	281
3.30	94	2.5	74	5.1	79	204
3.40	87	2.6	77	5.9	89	225
3.50	100	2.7	79	6.4	79	237

Table G.12: Maximum stress range $\Delta\sigma_{0,sc}$ and fatigue life time L_{sc} for irregular waves with $H_s = 1.0\,m$ and $T_p = 2.8\,s - 3.5\,s$. SN curve C2 is used. The critical point is the top point at the middle of a member perpendicular to the wave direction.

	Linear (L)		Nonlinear (NL)			
T_p	$\Delta\sigma_{0,sc}$	L_{sc}	$\Delta\sigma_{0,sc}$	L_{sc}	$\frac{\Delta\sigma_{0,sc,NL}}{\Delta\sigma_{0,sc,L}}$	$\frac{L_{sc,NL}}{L_{sc,L}}$
$[s]$	[MPa]	[year]	[MPa]	[year]	[%]	[%]
3.20	140	0.46	91	1.8	65	399
3.30	135	0.54	93	1.9	69	343
3.40	113	0.65	90	2.2	80	338
3.50	114	0.92	85	2.4	75	260
3.58	120	0.93	85	3.1	71	330
3.60	129	0.81	88	2.8	69	341
3.70	113	1.0	89	3.2	79	304
3.80	115	1.1	87	3.1	76	288

Table G.13: Maximum stress range $\Delta\sigma_{0,sc}$ and fatigue life time L_{sc} for irregular waves with $H_s = 1.3\,m$ and $T_p = 3.2\,s - 3.8\,s$. SN curve C2 is used. The critical point is the top point at the middle of a member perpendicular to the wave direction.

	Linear (L)		Nonlinear (NL)			
H_s	$\Delta\sigma_{0,sc}$	L_{sc}	$\Delta\sigma_{0,sc}$	L_{sc}	$\frac{\Delta\sigma_{0,sc,NL}}{\Delta\sigma_{0,sc,L}}$	$\frac{L_{sc,NL}}{L_{sc,L}}$
$[s]$	[MPa]	[year]	[MPa]	[year]	[%]	[%]
0.2	21	4441	20	4217	96	95
0.3	28	543	31	515	108	95
0.4	45	118	43	138	97	117
0.5	52	38	48	47	92	125
0.6	62	17	58	20	93	121
0.7	81	7	66	9	82	136

Table G.14: Maximum stress range $\Delta\sigma_{0,sc}$ and fatigue life time L_{sc} for irregular waves with $T_p = 2.4\,s$ and $H_s = 0.2\,m - 0.7\,m$. SN curve C2 is used. The critical point is the top point at the middle of a member perpendicular to the wave direction.

H_s [s]	Linear (L) $\Delta\sigma_{0,sc}$ [MPa]	Linear (L) L_{sc} [year]	Nonlinear (NL) $\Delta\sigma_{0,sc}$ [MPa]	Nonlinear (NL) L_{sc} [year]	$\frac{\Delta\sigma_{0,sc,NL}}{\Delta\sigma_{0,sc,L}}$ [%]	$\frac{L_{sc,NL}}{L_{sc,L}}$ [%]
0.4	45	170	39	245	87	144
0.5	46	70	45	76	96	109
0.6	63	22	54	32	85	143
0.7	72	11	67	16	93	141
0.8	79	5	66	9	84	174
0.9	90	3	71	6	79	179
1.0	100	2	77	4	77	191

Table G.15: Maximum stress range $\Delta\sigma_{0,sc}$ and fatigue life time L_{sc} for irregular waves with $T_p = 2.8s$ and $H_s = 0.4m - 1.0m$. SN curve C2 is used. The critical point is the top point at the middle of a member perpendicular to the wave direction.

H_s [s]	Linear (L) $\Delta\sigma_{0,sc}$ [MPa]	Linear (L) L_{sc} [year]	Nonlinear (NL) $\Delta\sigma_{0,sc}$ [MPa]	Nonlinear (NL) L_{sc} [year]	$\frac{\Delta\sigma_{0,sc,NL}}{\Delta\sigma_{0,sc,L}}$ [%]	$\frac{L_{sc,NL}}{L_{sc,L}}$ [%]
0.7	75	11	59	18	79	161
0.8	80	7	67	10	84	145
0.9	82	4	77	7	94	184
1.0	106	2	76	4	72	281
1.1	120	1	90	3	75	237
1.2	119	1	85	2	71	250
1.3	140	0	91	2	65	399

Table G.16: Maximum stress range $\Delta\sigma_{0,sc}$ and fatigue life time L_{sc} for irregular waves with $T_p = 3.2s$ and $H_s = 0.7m - 1.3m$. SN curve C2 is used. The critical point is the top point at the middle of a member perpendicular to the wave direction.

	Linear (L)		Nonlinear (NL)			
H_s	$\Delta\sigma_{0,sc}$	L_{sc}	$\Delta\sigma_{0,sc}$	L_{sc}	$\frac{\Delta\sigma_{0,sc,NL}}{\Delta\sigma_{0,sc,L}}$	$\frac{L_{sc,NL}}{L_{sc,L}}$
$[s]$	[MPa]	[year]	[MPa]	[year]	[%]	[%]
1.0	100	2.7	79	6.4	79	237
1.1	98	2.0	88	4.4	90	223
1.2	103	1.3	84	3.2	82	248
1.3	114	0.9	85	2.4	75	260
1.4	125	0.6	85	2.1	68	364
1.5	141	0.4	90	1.7	64	424
1.6	150	0.3	89	1.4	59	488

Table G.17: Maximum stress range $\Delta\sigma_{0,sc}$ and fatigue life time L_{sc} for irregular waves with $T_p = 3.5s$ and $H_s = 0.7m - 1.3m$. SN curve C2 is used. The critical point is the top point at the middle of a member perpendicular to the wave direction.

R A P P O R T E R
UTGITT VED
INSTITUTT FOR MARIN TEKNIKK
(tidligere: FAKULTET FOR MARIN TEKNIKK)
NORGES TEKNISK-NATURVITENSKAPELIGE UNIVERSITET

UR-79-01 Brigt Hatlestad, MK:	The finite element method used in a fatigue evaluation of fixed offshore platforms. (Dr.Ing. Thesis)
UR-79-02 Erik Pettersen, MK:	Analysis and design of cellular structures. (Dr.Ing. Thesis)
UR-79-03 Sverre Valsgård, MK:	Finite difference and finite element methods applied to nonlinear analysis of plated structures. (Dr.Ing. Thesis)
UR-79-04 Nils T. Nordsve, MK:	Finite element collapse analysis of structural members considering imperfections and stresses due to fabrication. (Dr.Ing. Thesis)
UR-79-05 Ivar J. Fylling, MK:	Analysis of towline forces in ocean towing systems. (Dr.Ing. Thesis)
UR-80-06 Nils Sandsmark, MM:	Analysis of Stationary and Transient Heat Conduction by the Use of the Finite Element Method. (Dr.Ing. Thesis)
UR-80-09 Sverre Haver, MK:	Analysis of uncertainties related to the stochastic modelling of ocean waves. (Dr.Ing. Thesis)
UR-85-46 Alf G. Engseth, MK:	Finite element collapse analysis of tubular steel offshore structures. (Dr.Ing. Thesis)
UR-86-47 Dengody Sheshappa, MP:	A Computer Design Model for Optimizing Fishing Vessel Designs Based on Techno-Economic Analysis. (Dr.Ing. Thesis)
UR-86-48 Vidar Aanesland, MH:	A Theoretical and Numerical Study of Ship Wave Resistance. (Dr.Ing. Thesis)
UR-86-49 Heinz-Joachim Wessel, MK:	Fracture Mechanics Analysis of Crack Growth in Plate Girders. (Dr.Ing. Thesis)
UR-86-50 Jon Taby, MK:	Ultimate and Post-ultimate Strength of Dented Tubular Members. (Dr.Ing. Thesis)

UR-86-51 Walter Lian, MH:	A Numerical Study of Two-Dimensional Separated Flow Past Bluff Bodies at Moderate KC-Numbers. (Dr.Ing. Thesis)
UR-86-52 Bjørn Sortland, MH:	Force Measurements in Oscillating Flow on Ship Sections and Circular Cylinders in a U-Tube Water Tank. (Dr.Ing. Thesis)
UR-86-53 Kurt Strand, MM:	A System Dynamic Approach to One-dimensional Fluid Flow. (Dr.Ing. Thesis)
UR-86-54 Arne Edvin Løken, MH:	Three Dimensional Second Order Hydrodynamic Effects on Ocean Structures in Waves. (Dr.Ing. Thesis)
UR-86-55 Sigurd Falch, MH:	A Numerical Study of Slamming of Two-Dimensional Bodies. (Dr.Ing. Thesis)
UR-87-56 Arne Braathen, MH:	Application of a Vortex Tracking Method to the Prediction of Roll Damping of a Two-Dimension Floating Body. (Dr.Ing. Thesis)
UR-87-57 Bernt Leira, MR:	Gaussian Vector Processes for Reliability Analysis involving Wave-Induced Load Effects. (Dr.Ing. Thesis)
UR-87-58 Magnus Småvik, MM:	Thermal Load and Process Characteristics in a Two-Stroke Diesel Engine with Thermal Barriers (in Norwegian). (Dr.Ing. Thesis)
MTA-88-59 Bernt Arild Bremdal, MP:	An Investigation of Marine Installation Processes - A Knowledge - Based Planning Approach. (Dr.Ing. Thesis)
MTA-88-60 Xu Jun, MK:	Non-linear Dynamic Analysis of Space-framed Offshore Structures. (Dr.Ing. Thesis)
MTA-89-61 Gang Miao, MH:	Hydrodynamic Forces and Dynamic Responses of Circular Cylinders in Wave Zones. (Dr.Ing. Thesis)
MTA-89-62 Martin Greenhow, MH:	Linear and Non-Linear Studies of Waves and Floating Bodies. Part I and Part II. (Dr.Techn. Thesis)
MTA-89-63 Chang Li, MH:	Force Coefficients of Spheres and Cubes in Oscillatory Flow with and without Current. (Dr.Ing. Thesis)
MTA-89-64 Hu Ying, MP:	A Study of Marketing and Design in

	Development of Marine Transport Systems. (Dr.Ing. Thesis)
MTA-89-65 Arild Jæger, MH:	Seakeeping, Dynamic Stability and Performance of a Wedge Shaped Planing Hull. (Dr.Ing. Thesis)
MTA-89-66 Chan Siu Hung, MM:	The dynamic characteristics of tilting-pad bearings.
MTA-89-67 Kim Wikstrøm, MP:	Analysis av projekteringen for ett offshore projekt. (Licenciat-avhandling)
MTA-89-68 Jiao Guoyang, MR:	Reliability Analysis of Crack Growth under Random Loading, considering Model Updating. (Dr.Ing. Thesis)
MTA-89-69 Arnt Olufsen, MK:	Uncertainty and Reliability Analysis of Fixed Offshore Structures. (Dr.Ing. Thesis)
MTA-89-70 Wu Yu-Lin, MR:	System Reliability Analyses of Offshore Structures using improved Truss and Beam Models. (Dr.Ing. Thesis)
MTA-90-71 Jan Roger Hoff, MH:	Three-dimensional Green function of a vessel with forward speed in waves. (Dr.Ing. Thesis)
MTA-90-72 Rong Zhao, MH:	Slow-Drift Motions of a Moored Two-Dimensional Body in Irregular Waves. (Dr.Ing. Thesis)
MTA-90-73 Atle Minsaas, MP:	Economical Risk Analysis. (Dr.Ing. Thesis)
MTA-90-74 Knut-Aril Farnes, MK:	Long-term Statistics of Response in Non-linear Marine Structures. (Dr.Ing. Thesis)
MTA-90-75 Torbjørn Sotberg, MK:	Application of Reliability Methods for Safety Assessment of Submarine Pipelines. (Dr.Ing. Thesis)
MTA-90-76 Zeuthen, Steffen, MP:	SEAMAID. A computational model of the design process in a constraint-based logic programming environment. An example from the offshore domain. (Dr.Ing. Thesis)
MTA-91-77 Haagensen, Sven, MM:	Fuel Dependant Cyclic Variability in a Spark Ignition Engine - An Optical Approach. (Dr.Ing. Thesis)
MTA-91-78 Løland, Geir, MH:	Current forces on and flow through fish farms.

	(Dr.Ing. Thesis)
MTA-91-79 Hoen, Christopher, MK:	System Identification of Structures Excited by Stochastic Load Processes. (Dr.Ing. Thesis)
MTA-91-80 Haugen, Stein, MK:	Probabilistic Evaluation of Frequency of Collision between Ships and Offshore Platforms. (Dr.Ing. Thesis)
MTA-91-81 Sødahl, Nils, MK:	Methods for Design and Analysis of Flexible Risers. (Dr.Ing. Thesis)
MTA-91-82 Ormberg, Harald, MK:	Non-linear Response Analysis of Floating Fish Farm Systems. (Dr.Ing. Thesis)
MTA-91-83 Marley, Mark J., MK:	Time Variant Reliability under Fatigue Degradation. (Dr.Ing. Thesis)
MTA-91-84 Krokstad, Jørgen R., MH:	Second-order Loads in Multidirectional Seas. (Dr.Ing. Thesis)
MTA-91-85 Molteberg, Gunnar A., MM:	The Application of System Identification Techniques to Performance Monitoring of Four Stroke Turbocharged Diesel Engines. (Dr.Ing. Thesis)
MTA-92-86 Mørch, Hans Jørgen Bjelke, MH:	Aspects of Hydrofoil Design: with Emphasis on Hydrofoil Interaction in Calm Water. (Dr.Ing. Thesis)
MTA-92-87 Chan Siu Hung, MM:	Nonlinear Analysis of Rotordynamic Instabilities in High-speed Turbomachinery. (Dr.Ing. Thesis)
MTA-92-88 Bessason, Bjarni, MK:	Assessment of Earthquake Loading and Response of Seismically Isolated Bridges. (Dr.Ing. Thesis)
MTA-92-89 Langli, Geir, MP:	Improving Operational Safety through exploitation of Design Knowledge - an investigation of offshore platform safety. (Dr.Ing. Thesis)
MTA-92-90 Sævik, Svein, MK:	On Stresses and Fatigue in Flexible Pipes. (Dr.Ing. Thesis)
MTA-92-91 Ask, Tor Ø., MM:	Ignition and Flame Growth in Lean Gas-Air Mixtures. An Experimental Study with a Schlieren System. (Dr.Ing. Thesis)

MTA-86-92 Hessen, Gunnar, MK:	Fracture Mechanics Analysis of Stiffened Tubular Members. (Dr.Ing. Thesis)
MTA-93-93 Steinebach, Christian, MM:	Knowledge Based Systems for Diagnosis of Rotating Machinery. (Dr.Ing. Thesis)
MTA-93-94 Dalane, Jan Inge, MK:	System Reliability in Design and Maintenance of Fixed Offshore Structures. (Dr.Ing. Thesis)
MTA-93-95 Steen, Sverre, MH:	Cobblestone Effect on SES. (Dr.Ing. Thesis)
MTA-93-96 Karunakaran, Daniel, MK:	Nonlinear Dynamic Response and Reliability Analysis of Drag-dominated Offshore Platforms. (Dr.Ing. Thesis)
MTA-93-97 Hagen, Arnulf, MP:	The Framework of a Design Process Language. (Dr.Ing. Thesis)
MTA-93-98 Nordrik, Rune, MM:	Investigation of Spark Ignition and Autoignition in Methane and Air Using Computational Fluid Dynamics and Chemical Reaction Kinetics. A Numerical Study of Ignition Processes in Internal Combustion Engines. (Dr.Ing. Thesis)
MTA-94-99 Passano, Elizabeth, MK:	Efficient Analysis of Nonlinear Slender Marine Structures. (Dr.Ing. Thesis)
MTA-94-100 Kvålsvold, Jan, MH:	Hydroelastic Modelling of Wetdeck Slamming on Multihull Vessels. (Dr.Ing. Thesis)
MTA-94-102 Bech, Sidsel M., MK:	Experimental and Numerical Determination of Stiffness and Strength of GRP/PVC Sandwich Structures. (Dr.Ing. Thesis)
MTA-95-103 Paulsen, Hallvard, MM:	A Study of Transient Jet and Spray using a Schlieren Method and Digital Image Processing. (Dr.Ing. Thesis)
MTA-95-104 Hovde, Geir Olav, MK:	Fatigue and Overload Reliability of Offshore Structural Systems, Considering the Effect of Inspection and Repair. (Dr.Ing. Thesis)
MTA-95-105 Wang, Xiaozhi, MK:	Reliability Analysis of Production Ships with Emphasis on Load Combination and Ultimate Strength. (Dr.Ing. Thesis)
MTA-95-106 Ulstein, Tore, MH:	Nonlinear Effects of a Flexible Stern Seal Bag on Cobblestone Oscillations of an SES. (Dr.Ing. Thesis)

MTA-95-107 Solaas, Frøydis, MH:	Analytical and Numerical Studies of Sloshing in Tanks. (Dr.Ing. Thesis)
MTA-95-108 Hellan, øyvind, MK:	Nonlinear Pushover and Cyclic Analyses in Ultimate Limit State Design and Reassessment of Tubular Steel Offshore Structures. (Dr.Ing. Thesis)
MTA-95-109 Hermundstad, Ole A., MK:	Theoretical and Experimental Hydroelastic Analysis of High Speed Vessels. (Dr.Ing. Thesis)
MTA-96-110 Bratland, Anne K., MH:	Wave-Current Interaction Effects on Large-Volume Bodies in Water of Finite Depth. (Dr.Ing. Thesis)
MTA-96-111 Herfjord, Kjell, MH:	A Study of Two-dimensional Separated Flow by a Combination of the Finite Element Method and Navier-Stokes Equations. (Dr.Ing. Thesis)
MTA-96-112 Æsøy, Vilmar, MM:	Hot Surface Assisted Compression Ignition in a Direct Injection Natural Gas Engine. (Dr.Ing. Thesis)
MTA-96-113 Eknes, Monika L., MK:	Escalation Scenarios Initiated by Gas Explosions on Offshore Installations. (Dr.Ing. Thesis)
MTA-96-114 Erikstad, Stein O., MP:	A Decision Support Model for Preliminary Ship Design. (Dr.Ing. Thesis)
MTA-96-115 Pedersen, Egil, MH:	A Nautical Study of Towed Marine Seismic Streamer Cable Configurations. (Dr.Ing. Thesis)
MTA-97-116 Moksnes, Paul O., MM:	Modelling Two-Phase Thermo-Fluid Systems Using Bond Graphs. (Dr.Ing. Thesis)
MTA-97-117 Halse, Karl H., MK:	On Vortex Shedding and Prediction of Vortex-Induced Vibrations of Circular Cylinders. (Dr.Ing. Thesis)
MTA-97-118 Igland, Ragnar T., MK:	Reliability Analysis of Pipelines during Laying, considering Ultimate Strength under Combined Loads. (Dr.Ing. Thesis)
MTA-97-119 Pedersen, Hans-P., MP:	Levendefiskteknologi for fiskefartøy. (Dr.Ing. Thesis)
MTA-98-120 Vikestad, Kyrre, MK:	Multi-Frequency Response of a Cylinder Subjected to Vortex Shedding and Support

	Motions. (Dr.Ing. Thesis)
MTA-98-121 Azadi, Mohammad R. E., MK:	Analysis of Static and Dynamic Pile-Soil-Jacket Behaviour. (Dr.Ing. Thesis)
MTA-98-122 Ulltang, Terje, MP:	A Communication Model for Product Information. (Dr.Ing. Thesis)
MTA-98-123 Torbergsen, Erik, MM:	Impeller/Diffuser Interaction Forces in Centrifugal Pumps. (Dr.Ing. Thesis)
MTA-98-124 Hansen, Edmond, MH:	A Discrete Element Model to Study Marginal Ice Zone Dynamics and the Behaviour of Vessels Moored in Broken Ice. (Dr.Ing. Thesis)
MTA-98-125 Videiro, Paulo M., MK:	Reliability Based Design of Marine Structures. (Dr.Ing. Thesis)
MTA-99-126 Mainçon, Philippe, MK:	Fatigue Reliability of Long Welds Application to Titanium Risers. (Dr.Ing. Thesis)
MTA-99-127 Haugen, Elin M., MH:	Hydroelastic Analysis of Slamming on Stiffened Plates with Application to Catamaran Wetdecks. (Dr.Ing. Thesis)
MTA-99-128 Langhelle, Nina K., MK:	Experimental Validation and Calibration of Nonlinear Finite Element Models for Use in Design of Aluminium Structures Exposed to Fire. (Dr.Ing. Thesis)
MTA-99-129 Berstad, Are J., MK:	Calculation of Fatigue Damage in Ship Structures. (Dr.Ing. Thesis)
MTA-99-130 Andersen, Trond M., MM:	Short Term Maintenance Planning. (Dr.Ing. Thesis)
MTA-99-131 Tveiten, Bård Wathne, MK:	Fatigue Assessment of Welded Aluminium Ship Details. (Dr.Ing. Thesis)
MTA-99-132 Søreide, Fredrik, MP:	Applications of underwater technology in deep water archaeology. Principles and practice. (Dr.Ing. Thesis)
MTA-99-133 Tønnessen, Rune, MH:	A Finite Element Method Applied to Unsteady Viscous Flow Around 2D Blunt Bodies With Sharp Corners. (Dr.Ing. Thesis)
MTA-99-134 Elvekrok, Dag R., MP:	Engineering Integration in Field Development Projects in the Norwegian Oil and Gas Industry. The Supplier Management of Norne. (Dr.Ing.

	Thesis)
MTA-99-135 Fagerholt, Kjetil, MP:	Optimeringsbaserte Metoder for Ruteplanlegging innen skipsfart. (Dr.Ing. Thesis)
MTA-99-136 Bysveen, Marie, MM:	Visualization in Two Directions on a Dynamic Combustion Rig for Studies of Fuel Quality. (Dr.Ing. Thesis)
MTA-2000-137 Storteig, Eskild, MM:	Dynamic characteristics and leakage performance of liquid annular seals in centrifugal pumps. (Dr.Ing. Thesis)
MTA-2000-138 Sagli, Gro, MK:	Model uncertainty and simplified estimates of long term extremes of hull girder loads in ships. (Dr.Ing. Thesis)
MTA-2000-139 Tronstad, Harald, MK:	Nonlinear analysis and design of cable net structures like fishing gear based on the finite element method. (Dr.Ing. Thesis)
MTA-2000-140 Kroneberg, André, MP:	Innovation in shipping by using scenarios. (Dr.Ing. Thesis)
MTA-2000-141 Haslum, Herbjørn Alf, MH:	Simplified methods applied to nonlinear motion of spar platforms. (Dr.Ing. Thesis)
MTA-2001-142 Samdal, Ole Johan, MM:	Modelling of Degradation Mechanisms and Stressor Interaction on Static Mechanical Equipment Residual Lifetime. (Dr.Ing. Thesis)
MTA-2001-143 Baarholm, Rolf Jarle, MH:	Theoretical and experimental studies of wave impact underneath decks of offshore platforms. (Dr.Ing. Thesis)
MTA-2001-144 Wang, Lihua, MK:	Probabilistic Analysis of Nonlinear Wave-induced Loads on Ships. (Dr.Ing. Thesis)
MTA-2001-145 Kristensen, Odd H. Holt, MK:	Ultimate Capacity of Aluminium Plates under Multiple Loads, Considering HAZ Properties. (Dr.Ing. Thesis)
MTA-2001-146 Greco, Marilena, MH:	A Two-Dimensional Study of Green-Water Loading. (Dr.Ing. Thesis)
MTA-2001-147 Heggelund, Svein E., MK:	Calculation of Global Design Loads and Load Effects in Large High Speed Catamarans. (Dr.Ing. Thesis)

MTA-2001-148 Babalola, Olusegun T., MK:	Fatigue Strength of Titanium Risers - Defect Sensitivity. (Dr.Ing. Thesis)
MTA-2001-149 Mohammed, Abuu K., MK:	Nonlinear Shell Finite Elements for Ultimate Strength and Collapse Analysis of Ship Structures. (Dr.Ing. Thesis)
MTA-2002-150 Holmedal, Lars E., MH:	Wave-current interactions in the vicinity of the sea bed. (Dr.Ing. Thesis)
MTA-2002-151 Rognebakke, Olav F., MH:	Sloshing in rectangular tanks and interaction with ship motions. (Dr.Ing. Thesis)
MTA-2002-152 Lader, Pål Furset, MH:	Geometry and Kinematics of Breaking Waves. (Dr.Ing. Thesis)
MTA-2002-153 Yang, Qinzheng, MH:	Wash and wave resistance of ships in finite water depth. (Dr.Ing. Thesis)
MTA-2002-154 Melhus, Øyvin, MM:	Utilization of VOC in Diesel Engines. Ignition and combustion of VOC released by crude oil tankers. (Dr.Ing. Thesis)
MTA-2002-155 Ronæss, Marit, MH:	Wave Induced Motions of Two Ships Advancing on Parallel Course. (Dr.Ing. Thesis)
MTA-2002-156 Økland, Ole D., MK:	Numerical and experimental investigation of whipping in twin hull vessels exposed to severe wet deck slamming. (Dr.Ing. Thesis)
MTA-2002-157 Ge, Chunhua, MK:	Global Hydroelastic Response of Catamarans due to Wet Deck Slamming. (Dr.Ing. Thesis)
MTA-2002-158 Byklum, Eirik, MK:	Nonlinear Shell Finite Elements for Ultimate Strength and Collapse Analysis of Ship Structures. (Dr.Ing. Thesis)
IMT-2003-1 Chen, Haibo, MK:	Probabilistic Evaluation of FPSO-Tanker Collision in Tandem Offloading Operation. (Dr.Ing. Thesis)
IMT-2003-2 Skaugset, Kjetil Bjørn, MK:	On the Suppression of Vortex Induced Vibrations of Circular Cylinders by Radial Water Jets. (Dr.Ing. Thesis)
IMT-2003-3 Chezhian, Muthu	Three-Dimensional Analysis of Slamming. (Dr.Ing. Thesis)
IMT-2003-4 Buhaug, Øyvind	Deposit Formation on Cylinder Liner Surfaces

	in Medium Speed Engines. (Dr.Ing. Thesis)
IMT-2003-5 Tregde, Vidar	Aspects of Ship Design: Optimization of Aft Hull with Inverse Geometry Design. (Dr.Ing. Thesis)
IMT-2003-6 Wist, Hanne Therese	Statistical Properties of Successive Ocean Wave Parameters. (Dr.Ing. Thesis)
IMT-2004-7 Ransau, Samuel	Numerical Methods for Flows with Evolving Interfaces. (Dr.Ing. Thesis)
IMT-2004-8 Soma, Torkel	Blue-Chip or Sub-Standard. A data interrogation approach of identity safety characteristics of shipping organization. (Dr.Ing. Thesis)
IMT-2004-9 Ersdal, Svein	An experimental study of hydrodynamic forces on cylinders and cables in near axial flow. (Dr.Ing. Thesis)
IMT-2005-10 Brodtkorb, Per Andreas	The Probability of Occurrence of Dangerous Wave Situations at Sea. (Dr.Ing. Thesis)
IMT-2005-11 Yttervik, Rune	Ocean current variability in relation to offshore engineering. (Dr.Ing. Thesis)
IMT-2005-12 Fredheim, Arne	Current Forces on Net-Structures. (Dr.Ing. Thesis)
IMT-2005-13 Heggernes, Kjetil	Flow around marine structures. (Dr.Ing. Thesis)
IMT-2005-14 Fouques, Sebastien	Lagrangian Modelling of Ocean Surface Waves and Synthetic Aperture Radar Wave Measurements. (Dr.Ing. Thesis)
IMT-2006-15 Holm, Håvard	Numerical calculation of viscous free surface flow around marine structures. (Dr.Ing. Thesis)
IMT-2006-16 Bjørheim, Lars G.	Failure Assessment of Long Through Thickness Fatigue Cracks in Ship Hulls. (Dr.Ing. Thesis)
IMT-2006-17 Hansson, Lisbeth	Safety Management for Prevention of Occupational Accidents. (Dr.Ing. Thesis)
IMT-2006-18 Zhu, Xinying	Application of the CIP Method to Strongly Nonlinear Wave-Body Interaction Problems. (Dr.Ing. Thesis)
IMT-2006-19 Reite, Karl Johan	Modelling and Control of Trawl Systems.

	(Dr.Ing. Thesis)
IMT-2006-20 Smogeli, Øyvind Notland	Control of Marine Propellers. From Normal to Extreme Conditions. (Dr.Ing. Thesis)
IMT-2007-21 Storhaug, Gaute	Experimental Investigation of Wave Induced Vibrations and Their Effect on the Fatigue Loading of Ships. (Dr.Ing. Thesis)
IMT-2007-22 Sun, Hui	A Boundary Element Method Applied to Strongly Nonlinear Wave-Body Interaction Problems. (PhD Thesis, CeSOS)
IMT-2007-23 Rustad, Anne Marthine	Modelling and Control of Top Tensioned Risers. (PhD Thesis, CeSOS)
IMT-2007-24 Johansen, Vegar	Modelling flexible slender system for real-time simulations and control applications.
IMT-2007-25 Wroldsen, Anders Sunde	Modelling and control of tensegrity structures. (PhD Thesis, CeSOS)
IMT-2007-26 Aronsen, Kristoffer Høye	An experimental investigation of in-line and combined in-line and cross flow vortex induced vibrations. (Dr.avhandling, IMT)
IMT-2007-27 Zhen, Gao	Stochastic response analysis of mooring systems with emphasis on frequency-domain analysis of fatgue due to wide-band processes. (PhD-thesis CeSOS).
IMT-2007-28 Thorstensen, Tom Anders	Lifetime Profit Modelling of Ageing Systems Utilizing Information about Technical Condition. Dr.ing. thesis, IMT.
IMT-2008-39 Refsnes, Jon Erling Gorset	Nonlinear Model-Based Control of Slender Body AUVs, PhD-Thesis, IMT
IMT-2008-30 Pákozdi, Csaba	A Smoothed Particle Hydrodynamics Study of Two-dimensional Nonlinear Sloshing in Rectangular Tanks. Dr.ing.thesis, IMT.
IMT-2008-31 Berntsen, Per Ivar B.	Structural Reliability Based Position Mooring. PhD-Thesis, IMT.

IMT-2008-32 Ye, Naiquan	Fatigues Assessment of Aluminium Welded Box stiffener Joints in ships. Dr.ing.-Thesis, IMT.
IMT-2008-33 Radan, Damir	Integrated Control of Marine Electrical Power Systems. PhD-Thesis, IMT.